Real-time and *in situ* hyperspectral Raman imaging of high-temperature solid-solid reactions in silicate ceramics

Dissertation

zur

Erlangung des Doktorgrades (Dr. rer. nat.)

der

Mathematisch-Naturwissenschaftlichen Fakultät

der

Rheinischen Friedrich-Wilhelms-Universität Bonn

vorgelegt von

Kerstin Hauke

aus

Hannover

Abgegeben am 28.09.2021

Bonn

Angefertigt mit Genehmigung der Mathematisch-Naturwissenschaftlichen Fakultät der
Rheinischen Friedrich-Wilhelms-Universität Bonn

1. Gutachter: Prof. Dr. Thorsten Geisler-Wierwille

2. Gutachter: Prof. Dr. Helge Jansen

Tag der Promotion: 20.12.2021

Erscheinungsjahr: 2022

Table of Content

I Preface

This thesis comprises two articles published in the *'Journal of the American Ceramic Society'* and in *'Applied Sciences'* and one manuscript which will be submitted soon to an international peer-reviewed journal.

Published in a peer-reviewed Journal:

Chapter 2:

STANGE, K.; Lenting, C.; Geisler, T. (2018) Insights into the evolution of carbonate-bearing kaolin during sintering revealed by in situ hyperspectral Raman imaging. In *J. Am. Ceram. Soc.*; 101, 897–910. DOI:10.1111/JACE.15209

Chapter 3:

HAUKE, K.; Kehren, J.; Böhme, N.; Zimmer, S.; Geisler, T.: In Situ Hyperspectral Raman Imaging: A New Method to Investigate Sintering Processes of Ceramic Material at High-temperature. Appl. Sci. 2012, 9 (7), 1310. DOI: 10.3390/app9071310

Chapter 4 is an unpublished manuscript which will be submitted to a peer-reviewed Journal soon.

Chapter 5 - 7 are three additional chapters of unpublished data complementing the thesis and will be published in the future.

Chapter 8 is a summary discussion of the Chapters 1 - 7.

Chapter 9 gives a short conclusion and an outlook

Chapter 10 contains the reference list of the main thesis

Chapter V contains supplementary and additional material for all chapters outlined above, as well as co-authored publication abstracts, conference abstracts and posters and co-authored conference abstracts that have been generated during PhD candidature and that are related to the PhD project.

The supplementary and additional material is as follows:

Co-authored articles that are closely related to the PhD project, but are part of the PhD thesis of Nadine Böhme:

Böhme, N., **Hauke, K**., Neuroth, M., Geisler. T. (2020) In Situ Hyperspectral Raman Imaging of Ternesite Formation and Decomposition at High Temperatures Article in *Minerals*, 10, 287. DOI: 10.3390/min10030287

Böhme N., **Hauke K**., Neuroth M., Geisler, T. (2019) In situ Raman imaging of high-temperature solid state reactions in the $CaSO_4$–SiO_2 system. Article in *Int. J. Coal. Sci.Technol.,* 6, 247-259.
DOI: 10.1007/s40789-019-0252-7

Supervised Bachelor- and Master theses that are related to the PhD project:

Wintersberg F. (2017) Synthese und Charakterisierung eines Aluminium-Silizium-Spinells *Bachelor thesis*

Brohsonn N. (2017) High temperature Raman spectroscopy of wollastonite *Bachelor thesis*

Kehren J. (2018) The formation of calcium silicates in the CaO-SiO_2-system studied by in situ hyperspectral Raman imaging (HSRI) *Master thesis*

Zimmer S. (2019) In situ hyperspectral Raman imaging of high temperature solid-solid reactions in the system Al_2O_3-SiO_2-CaO *Master thesis*

Zöller A. (2019) Investigation of high temperature processes in the CaO-FeO-Al_2O_3-SiO_2-System studied by in situ hyperspectral Raman imaging *Bachelor thesis*

First author conference abstracts (oral presentation)

Stange K., Lenting, C., and Geisler T. (2017) Space-, time-, and temperature-resolved hyperspectral Raman imaging of high-temperature sintering reactions in kaolinite-based ceramics. Conference Abstract *PacRim12, Abstracts 2017*, 2685900.

Stange K., Böhme N., Geisler T. (2018) Untersuchungen von keramischen Sinterprozessen im System CaO-Al_2O_3-SiO_2 mit Hilfe der bildgebenden in situ Raman-Spektroskopie. Conference Abstract *Deutsche Mineralogische Gesellschaft Workshop.*

Stange K., Kehren J., Böhme N., Zimmer S., Geisler T. (2018) In situ hyperspectral Raman imaging: A new method to investigate solid-solid reactions in Ceramic materials during firing. Conference abstract *GeoBonn Abstracts 2019,* 12092018.

Hauke K, Zimmer S., Böhme N., Geisler T. (2019) In situ Untersuchungen von Mineralreaktionen
während des keramischen Sinterprozesses mit Zeit-, Raum-, und Temperaturaufgelöster Ramanspektroskopie Conference Abstract *Deutsche Mineralogische Gesellschaft Workshop.*

Hauke K., Kehren J., Böhme N., Zimmer S. and Geisler T. (2019) Investigation of phase reactions during firing with in situ hyperspectral Raman imaging with temperature and time. Conference Abstract *Inside Raman Seminar*, Reutlingen, *invited talk*

Hauke K, Zimmer S., Böhme N., Geisler T. (2021) In situ Untersuchung der Bildungskinetik von
Gehlenit bei verschiedenen Brenntemperaturen mit bildgebender Ramanspektroskopie Conference Abstract *Deutsche Mineralogische Gesellschaft virtual Workshop.*

First author conference abstracts (poster presentation)

Hauke K., Kehren J., Böhme N., Zimmer S. and Geisler T. (2019) Studying the mineralogical and
textural evolution of a kaolinite-calcite mixture with time at temperatures between 800 and 1100°C with hyperspectral Raman imaging Conference Abstract *16th Confocal Raman Imaging Symposium,* Ulm, *awarded with the poster prize in bronze*

Hauke K, Zimmer S., Böhme N., Geisler T. (2019) Crystallization Kinetics and Phase Relations of
Calcium-Aluminate-Silicates Investigated by In Situ Hyperspectral Raman Imaging Conference Abstract *Deutsche Mineralogische Gesellschaft* virtual poster session.

II Danksagung

Großer Dank gilt meinem Doktorvater Prof. Dr. Thorsten Geisler-Wierwille. Er hatte die Idee *in situ* Hochtemperatur-Raman-Bildgebung an Keramiken auszuprobieren. Ich bin ihm sehr dankbar, dass er mir dieses unglaublich spannende Thema als Masterarbeitsthema angeboten und darin das Potential für ein Promotionsprojekt gesehen hat. Er hat mir zwei Jahre ein Stipendium der Universität Bonn ermöglicht und mir während der Promotion die Möglichkeit gegeben viele Workshops und Konferenzen zu besuchen, die mich alle sehr weitergebracht haben. Vielen Dank dafür!

Ich möchte meinem Zweitgutachter Prof. Dr. Helge Jansen und den weiteren Mitgliedern meiner Prüfungskommission Prof. Dr. Niko Froitzheim und Prof. Dr. Weigend danken.

Ich danke Dr. Harald Euler und Hans-Henning Friedrich für die Durchführung der XRD-Messungen. Dorothee Paßman und Dr. Sven Oliver Franz danke ich für die Durchführung der RFA-Analysen und Nils Jung für die Präparation meiner Proben. Thomas Schulz, Henrick Blanchard, Dieter Lülsdorf und Philipp Krämer haben mich sehr bei der Installation, Reparatur und technischen Weiterentwicklung des Heizofens bzw. allem Zubehör unterstützt. Dafür bin ich Ihnen sehr dankbar. Große Unterstützung und immer liebe Worte kamen auch von Daniela Bungartz und Dagmar Hambach aus dem Sekretariat. Ihr seid die Seele des Institutes!

Besonderer Dank gilt auch meinen beiden ehemaligen Masterstudierenden Sinje Zimmer und Johannes Kehren. Beide haben außergewöhnlich gute Arbeit geleistet und mich durch viele angeregte Diskussionen unterstützt und weitergebracht. Desweiteren danke ich meinen ehemaligen Bachelorstudierenden Annika Maerks, Nils Brohsonn und Florian Wintersberg. Sie alle haben Teilbereiche des Projektes bearbeitet und es vorangebracht.

Nadine Böhme möchte ich für eine nette Bürogemeinschaft und gute Diskussionen danken.

Ich bin Dr. Christoph Lenting sehr dankbar dafür, dass er mir anfangs geduldig mit dem Ramanspektrometer geholfen und mir viele Fragen beantwortet hat.

Ich möchte Prof. Dr. Olaf Krause für die Unterstützung in den letzten Jahren danken. Ich freue mich auf die weitere Zusammenarbeit!

Vielen Dank auch an meine Kollegen und Freunde, die mich während meines PhDs begleitet haben, die da wären: Mara, Robin, Anna, Linus, Nora, Lars, Micha, Gerrit, Merle, Christoph, Franzi, Kathrin, Moritz und Raùl.

Ganz besonderer Dank gilt meinen Eltern, die mich immer unterstützt haben und die mir die Freiheit gelassen haben mich zu einem neugierigen und alles-in-Frage-stellenden Menschen haben werden lassen. Ohne Euch wäre ich nicht da, wo ich jetzt bin. Auch möchte ich meinen Schwestern danken, die immer für mich da sind und auf deren Unterstützung ich zählen kann! Besonders Katrin gilt ein großes Dankeschön für das Korrekturlesen dieser Arbeit. Vielen Dank auch an meine Patentante Helga für die Unterstützung!

Matthias, Knut und Mikasz, ihr seid meine Familie und ich bin euch für jeden Tag dankbar, den ich mit euch verbringen darf. Ihr macht mein Leben schöner.

***

Für die finanzielle Unterstützung des Projektes danke ich der Deutschen Forschungs-gemeinschaft (Projektnummer: GE1094/22-1).

Ich danke der Universität Bonn für das Promotionsstipendium.

III Abstract

Raman spectroscopy has become one of the most important analytical tools for a wide range of research areas in all sub-disciplines of physics, chemistry, biology and medicine. In the beginning the applications were limited by weak Raman signals and interfering fluorescence. Technical progress leads to higher sensitivity and a better spectral and confocal resolution. Besides point measurements there is nowadays the possibility to record false-color hyperspectral Raman images in two- or three dimensions. Acquisition times of a few milliseconds make it possible to analyze (mineral-) reactions *in situ*. Therefore, Raman spectroscopy is one of only a few techniques that allow an investigation of running processes on a micrometer scale. In combination with heating- or cooling stages or pressure cells it has also become possible to examine the samples under different pressure and temperature conditions, which helps to better understand technical and natural high-temperature processes such as, for instance, metamorphism.

In this study the firing process of silicate ceramics in the system CaO - SiO_2 ± Al_2O_3 ± K_2O were studied *in operando* for the first time by *in situ* hyperspectral Raman spectroscopy. The samples were fired to temperatures of 650 to 1100°C and during this time analyzed *in situ* by hyperspectral Raman imaging. The breakdown of kaolinite and calcite and the formation of calcium (alumina) silicates could be investigated in operando, i.e., while the processes are running, and thus also without the need to quench the sample down to room temperature. Therefore, the formation temperature or -time was determined more precisely than with common *ex situ* temperature- or time series. Moreover, metastable or intermediate phases like pseudowollastonite and an unknown hydrous calcium aluminosilicate, possibly a zeolite, were detected, which have not been detected in *ex situ* experiments. The micrometer-sized spatial resolution enabled the investigation of the formation of dicalcium silicate reaction rims that formed by the reaction between lime and quartz and involves a turnover of the reaction direction. Moreover, the crystallization kinetics and the grain growth of gehlenite were studied in a series of isothermal experiments that was performed at six temperatures between 803 and 1020 ± 5°C. A single experiment thereby contained the information of a multitude of conventional sintering experiments, involving heating and quenching of different samples. A change in the activation energy of gehlenite was observed around 880°C, which may be related to the breakdown of the unknown hydrous aluminosilicate phase.

The application of hyperspectral Raman spectroscopy to investigate ceramic sintering reactions combines for the first time the advantages of in situ high-temperature measurements and the spatial resolution on a micrometer scale of hyperspectral Raman imaging. With this technology, further new insights into the mechanisms and kinetics of the various solid-state reactions during ceramic firing can be expected in the future.

IV Zusammenfassung

Ramanspektroskopie ist eine der wichtigsten Analysemethoden für eine große Bandbreite an Forschungsgebieten in allen Unterdisziplinen der Physik, Chemie, Biologie und Medizin geworden. Anfangs waren die Anwendungen durch geringe Raman Signale und auftretende Fluoreszenzen limitiert. Durch den technischen Fortschritt verbessert sich die Intensitätsausbeute und spektrale, sowie die konfokale Auflösung stetig, sodass sich ständig neue Anwendungsmöglichkeiten erschließen. Seit einigen Jahrzenten ist es möglich nicht nur Punktmessungen durchzuführen, sondern auch zwei- oder gar dreidimensionale falschfarben-Raman Karten anzufertigen und somit ganze Probenkörper zu analysieren. Zählzeiten von wenigen Millisekunden erlauben es (Mineral-) Reaktionen *in situ* zu untersuchen. Ramanspektroskopie gehört somit zu einer der wenigen Techniken, die es möglich machen laufende Prozesse auf Mikrometerebene in operando zu untersuchen. Mit Hilfe von zusätzlichen Heizöfen, Kühlzellen und Druckzellen ist es auch möglich geworden die Proben bei unterschiedlichen Druck- und Temperaturbedingungen zu untersuchen. Das ermöglicht ein besseres Verständnis von technischen und natürlichen Hochtemperatur-prozessen, wie zum Beispiel Metamorphismus.

In diesem Projekt wird der Brennprozess von Silikatkeramiken im System CaO-SiO_2±Al_2O_3±K_2O zum ersten Mal in operando mit in situ Raman-spektroskopie untersucht. The Proben werden bei Temperaturen zwischen ungefähr 650 und 1100 °C gebrannt und währenddessen mit hyperspektralem Raman mapping untersucht. Der Zerfall von Kaolinit und Calcit, sowie die Neubildung und Umwandlung von Calcium (-aluminium) Silikaten kann so direkt untersucht werden, ohne die Probe erst vorher abkühlen zu müssen. Dies hat den Vorteil, dass die Temperatur bzw. Zeit, bei der die Reaktion stattgefunden hat, exakter und direkter bestimmt werden kann, als in herkömmlichen *ex situ* Temperatur- oder Zeitreihen. Zudem konnten metastabile oder intermediäre Phasen wie Pseudowollastonit und eine bisher unbekannte Phase, möglicherweise ein wasserhaltiges Calcium Alumosilikat (Zeolith) registriert werden, die bei einer *ex situ* Messung wahrscheinlich unentdeckt geblieben wären. Die räumliche Auflösung hat es ermöglicht, einen Reaktionssaum aus Dicalcium Silikat zu beobachten, der eine Barriere zwischen den Edukten aus Branntkalk und Quarz bildet und so den Reaktionsmechanismus ändert und einen Wechsel in der Reaktionsrichtung auslöst.

Die Kristallisationskinetik und das Kornwachstum von Gehlenit wurden mit Hilfe einer isothermen Experimentserie bei sechs Temperaturen zwischen 803 und 1020 ± 5°C untersucht. Ein einziges Experiment liefert hierbei die Informationen zahlreicher konventioneller Sinterexperimente, bei denen mehrere Proben aufgeheizt und abgekühlt werden müssten. Die beobachtete Änderung der Aktivierungsenergie bei 880°C könnte möglicherweise im Zusammenhang mit dem Verschwinden des unbekannten wasserhaltigen Alumosilikats stehen.

Dieses Projekt vereint erstmals die Vorteile von räumlich aufgelöster Ramanspektroskopie mit der Möglichkeit die Probe *in situ* bei höheren Temperaturen zu untersuchen. Es ist zu erwarten, das mit dieser Technik viele neue Einblicke in die Mechanismen und Kinetik von verschiedensten Festkörperreaktionen während des (keramischen) Brandes gewonnen werden können.

1 Introduction

Since humankind's earliest history pottery has played an important role in daily and cultural life in the form of craft and art objects[1]. The early importance of pottery in humankind is demonstrated by ancient finds, such as a pottery statuette of a nude female figure dated to 29,000 - 25,000 BC[2] and pottery vessels discovered in the Xianrendong cave in Jiangxi, China, dated back to 20,000 BC[3]. From early on pottery was produced under different firing conditions and from different clays, with kaolinite as primary mineral component. Other minerals such as quartz, feldspar, phyllosilicates, and iron- or titanium oxides were either specifically added to the clay body or occurred naturally in the mined raw material kaolin. This resulted in diverse ceramic end products such as earthenware, stoneware, or porcelain, which have a different phase composition, texture, optical appearance, and different physical properties and, therefore, were and are used for different applications[1,4].

The sequence and interplay of various solid-solid and solid-melt reactions control the resulting properties of the final ceramic product such as chemical permeability, elasticity, mechanical strength, hardness, toughness, whiteness, translucency, resonance, as well as resistance to chemical attack and thermal shock[4]. In particular, understanding the interplay between the microstructure, the phase assemblage, and the bulk material properties has always been a major and formidable challenge for material scientists. A detailed knowledge about the different transformation mechanisms and the temperature-time-transformation dependence of individual reactions during firing of polyphase clay bodies is essential to optimize production technologies and design new ceramic materials with specific physical properties. Recently, additional motivation for understanding the sintering processes at the grain scale has arisen from the possibility of simulating industrial sintering processes of real, complex-shaped parts using the finite element method[5]. Moreover, such understanding is necessary in the field of archaeology to reconstruct ancient pottery production technologies which may in turn give information about ancient trading routes and relationships, and thus about socio-economic aspects in human history[6].

Due to the importance of silicate ceramics, sintering reactions of polyphase clay bodies have been studied intensively by numerous firing experiments that involved quenching of the sintered ceramic bodies to room temperature (RT) and analyzing the reaction product by means of different analytical techniques[7–14]. However, such conventional sintering experiments have several shortcomings, related to the inevitability to quench several different polyphase samples to RT, which makes it difficult to gain information about the textural evolution, the mechanisms, and the kinetics of individual transformation steps, and the possible crystallization of metastable phases. Differential thermal analysis and X-ray diffraction are the only techniques that have routinely been used to investigate the sintering process of polyphase ceramic precursors *in situ* at high temperatures, i.e., while the reactions are proceeding[15]. However, both techniques only provide thermodynamic and mineralogical data about the predominant transformation reactions during sintering (such as dehydroxylation, phase decomposition, polymorphic phase transformations, melting, crystallization, and glass transitions) averaged out over the whole volume of the green body. In these experiments, no information about the textural evolution as a function of temperature, space, and time, can be gained and thus information about the mechanism of single transformation steps involving consecutive or competing elementary

reactions is limited. Therefore, our current knowledge about the mechanisms and kinetics of mineral transformation reactions during sintering mainly relies on the results of a few bulk *in situ* studies, but mostly on observations made by *ex situ* experiments involving quenching the ceramic body to RT. A detailed comparison of these studies reveals that different studies yielded, for instance, different stability fields for certain mineral phases[16]. Whereas the sensitivity of the different techniques used to identify the phase composition and reactions may in part explain this observation, this discrepancy likely reflects the fact that sintering of silica ceramics is a complex process which is difficult to study systematically due to several control variables such as, e.g., heating rate, composition, oxygen fugacity, and particle size.

What is needed is an analytical technique that allows studying of sintering reactions *in situ* at high temperatures and thereby spatially and temporally resolved. Raman spectroscopy is a frequently used technique for the *in situ* study of high-temperature single phase transformations by following the temperature behavior of optical phonons[17–20]. Modern state-of-the-art Raman spectrometer systems with confocal microscope, motorized *x-y-z* stage, electron multiplier charge coupled device (CCD) detector, and high-power lasers principally permit imaging of mineral reactions and textures *in situ* at the micrometer scale as a function of temperature and time in minutes (Figure 1.1).

This in turn could facilitate the study of the textural evolution and mechanisms underlying the various thermal sintering reactions without quenching the sample to room temperature (RT). In addition, thermodynamic and kinetic information about the growth and breakdown of distinct phases, including the detection of metastable phases, can potentially be gained by applying a high temperature and time resolution.

Raman scattering, the inelastic scattering of a photon, occurs when a small fraction of the light directed onto, for instance, a molecule is scattered by that molecule, causing the scattered photons to have a different frequency than the incident photon (Figure 1.2). For the first time, Chandrasekhara Venkata Raman and Kariamanickham Srinivasa Krishnan were able to demonstrate the inelastic scattering of monochromatic light by

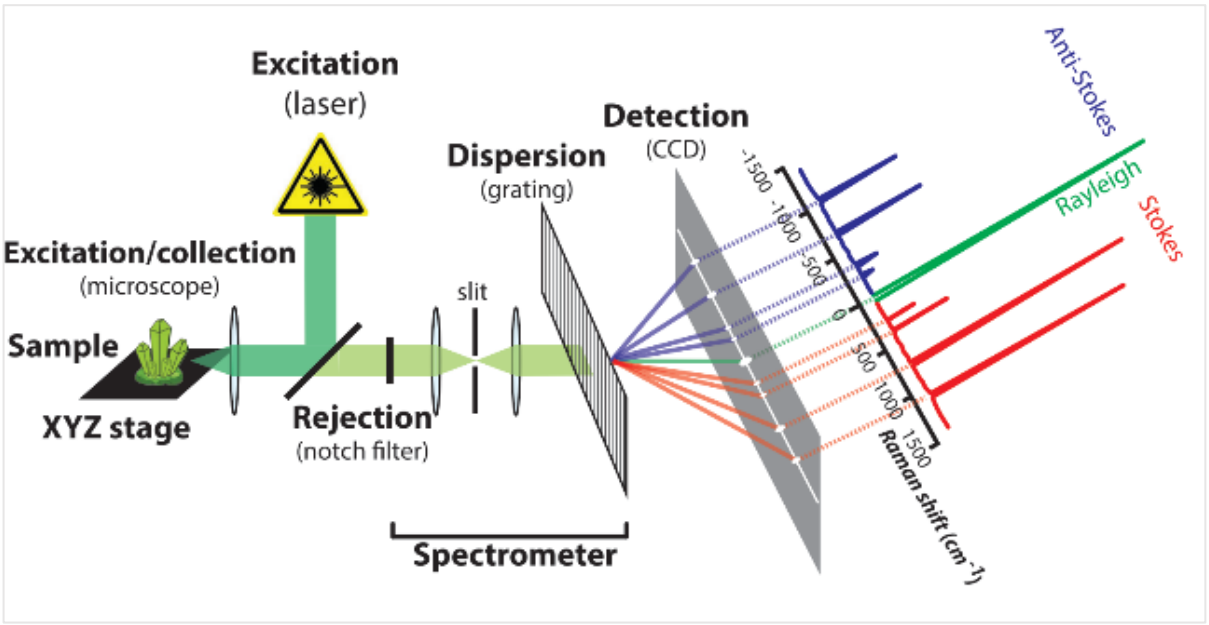

Figure 1.1: Schematic overview of a basic instrumental setup of a Raman spectrometer[27].

a fluid in 1928. Two years later, C.V. Raman was honored by the Nobel Prize for this work.

Since the 1950s and 1960s Raman spectroscopy has become one of the most important analytical tools for a wide range of research areas in all sub-disciplines of physics, chemistry, biology, and medicine. A wide range of materials from simple chemical and biological structures[21] to advanced materials like polymers[22], ceramics[23–25], or semiconductor[26] can be investigated by Raman spectroscopy. Initially, it was a very complex and time-consuming technique and therefore limited to scientific applications. In Earth sciences, Raman spectroscopy became popular in the late 1980s with the development and commercial availability of Raman microprobes[27]. Nowadays Raman spectroscopy is increasingly used for process- and quality control[22,28,29]. In the beginning, the applications were limited due to weak Raman signals and interfering fluorescence of some natural samples. Technical progress in laser technologies, filters, spectrometers, and detection devices led to a much higher sensitivity and a better spectral and confocal resolution. The development of stages that are moveable in x-, y-, and z- direction allows recording of hyperspectral Raman images in two or three dimensions. This enables the 2-dimensional investigation of multiphase solid samples, and makes Raman microscopy to one of the techniques of choice for the analysis of heterogeneous systems on the micrometer scale[30]. Acquisition times of a few milliseconds make it nowadays possible to analyze (mineral) reactions *in situ* and realtime[31–33]. Therefore, Raman spectroscopy is one of only a few techniques that allows the *in operando* investigation of mineral reaction processes on a micrometer scale.

In combination with heating or cooling stages or pressure cells it has also become possible to examine the samples under different pressure

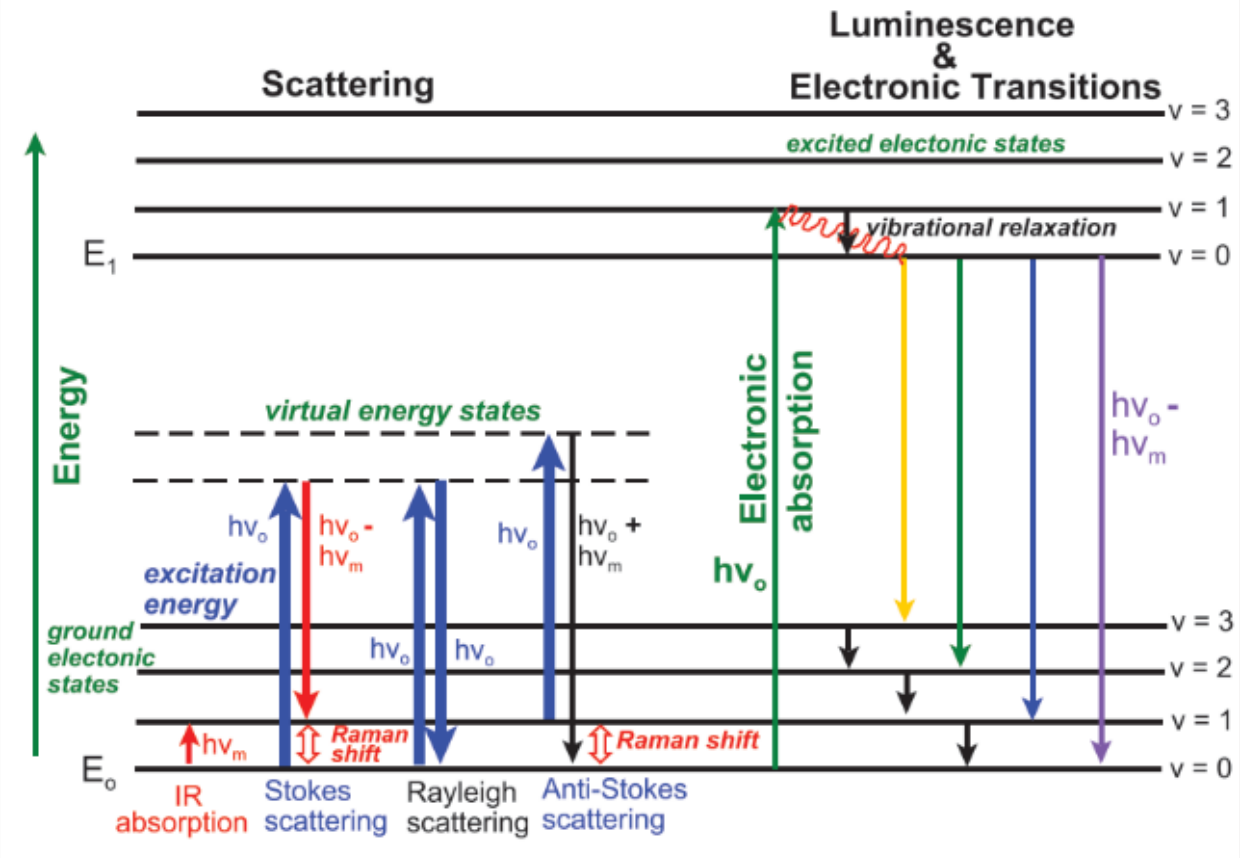

Figure 1.2: Different types of scattering processes and electronic transitions (x axis) that may be recorded by the photon detector and the relative energies (y axis) at which they occur. Stokes, anti-Stokes, and Rayleigh scattering can be seen[27]

and temperature conditions. There are several Raman studies that deal with the temperature behavior of liquids[34] and minerals[35–43], as well as with premelting effects[20]. Besides the temperature dependence of Raman scattering, mineralogical phenomena like polymorphism[44], formation or decomposition[13,45] of minerals or (pre-)melting[46] can be studied. This is important for our understanding of technical and natural processes like, e.g., metamorphism.

During the firing of a ceramic green body several reactions are involved that include polymorphic transformations, solid-solid and solid-melt reactions through different reaction-diffusion mechanisms, nucleation and growth, phase decomposition reactions and, associated with these, the densification of the ceramic[47]. The kinetics of the various transformation reactions depends on the composition of the precursor material, the mixing and milling procedure, the temperature, and dwell time.

The temperature range between 500 and 700°C of ceramic firing is dominated by devolatilization reactions that are net-transfer reactions involving the liberation of a volatile phase, such as the dehydroxylation of kaolinite ($Al_2Si_2O_5(OH)_4$) or illite ($(K,H_3O)Al_2(Si_3Al)O_{10}(H_2O,OH)_2$ and the decarbonation of calcite or dolomite. These devolatilization reactions have been intensively studied, but the mechanisms of the structural transformations and their kinetics are not yet fully understood ([48] and references therein). For instance, the question whether the decarbonation reaction is reversible is still a matter of debate[48].

At intermediate temperatures between about 700 and 1000°C solid-solid reactions are the dominating processes during firing of silicate ceramics[49,50]. In metals and alloys solid-state reactions have been studied extensively and are relatively well understood. In contrast to that, there are many question marks regarding solid-solid reactions in oxide and silicate systems. Such knowledge is essential for our understanding of the textural and mineralogical evolution of clay-based green bodies during firing and also of high- to ultra-high temperature metamorphic reactions[51,52]. Solid-solid reactions involve (inter)diffusion of elements across grain boundaries, their adsorption at interfaces, diffusion through the product layer, and the nucleation and growth of a new phase from the solid state without the formation of a melt phase.

At excess temperatures of about 1000°C, local congruent and incongruent melting reactions at grain boundaries may occur[53,54]. Nucleation and growth (crystallization) of new phases from a melt may occur during cooling of a ceramic body that was heated to temperatures, where partial melting occurred, but also when during increased melting the saturation composition of a new phase in the melt is reached[55]. The ceramic sintering process is divided into three successive steps that lead to densification of ceramic materials. The initial stage is characterized by neck formation between grains, leading to the mechanical consolidation of the material, followed by the intermediate stage containing the elimination of open porosity[56]. Nkou Bouala and colleagues studied the initial stage of sintering for CeO_2 microspheres *in situ* at temperatures up to 1225°C by environmental scanning electron microscopy and found that there is no clear boundary between the first and second stage of sintering[56]. The final stage of sintering involves simultaneous pore shrinkage and grain growth, which is related to the mobility of chemical constituents[57] and comprises grain growth phenomena like Ostwald ripening and oriented attachment[58].

This study focused on the investigation of intermediate temperatures between about 600°C and 1000°C, because most of the important solid-solid reactions in the system $CaO\text{-}SiO_2\text{-}Al_2O_3$ occur within this temperature range. In addition, the Raman spectrum is

increasingly disturbed by black body radiation at temperatures above 1000°C. The black body radiation is emitted by the sample and the furnace material and increases by factor of four between RT and 1000°C.

The major aims and objectives of the project were

(1) to set up an experimental procedure and a protocol for data evaluation,

(2) to acquire high-temperature Raman spectra from relevant ceramic phases as references for (semi-)quantitative phase determination and to study single-phase transitions and decomposition reactions,

(3) to investigate the dependence of the textural and phase evolution on the starting phase composition during high-temperature sintering and cooling of ceramic systems,

(4) to investigate mesoscopic mechanisms of high-temperature, two-phase, solid-state sintering reactions, and

(5) to gain semi-quantitative information about the mineral content and to study crystallization kinetics and the evolution of the grain size during isothermal firing.

These five overall goals and objectives are outlined in more detail in the following.

1.1 Aims and objectives

1.1.1 Experimental procedure and data treatment

This project unifies for the first time the advantages of the spatial resolution of hyperspectral Raman imaging with the time and temperature resolution of an *in situ* firing experiment. All experiments are performed with a TS1500 (Linkam Scientific Instruments, Surrey, UK) heating stage that was mounted onto an automated x-y-z stage below the Olympus BX41 microscope objective (Figure 1.3 A), which facilitated to move the heating stage in all three directions with a reproducibility of ± 0.5 µm in *x* and *y* and ± 0.2 µm in *z* direction. The samples for the single-phase-, two-phase-, and multi-phase experiments were 3 mm in diameter and about 2.7 mm in height (Figure 1.3 B). Most of the recorded Raman images are 100 x 100 µm in size (Figure 1.3 C). A 1 µm step size results in 10000 pixels in total, which corresponds to 10000 Raman spectra for one single image.

The first attempts were performed with carbonate-bearing kaolin fired to temperatures between about 660°C and 1070°C[59] to find out if it is possible to investigate the sintering process of silicate ceramics *in situ* with hyperspectral Raman imaging. This was followed by experiments that show the difference between *in situ* experiments and conventional quenching experiments[59,60]. The

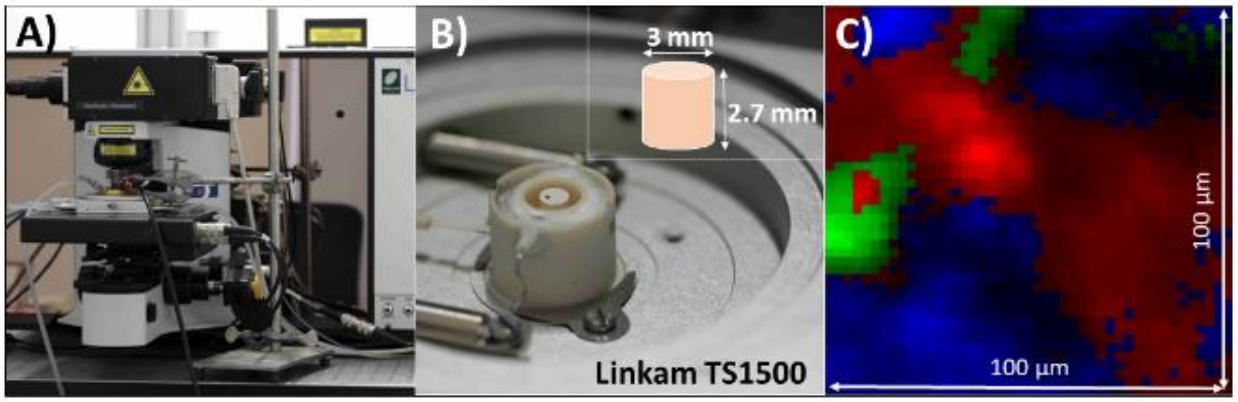

Figure 1.3: Experimental setup. (A) Photograph of the Raman microscope with a Linkam heating stage TS1500, which is mounted on top of the x-y-z stage under the objective of the microscope. (B) Linkam heating stage with a sample. The samples used in the experiments were 3 mm in diameter and about 2.7 mm in height. (C) Example of a false-color Raman image. Most of the recorded images are 100 x 100 µm in size with 1 µm pixel size, which results in 10000 pixels in total.

project was completed by a series of isothermal experiments at six firing temperatures between about 800 and 1010°C to study the mineralogical evolution and sintering kinetics along the time and temperature scales. Besides the mineralogical aspects a focus of this project was the development and refinement of the data processing, quantification, and image visualization procedure. Since hyperspectral Raman imaging is, in contrast to the classic analyzation tools like polarization microscopy or scanning electron microscopy (SEM), a relatively new tool, there are still some unsolved problems concerning data reduction and interpretation. To the best of my knowledge, there exists no standardized procedure for hyperspectral data treatment and image processing in the literature. Nevertheless, the development of measurement automation procedures have extended Raman imaging to users other than scientists[61]. The usage of Raman images for quality control processes or medical diagnostics as a black box must be questioned, because you will always get an image, but it is questionable whether this image is a correct image of reality[30]. This study, especially Chapters 3 and 4, resulted in recommendations for hyperspectral Raman imaging regarding data treatment, data evaluation, and error analysis.

The combination of high-temperature measurements and hyperspectral Raman imaging poses new challenges, since there is no database for high-temperature Raman spectra that are different to their RT counterpart in terms of band positions and widths. Unfortunately, Raman spectra from pure phases in a multi-phase ceramic precursor mixture are also rare within a typical Raman image, because in most cases the laser excites a volume that is greater than a single grain. One objective of this project was to develop a method for data processing and evaluation for high-temperature Raman imaging.

As a first approach to visualize the phase distribution and their textural relationship during firing as a function of temperature, space, and time from a multi-dimensional hyperspectral Raman data set three data reduction methods were tested[59]. In the main band method, only the intensity of one intense and characteristic Raman band of the identified phases was used to visualize their special distribution. The other methods are based on the classical least squares (CLS) fitting method. The CLS method assumes that a spectrum from a polyphase material is a simple mixture of the spectra from the pure phases. Within the multidimensional spectral array, the CLS fitting procedure finds a linear combination of reference spectra from the pure phases, which best fits the raw spectrum at each position (pixel). The CLS fitting method 1 uses a representative, background-corrected, average Raman spectrum (n = 8) from each phase in the imaged area as reference spectrum. In the CLS fitting method 2 a synthetic spectrum from each phase is used as refence. For this, a spectrum is chosen, in which the phase of interest dominates, and all detectable bands are fitted with a Gauss-Lorentz function. Those bands, that do not belong to the respective phase, are deleted and the remaining functions are added together and saved as a synthetic spectrum of that phase. The drawback of all three methods was that some (weak) bands could not be assigned, in some cases leaving high residuals or leading to an overestimation of minor phases.

In order to improve the CLS fitting results, an in-house database with high-temperature Raman spectra of more than 20 mineral phases, which occur in the investigated systems¸ was built up. The number is constantly increasing. These HT-reference spectra were used for the CLS fitting procedure when available[60].

1.1.2 High-temperature Raman spectroscopy on relevant ceramic phases

Room temperature Raman spectra of all minerals that occur during the firing of a kaolinite-calcite mixture are published in literature. For some of these phases such as calcite[43], kaolinite[13], quartz[62], wollastonite[63], gehlenite[64], anorthite[64,65], anatase[41], and alumosilicate liquids[34,64] high-temperature Raman spectra already exist. However, the high-temperature (HT) Raman spectra reported in these studies are not accessible and were also performed with different instruments and different analytical and experimental conditions (e.g., larger temperature steps). In this project, high-precision HT Raman spectra of relevant ceramic phases were collected for:

(a) having high-temperature reference spectra and v_1-T relationships at our disposal that will help to identify individual high-temperature phases in mixed spectra, which is important to improve the CLS fitting results.

(b) the estimation of relative Raman cross sections that are needed to be able to more accurately determine the relative phase proportions from a mixed Raman spectrum.

(c) the calibration of local mineral thermometers to account for the temperature gradient that almost unavoidably exists between the position of the thermocouple and the location where the reactions take place. Accurate and precise v_i -*T* relationships should be determined from which the local temperature can potentially be determined precisely and accurately at the locations where the reactions take place. This methodology is expected to be more precise and accurate than a thermocouple in a conventional quench experiment even if it is located close to the sample.

The new high-precision HT Raman data, collected with a high-temperature resolution, should also be examined for potential phase transitions, including solid-melt transitions and decomposition reactions. Moreover, such data is needed to test quasi-harmonic force field models[66] and first-principle, *ab initio*, and/or other simulation codes to model solid materials[67]. It follows that the results of this part of the project alone will be of broad scientific interest.

In particular, it was intended to address following open questions:

- *Is there another phase transition in wollastonite?*

Swamy and Dubrovinsky reported subtle discontinuities of the frequency, width, and intensity of Ca−O stretching and Si−O bending modes of wollastonite in the temperature range between 677 and 707°C with no corresponding changes in the temperature dependencies of the lattice parameters[18]. Currently, it is not fully clear whether these discontinuities reflect (a) a minor displacive transformation, (b) premonitory behavior leading to a first-order phase transition at 722 ± 10°C that is indicated by the results of drop colorimetric measurements[68], or (c) the ordering of polytypic stacking faults, the latter of which is the preferred explanation of Swamy and Dubrovinsky[18]. Due to the high sensitivity and precision of modern Raman spectrometers, it seems safe to state that new details about the subtle discontinuities of the vibrational properties as a function of temperature will be detectable if present.

The occurrence or non-occurrence of certain mineral phases and their relative proportions are often used, for instance, to determine the firing temperature of ancient ceramics or to estimate the formation temperature of natural rocks[69]. Tschegg and colleagues[70] for example, could not solve the question whether large sparitic carbonate inclusions, observed in Cypriot Bronze-age plain white ceramics, represent incompletely decomposed or secondary calcites that were formed by a recarbonation process after firing. It has been suggested that under ambient conditions calcite may crystallize from non-reacted lime[71,72]. During this process, the hygroscopic

lime picks up moisture from the air, forming portlandite, $Ca(OH)_2$. Portlandite then slowly reacts with atmospheric CO_2 and calcite is formed. This hypothesis could be tested using the advantages of *in situ* and real-time CHRS imaging. Because portlandite is a good Raman scatterer it can easily be detected by its sharp and intense Raman ν_s(OH) band near 3620 cm^{-1} [73]

1.1.3 Textural and phase evolution during high-temperature sintering and cooling

In this project, the power of hyperspectral Raman imaging should be used to systematically study the effect of heating-quenching cycles in the CaO - SiO_2 ± Al_2O_3 system on the evolution of the texture and phase assemblage as a function of temperature and time. The data will provide a novel archive for testing and refining numerical models, in particular those that are based on the finite element method used to model the dynamics of sintering reactions at the grain scale. The *in situ* Raman experiments were designed to give answers to following open questions:

- *What is the effect of quenching on the phase assemblage and the final texture?*
- *Do metastable phases form during firing?*
- *Does a partial melt occur during firing?*
- *Do the minerals form during solid-state-sintering or from a (partial) melt?*
- *Is the decarbonation of calcite reversible?*

1.1.4 Mechanisms of high-temperature solid-solid reactions

Due to the simple stoichiometry of the reaction

$$SiO_2 + CaCO_3 \rightarrow CaSiO_3 + CO_2 \uparrow$$

and its importance in silicate ceramics[53] and in metamorphic rocks[52], this reaction has been considered a model reaction to start the investigation of two-phase solid-state reactions at the mesoscopic scale. To obtain information about the solid-state reaction mechanism(s), the diffusion of oxygen in quartz during its reaction with calcite or lime should be monitored and quantified as a function of space and time. For this, it was planned to use precursor reactants that are enriched in ^{18}O, acting as isotope tracer. With such measurements it should, for instance, be possible to depict the direction of the migrating reaction front, which is very difficult and uncertain in quenched samples[52].

1.1.5 Crystallization kinetics during isothermal firing

Understanding the kinetics of sintering reactions is necessary to systematically control the manufacturing process of a material, but also to understand natural metamorphic processes. Even if a mineral transformation is thermo-dynamically favoured, it is not guaranteed that the transformation will occur at any measurable rate[74]. The reaction rate strongly depends on the mechanisms involved in the reaction process and can change with time and temperature. Grain boundaries move and rearrange with increasing dwell time associated with an increase in the average size and decrease in the grain boundary area per unit volume[75].

Hyperspectral Raman images can be used to semi-quantify the mineral content of a calcium alumina silicate ceramic during isothermal firing for 48 h at six different temperatures. The crystallization of gehlenite from metakaolinite and lime was selected as a kind of model reaction to estimate the activation energy for gehlenite nucleation and growth in order to address following general questions:

- *Is it possible to determine the activation energy for nucleation and growth and degradation?*
- *How does the grain size depend on the dwell time and firing temperature?*
- *What are the mechanisms of grain growth (e.g., Ostwald ripening or oriented attachment)?*

1.2 Ceramics reactions: State of the art

1.2.1 Nucleation and growth

Crystallization of melt can occur during cooling of a ceramic body that was heated above the liquidus temperature or when during increased

melting the saturation composition of a new phase in the melt is reached[55]. While the crystallization of new phases from a melt during sintering of ceramic bodies is a well-known phenomenon[55], very little is known about mineral replacement reactions mediated by a partial melt[76]. One hypothesis is that the parent phase dissolves into the melt, which results in the local supersaturation of the product phase in the melt at the reaction interface, triggering the nucleation and growth of the product phase at the surface of the dissolving parent phase. Such a coupled dissolution-reprecipitation process operating along an inwardly moving dissolution-reprecipitation interface has been proposed for many mineral replacement processes that occur in aqueous solutions[76,77], but has also been identified during plagioclase melting experiments[78] and in high-uranium zircons grown in the melt formed in 1986 during the nuclear accident in Chernobyl, Ukraine[79].

1.2.2 Solid-solid reactions

Extensive theoretical work has been carried out to model solid-state sintering reactions at different length scales[50,80,81], but many atomistic details of reactions of this kind are still not fully understood. As stated by German[81], more fundamental research is necessary that should focus on the various mechanisms occurring during sintering. This research is needed to refine and test models and hypothesis. Current theoretical work on sintering is considering effects such as anisotropic shrinkage and the dynamics of the rearrangement of grains, especially during the initial stages of sintering. Space-, time-, and temperature-resolved hyperspectral Raman imaging of high-temperature solid-state reactions at the micrometer-scale along with information about the diffusion and exchange of oxygen atoms between the individual phases could give important insights into these and other microscopic mechanisms of sintering. Such knowledge is essential for many industrial applications, for forensic archeology, and generally for all applications that use mineral reactions to unravel the temperature (and pressure) history of sintered products, e.g., from sintered crusts in high-temperature coal kilns[82,83] used for energy production or from metamorphic rocks.

1.2.3 Reaction textures

Reaction rims and corona textures are common non-equilibrium features in many metamorphic rocks[52,84] and ancient ceramics[70]. As the reactant and product phases have different compositions, interlayer growth requires chemical mass-transfer which, in the absence of melts and fluids, can occur by diffusion only. At the same time, localized reactions must proceed at the 'reaction interfaces', which divide the growing layers on either side[84]. Both processes may be rate-limiting and the coupling between the two processes determines the overall reaction kinetics[84]. To identify the direction of the migration front, two ex situ approaches are possible: (i) rim growth experiments and (ii) experiments with isotopically doped reactants[51,52,85] that allow reconstructing the overall reaction dynamics.

1.2.4 Polymorphic transitions

A special type of solid-solid reactions are polymorphic reactions during which phases of identical composition transform via displacive or reconstructive mechanisms. For instance, the displacive phase transition of α- to β-quartz at 573°C which is accompanied by a significant change in volume, inducing extensive micro-structural strain in the ceramic. Monocalcium silicates ($CaSiO_3$) are common essentials of slag and ceramic substances[69] or of crustal rocks[86] . A series of natural polytypes with different packing arrangements of the single chains have been reported: triclinic polytypes (1T, 3T, 4T, 5T, 7T) and monoclinic parawollastonite (wollastonite- 2M)[86]. The polymorphs wollastonite and parawollastonite often occur in nature. In contrast, the polymorph pseudowollastonite is rare and has only

identified in nature in ultrahigh-temperature rocks and in very low pressure, Ca-rich combustion metamorphic (CM) rocks[69]. Dicalcium silicate that is one of the most important constituents of Portland cement clinker and appears in refractories crystallizes in five different polymorphs (γ-, β-, α'_L-, α'_H-, and α-Ca_2SiO_4)[87]. However, polymorphism plays an important role in calcium silicates. Therefore, an analytical technique is required that enables the differentiation between the chemically similar minerals and especially the polymorphs.

1.2.5 The investigated CaO-SiO_2-Al_2O_3 system

The ternary system CaO-SiO_2-Al_2O_3 is a relevant system for ancient ceramics[1], slags[88] and cement clinker (Figure 1.4). Within the system only two ternary mineral phases are existing: Anorthite ($CaAl_2Si_2O_8$) and gehlenite ($Ca_2Al_2SiO_7$). The calcium aluminate phases Tricalciumaluminat (C_3A) and $C_{12}A_7$, and the calcium silicate phases Tricalcium silicate (Alite, C_3S) and Dicalcium silicate (Belite, C_2S) are important clinker phases of cement. (Di-) calcium silicates are an important material for bioactive coatings[89,90] or artificial bones and dental root[91]. Because of the low price and the high availability chalk is frequently used as a slag former and to reduce the liquidus temperature[88]. Due to similar precursor materials and formation conditions, ceramic-like mineral assemblages naturally occur in ultrahigh-temperature and very low-pressure metamorphic rocks. During the last century, the areas of applications of calcium silicates drastically evolved, as reflected by numerous sintering experiments[7–9]. Due to the relative low temperature required for its synthesis, dicalcium silicate is one of the most abundant component of Portland cement clinker[92], heat resistant coatings, and refractories[93]. Properties such as low shrinkage, good strength, lack of volatile constituents, body permeability, fluxing characteristics, and acicular shape qualify materials like wollastonite to be widely used in several ceramic applications[93]. During the 1960s and 1970s, material for the application inside the human body was specially developed and a new application area for biomaterials was born[94]. In the past twenty years the demand for synthetic biomaterials to replace and repair bone tissue, that was lost through injury or diseases, has significantly increased[95]. Silicate ceramics attained an important role in modern biomedicine. Biomaterials generally perform poorly in bonding with the host tissue, but they need to physically and/or biologically function in intimate contact with living tissue. So-called bioactive ceramics, such as Bioglass®, hydroxyapatite (HAp), beta-tricalcium phosphate (TCP), and glass-ceramic, are materials that induce biological tissue-integration in a tissue defect *in situ*[96]. Calcium silicate ceramics, especially the chain-like silicate minerals such as wollastonite (triclinic $CaSiO_3$) and pseudowollastonite (monoclinic $CaSiO_3$), tricalcium silicate (Ca_3SiO_5)[97], β-dicalcium silicate (monoclinic β-Ca_2SiO_4)[89,98], and γ-dicalcium silicate (orthorhombic γ-Ca_2SiO_4)[89] exhibit excellent bioactivity. Ca_3SiO_5 ceramics possess bone-like apatite-formation ability and degradability, and can release soluble ionic products to stimulate cell proliferation[99].

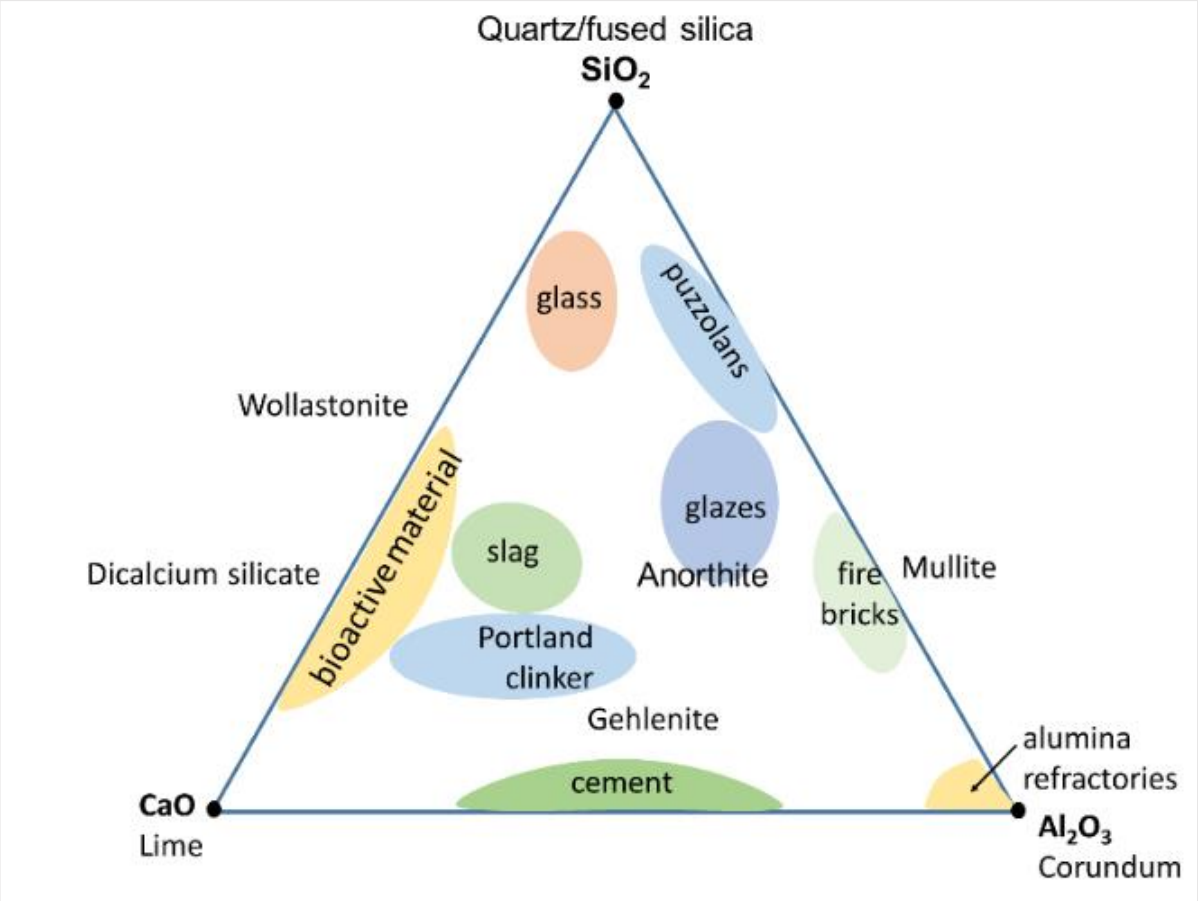

Figure 1.4: The system CaO-SiO_2-Al_2O_3 is important for many products of the daily life. Cement, glass, and fire bricks contain minerals like anorthite or gehlenite.

1.3. Main thesis structure

The main body of this thesis comprises three chapters 2, 3, and 4, which present two published and one manuscript for future submission, respectively. In addition, the chapters 5, 6, and 7 are short chapters with further unpublished experiments. Each of these chapters are to be read independently, in which the individual samples and analytical methodologies are explained in detail or are provided in the Supplements. Finally, the results of these six individual contributions will be integrated, discussed, and summarized in Chapter 8.

Chapter 2, entitled "Insights into the evolution of carbonate-bearing kaolin during sintering revealed by *in situ* hyperspectral Raman imaging", was published in 2018 in the *Journal of American Ceramic Society*[59]. This paper reports the results of the first experiments that were designed to *in operando* study the textural and mineralogical evolution of calcite-bearing kaolin during sintering between 650 and 1100°C by Raman spectroscopy. Three methods to fit the Raman data and to generate hyperspectral images from the raw data were tested and their results were compared. So-called synthetic spectra were used as reference spectra for the CLS fitting procedure. The study focused on the investigation of the formation and breakdown of Ca-Al-silicates, such as gehlenite and wollastonite, during heating, cooling, and quenching. Two types of experiments were performed. In the quench experiment the sample was repeatedly fired to the sintering temperatures for a dwell time of two hours and then consequently cooled to RT, before Raman images were recorded. This type of experiment mimics common *ex situ* experiments. In contrast to that two *in situ*

experiments with 10°C-steps and 100°C-steps, respectively were performed to evaluate the difference between *in situ* and *ex situ* experiments. The results show that important information about intermediate or metastable phases is lost when only *ex situ* experiments are performed.

In Chapter 3, the second paper, entitled "*In situ* hyperspectral Raman imaging: A new method to investigate sintering processes of ceramic material at high temperature", is presented that was published in 2019 in *Applied Sciences*[60]. This paper describes a novel approach to study the sintering process of silicate ceramics *in situ* and *in operando* by hyperspectral Raman imaging. The CLS fitting procedure was optimized by using, instead of so-called synthetic spectra, an in-house Raman database with high-temperature reference spectra that were collected as input reference spectra to improve the CLS fitting procedure. The data reduction was described in very detail. Important factors that affect the quantification and visualization like crystal orientation, the Raman scattering cross-sections of the mineral phases, and the lateral and axial resolution were discussed. Three application examples are given that demonstrate the power of hyperspectral Raman imaging to *in operando* study sintering processes. The first example showed that certain mineral reactions can be assigned to the firing- or to the cooling-path, respectively. This information can only be gained by an *in situ* experiment. In the second example isothermal mineral reactions and grain growth in the system $CaO\text{-}SiO_2$ were studied. The last application example dealt with *in operando* observations of the migration of a solid-solid reaction front.

Chapter 4 reports the results of a number of isothermal experiments with kaolinite-calcite green bodies in form of a manuscript that is ready for submission to a peer reviewed international journal. In this chapter, the possibility to gain quantitative information from the hyperspectral Raman images is explored and the results of a kinetic analysis of grain growth are presented. In this study, the focus was on the interpretation of the *T-t* evolution of the phase assemblage. Six samples of a kaolinite-calcite mixture were fired for about 48 hours at six sintering temperatures between about 800 and 1010°C. For every experiment 26 hyperspectral Raman images were recorded. During a dwell time of about 48 hours, 24 images with a mapping time of about two hours were subsequently recorded at the sintering temperature. In addition, two RT images were recorded. One image of the unfired sample was recorded and another after cooling the sample to RT. From the matrices of the CLS fit a semi-quantitative phase content was calculated. Calcite and kaolinite were dissolved during firing and new calcium silicates and calcium alumina silicates were formed. The manuscript was focused on the crystallization kinetics of gehlenite which the dominating phase in most of the experiments was. The activation energy of gehlenite nucleation and growth was determined by the isoconversional 'time-to-a-given-fraction' method from the gehlenite fraction and average grain size with increasing reaction time.

Chapter 2

Insights into the evolution of carbonate-bearing kaolin during sintering revealed by in situ hyperspectral Raman imaging

Kerstin Stange | Christoph Lenting | Thorsten Geisler

Steinmann-Institut für Geologie, Mineralogie und Paläontologie, Rheinische Friedrich-Wilhelms-Universität, Bonn, Germany

Abstract

Sintering reactions of clay bodies have previously been studied by numerous experiments that involve quenching of the sintered ceramic bodies to room temperature and analyzing the reaction product by different analytical techniques. In this study, green bodies containing quartz, alkali feldspar, kaolinite, and calcite, were progressively fired in air at various temperatures from room temperature to about 1060°C. For the first time, mineral reactions and textural relationships were studied *in situ* as a function of temperature and time with a spatial resolution of a few micrometers by confocal hyperspectral Raman imaging. Gehlenite, wollastonite, and pseudowollastonite could unambiguously be identified as newly formed phases during sintering, and their textural evolution could be followed with temperature and time. From 800°C onwards wollastonite formed at the direct contact to gehlenite, whereby at temperatures higher than 990°C wollastonite seems to be gradually replacing gehlenite. The crystallization of pseudowollastonite was observed already ~290°C below the accepted critical temperature (~1125°C) for the wollastonite-to-pseudowollastonite transformation, suggesting that pseudowollastonite can form metastably. The results of this study demonstrate that hyperspectral Raman imaging is a powerful method to study *in situ* phase transitions and recrystallization processes at grain boundaries during high-temperature sintering of ceramic materials.

I. Introduction

Since the earliest history of humankind, pottery has played an important role in daily life as well as in human culture in the form of craft and art objects. This is documented, for instance, by a pottery statuette of a nude female figure dated to 29,000 - 25,000 BC [1] and pottery vessels discovered in the Xianrendong cave in Jiangxi, China, dated back to 20,000 BC [2]. From early on, pottery was produced under different sintering conditions and from different clays with kaolinite as primary mineral component. Other minerals such as phyllosilicates, iron- or titanium oxides, feldspar and/or quartz were either specifically added to the clay body or occurred naturally in the mined raw material. This resulted in diverse ceramic end products such as earthenware, stoneware, or porcelain, which have a different phase composition, texture, optical appearance, and different physical properties and, therefore, were and are used for different applications (*e.g.,* [3-4]).

During sintering to temperatures of up to 1400°C, minerals in the polyphase clay body transform via various reactions to a new phase assemblage [4]. Depending on the composition of the precursor material, a number of inter- and intragrain transformation reactions are possible that partly involve moving grain boundaries and rotating grains [5]. The sintering process is divided into three successive steps which lead in densification of ceramic materials. The initial stage is characterized by neck formation between grains, leading the mechanical consolidation of the material followed by the intermediate stage containing the elimination of open porosity [5]. Nkou Bouala and coauthors [5] studied the initial stage of sintering for CeO_2 microspheres by using environmental scanning electron microscopy *in situ* at temperatures up to 1225°C and found that there is no clear boundary between the first and second stages of sintering. The final stage of sintering involves simultaneous pore shrinkage and grain growth, which is related to the mobility of chemical constituents [6] and comprises grain growth phenomena like Ostwald ripening and oriented attachment [7].

At low temperatures, mainly *devolatilization reactions* occur that are *net-transfer* reactions involving the release of a volatile phase, such

as the dehydration of kaolinite ($Al_2Si_2O_5(OH)_4$) and the decarbonation of calcite or dolomite. Although the decarbonation reactions have been intensively studied, many details of the mechanism and kinetics of the process are not yet fully understood ([8], and reference therein). In particular, the question of whether this reaction is reversible is still a matter of debate [8].

Due to the importance of silicate ceramics in daily life and many technical applications, sintering reactions of polyphase clay bodies have previously been studied intensively by numerous sintering experiments that involve quenching of the sintered ceramic bodies to room temperature (RT) and analyzing the reaction product by means of different analytical techniques (*e.g.*, [9-16]). Such studies have a number of shortcomings related to the inevitability to quench several different polyphase samples to RT, which makes it difficult to gain information about details of the textural evolution, the mechanism, and kinetics of individual transformation steps, and the possible crystallization of metastable phases. Differential thermal analysis and X-ray diffraction are the only techniques that have more frequently been used to investigate the sintering process of polyphase ceramic precursors *in situ* at high temperature (HT), *i.e.*, while the reactions are proceeding (*e.g.*, [17]). Both techniques, however, only provide thermodynamic and mineralogical data about the predominant transformation reactions during sintering (such as melting, phase decomposition, dehydration, polymorphic phase transformations, glass transitions, and crystallization) averaged out over the whole volume of the green body. Only limited information is gained about the textural evolution as a function of space, time, and temperature, and about the mechanism of single transformation steps, involving consecutive or competing elementary reactions. Therefore, our current knowledge about the mechanisms and kinetics of mineral transformation reactions during sintering mainly relies on the results of a few bulk *in situ* studies, but mostly on observations made by *ex situ* experiments involving quenching the ceramic body to RT.

What is needed is an analytical technique that allows studying the sintering reactions *in situ* at high temperature and thereby spatially and temporally resolved. Raman spectroscopy is a well-used technique to *in situ* study high-temperature phase transformations by following the temperature behavior of optical phonons (*e.g.*, [18-21]). However, sensitive modern state-of-the-art Raman spectrometer systems with confocal microscope and an automated x-y-z stage, principally permit to even image the mineral reactions and texture *in situ* at the micrometer-scale as a function of temperature and time, and thus to study the mesoscopic mechanisms underlying the various thermal sintering reactions without quenching the sample to RT. Additionally, thermodynamic and kinetic information about the growth and breakdown of distinct phases, including the detection of metastable phases, can potentially be gained with a high temperature and time resolution. To the best of the authors' knowledge, the imaging capability of confocal Raman spectroscopy has not yet been used to study solid-solid reactions at high temperatures. Our first experiments were designed to study the textural and mineralogical evolution of calcite-bearing kaolin during sintering at temperatures in excess of 1000°C. We were in particular interested in studying the formation and breakdown of Ca-Al silicates, such as gehlenite and wollastonite, during heating and cooling/quenching. One of the main aim of this contribution is thus also to demonstrate the power (and limitations) of Raman spectroscopy for *in situ* investigations of mineral reactions during ceramic sintering.

We present novel *in situ* hyperspectral Raman images of the textural and mineralogical evolution of a calcite-bearing kaolinite during sintering. The results may inspire other researchers to use Raman spectroscopy to *in situ* image sintering reactions in other ceramic materials.

II. Materials and methods

(1) Raw material and sample preparation

As starting material we chose kaolin (provided by Carl Jäger GmbH, Germany) containing kaolinite, alkali feldspar, and quartz that is used to manufacture whiteware. Calcium carbonate was added in order to reduce shrinkage of the green body during thermal annealing, because a changing surface complicates the focusing of the laser light for hyperspectral Raman imaging. The precursor material contains 15 vol.% quartz, 18 vol.% alkalifeldspar, 40 vol.% kaolinite, and 27 vol.% calcite, as determined by X-ray diffraction (XRD) and Rietveld analysis. The chemical composition of the final mixture was determined by X-ray fluorescence analysis (wt.%): LOI: 13.10; SiO_2: 51.69; Al_2O_3: 22.62; Fe_2O_3: 0.22; MgO: 0.03; CaO : 8.61; Na_2O: 02.18; K_2O: 1.89; TiO_2: 0.06; P_2O_5: 0.01; SO_3: 0.06. From this precursor material, several green bodies were produced by compacting 4.3 mg of precursor material (dried at 100°C for 24 h) into cylinders (3mm x 2.7 mm) at a pressure of 0.01 MPa.

(2) X-ray diffraction analysis

The X-ray diffraction analysis was performed with a Siemens D-5000 diffractometer, using a Cu-Kα (0.15418 nm) source (40kV, 40mA), a graphite secondary monochromator, and a scintillation detector. The scans were performed at room temperature using a step scan of 0.02°, with a recording time of 1 s for each step. The mineral phases were identified by the software EVA (Bruker). A quantitative determination of the mineral content was performed with the software TOPAS (Bruker) that is based on Rietveld analysis.

(3) Raman spectroscopy

Raman spectra were obtained with a Horiba Scientific HR800 Raman spectrometer equipped with an Olympus BX41 microscope, a 2 W Nd:YAG laser (532.09 nm), and an electron-multiplier CCD detector. A 600 grooves/mm grating was used that covered a wavenumber range from 100 to 1750 cm^{-1} in a single window. With this grating the spectral resolution was ~3.5 cm^{-1}, as given by the intense Ne line at 585.24878 (± 0.00005) nm [22] that occurs at a Raman shift of 1707.461 cm^{-1} in the spectra. In order to correct for any spectrometer shift during imaging, this Ne line was continuously monitored during the measurements by placing a Ne lamp alongside the beam path of the scattered light. A 50x long-working distance (LWD) objective (numerical aperture (NA) = 0.5; working distance = 10.6 mm) was used. With this objective the diffraction limited theoretical lateral, d_l, and axial resolution, d_a, at the sample surface was 1.3 and 8.5 µm, as given by $d_l \approx 1.22\ \lambda/NA$ and $d_a \approx 4\lambda/NA^2$, respectively, where λ is the wavelength of the incident laser. The real resolution is certainly worse than this, i.e., in the order of 2 µm lateral and 10 to 15 µm axial, which has to be considered when interpreting hyperspectral Raman images.

(4) Experimental details

All sintering experiments were carried out in a Linkam TS 1500 heating stage that was mounted on an automated x-y-z stage below the objective of the Raman microscope to record hyperspectral Raman images at RT and during firing. Two types of experiments were performed. In the quench experiment (Q-Exp, Table 2.1 and Fig. 2.1), the green body was repeatedly fired to higher sintering temperatures for a dwell time of 2 hours and consequently quenched to RT with a cooling rate of 50°C/min before a hyperspectral Raman image with 1 µm step size (90 x 90 μm^2) was recorded (= 8100 spectra per image). Such an experiment mimics normal sintering

experiments by which the ceramic products are quenched to RT before they will be analyzed. However, the advantage of *in situ* Raman imaging is that after each sintering step the same area of the same sample can be studied. In the second type of experiments (Table 2.1 and Fig. 2.1) the samples were stepwise fired to higher temperatures and the Raman spectra were taken *in situ*. One of the latter experiments was performed with temperature steps of 100°C (F-Exp) and the other with temperature steps of 10°C (S-Exp).

Table 2.1: Experimental conditions.

Experiment	Q-Exp	F-Exp	S-Exp
Type	*Ex situ*	*In situ*	
	Firing conditions		
T range (°C)	659- 1016	749-1016	749-1069
T-steps (°C)	~100	~10	
Heating rate (°C/min)	10; 5	5	
Cooling rate (°C/min)		50	
Dwell time (min)		120	
Time-steps	1	5	6
Tmax (°C)	1016		1069
	Hyperspectral Raman images		
Method	Point-by-point	SWIFT (continuous moving table)	
Image size (µm)	90x90	40x40	45x45
Pixel size (µm)		1x1	
Counting times (s)	10	0.5	

For both *in situ* experiments (F-Exp and S-Exp) fast hyperspectral Raman images were recorded at high temperatures with a 1 µm step size. For each image the acquisition time lasts 14 min (F-Exp.) and 17 min (S-Exp.), respectively. The imaged area of the *in situ* experiments (40x40 µm^2 and 45x45 µm^2 is drastically reduced, compared to the ex situ experiments (90x90 µm^2), in order to take multiple Raman images at each temperature step to record any isothermal reactions within 2 hours dwell time. At the beginning of each experiment, a RT image of the chosen area was recorded. The green bodies were then fired with heating rates of 5 and 10°C per minute to temperatures between 659 and 1069°C in air atmosphere (Table 2.1). After having acquired the last high-temperature image, the sample

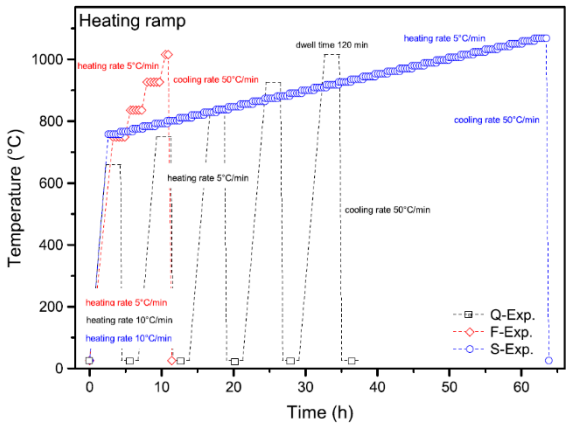

Figure 2.1: Firing conditions of the quench- and the two in situ experiments. In the quench experiment (Q-Exp), the green body was repeatedly fired to the sintering temperatures for a dwell time of 2 hours and consequently quenched to RT before a hyperspectral Raman image was recorded at RT. In the second type of experiments the samples were stepwise fired to higher temperatures and the Raman spectra were taken in situ. One of the latter experiments was performed with temperature steps of 100°C (F-Exp) and the other with temperature steps of 10°C (S-Exp).

was quenched to RT with a cooling rate of 50°C/min. A last image was then recorded at RT with an acquisition time of 10 s (acquisition time of 1 s with 10 accumulations). The temperature measured with a Rh/Pt thermocouple at the bottom of the heating stage was accurate within ± 0.1°C. However, due to the height and volume of the ceramic green body, the temperature had to be corrected for a temperature gradient (~ 5 %) from the bottom to the surface of the green body. Details about an empirical temperature correction procedure are given in the Supplement (Sec. 1). With this correction the temperature is accurate within ± 5°C.

(5) Raman data analysis and reduction

The mineral phases were identified by characteristic positions and relative intensities of their fundamental Raman bands using the RRUFF database [23 and 24] and corresponding literature (see Supplement, Sec. 1). The assignment of the observed Raman bands to the different ceramic mineral phases at high temperature is discussed in detail in the

Supplement (Sec. 1) and a full list of the observed Raman bands is given in Tab. S2.1.

Ultimately, the data sets were analyzed by the classic least-squares (CLS) fitting procedure. This mathematical procedure is based on the assumption that a multiphase spectrum is a simple mixture of the spectra from each single phase. At each position within the multidimensional spectral array the CLS fitting procedure finds a linear combination of reference spectra from the pure phases, which best fits the raw spectrum at each position (pixel). The resulting image is created by false-coloring each pixel of the image relative to the fraction of each component in the spectrum. In the unmixed color-coding algorithm that is used here, the phase with the highest intensity contribution in a Raman spectrum will be displayed in a color assigned to that particular phase. Since pure high-temperature reference spectra were not are available, synthetic spectra for each phase at each temperature were created by fitting Gauss-Lorentz functions to the observed mixed spectra (more details about such a procedure are given in the Supplement (Sec. 3).

It is important to note that the Raman scattering cross-sections, which vary for each mineral phase, and orientational effects, which could arise in non-isometric species, where the changes of the relative intensity of the Raman bands with the crystal orientation is stronger than in isometric crystals, were not taken into account. Thus, even a perfect match does not reflect the "real" phase composition. Furthermore, only small areas (40 x 40, 45 x 45, and 90 x 90 μm^2) were imaged, which cannot be taken as representing the bulk ceramic body. Despite these shortcomings, the relative phase changes within a certain area can be monitored as a function of temperature, time, and space.

III. Results

All experiments were carried out using cylindrical green bodies formed from the same precursor materials. The first hyperspectral Raman image of each green body, recorded at RT, include grains of feldspar, quartz, and calcite. In addition, the area investigated in the Q-Exp contained a titanite grain that is an accessory phase in the kaolinite clay. Kaolinite bands could not be detected due to weak polarizabilities of the bonds in the kaolinite structure and thus weak Raman intensities ([15]; see Supplement, Sec. 1) as visualized in Figs. 2.2 to 2.4, the textural and mineralogical evolution significantly differs among the quench and both *in situ* experiments.

(1) Quench experiment (Q-Exp, 659 - 1016°C, ~100°C-steps; measurements at RT)

Normalized false-color hyperspectral Raman images (unmixed mode) of an area of 90 x 90 μm^2 that were recorded at RT after each sintering step (100°C) from 695 to 1016°C are shown in Fig. 2.2. After firing the green body to the different temperatures, primary feldspar (oligoclase, microcline, and albite), titanite,

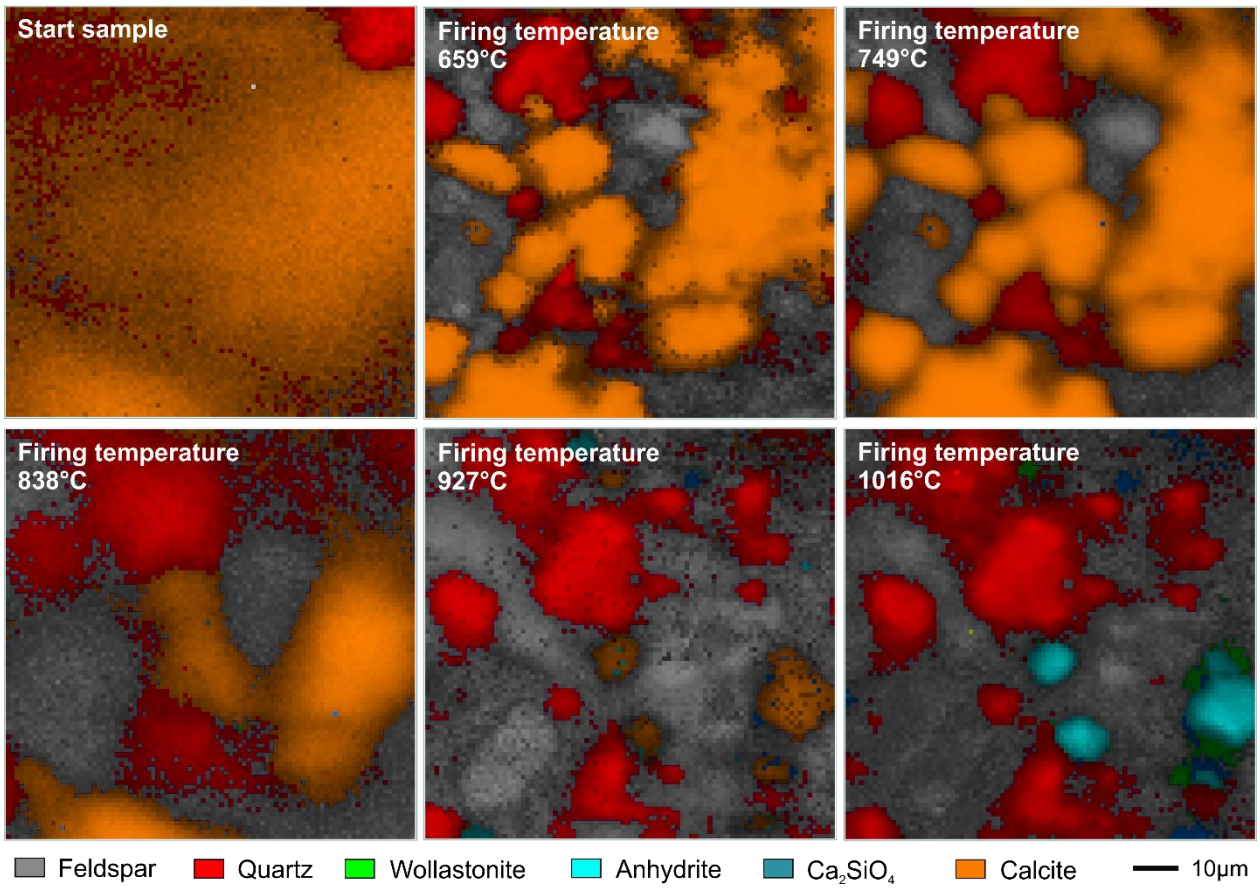

Figure 2.2 Normalized false-color hyperspectral Raman images (unmixed mode) within an area of 90 x 90 µm² that were recorded at RT (Q-Exp). The ceramic green body containing kaolinite, quartz, kalifeldspar, and calcite was heated up to firing temperatures between 659°C and 1016°C with soaking times of two hours per temperature step and then cooled down to RT before each measurement.

and quartz could still be detected at RT within the imaged area. However, calcite became unstable at 927°C, but relicts of calcite grains remained, even after sintering the green body at a temperature of 1016°C (Fig. 2.2). However, in those areas, where calcite was located wollastonite, anhydrite, and Ca_2SiO_4 newly crystallized during the course of the experiment. Anhydrite appeared after a firing to a peak temperature of 927°C (Fig. 2.2). After firing to 1016°C the former calcite relicts were fully replaced by anhydrite. It is noteworthy that anhydrite was not observed in the two *in situ* experiments that did not involve quenching (see below F-Exp and S-Exp). In addition, wollastonite occurs as a rim around anhydrite and around another phase with two intense Raman bands at 847 and 895 cm^{-1} that, however, could not yet confidently been identified (Fig. 2.2). Nevertheless, considering the chemical composition of the green body, the stoichiometry of this phase may be defined as Ca_2SiO_4, which can occur as two polymorphs, namely β-Ca_2SiO_4 (larnite) and γ-Ca_2SiO_4 (calcio-olivine). However, reference Raman spectra from the RRUFF database and literature [33] do not allow the unambiguous distinction of larnite and calcio-olivine, because available Raman spectra for these phases are contradictory. It is noted, that this phase was detected at RT after sintering the body to 927°C. No indication of this phase, however, was found *in situ* at HT, only in the sample of the F-Exp after it was cooled down to RT (see below).

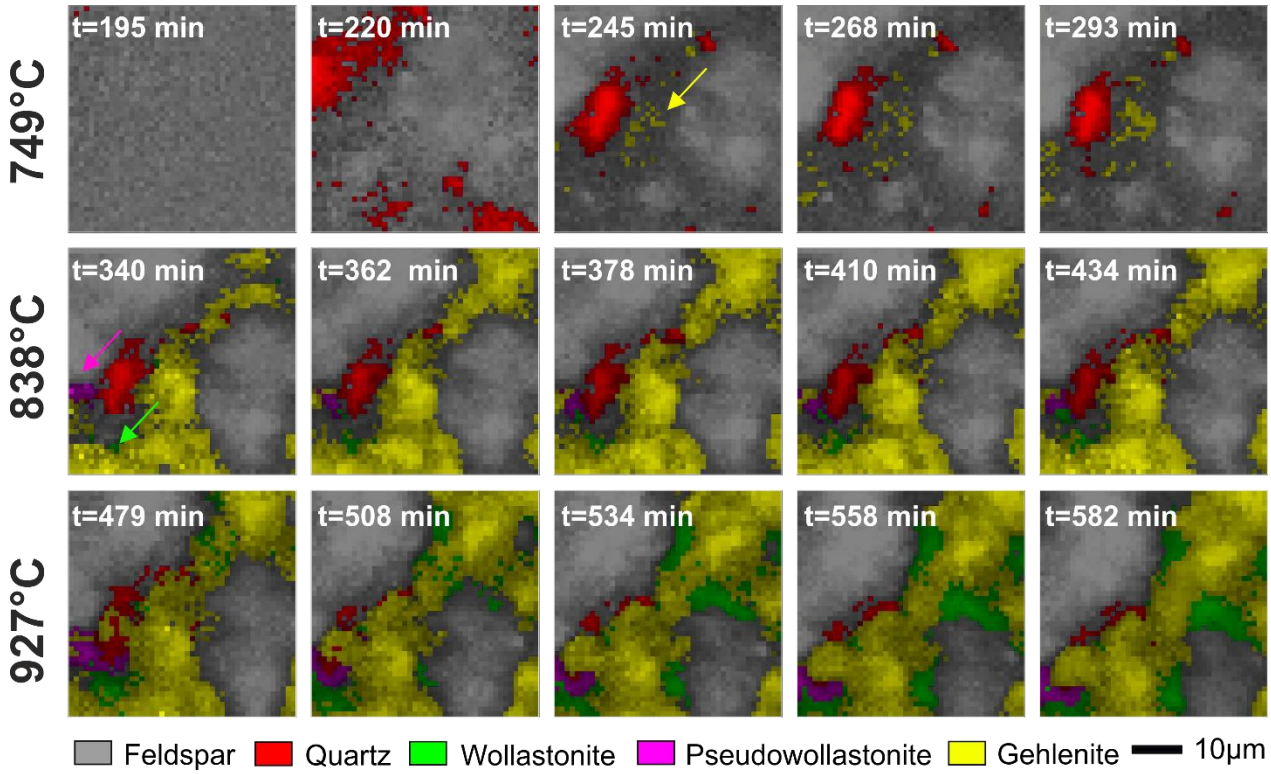

Figure 2.3: Normalized false-color hyperspectral Raman images (unmixed mode) within an area of 45x45 µm² that was imaged during stepwise high-temperature sintering (2.5 h soaking time per temperature step) of a ceramic green body containing kaolinite, quartz, kalifeldspar, and calcite (F-Exp). The yellow arrow points to the location of gehlenite at 749°C, whereas the pink and the green arrow point to the location of newly formed pseudowollastonite and wollastonite, respectively.

(2) Fast-heating experiment (F-Exp, 749 - 1016°C, ~100°C-steps; measurements in situ at HT)

Normalized false-color hyperspectral Raman images (unmixed mode) of an area of 45 x 45 µm² that were recorded *in situ* during stepwise high-temperature sintering (100°C steps; 150 min dwell time per temperature step) are displayed in Fig. 2.3. While the time-series images of S-Exp acquired during the 2 h dwell time are essentially equal, the time-series images of the F-Exp are different in that in this experiment isothermal progressions of reactions could be detected (Fig. 2.3). Within the imaged area, three new phases could be identified during thermal annealing from about 750 to 930°C, namely wollastonite, gehlenite, and pseudowollastonite.

After 50 min (245 min total run time) firing at 749°C, gehlenite was the first new phase that was detectable within the imaged area. With heating to a temperature of 838°C the apparent gehlenite fraction increased rapidly (Fig. 2.3). At this temperature wollastonite and, unexpectedly, pseudowollastonite crystallized in contact with gehlenite (Fig. 2.3). At a temperature of 927°C and with increasing dwell time, more wollastonite crystallized at the direct contact to and in expense of gehlenite (Fig. 2.3). Concurrently, the fraction of gehlenite further increased (Fig. 2.3), while the quartz grain located left of the center of the image steadily disappeared, i.e., was replaced by gehlenite. After quenching the sample to RT, gehlenite itself was fully replaced by the dicalcium silicate phase, i.e., either by larnite or calcio-olivine.

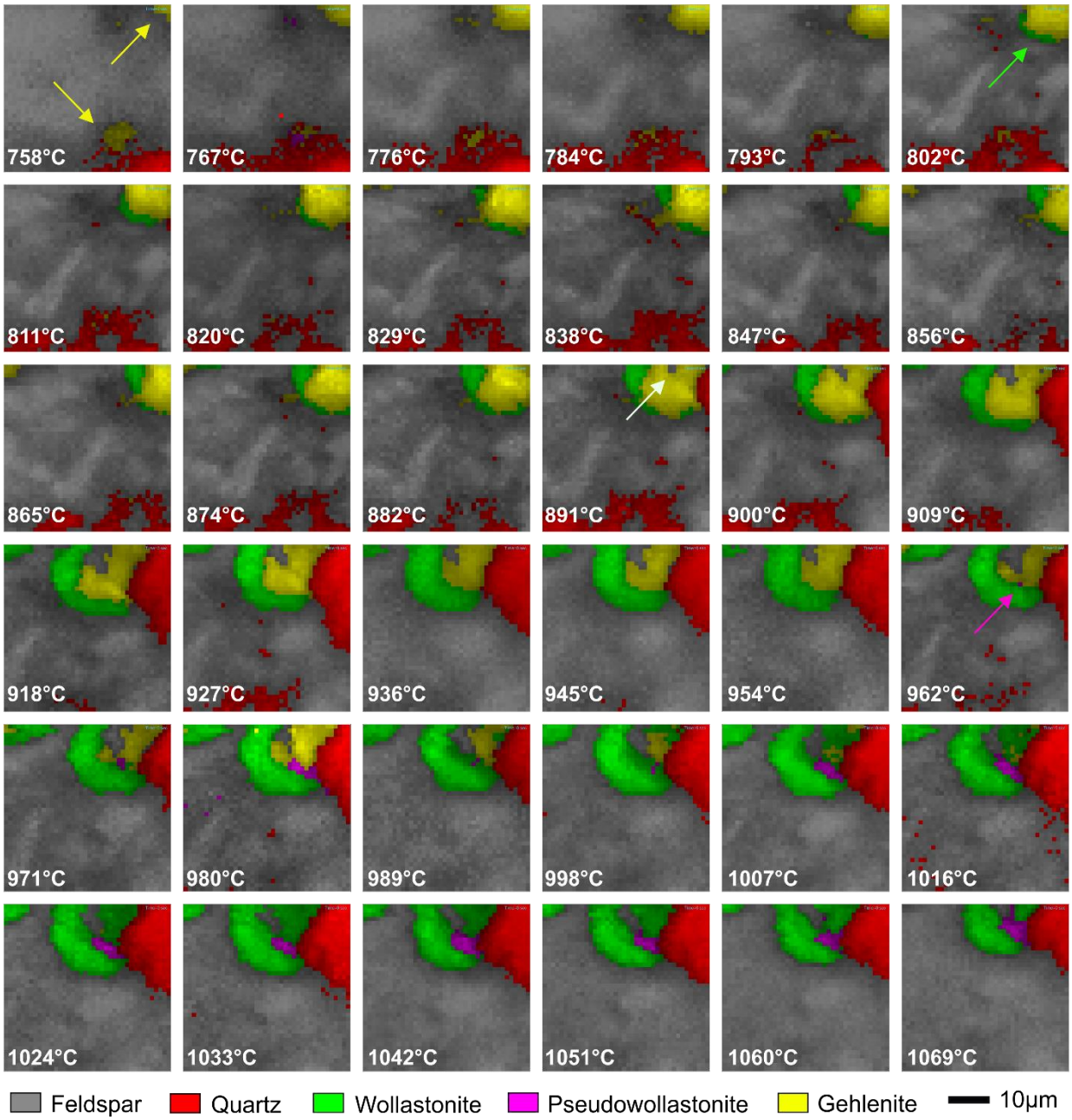

Figure 2.4: False-color hyperspectral Raman images showing the phase distribution within an area of 40 x 40 µm² that was imaged in situ during stepwise high-temperature sintering (two hours soaking time per temperature step) of a ceramic green body containing kaolinite, quartz, kalifeldspar, albite, and calcite (S-Exp). Note that dark (black) areas correspond to grain boundaries or undetectable phases such as lime, metakaolinite, or possibly a melt phase. The yellow and green arrows point to the location of newly formed gehlenite and wollastonite, respectively. The white arrow points to the location where gehlenite starts to break down, whereas the pink arrow marks the first appearance of pseudowollastonite. The slight shift of the imaged areas resulted from shrinking of the green body.

(3) Slow-heating experiment (S-Exp, 749-1069°C, ~10°C-steps; measurement in situ at HT)

Whereas the fast-heating experiment was carried out with about 100°C steps (like in the Q-Exp), in this experiment a 40 x 40 µm² area was imaged from about 750 to 1070°C in temperature steps of 10°C with a dwell time of 2 h to observe more details about the temperature- and time-dependence of the sintering reactions. The six isothermal images at each temperature step, however, did not reveal any changes within this time frame. Hence, only the first image of each temperature step is shown in Fig. 2.4.

Gehlenite, wollastonite, pseudowollastonite, and feldspar were identified as new phases that formed during the course of the experiments. Gehlenite was again the first detectable new phase that appeared at 758°C particularly in the upper right part of the imaged area (Fig. 2.4). Another gehlenite grain that formed in the lower right of the image disappeared again with increasing temperature. At 802°C wollastonite started to crystallize at the contact to the gehlenite grain in the upper right part of the image. With increasing temperature wollastonite seem to grow at the expense of the gehlenite grain. At about 1000°C, the gehlenite grain was fully replaced by wollastonite, and partly by pseudowollastonite. Pseudowollastonite could be detected already at 962°C at a triple junction between gehlenite, wollastonite, and quartz (pink arrow in Fig. 2.4). With the exception of pseudowollastonite, the occurrence of all phases in the final ceramic was further verified by powder X-ray diffraction analysis that yielded an average phase composition of 58 vol.% feldspar, 24 vol.% quartz 5 vol.% wollastonite, and 13 vol.% gehlenite, revealing that gehlenite was still a stable phase at the maximum firing temperature, although it completely disappeared from the imaged area already at about 1000°C. It is noteworthy, that due to the minor quantities of gehlenite relative to the other phases, gehlenite is no longer displayed in the hyperspectral Raman images, even though gehlenite Raman signals could still be detected in the Raman spectra until the end of the experiment. Contrary to Q-Exp and F-Exp, gehlenite was not replaced by a dicalcium silicate phase during quenching of the sample at the end of the experiment.

A broad band near 1046 cm^{-1} was observed at high temperatures (> 960°C) that could not be assigned to any phase. This band may be related to a melt (glass) phase. However, even if a melt phase was present, its quantity must either have been low, as it has neither been detected at room temperature by XRD (i.e., by a broad hump in the XRD spectrum) nor by Raman spectroscopy in the burnt ceramic, or the melt might have been recrystallized during cooling.

IV. Discussion

At low temperatures the firing process is dominated by a series of dehydroxylation and decomposition reactions, like the devolatilization of kaolinite and the decomposition of calcite. At temperatures higher than about 750°C, the calcium, aluminium and silica, provided by the decomposition of carbonate and kaolinites, form new silicates phases such as gehlenite, wollastonite, and pseudowollastonite. All inferred reactions in the quench- and *in situ* experiments are discussed in the following and summarized schematically in Figure 2.5.

(1) Devolatilization/decomposition and reverse reactions

During heating from RT to 749°C, kaolinite lost its chemically bound water and metakaolinite was formed (*e.g.*, [11]; [25]), according to the reaction:

$$\underset{Kaolinite}{Al_2Si_2O_5(OH)_4} \xrightarrow{\Delta\,(T)<600°C} \underset{Metakaolinite}{Al_2O_3 * SiO_2} + 2H_2O\ (g)\uparrow \qquad (1)$$

This reaction could be recognized by the rising water vapor that steamed up the quartz window for several minutes, but could otherwise not be followed *in situ* at high temperatures by conventional dispersive Raman spectroscopy. This is because the detection of the fundamental Raman bands of disordered, powdered kaolinite and metakaolinite is not straightforward, because

these mineral cause severe fluorescence when excited with a 532 nm laser and are characterized by relative weak Raman bands [26, 15] that are covered by bands of other minerals in the ceramic. For these reasons, the experiments were focused on high-temperature reactions. From a Raman heating study of ordered kaolinite (KGa-1 international standard) from RT to 1250°C in 10°C-steps (data not presented here), the dehydroxylation of kaolinite appeared to takes place over a temperature range from 450°C to 600°C, which

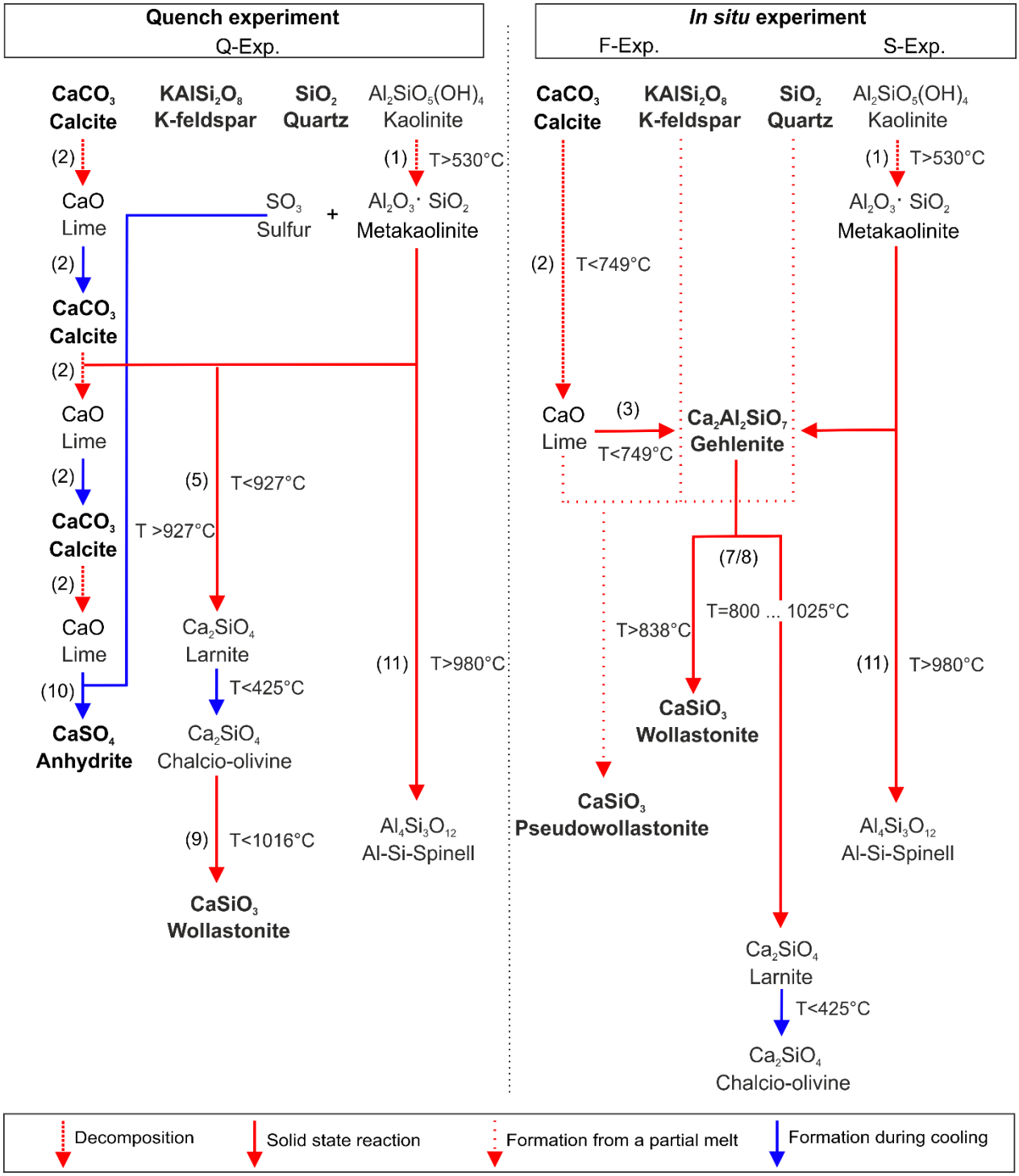

Figure 2.5: Proposed reaction scheme for the quench- and in situ experiments. The mineral phases that are detected by Raman spectroscopy beyond doubt are given in bold letters, whereas the other mineral phases could not be detected by Raman spectroscopy or were not identified without doubt (e.g. the Raman spectrum of Ca_2SiO_4 cannot be assigned to either larnite or calcio-olivine, see text for further details. Number in brackets refer to the reaction equations that are given in the discussion section.

is in a good agreement with an high temperature infrared emission spectroscopy study of Frost and co-authors [37]. The dehydroxylation process is dependent of the temperature, the partial pressure of H_2O, and the structural disorder of the kaolinite [37]. Dehydroxylation results in the disturbance of the $Al(O,OH)_6$ octahedral sheet and involve a change in the Al- coordination from 6 to 4 [38].

At temperatures greater than about 600°C, the decarbonation of calcite started as described by:

$$\underset{Calcite}{CaCO_3} \xrightarrow{\Delta\,(T)<749°C} \underset{Lime}{CaO} + CO_{2\,(g)}\uparrow \qquad (2)$$

This reaction was found to be partly reversible (*e.g.*, [27]).

Indeed, whereas in none of the spectra of the imaged area of the *in situ* experiments, the intense $v_1(CO_3)$ band of calcite near 1085 cm^{-1} (at RT) could be detected, calcite could clearly be identified in the quench experiment (Q-Exp), even after sintering the same green body material to temperatures up to 1016°C. (Figs. 2.2 and 2.6). This is clear evidence that the decarbonation reaction is reversible, i.e., that calcite re-crystallizes during cooling in CO_2-bearing atmosphere. It is known that during the topotactic solid-state transformation of calcite to CaO, the external shape of the {1014} rhombohedron is fully preserved, despite of the porosity of 54.2% generated by full release of CO_2 from calcite ([28] and ref. therein). Theses pores and cracks are represented by darker areas in and around the calcite grains (Fig. 2.6). Calcite therefore reformed during cooling at the same position, where the calcite had been transformed to CaO during heating before (Fig. 2.6). Such reaction can be considered as a reversible pseudomorphic mineral-gas replacement reaction.

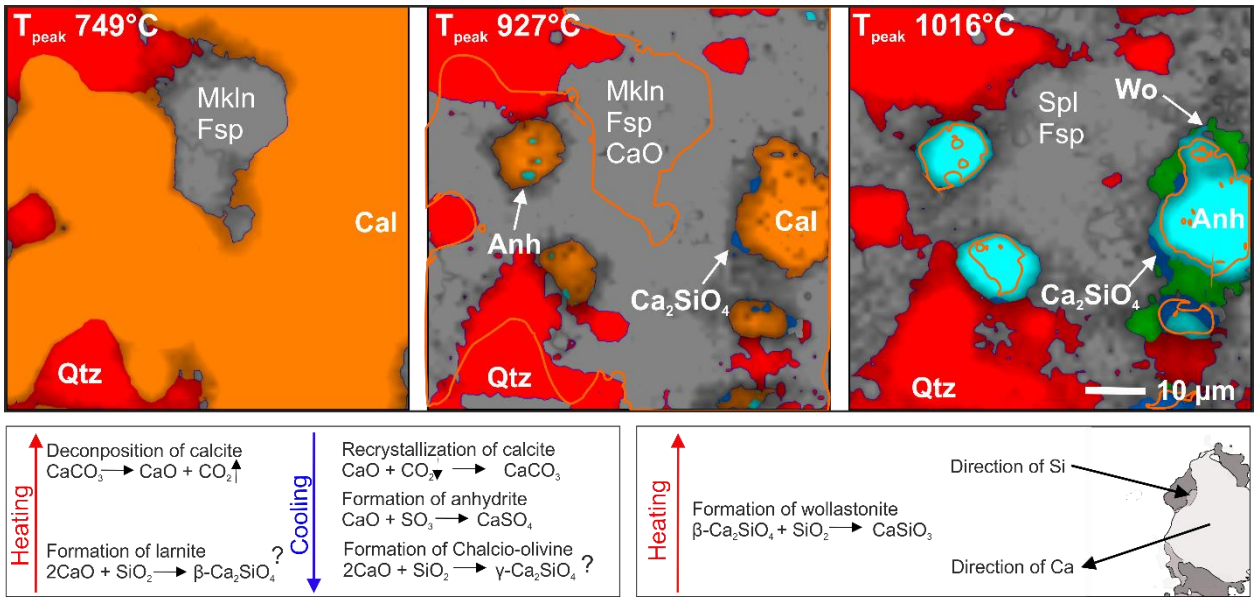

Figure 2.6: Smoothed hyperspectral Raman images of the same area recorded at room temperature after firing the green body to the given temperatures (T_{peak}). Note that the grey area in each image marks those areas where feldspar and phases that were not detectable (i.e, lime, metakaolinite, and Al-Si spinel) are located. Calcite ($CaCO_3$) decomposes during firing to lime (CaO) and CO_2. Lime has no first-order Raman spectrum and therefore is displayed by an orange line that marks the area where calcite was detected before. The presence of calcite relicts after firing the sample to 927°C suggests that the decomposition is reversible and calcite recrystallizes during cooling in CO_2-bearing atmosphere. The pores of calcite grains, caused by the CO_2 loss during decomposition, were filled by anhydrite ($CaSO_4$). Around the calcite relicts a rim of dicalcium silicate (larnite or chalcio-olivine) has formed. After firing to 1016°C the former calcite relicts are fully replaced by anhydrite. The monocalcium silicate wollastonite has formed a rim around the dicalcium silicate and anhydrite. Abbreviations: Cal=calcite, Qtz=quartz, Mkln=metakaolinite, Fsp=feldspar, Anh=anhydrite, Wo=wollastonite, Spl=Al-Si spinel.

Unexpectedly related to the sintering of ceramics is the formation of anhydrite at 927°C in the quench experiment (Q-Exp). Although the presence of sulfate is unusual in silicate ceramics, a Ca-bearing sulfate was identified by Trindade and co-authors [14] after sintering calcareous clay to temperatures above 900°C. Since a sulfur phase could neither be detected by Raman spectroscopy nor by XRD in the green body, sulfur must have been released from kaolinite during its decomposition, resulting in a high partial SO_2 pressure inside cracks and pores. Nevertheless, it cannot completely be ruled out that sulfur was provided by minor amounts of accessory sulfides that have not been detected. In any case, sulfur must have been present in significant amounts as it reacted with lime, formed by the decarbonation of the carbonate grains, to anhydrite during cooling:

$$\underset{Lime}{CaO} + \underset{Sulfur}{SO_3} \xrightarrow{\Delta(T)<927°C} \underset{Anhydrite}{CaSO_4} \quad (3)$$

At sintering temperatures above 927°C, the formation of anhydrite seems to suppress the recrystallization of calcite during cooling, so that anhydrite basically replaced former carbonate grains. After sintering at 927°C, anhydrite begins to crystallize in CaO pores generated by CO_2 release during the thermal decomposition of calcite (Fig. 2.6). After sintering to 1016°C, anhydrite completely replaced the calcite grains (Fig. 2.2 and 2,6).

(2) Formation of calcium silicates

Gehlenite was already identified at a temperature of about 750°C (F-Exp and S-Exp) that is about 50°C lower than previously reported [230]. The cause for this differences might be: (i) the low sensitivity (for traces of mineral phases) of the analytical techniques used in previous work (i.e., XRD) that did not allow the detection of small reaction rims between silicates and carbonates, (ii) the use of a different composition of the starting material, such as Ca or Mg which may suppress or support the formation of new phases or trigger the formation of partial melts, and/or iii) the pre-experimental intensive milling procedure which facilitates the formation of gehlenite from intermediate phases such as dicalcium silicate and tricalcium aluminate phase [36] and the multiple solid-solid interfaces created by the pressing during sample preparation. In addition, the presence of multiple interfaces among different crystals may enhance finger development (an interface geometry that is observed at carbonate-silicate interface), resulting in kinetic changes favoring phase formations at lower temperatures [30]. Gehlenite likely formed by the reaction of metakaolinite with lime as follows [10]:

$$\underset{Metakaolinite}{Al_2O_3 * SiO_2} + \underset{Lime}{2CaO} \xrightarrow{\Delta(T)\geq 750°C} \underset{Gehlenite}{Ca_2Al_2SiO_7} \quad (4)$$

It has been suggested that gehlenite reacts with quartz and corundum to anorthite, according to the reaction [31]:

$$\underset{Gehlenite}{Ca_2Al_2SiO_7} + \underset{Quartz}{3SiO_2} + \underset{Corundum}{Al_2O_3} \xrightarrow{\Delta(T)>1000°C} \underset{Anorthite}{2CaAl_2Si_2O_8} \quad (5)$$

However, anorthite could not be detected in any of the experiments by its band near 504 cm^{-1}, which clearly distinguishes anorthite from K-feldspar.

With increasing temperature most of the gehlenite seems to disappear at the expense of wollastonite ($CaSiO_3$). This solid-solid replacement was first identified at 802°C (S-Exp) and 838°C (F-Exp) (Figs. 2.3 and 2.4). At temperatures higher than ~1020°C (S-Exp) the gehlenite grains within the imaged area seem to be fully replaced by wollastonite, although gehlenite could still be detected by Raman spectroscopy and XRD in the finally quenched ceramic. Tschegg et al. [32] found that the

stability field of gehlenite is affected by the concentration of SiO_2 that is available in the system. It is thus conceivable that wollastonite crystallized from a reaction of gehlenite with free SiO_2 provided by the slow decomposition of metakaolinite.

$$\underset{Gehlenite}{Ca_2Al_2SiO_7} + \underset{Silica}{SiO_2} \xrightarrow{\Delta(T)>800°C} \underset{Wollastonite}{2CaSiO_3} + \underset{Corundum}{Al_2O_3} \quad (6)$$

Such reaction would release Al_2O_3, which could occur as a corundum phase. However, corundum could neither be detected by Raman spectroscopy nor by XRD at the end of the experiments. In the case, more silica is available, an Al-Si spinel might have been formed according to the reaction:

$$\underset{Gehlenite}{2\ Ca_2Al_2SiO_7} + \underset{Silica}{5\ SiO_2} \xrightarrow{\Delta(T)>800\ ^\circ C} \underset{Wollastonite}{4\ \beta - CaSiO_3} + \underset{Al-Si\ spinel}{Al_4Si_3O_{12}} \quad (7)$$

Al-Si spinel, however, has also not been detected. However, this phase is difficult to identify, in particular at high temperatures, due to its weak Raman bands [15]. In any case, the formation of wollastonite in the carbonate-bearing green bodies used in this study cannot been explained by the commonly presumed solid-state reaction between carbonate and quartz (*e.g.,* [30]), given as:

$$\underset{Calcite}{CaCO_3} + \underset{Quartz}{SiO_2} \xrightarrow{\Delta(T)800°C} \underset{Wollastonite}{CaSiO_3} \quad (8)$$

No textural evidence, such as the formation of a wollastonite rim around quartz grains for such a reaction was found in any of the experiments. It follows that the close textural relationship between gehlenite and wollastonite rather supports reaction (6) or (7) for the formation of wollastonite in those experiments that did not involve quenching.

The dicalcium silicate phase occurs in during the Q-Exp and F-Exp after firing to 927°C and 1016°C, respectively, and subsequent cooling to RT, but was not observed in the *in situ* experiments. This is evidence that this phase is a quench phase that formed during cooling. A larnite-like composition was also found by electron microprobe analyses in the study of Cultrone et al. [30], although XRD results did not show the presence of larnite, which, however, could be due to a low amount of this phase in the bulk ceramic. It has been suggested that dicalcium silicate, like wollastonite, forms by a reaction between lime and quartz [34]:

$$\underset{Lime}{2\ CaO} + \underset{Quartz}{SiO_2} \xrightarrow{\Delta(T)\ 930-1020°C} \underset{Larnite\ or\ chalcio-olivine}{Ca_2SiO_4} \quad (9)$$

The formation of Ca_2SiO_4 in our experiments is not spatially related to quartz (Fig. 2.2 and 2.6), which suggests that amorphous silica related to the breakdown of metakaolinite is more likely the source of SiO_2 than quartz. It is finally noted here that pure β-Ca_2SiO_4 inverts completely to stable γ-Ca_2SiO_4 below 425°C according to the phase diagram of the Ca_2SiO_4-$Ca_3(PO_4)_2$ system that was published by Sokol et al. [33], who modified the diagram after Fix et al [35].

Ptácek et al. [36] ascribes the occurrence of wollastonite at 1050°C in a mixture of kaolin and calcite to a reaction of dicalcium silicate with free silica:

$$\underset{Chalcio-olivine\ or\ larnit}{Ca_2SiO_4} + \underset{Silica}{SiO_2} \xrightarrow{\Delta(T)1025-1050°C} \underset{Wollastonite}{2\ \beta - CaSiO_3} \quad (10)$$

Such reaction would be in agreement with the observation made in the quenched ceramic fired at 1016°C (Q-Exp), where wollastonite occurs as rim around Ca_2SiO_4 (Fig. 2.6). Since the wollastonite is not spatially related to quartz in any of the experiments, a solid state

reaction between lime or calcite and quartz is again rather unlikely. However, the formation mechanism of wollastonite seems to differ in the *in situ* and the quench experiment. In the quench experiment (Q-Exp) wollastonite forms as a rim around Ca_2SiO_4, which suggests a reaction between amorphous silica and Ca_2SiO_4 (i.e. reaction 10). In the *in situ* experiments (F-Exp and S-Exp) wollastonite formation is spatially related to gehlenite grains and a dicalcium silicate phase could not be detected. It is noted that the formation of wollastonite from gehlenite was also reported from carbonate rich ceramics [30].

In the temperature range of 950-1000°C feldspar reacts with silica and forms eutectic melt [39]. The eutectic melting point for K-feldspar and quartz is at 980°C and thus lower than that of Ca-bearing feldspar and quartz [17]. This is confirmed by the observation of Das & Dana [39] who showed that above 980°C rapid shrinkage occurs in samples containing K-feldspar, quartz, and clay, due to the formation of liquid phases. Melting is also affected by the presence of carbonates. Ca and Mg act as melting agents. When carbonates are present, the melting temperature of kaolin-based materials is lowered down to ~ 800°C [40]. Considering the high carbonate content in the starting material, the broad band near 1050 cm^{-1} that appeared in the Raman spectra recorded above 960°C (S-Exp) may thus be related to the formation of a partial melt. Kalampounias [41] assign the band at 1050 cm^{-1} to the Q^3 species in a quenched melt of 0.4 $CaO \cdot 0.6\ SiO_2$. On the other hand, Ca and Mg also seem to limit the extent of vitrification at temperatures in excess of 1000°C ([30], and references therein), which might be due to the crystallization of new Ca- or Mg-silicates at higher firing temperatures consuming the melt.

Previous works has suggested that pseudowollastonite is the stable polymorph at temperatures in excess of about 1125°C if no Mg is present in the system [42; 43]. However, this is not consistent with the observation that in the *in situ* experiments pseudowollastonite already crystallized in contact wollastonite, gehlenite, and quartz at a sintering temperature of 838°C (F-Exp) and of 962°C (S-Exp), surprisingly even in concurrence with its low-temperature polymorph wollastonite. Since the occurrence of pseudowollastonite could clearly be confirmed by the RT Raman spectra (Fig. S2.3 and S2.4), the fact that it was not detected by XRD suggests that it is either only a minor phase within the burnt ceramic or partly broke down to the low-temperature polymorph wollastonite during cooling. Considering the established stability field of pseudowollastonite in the SiO_2-Al_2O_3-CaO system of <1125°C [42], the unambiguous appearance of pseudowollastonite at temperatures as low as 838°C implies that it can form metastably, assuming that the previously determined phase transition temperature for pure $CaSiO_3$ is accurate.

The polymorphs pseudowollastonite and wollastonite crystallized contemporaneously and in close contact to each other (F-Exp and S-Exp), which suggests that the very local conditions had to be disparate. This could be due to (i) a different reaction mechanism, e. g., the formation of wollastonite by a solid state reaction between gehlenite and silica and pseudowollastonite by crystallization from a partial melt or (ii) different crystallographic structures or orientations of the educts, which either favor the formation of a single chain inosilicate (Wo) or a cyclosilicate (PWo).

(3) High temperature sintering

In the temperature range of 950-1000°C metakaolinite is known to decompose into non-equilibrium spinel-type phases with the liberation of amorphous silica [15].

$$\underset{Metakaolinite}{2\,Al_2O_3 * SiO_2} \xrightarrow{\Delta\,(T)\geq 950°C} \underset{Al-Si\ spinel}{Ca_4Al_3SiO_{12}} \quad (11)$$

However, Al-Si spinel could not be detected by micro Raman spectroscopy, likely due to relative weak Raman bands [15]. Furthermore, mullite, which is assumed to form from Al-Si spinel at temperatures higher than about 950°C (*e.g.*, [11]; [25]), could not be detected. This is probably caused by a suppression of mullite formation by the combination of decomposition of clay minerals with the excess of CaO, yielding gehlenite instead of mullite [14]. Ptácek et al. [36] suggested that a pre-experimental intensive milling procedure could facilitates the formation of gehlenite from intermediate phases such as dicalcium silicate and tricalcium aluminate, that however, have not been observed as precursor phases of gehlenite in this study. In contrast, dicalcium silicate was found to replace gehlenite during cooling.

V. Conclusion

This study reports results of first experiments using confocal hyperspectral Raman imaging to *in situ* study sintering reactions in kaolin-based green bodies. The possibly most unexpected result of this study is that the formation of pseudowollastonite occurred already at temperatures as low as 840°C, which is about 290°C below the critical temperature for the wollastonite-pseudowollastonite transformation [42, 43], and thereby in direct contact to its low-temperature pseudomorph wollastonite. This implies that pseudowollastonite can form metastably, which raises doubts on the interpretation of the temperature conditions of pyrometamorphic rocks from the presence or absence of pseudowollastonite in a rock [44]. Another striking observation from our experiments is that wollastonite did not form by a reaction between lime and quartz, although both phases were present in significant amounts in the green body. Instead, wollastonite crystallized as a replacement product around gehlenite, possibly by a solid-state reaction of gehlenite with silica that was released by the slow breakdown of metakaolinite. From textural observations it appears that free silica must also play a major role in another wollastonite-forming reaction that, however, was only observed in the quench experiment. Here, wollastonite formed during quenching by a reaction of dicalcium silicate (larnite and/or calcio-olivine) with silica.

From the results of this study it is apparent that important information is lost when investigating sintering reactions only by *ex situ* studies. The new results highlight the power of *in situ* Raman spectroscopy as an analytical tool that can deliver *in situ* information about the growth and breakdown of distinct phases, including the detection of metastable or intermediate phases, without the necessity to quench the sample to RT. Raman images can be taken during heating and cooling with a high temperature, time, and space resolution, enabling the kinetics of individual reaction steps to be quantified. A single experiment therefore contains the information of a multitude of conventional sintering experiments, involving heating and quenching of different samples. A detailed understanding of the kinetics of sintering reactions is essential in a number of scientific or technical fields, where mineral reactions and parageneses are used to unravel the temperature history of sintered products such as, e.g., metamorphic rocks, archeological ceramics, or sintered crusts in high-temperature coal kilns that are used for energy production. *In situ* hyperspectral Raman imaging provides further information about the textural evolution and interaction between individual mineral grains and possibly between mineral grains and a melt, potentially giving insight into mesoscopic

details about the reaction mechanisms. For instance, due to the polarization-dependence of Raman band intensities, the rotation of individual grains can potentially be monitored along with reactions among the grains. Such data provide important experimental insights necessary to develop and test theoretical models and simulations that consider effects such as anisotropic shrinkage and the dynamics of the rearrangement of grains, especially during the initial stages of sintering. Space-, time-, and temperature-resolved hyperspectral Raman imaging of HT solid-state reactions at the micrometer-scale could give direct insights into these and other mechanisms of sintering reactions against which numerical models can be tested.

Acknowledgements

Many thanks go to T. Schulz and D. Lülsdorf for the technical support with the heating stage. We further acknowledge D. Paßman and Dr. S. Franz for carrying out the XRF analyses and Dr. H. Euler and H.-H. Friedrich for performing the XRD measurements. Financial support by the Rheinische Friedrich-Wilhelms-Universität Bonn, Germany in the form of a scholarship is gratefully acknowledged.

References

[1] Vandiver PB, Soffer O, Klima B, et al. The origins of ceramic technology at dolni vecaronstonice, czechoslovakia. *Science*.1989;246:1002-1008.

[2] Wu X, Zhang C, Goldberg P, et al. Early pottery at 20,000 years ago in Xianrendong Cave, China.*Science*.2012;336:1696-1700.

[3] Berto AM. Ceramic tiles: Above and beyond traditional applications. *J. Eur. Ceram. Soc.* 2007; 27:1607-1613.

[4] Carter CB, Norton MG. Ceramic Materials: Science and Engineering. 2thed. New York, NY: Springer Science & Business Media; 2007.

[5] Nkou Bouala GI, Clavier N, Martin S, et al. From in Situ HT-ESEM Observations to Simulation: How Does Polycrystallinity Affects the Sintering of CeO2 Microspheres? *J. Phys. Chem. C.* 2016;120:386-395.

[6] Podor R, Clavier N, Ravaux J, et al. Dynamic aspects of cerium dioxide sintering: HT-ESEM study of grain growth and pore elimination. *J. Eur. Ceram. Soc*. 2012;32:353-362.

[7] Zhang J, Huang F, Lin Z. Progress of nanocrystalline growth kinetics based on oriented attachment. *Nanoscale*. 2010;2:18-34

[8] L'vov BV. Mechanism and kinetics of thermal decomposition of carbonates. *Thermochim. Acta*. 2002;386:1-16.

[9] Elert K, Cultrone G, Navarro C, et al. Durability of bricks used in the conservation of historic buildings - influence of composition and microstructure. *J. Cult. Herit*. 2003;4: 91-99.

[10] Traoré K, Kabré TS, Blanchart P. Gehlenite and anorthite crystallisation from kaolinite and calcite mix. *Ceram. Int*. 2003;29:377-383.

[11] Chen YF, Wang MC, Hon MH. Phase transformation and growth of mullite in kaolin ceramics," *J. Eur. Ceram. Soc*. 2004;24:2389-2397.

[12] Cultrone G, Sebastián E, de la Torre MJ. Mineralogical and physical behaviour of solid bricks with additives. *Constr. Build. Mater*. 2005;19:39-48.

[13] Saboya F, Xavier GC, Alexandre J. The use of the powder marble by-product to enhance the properties of brick ceramic. *Constr. Build. Mater*. 2007;21:1950-1960.

[14] Trindade MJ, Dias MI, Coroado J, et al. Mineralogical transformations of calcareous rich clays with firing: A comparative study between calcite and dolomite rich clay from Algarve, Portugal. *Appl. Clay Sci.* 2009;42:345-355.

[15] Shoval S, Boudeulle M, Panczer G. Identification of the thermal phases in firing of kaolinite to mullite by using micro-Raman spectroscopy and curve-fitting. *Opt. Mater*. 2011;34:404-409.

[16] Sokoláir R, Vadová L, Grygarová S, et al. Mechanical properties of ceramic bodies based on calcite waste. *Ceram. Int*. 2012;38:6607-6612.

[17] Aras A. The change of phase composition in kaolinite- and illite-rich clay-based ceramic bodies. *Appl. Clay Sci*.2004;24:257-269.

[18] McMillan PF, Poe BT, Gillet PH, et al. A study of SiO_2 glass and supercooled liquid to 1950 K via high-temperature Raman spectroscopy. *Geochim. Cosmochim. Acta*. 1994;58:3653-3664.

[19] Swamy V, Dubrovinsky LS, Tutti F. High-Temperature Raman Spectra and Thermal Expansion of Wollastonite. *J. Amer. Ceram. Soc.* 1997;80:2237-2247.

[20] Richet P, Mysen BO, Ingrin J. High-temperature X-ray diffraction and Raman spectroscopy of diopside and pseudowollastonite. *Phys. Chem. Miner*. 1998;25:401-414.

[21] Bouhifd MA, Gruener G, Mysen BO, et al. Premelting and calcium mobility in gehlenite ($Ca_2Al_2SiO_7$) and pseudowollastonite (CaSiO3). *Phys. Chem. Min.* 2002;29:655-662.

[22] Salomon EB, Sansonetti CJ. Wavelengths, Energy Level Classifications, and Energy Levels for the Spectrum of Neutral Neon. *J. Phys. Chem. Ref. Data*. 2004;33:1113-1158.

[23] Laetsch T, Downs R. Software for Identification and Refinement of Cell Parameters from Powder Diffraction Data of Minerals Using the RRUFF Project and American Mineralogist Crystal Structure Databases. Abstracts from the 19th General Meeting of the International Mineralogical Association, Kobe, Japan, 23-28 July (2006).

[24] Lafuente B, Downs RT, Yang H, et al. The power of databases: the RRUFF project. In: Armbruster T, Danisi RM, *eds. Highlights in Mineralogical Crystallography.* Berlin, DE: De Gruyter; 2015:1-30.

[25] Santana LNL, Gomes J, Neves GA, et al. Mullite formation from bentonites containing kaolinite: Effect of composition and synthesis parameters. *Appl. Clay Sci*. 2014;87:28-33

[26] Frost RL. The structure of the kaolinite minerals FT-Raman study. *Clay Miner*. 1997;32:65-77.

[27] Escardino A, García-Ten J, Feliu C, et al. Calcium carbonate thermal decomposition in white-body wall tile during firing. I. Kinetic study. *J. Eur. Ceram. Soc*. 2010;30:1989-2001.

[28] Rodriguez-Navarro C, Ruiz-Agudo E, Luque A, et al. Thermal decomposition of calcite: Mechanisms of formation and textural evolution of CaO nanocrystals. *Am. Mineral.* 2009;94:578-593.

[29] Schmid T, Dariz P. Shedding light onto the spectra of lime: Raman and luminescence bands of CaO, $Ca(OH)_2$ and $CaCO_3$. *J. Raman Spectrosc*.2014;46:141-146.

[30] Cultrone G, Rodriguez-Navarro C, Sebastian E, et al. Carbonate and silicate phase reactions during ceramic firing. *Eur. J. Mineral*. 2001;13:621-634.

[31] Traoré K, Kabré TS, Blanchart P. Low temperature sintering of a pottery clay from Burkina Faso. *Appl. Clay Sci.* 2000;17:279-292.

[32] Tschegg C, Ntaflos T, Hein I. Thermally triggered two-stage reaction of carbonates and clay during ceramic firing — A case study on Bronze Age Cypriot ceramics. *Appl. Clay Sci.* 2009;43:69-78.

[33] Sokol EV, Seryotkin YV, Kokh SN. Flamite, $(Ca,Na,K)_2(Si,P)O_4$, a new mineral from ultrahigh-temperature combustion metamorphic rocks, Hatrurim Basin, Negev Desert, Israel. *Mineral. Mag.* 2015;79:583-596.

[34] Rashid RA, Shamsudin R, Hamid MAA et al. Low temperature production of wollastonite from limestone and silica sand through solid-state reaction. *J. Asian Ceram. Soc.* 2014;2:77-81.

[35] Fix W, Heymann H, Heinke R. Subsolidus relations in the system $2CaO{\cdot}SiO_2$-$3CaO{\cdot}P_2O_5$. J. Amer. Ceram. Soc- Discussion and Notes. 1969;52:346-347.

[36] Ptácek P, Opravil T, Soukal F, et al. Kinetics and mechanism of formation of gehlenite, Al-Si spinel and anorthite from the mixture of kaolinite and calcite. *Solid State Sci*. 2013;26:53-58.

[37] Frost RL, Vassallo AM. The dehydroxylation of the kaolinite clay minerals using infrared emission spectroscopy. *Clays Clay Miner*. 1996;44:635-651.

[38] Gualtieri A, Bellotto M. Modelling the structure of the metastable phases in the reaction sequence kaolinite-mullite by X-ray scattering experiments. Phys. Chem. Minerals. 1998;44:442-452.

[39] Das S, Dana D. Differences in densification behaviour of K- and Na-feldspar-containing porcelain bodies. *Thermochim. Acta.* 2003;406:199-206.

[40] Tite MS, Maniatis Y. Examination of ancient pottery using the scanning electron microscope. *Nature.* 1975;257:122-123.

[41] Kalampounias AG. IR and Raman spectroscopic studies of sol–gel derived alkaline-earth silicate glasses. *Bull. Mater. Sci.*2011;34:299-303.

[42] Osborn FF, Schairer JF. The ternary system pseudowollastonite-akermanite-gehlenite. *Am. J. Sci.* 1941;239:715-763.

Annotations

This chapter is published in the *Journal of American Ceramic Society*[59]. The conceptualization is done by T. Geisler and myself. I performed all Raman measurements. C. Lenting and T. Geisler contributed to the interpretation. I wrote the manuscript and produced all figures. T. Geisler and C. Lenting reviewed and edited the manuscript.

Chapter 3

In Situ Hyperspectral Raman Imaging: A New Method to Investigate Sintering Processes of Ceramic Material at High-temperature

Kerstin Hauke | Johannes Kehren | Nadine Böhme | Sinje Zimmer | Thorsten Geisler

Institut für Geowissenschaften, Rheinische Friedrich-Wilhelms-Universität Bonn, Bonn, Germany

Abstract

In the last decades Raman spectroscopy has become an important tool to investigate minerals, gases, glasses, and organic material at room temperature. In combination with high temperature and high pressure devices the *in situ* investigation of mineral reactions and their kinetic is also possible. Here, we present a novel approach to study the sintering process in silicate ceramics by *in situ* hyperspectral Raman imaging, which allows studying high temperature solid-solid and/or solid-melt reactions spatially and temporally resolved, providing new possibilities to study and visualize high temperature sintering processes in multi-component systems. By briefly presenting three application examples, we demonstrate that hyperspectral Raman imaging facilitates to *in situ* follow the migration of (i) solid-solid or solid-melt reaction fronts at high temperature and with micrometer scale resolution, as well as (ii) the temperature and time-dependent growth and breakdown of minerals from which kinetic information can be gained.

1. Introduction

In the last decades Raman spectroscopy has become one of the most important analytical tools for a wide range of research areas in all sub disciplines of physics, chemistry, biology, geosciences, and medicine. Initially, Raman spectroscopy was limited to scientific applications, but a low preparation effort, the ease of implementation, and developments in measurement automation have made Raman spectroscopy also interesting to users other than pure scientists. In particular, Raman spectroscopy is used for quality and process control applications [26]. In an early stage of Raman spectroscopy, the applications were limited due to generally weak Raman signals and interfering fluorescence caused by impurities of (natural) samples. However, the development of new laser technologies, filters, spectrometers, detection devices has enabled the investigation of all kinds of condensed matter. The resulting sensitivity of modern Raman spectrometer systems, combined with the high spatial resolution of confocal optical microscopes, nowadays also facilitates to image certain properties of solid materials or liquids at the micrometer scale.

In many industries, including food processing pharmaceuticals, and biomedicine, the demand for multidimensional assessment of the sample composition has increased dramatically [61]. Hyperspectral Raman imaging enables a rapid, routinely practicable, non-destructive food quality and safety evaluation [28] and has turned into a novel clinical diagnostic tool in biomedical applications [100]. It facilitates the investigation of heterogeneous systems and thereby reveals a wealth of chemical and physical information about the chemical composition, short-range atomic structure, structural strain, crystallite orientation [30]. This information is provided with a spatial resolution down to the micrometer length scale. In earth and materials sciences, Raman imaging has been used, for example, (i) for (mineral) phase identification in the mineralogical context of the parent rock [101], (ii) to study internal structures of minerals like zonation or the substitution of elements in solid solutions [102,103], (iii) to investigate isotope substitution and replacement mechanism [33], and to *in situ* study transport and reaction phenomena during silicate glass corrosion in aqueous solutions at elevated temperature [10, in press]

With the development of diamond anvil cells and heating devices the investigation of mineral transformation and reactions and their kinetics at high temperatures and pressures became also possible. *In situ* high temperature Raman spectroscopy has been used to study the temperature dependence of first-order phonon bands [36,39,104,105], pre-melting effects [20,106], the structure of melts [20,107–111], as well as solid state phase transitions [46,87]. In this work, we combined the advantages of *in situ* high temperature Raman spectroscopy with the possibility of 2-dimensional Raman imaging with a micrometer-scale resolution as a powerful tool for the *in situ* investigation of sintering processes. In a recently published study, we reported first results of sintering experiments using confocal hyperspectral Raman imaging (CHRI) to *in situ* study high-temperature, solid state reactions in kaolin-based green bodies [59]. The most striking results of this study were (i) the formation of

pseudowollastonite occurring already at temperatures as low as 840°C, which is about 290°C below the critical temperature for the wollastonite-pseudowollastonite transformation, and (ii) the observation that both polymorphs formed in direct contact to each other. These observations imply that pseudowollastonite can form metastably, which, for instance, raises doubts on the interpretation of the temperature conditions of pyrometamorphic rocks that is based on the presence or absence of pseudowollastonite in a rock [69]. These first results already highlighted the power of Raman spectroscopy as an analytical tool that can deliver *in situ* information about the growth and breakdown of distinct phases, including the detection of metastable or intermediate phases, without the necessity to quench the sample to RT. Raman images can be taken during heating and cooling with a high temperature, time, and space resolution, enabling the kinetics of individual reaction steps to be quantified. A single experiment therefore contains the information of a multitude of conventional sintering experiments, involving heating and quenching of different samples. In this work, we describe our novel approach to *in situ* study the sintering process of silicate ceramics by hyperspectral Raman imaging. The article mainly focusses on the experimental setup, the analytical methodology, and data analysis and visualization. However, the power of *in situ* Raman imaging for studying high temperature sintering reactions is briefly illustrated by three application examples.

2. High temperature hyperspectral Raman imaging

2.1. Analytical details

All Raman data presented in this work were collected with a Horiba Scientific HR 800 Vis confocal Raman spectrometer equipped with an Olympus BX41 microscope and an electron-multiplier CCD detector. The Raman spectra were excited with a frequency-doubled, solid state Nd:YAG laser (532 nm) with a maximum power of 2 W, which is significantly lower at the sample surface. During its five-years lifetime the laser lost about 20% of its power. Furthermore, about 35% of the intensity are lost through the pathway in the instrument and additionally due to light scattering and absorption of the cell window. A 17 mW He-Ne laser was also tested, but already at temperatures of 900°C the Raman signal was too weak and masked by black body radiation. To correct for any spectrometer shift during long-time measurements, the intense Ne line at 585.24878 (±0.00005) nm [112] that occurs at a Raman shift of 1707.06 cm^{-1} in the spectra (note the typo in Stange et al. 2018 [59]) was continuously monitored by placing a Ne lamp alongside the beam path of the scattered light. A 50x long-working distance (LWD) objective with a numerical aperture (NA) of 0.5 and a working distance of 10.6 mm was used for all experiments. Because the width of a Raman band usually broadens with increasing temperature to values of up to several tenths of wavenumbers, the spectral resolution was not a major issue. Therefore, we used a grating with 600 groves/mm so that a wavenumber range from about 100 to 1750 cm^{-1} could be measured in a single window. With this grating the spectral resolution was ~3.5 cm^{-1}, as given by the width of the intense Ne line at 1707.06 cm^{-1}. The LabSpec 6.4.4.15 software was used to control the instrument, the heating, soaking, and cooling cycles, to refine the data, and finally to create the images.

2.2. Experimental series

Three types of experiments were performed in this work. The first experimental series (E1) involved heating studies with pure mineral phases that occur in silicate ceramics. These experiments were carried out to obtain high temperature reference spectra that served as a basis for phase identification at high temperatures and the visualization of the Raman data from the *in situ* sintering experiments. They were performed with both single crystals (E1A) and powder pellets (E1B). Pure phase Raman spectra were taken every 10°C from RT to 1200°C with a total acquisition time of 100 s. The heating rate was 10°C/min. After having recorded a spectrum at maximum temperature, the sample was cooled to RT with a cooling rate of 10°C/min and a last spectrum was recorded. At each temperature step, depth profiles were acquired (auto-focus function) after an equilibration time of 300 s to obtain (i)

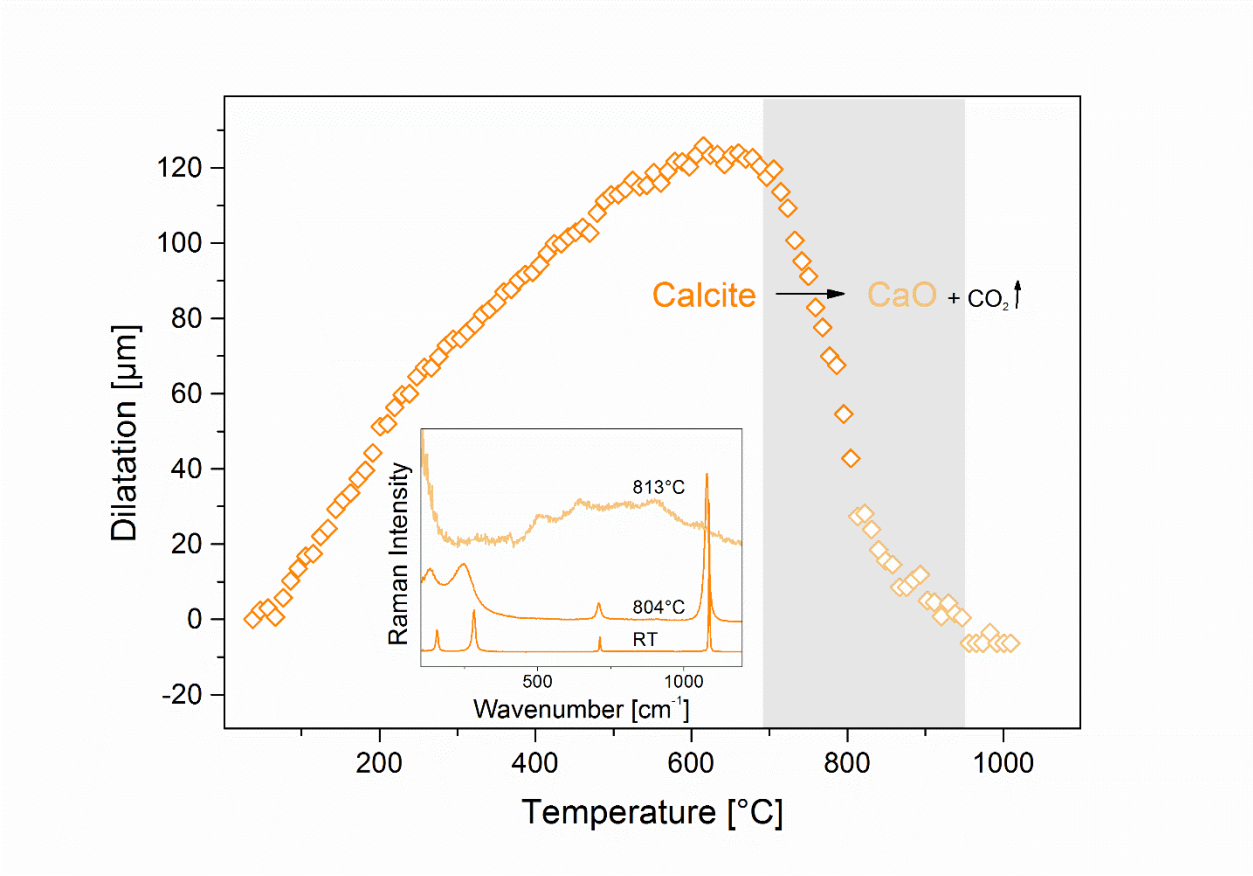

Figure 3.1: Dilatation of a pellet composed of calcite powder as a function of temperature. The dilatation was measured during the automated measurements by depth profiling. Note the dramatic shrinkage above 740°C due to the decarbonation of calcite. The decarbonation is taking place between 700 and 950°C, which can be followed by the shrinkage of the sample. At 804°C the calcite bands are broaden and shifted to lower wavenumbers (inset). Above 813°C calcite at the sample surface is fully decomposed to CaO (lime) that only shows a second order Raman spectrum. Note that the Raman spectra were recorded at the sample surface.

an optimal signal-to-noise ratio and (ii) a measure of reaction- and temperature-related shrinking or expansion effects. One example for the latter is the decomposition reaction of calcite to lime (CaO) and CO_2 between about 650 and 950°C, which could be followed by spectral focusing (Figure 3.1).

The second series of experiments (E2) involved multi-component sintering experiments and were carried out under very similar conditions as the pure phase experiments. After selecting a representative area of the sample surface, a hyperspectral Raman image was first recorded at RT. The sample was then fired with a heating rate of 10°C/min to 700°C (corrected temperature ~650°C, see below), where two images were subsequently recorded before heating the sample to the next temperature step. After having recorded the last high temperature image at 1200°C (corrected temperature ~1100°C) the sample was cooled to RT with a cooling rate of 10°C/min and a final image was taken.

The third series of experiments (E3) involved multi-component isothermal sintering experiments. The first image was recorded at RT to select a representative area. After that the sample was fired with a heating rate of 10°C/min to the target temperature of ~850°C. Within a dwell time of 24 h 12 Raman images (~2 hours per image) were recorded. The sample was then cooled down with a cooling rate of 10°C/min before recording a last image at RT.

2.3. Sample preparation

One of the major advantages of Raman micro spectroscopy is the ability to nondestructively derive spectral information with minimal sample preparation. However, the flatness of the sample surface can be crucial because light scattering at uneven

surfaces may negatively affect the quality of the spectra. The samples used for the high temperature, pure phase (E1A and E1B) and the multi-component sintering experiments (E2 and E3) were similarly prepared to minimize any systematic errors. Since high temperature Raman spectra of single crystals (E1A) and those of their powdered counterpart (E1B) revealed differences in intensity and linewidth of fundamental Raman bands [113], the heating studies were performed with both powdered material and single crystals that were placed at the bottom of the cell close to the thermocouple. The powdered minerals used for the heating studies (E1B) were pressed into cylinders with a diameter of 3 mm and a height of less than 1 mm to minimize the temperature deviation caused by the temperature gradient in the heating stage (cf. Sec. 2.4).

Table 3.1 Characteristics of the precursor material used for experiment E2 and E3.

Mineral	Company	Level of purity	Particle size
Quartz	Merck	99.900 %	5-50 µm[1]
Calcite	Alfa Aesar	99.950 %	2-20 µm[2]
CaO	Alfa Aesar	99.995 %	<10 µm
Amorphous SiO_2	Alfa Aesar	99.900 %	2-20 µm[2]
Kaolinite China-Clay	Carl Jäger Tonindustriebedarf GmbH	-	< 2 µm (58 %) 8-53 µm (8%) > 58 µm (0.05 %)

[1] The initial grain size of quartz was 200 to 800 µm. The grains were milled by hand in an agate mortar to a size of approximately 5 to 50 µm.

2 The grain size was not declared so the grain size has been determined from the Raman images.

For the multi-component sintering experiments (E2 and E3) several green bodies were produced by compacting about 4.3 mg of powdered precursor material (dried at 100°C for 24 h) into cylinders (3 x 2.7 mm^2) at a pressure of 0.01 MPa, which resulted in a flat sample surface.

2.4. Heating stage and temperature calibration

For all experiments, a TS1500 (Linkam Scientific Instruments, Surrey, UK) heating stage was mounted onto an automated x-y-z stage below the Olympus BX41 microscope objective, which facilitated to move the heating stage in all three directions with a reproducibility of ± 0.5 µm in x and y and ± 0.25 µm in z direction and thus to record hyperspectral Raman images at high temperatures. The temperature of the heating device can be varied between RT and 1500°C with a temperature stability of ± 1°C and a maximal heating rate of 200°C/min [114]. A platinum resistor sensor, accurate within ± 0.01°C, measures the temperature at the bottom of the cell. The sample cup has a diameter of 7 mm and height of 6 mm. A ceramic heating shield with a pinhole aperture of 1 mm diameter is mounted above the heating chamber to reduce the black body radiation reaching the objective and to reduce heat loss. However, due to height and volume of the sample cylinder, a strong temperature gradient occurs within the furnace. This gradient was empirically determined by a procedure that is described in detail in Stange et al. [59], which was also used here to determine the "real" temperature at the sample surface.

2.5. Map programming

Depending on the exact nature of the experiment one or several hyperspectral Raman images were recorded before having fired the sample to the next temperature step. At each temperature step a spectrum of the black body radiation was first recorded. Thereby, the acquisition parameters were identical, except that the sample was not excited by the laser. Depth profiles were acquired using the auto-focus function (depth profiling) before recording the first image at each temperature step to monitor reaction- and temperature-related shrinking or expansion effects and to obtain an optimal signal-to-noise ratio. The "tilt at limits" mode acquires depth profiles of the image center and the four corners, and determines the best focus regarding the Raman signal from which the focus at each position (pixel) in the image is interpolated. Thereby an inclined sample surface can be compensated.

The quality of the Raman spectra and therefore also of the Raman images depends on (i) the experimental parameters of the instrument

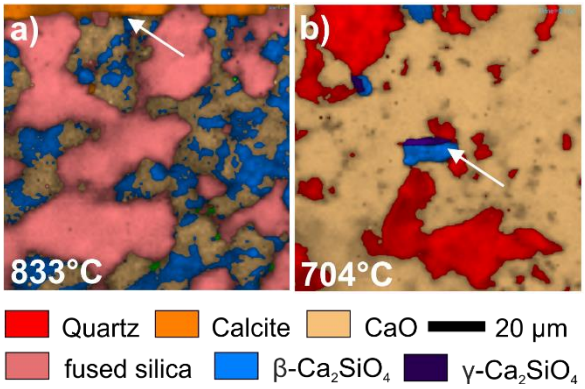

Figure 3.2: Hyperspectral Raman images of (a) fused silica-calcite and (b) quartz-lime green bodies recorded at 833 and 704°C with a total exposure time of about 2 h, showing line-by-line image shifts. The sudden phase changes (white arrows) indicate that the respective reactions in (a), i.e., $CaCO_3 \rightarrow CaO + CO_2\uparrow$, and (b), i.e., $\gamma\text{-}Ca_2SiO_4 \rightarrow \beta\text{-}Ca_2SiO_4$, were faster than the total imaging time.

(laser power, quality of lens, grating, detector, the size of confocal hole, the microscope objective used), (ii) sample parameters (surface, color, heterogeneity, the refractive index of the sample) [115], and (iii) on the acquisition time. Raman spectra were collected during continuous x-y stage movement with a speed of 1.6 µm/s (SWIFT© mode). During movement, Raman intensities were recorded for 0.6 s in the wavenumber range from 100 to 1750 cm^{-1}. All recorded images comprised an area of 100 × 100 $µm^2$ in size. The step size was 1 µm, yielding 10,000 spectra per image. Despite the short acquisition time per spectrum, the total exposure time was still about 2 h for a single image. This has to be taken into account when interpreting the hyperspectral Raman images since an image is not always an accurate snapshot, because processes still run while recording the image. However, reactions that are faster than image acquisition can easily be detected by line-by-line shifts in the image (Figure 3.2) so that the total acquisition time can be adjusted, e.g., by imaging a smaller area or by using shorter single point acquisition times.

In general, superior spectral quality can be obtained using a point-by-point mapping approach, as data sets can benefit from longer acquisition times. However, in this work the hyperspectral Raman images were recorded with a continuous moving table to save imaging time and maximizing the imaged area. It is noted that even poor-quality spectra usually provide sufficient detail for phase identification. The situation will be different, however, when other band parameters than the amplitude are needed, for instance to visualize structural or chemical variations reflected by the width and frequency of a Raman band. For Raman phase images, the quality of the reference spectra is more crucial for their quality than the signal-to-noise ratio [116]. A comparison of a map recorded in the fast scanning mode (SWIFT© mode, 0.6 s per spectrum, recording time of 50 minutes) and in the point-by-point mode with an acquisition time of 10 s per spectrum (1 s times 10 accumulation, recording time of 8 h 43 min) shows that the large increase in acquisition time has only a minor influence on the hyperspectral Raman image (Figure 3.3). A semi quantitative estimate of the increase or decrease of a mineral phase within the analyzed volume as a function of temperature and time is still reliable. Generally, analytical

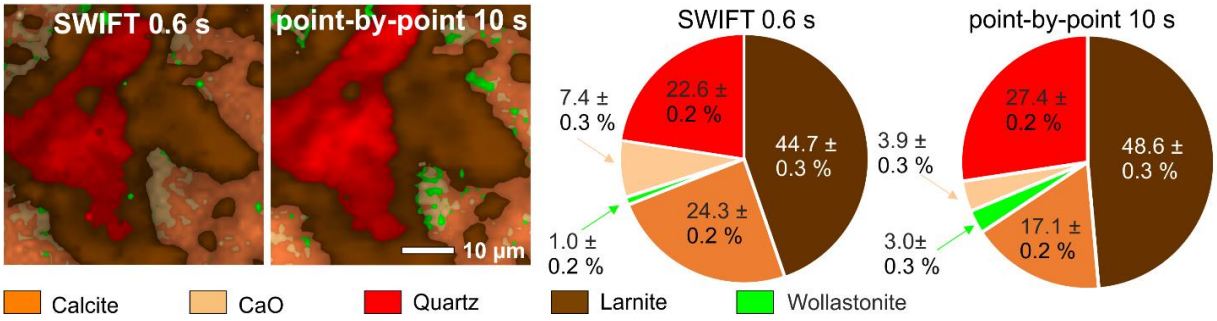

Figure 3.3: Comparison between the fast scanning mode (SWIFT© mode) with 0.6 s per spectrum (recording time 50 min) and the point-by-point method with 1 s times 10 accumulation per spectrum (recording time 8 h 43 min). Note that the acquisition time has to be faster than the mineral reactions under investigation. Grain boundaries are slightly different, when using the fast scanning mode that is negligible when comparing only images recorded with the same acquisition time. A semi quantitative statement is still possible.

parameters (e.g., image size and EM-CCD settings) are always a compromise between (i) the required signal-to-noise ratio that depends on the spectral details to be imaged, (ii) the spatial resolution necessary to separate chemical, structural, and/or textural features, and (iii) the total imaging time that should be significantly faster than the progress of the reaction under investigation.

2.6. Data reduction, quantification, and visualization

2.6.1. Data reduction

In a first step undesirable spectral features have to be separated from the Raman bands. This preprocessing step has to be done with care, because it is easy to introduce, but not necessarily to detect artifacts in a Raman image [117]. All spectra were corrected for (i) the wavelength-depended instrumental sensitivity (white light correction), (ii) a possible spectrometer shift by using the "internal" Ne standard, (iii) cosmic spikes, and (iv) background contributions that at high temperature are mainly composed of black body radiation and in some case of continuous fluorescence signals. As a first step, the white-light spectrum measured by the manufacturer was used to correct every spectrum of an image for the wavelength-dependent instrumental response or sensitivity. Then, the spectra were corrected for a possible spectrometer shift during long-time image acquisition using the position of the intense Ne line at 1707.06 cm^{-1} of each spectrum [118]. For this, a Gaussian function was fitted to this Ne spectral line and the line position was then used to correct for any frequency shift during long-time imaging. With such an internal standard, the propagated precision of the frequency of a Raman band, obtained by least-squares fitting, was usually between ± 0.05 and ± 0.10 cm^{-1} (2σ) for RT spectra. The accuracy is thereby coupled to the precision of the Ne line wavelength determination, which is better than ± 10^{-5} % [112].

As a next step, all spectra collected in the SWIFT©, mode excluding the spectra taken at RT, were corrected for cosmic spikes by the spike correction function implemented in the LabSpec software. This procedure identifies all signals with a full width of half maximum (FWHM) smaller than 6 cm^{-1} as cosmic signals, which are removed. The analyzed spectral range was then reduced to the range between 100 and 1200 cm^{-1} to simplify the following band fitting procedures. This area covers the main rocking and bending (between 100 and 700 cm^{-1}) and stretching vibrations (between 700 and 1200 cm^{-1}) of all mineral phases of interest.

For quantification and image visualization the spectra had to be further corrected for background contributions. Two fundamental background contributions often occur within this frequency range that are related to sample fluorescence and black body radiation which is electromagnetic radiation emitted by sample and the furnace material at temperatures above ~800°C [119]. Fluorescence can be caused by the presence of specific fluorescing cations (e.g. Cr^{3+}, Fe^{2+}, etc.) [119]incorporated in the crystal structure. Fortunately, the fluorescence effects are more significant at lower temperatures. The Raman spectrum of a natural wollastonite, for instance, recorded at RT shows strong fluorescence (Figure 4), but at temperatures between 900 and 1000°C the Raman spectrum of wollastonite has the lowest background. Above 1100°C the background is mainly influenced by the black body radiation which increases with increasing wavenumber

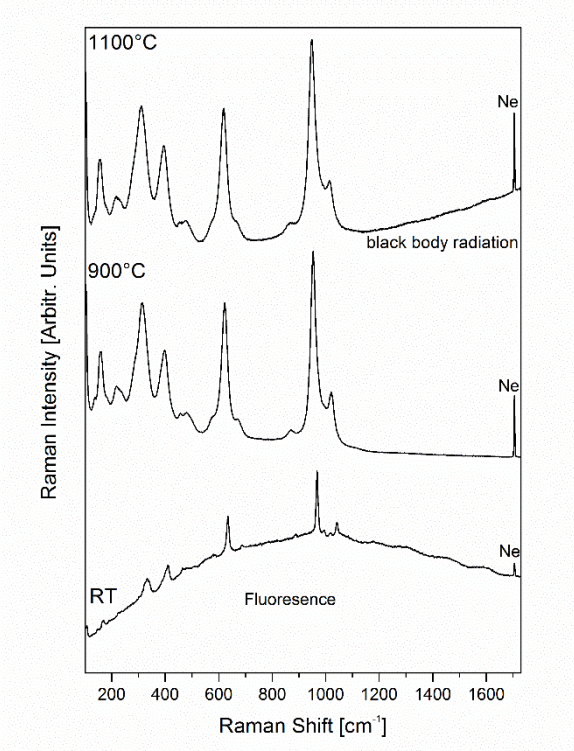

Figure 3.4: Raw spectra of wollastonite recorded at RT, 900°C, and 1100°C, showing the temperature-dependent difference of the background that is dominated by fluorescence and black body radiation at low and high temperatures, respectively.

(Figure 3.4 and 3.5). Significant portions of the black body radiation are in the region of Raman-active vibrations and therefore mask the Raman signals [120]. However, the black body radiation was reduced by (i) the addition of a radiation shield located between heating chamber and objective, (ii) working with a small heating system, and by (iii) decreasing the confocal pinhole, which also decreases the Raman signal.

The latter effect is illustrated in Figure 5b. With increasing confocal pinhole, the intensity of the A_1 band of quartz near 464 cm^{-1} at RT increases linearly in the range of 400 to 1300 µm. A pinhole larger than 1000 µm increases the intensity of the black body radiation to a lesser extent than the intensity of the quartz band, which leads to a better signal-to-noise ratio. Considering the intensity, closing the confocal pinhole is only a benefit if the spatial resolution of the measurement is of concern as it is for Raman imaging of multi-component sintering reactions. All measurements were thus made with a confocal pinhole of 300 µm, which was found to be a good compromise between spatial resolution, overall image recording time, and signal-to-noise ratio. To correct for the black body radiation a spectrum of the black body radiation was recorded at the beginning of each temperature step. The spectrum was then subtracted from every spectrum of the image before a polynomial baseline function of 2nd order was fitted to the spectrum and subtracted to further correct the spectrum for fluorescence and any background noise.

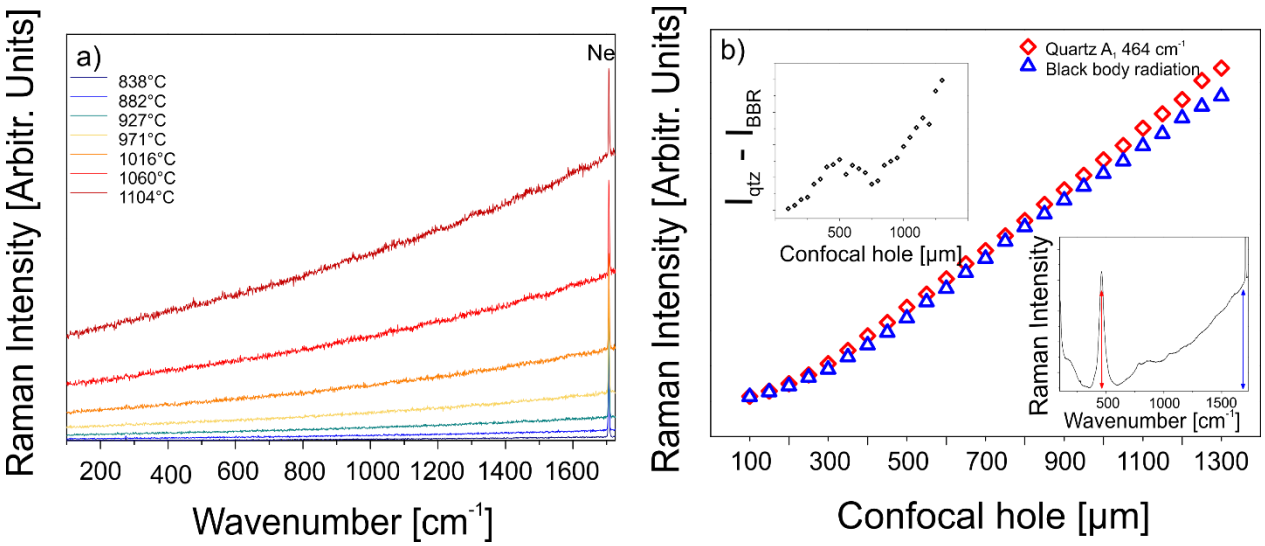

Figure 3.5 (a) The black body radiation as a function of temperature. (b) The Raman intensity of the A_1 quartz band at 464 cm^{-1} (lower inset diagram) and the intensity of the black body radiation at 1100°C as a function of the confocal pinhole.

2.6.2. Quantification and image visualization

The classical least squares (CLS) fitting procedure was used to determine the phase proportion at each pixel of an image. This method is based on the assumption that a spectrum from a polyphase material is a linear mixture of the spectra from the pure phases. Within the multidimensional spectral array, the CLS fitting procedure finds a linear combination of reference spectra from the pure phases, which best fits the raw spectrum at each position (pixel). The CLS fitting procedure is explained in more detail elsewhere [59]. The resulting image is created by false-coloring each pixel of the image relative to the fraction of each component in the spectrum. In the unmixed color-coding algorithm that is used in this work, the phase with the highest intensity contribution in a Raman spectrum will be displayed in a color assigned to that particular phase. The brightness of the color displays the overall intensity of the spectrum. The analyzed hyperspectral Raman images are displayed in the "normalized scores" mode, where the proportions of the phases are normalized to 100%. Additionally, the images are smoothed, which improves the visualization of grain boundaries (compare Figure 3.6 a and b). Such a procedure is straightforward if pure reference spectra are available. Due to the small grain size of the mineral phases and the limits of the spatial resolution most spectra of an image are composed of contributions from multiple phases. Therefore, the temperature-dependent in-house reference spectra (E1A and E1B) were used as input reference spectra for the CLS fitting routine.

2.6.3. Factors affecting phase quantification

There are four main factors affecting the phase quantification that has to be taken into account when interpreting the hyperspectral Raman images, namely (i) crystal orientation, (ii) grain size, (iii) temperature dependence of band position and linewidth, and (iv) the Raman scattering cross-sections of the mineral phases.

For anisotropic crystals, the intensity of a Raman band depends on the angle of incidence of the laser beam in relation to crystal lattice

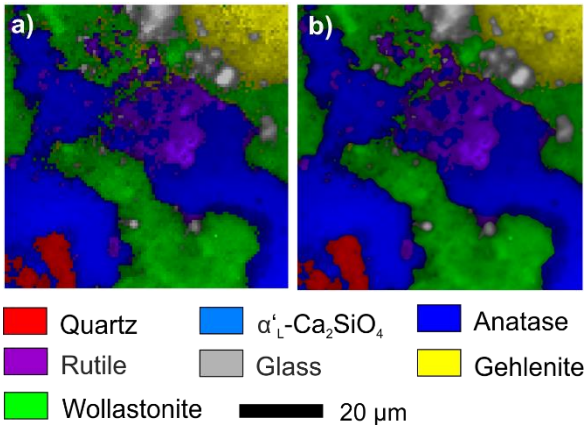

Figure 3.6: The effect of image smoothing on a hyperspectral Raman image of a sintered ceramic (Kln60Qtz15Cal25, T_{max} = 1097°C). (a) unsmoothed and (b) smoothed image. Note that in particular grain boundaries are better displayed in the smoothed image.

orientation, bond polarizabilities, and the state of polarization of the incident laser beam and therefore also relative intensities of a mineral phase change with crystal orientation, whereas the band shape and position is independent of crystal orientation. Room-temperature, unpolarized Raman spectra of fibrous Kopparberg wollastonite collected with the crystal fiber axis parallel and vertical to the electric field vector of the incident light are very similar, i.e., only the weak Raman bands are strongly polarized [63]. In contrast, due to the symmetry of the crystal structure, Raman spectra of rutile oriented with the crystal c axis parallel and perpendicular to the polarization of the laser beam vary strongly [121]. It is clear that any differences in relative Raman band intensities due to the orientation of the crystal affects the CLS fitting procedure. However, most of the mineral phases occurring during the experiments presented here exhibit limited orientation effects that do not significantly affect the fitting result. Nevertheless, for minerals with relative large orientation effects like gehlenite, reference spectra were recorded in a number of different orientations and implemented in the CLS fitting procedure. A positive side effect is that the orientation effect can be used to systematically study grain rotation during firing, which is a particularly important for our understanding of the dynamics of crystal growth processes in ceramics with potential for certain device

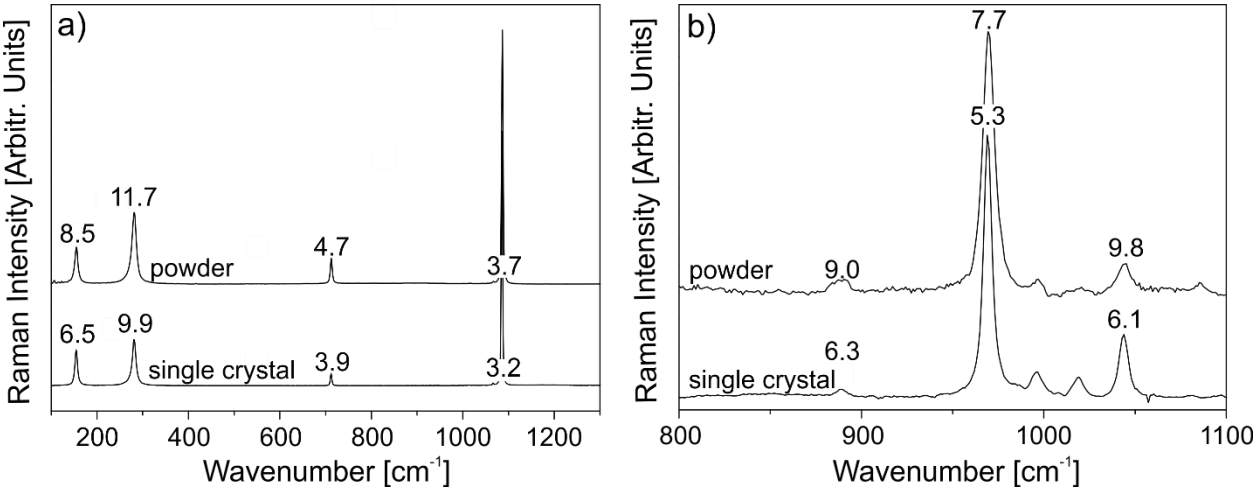

Figure 3.7 Comparison of Raman spectra from single crystals (E1A) and powders (E1B) of (a) calcite and (b) wollastonite. Numbers give the full width at half maximum (FWHM) of the respective band. Note that the Raman bands measured on powders are characterized by larger FWHM values.

applications [122]. With Raman spectroscopy relative crystal orientations can be determined rapidly and accurately without the necessity of sample preparation [122].

Raman spectra of single crystals compared to those of powders reveal differences in linewidth and intensity of the fundamental Raman bands (Figure 3.7). In addition, the spectra of some mineral powders show additional bands which are likely due to surface scattering [113]. The former can be due to local heating and/or quantum confinement[123], whereby the latter becomes significant only in nanocrystalline materials and here mainly effects the lattice modes. The dependence of linewidth on grain size was already studied, for instance, by several authors for TiO_2 nanocrystals [124–126] and nanometer-sized diamonds [123,127,128]. Zhao et al. studied the influence of the size of diamond powders from 0.25 to 10 µm and the beam power from 8 to 100 mW on the main Raman band at 1332 cm^{-1} [129]. They explain the systematic downshift of the Raman band with both the decrease of size and by a local temperature increase of about 500°C depending on the thermal conductivity path available in the specific configuration [129]. Therefore, the reference spectra used for the CLS fitting procedure were mainly obtained from pellets made from powdered samples with grain sizes between 5 and 30 µm (E1B) rather than from single crystals.

The temperature-dependent mode behavior of most of the relevant phases in silicate ceramics have already been studied by Raman spectroscopy, such as albite [46], wollastonite [63], gehlenite [20], diopside [19], pseudowollastonite [19,20], and quartz [62]. However, the high temperature Raman spectra reported in these studies were performed with different instruments and different analytical and experimental conditions (e.g., larger temperature steps) and are also not precise enough. We therefore collected in-house, high-precision, high temperature reference Raman spectra of the relevant ceramic phases. These were used for the estimation of relative Raman cross sections that are needed (i) to determine the relative phase proportions from a mixed Raman spectrum, and (ii) to identify individual high temperature phases in mixed spectra.

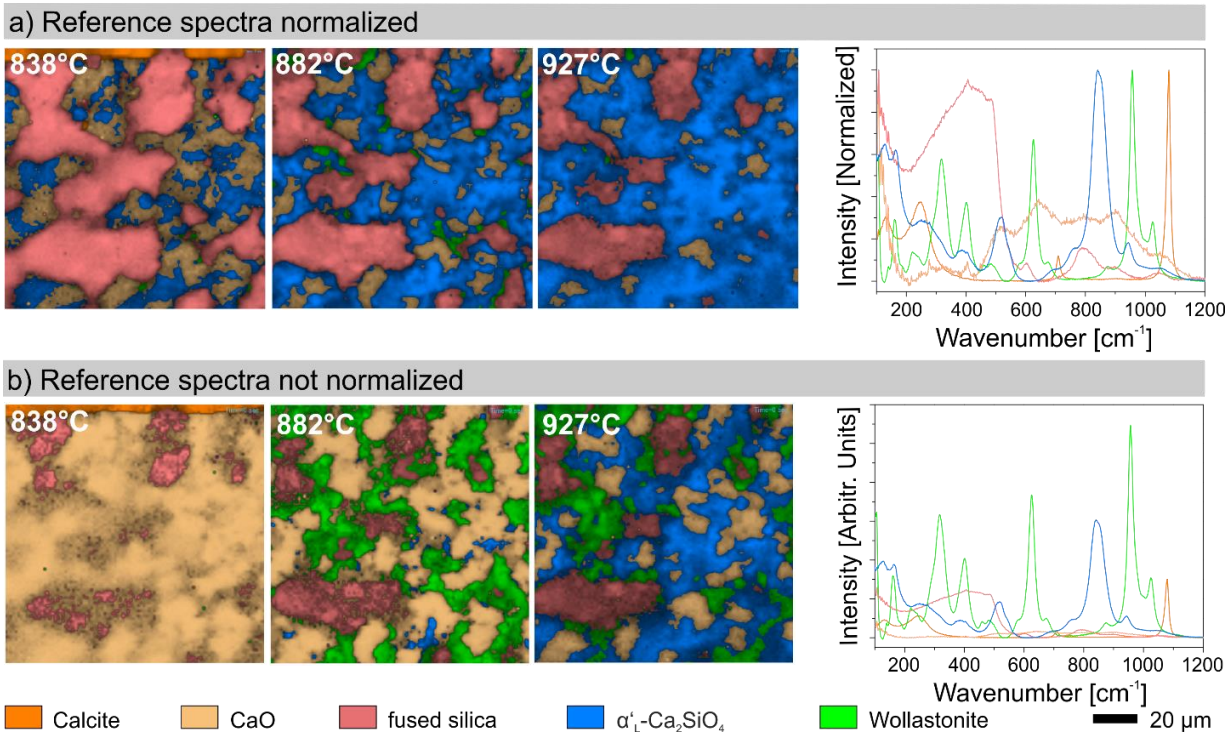

Figure 3.8: A series of three hyperspectral Raman images taken between 838°C and 927°C which are generated with the classical least-squares (CLS) fitting method using in-house reference spectra that are (a) normalized and (b) not normalized before loading. The reference spectra in (b) are recorded at the same measurement setup and thereby the Raman cross-sections of the individual mineral phases are considered. Note that the normalization of the reference spectra causes mineral phases with low Raman scattering cross-sections such as CaO to be underrepresented in the image.

The transverse Raman scattering cross-section depends on many factors like pressure [130], temperature [131], and the crystal orientation with respect to the polarization direction of the incoming laser light [132]. The correct calculation of Raman intensities in the context of the polarization theory is difficult and involves an enormous calculation effort. Therefore, theoretical calculations of Raman intensities are less common than calculations of infrared or nuclear magnetic resonance spectra [133]. It is common practice to normalize Raman spectra to the maximum intensity [108,134–136] or to divide the intensity of the Raman spectra by the power of the laser and the acquisition time [135,137] to compare several Raman spectra. Therefore, in our first attempt [59] we normalized the reference spectra between 0 and 1 before using them for the CLS fitting (Figure 3.8a). However, this procedure neglects the Raman cross sections of the mineral phases. In the present work, we therefore recorded the reference spectra at the same measurement conditions (i.e., laser wavelength and power, acquisition time, internal Ne lines, etc.) and used the processed reference spectra without normalizing the intensity for the CLS fitting procedure (Figure 3.8b).

However, this approach does not consider all factors that affect the Raman intensities. The main source of errors, aside of instrument calibration errors, is related to the unpredictable loss of light at uneven surfaces by surface scattering. However, due to the equal procedure during data treatment it is still possible to semi quantify changes of mineral fractions and to monitor grain boundary movements during the experiment. From multiple Raman imaging of the same area of a fired $CaO\text{-}SiO_2\text{-}Al_2O_3$ ceramic (T_{max} = 1097°C), using the same analytical parameters as for the *in situ* experiments, we obtained empirical errors that scale with the square root of the average mineral fraction within the analyzed area (volume), as expected for errors relating to the Poisson statistics of count rates, in order of ± 20 and ± 1 % at a volume fraction of 0.3 and 75.00 %, respectively.

2.7. Lateral and axial resolution

The spatial resolution is an essential factor for interpreting hyperspectral Raman images. Unfortunately, only a few studies have dealt with this topic until now [30,138–143]. The spatial resolution of optical Raman micro spectroscopy is governed mainly by the diffraction limit of light, and therefore dependents on the laser wavelength (λ) as well as on the numerical aperture (*NA*) of the objective [30]. In the first approximation the theoretical lateral (d_l) and axial (d_a) resolution is linearly dependent of the wavelength of the incident laser, and inversely proportional to the numerical aperture (NA) of the objective. It follows that, a high spatial resolution can be achieved with lasers at shorter wavelengths and a high-magnification optics.

With the 50x long-working distance objective (NA = 0.5) used in this study, the diffraction limited theoretical lateral and axial resolution at the sample surface is 1.3 and 8.5 µm, as given by $d_l \approx 1.22\ \lambda/NA$ and $d_a \approx 4\lambda/NA^2$, respectively, where λ is the excitation wavelength [144]. In practice, the real resolution is certainly worse than the theoretically calculated values due to (i) imperfect optics, (ii) light scattering at the samples surface and interfaces (iii), and light refraction at the top window of the heating stage. The axial resolution can principally be improved by using a confocal aperture, reducing the volume from which the scattered light is collected by blocking radiation generated from the surrounding volume [138]. A convenient side effect is the reduction of the black body radiation, which is emitted by the sample at elevated temperatures by reducing the confocal aperture. A drawback of narrowing the confocal hole is that the overall intensity becomes lower (Figure 3.5).

To interpret hyperspectral Raman images and especially to interpret the spectrum arising from a specific point in the map (for example grain boundaries), it is essential to know how much of the observed Raman signal originates within the focal volume and how the response tails off with depth [140]. Two factors are primarily important for the depth resolution, the volume of the laser focus and how Raman photons generated within this volume are relayed back into the spectrometer via the confocal aperture [30]. The axial resolution obtainable in confocal microscopy can be calculated by the following equation [145]:

$$d_a = \frac{2.2\ n\lambda}{2\pi NA^2} \quad (1)$$

where *n* is the refractive index of the immersion medium. This equation is only valid with the focus at the surface of the sample.

Based on the theoretic consideration, Everall [30] showed that the true laser focus is always deeper within a transparent sample than the so-called nominal depth (Δ), i.e., the distance below surface given by the z drive of the stage. The axial laser focus also broadens upon moving deeper into the sample. The depth resolution gets worse linearly with the nominal depth (distance below the surface)[138]:

$$d_a = \Delta\left[\left[\frac{NA^2(n^2-1)}{(1-NA^2)} + n^2\right]^{\frac{1}{2}} - n\right] \quad (2)$$

Apart from the point of focus also the depth of focus increases with increasing depth of focus, so it becomes impossible to obtain “pure” spectra at interfaces[144].

To study the influence of the confocal hole on the depth resolution, 13 hyperspectral Raman images of a fired $CaO\text{-}SiO_2\text{-}Al_2O_3$ ceramic (T_{max} 1097°C) were recorded at RT at the same location with a different confocal pinhole (100 to 1300 µm). With decreasing pinhole, the depth resolution increases, but at the price of intensity loss (cf. Figure 5b and 9). Small rutile grains

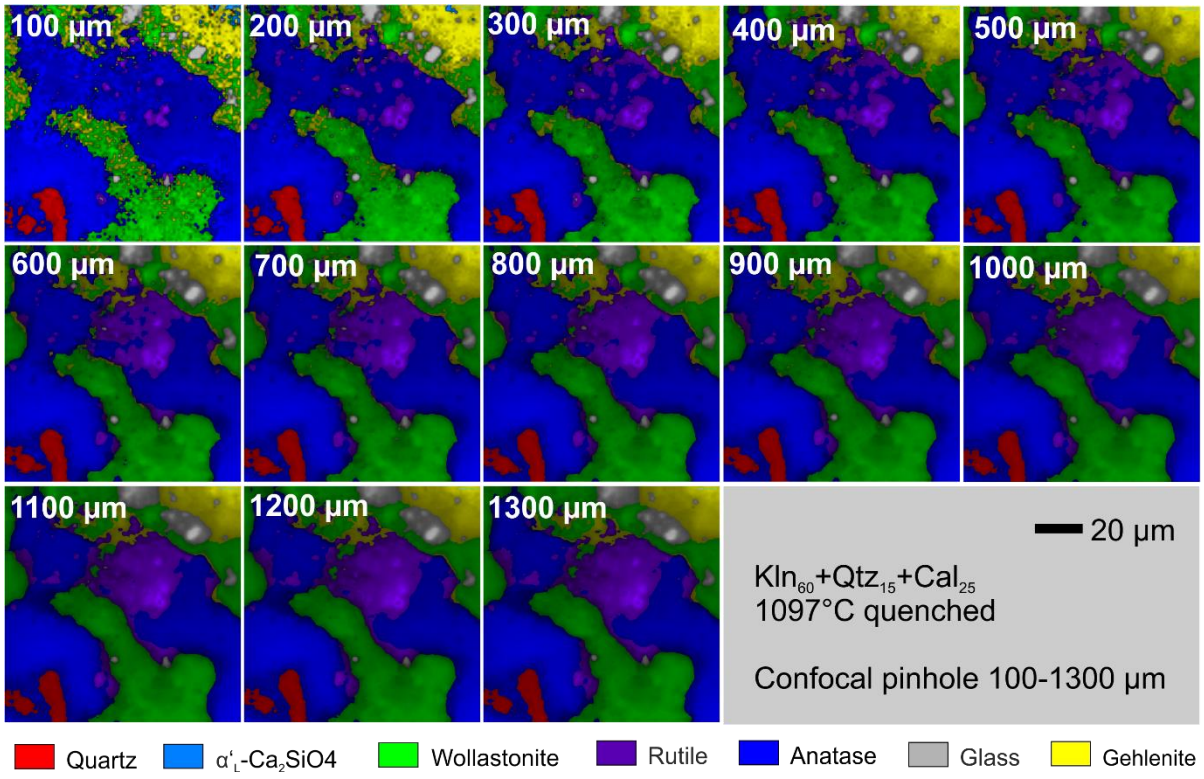

Figure 3.9: RT hyperspectral Raman images of a fired CaO-SiO_2-Al_2O_3 ceramic recorded with a different confocal pinhole. Note that images acquired with a pinhole smaller than 300 µm show the worst quality due to decreased band intensities, whereas with larger confocal pinholes morphological details get lost. For instance, the small rutile grains (purple) that are clearly distinguishable in those images recorded with a pinhole smaller than 400 µm are increasingly "grown" together and appear to be one single grain in the images recorded with a confocal pinhole larger than about 800 µm.

(purple) are clearly distinguishable within the Raman images recorded with a confocal hole of up to 400 µm, whereas they appear to have "grown" together in images recorded with a larger confocal aperture (Figure 3.9). Furthermore, due to the overall lower intensity of the images recorded with a confocal hole smaller than 300 µm most of the grain boundaries are blurry. As already shown in Figure 3.5b, the intensity decrease with decreasing confocal hole is over a large range linear with a slight kink at a confocal hole of 300 µm. For our Raman system and the chosen instrumental settings, a confocal hole of 300 µm appears to be the best compromise between sufficient intensity and spatial resolution.

It is important to note that the axial resolution at the surface also depends on the absorption properties of the material investigated. To study this dependence, a series of hyperspectral Raman images of a fired ceramic ($Kln_{60}Qtz_{15}Cal_{25}$, T_{max} 1097°C) were recorded at different z values to investigate the effect of the laser focus on the quality and details of the image (inset of Figure 3.10). As expected, the intensity of the Raman bands of the individual phases decreases with increasing depth of focus (Figure 3.10). A Raman intensity loss of 20 to 40 % is observed within the first ten micrometers, whereas within the first 20 µm, which is a typical grain diameter, already about half of the intensity of the Raman bands is lost. At a depth of about 50 µm, Raman signals from any of the analyzed phases are hardly detectable anymore due to strong absorption of the incident and scattered light.

This is also reflected by the observation that the Raman images recorded at different focal depths from the surface (z = 0 µm) to a depth of z = 15 µm are very similar (Figure 3.11). As a matter of fact, the statistical variations of the average mineral fractions, obtained from all 16 images, are in the same order of magnitude of those that were estimated from multiple images that were recorded from the same area (volume) with

identical focus (cf. Sec. 2.6.3). It follows that slight variations of the focus among different images (e.g., due to a failing autofocus, shrinking or expansion of the sample during

image acquisition) do not significantly affect the recorded mineral fractions and morphological details (e.g., location of grain boundaries).

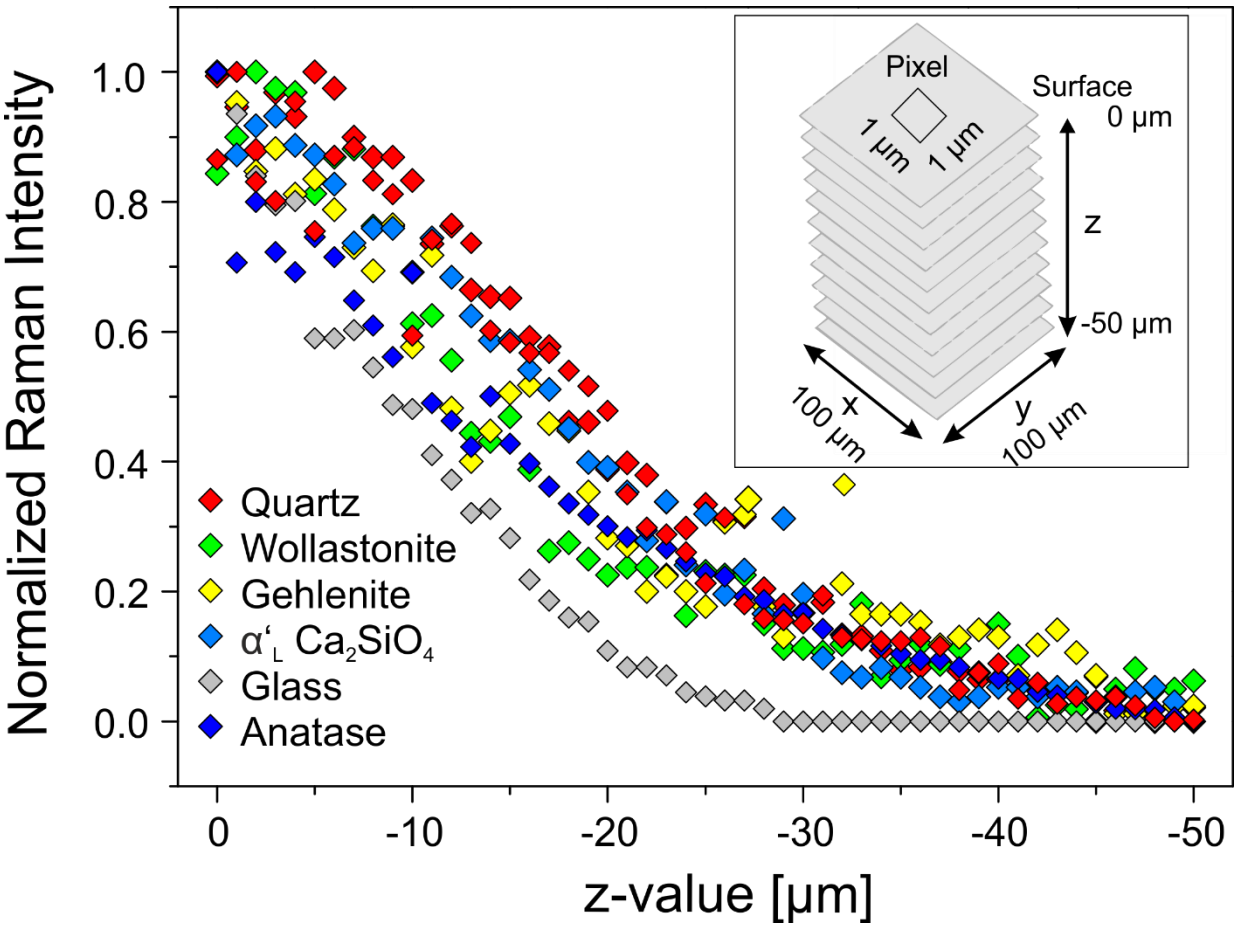

Figure 3.10: Normalized intensities of the main Raman band of the respective phase at six x-y positions as a function of depth (z = 0, focus at the sample surface). The data was extracted from 50 hyperspectral Raman images of a fired ceramic that were recorded at RT at a focal depth between 0 and -50 µm (z-axis) with a step size of 1 µm (inset diagram) and a confocal hole of 300 µm.

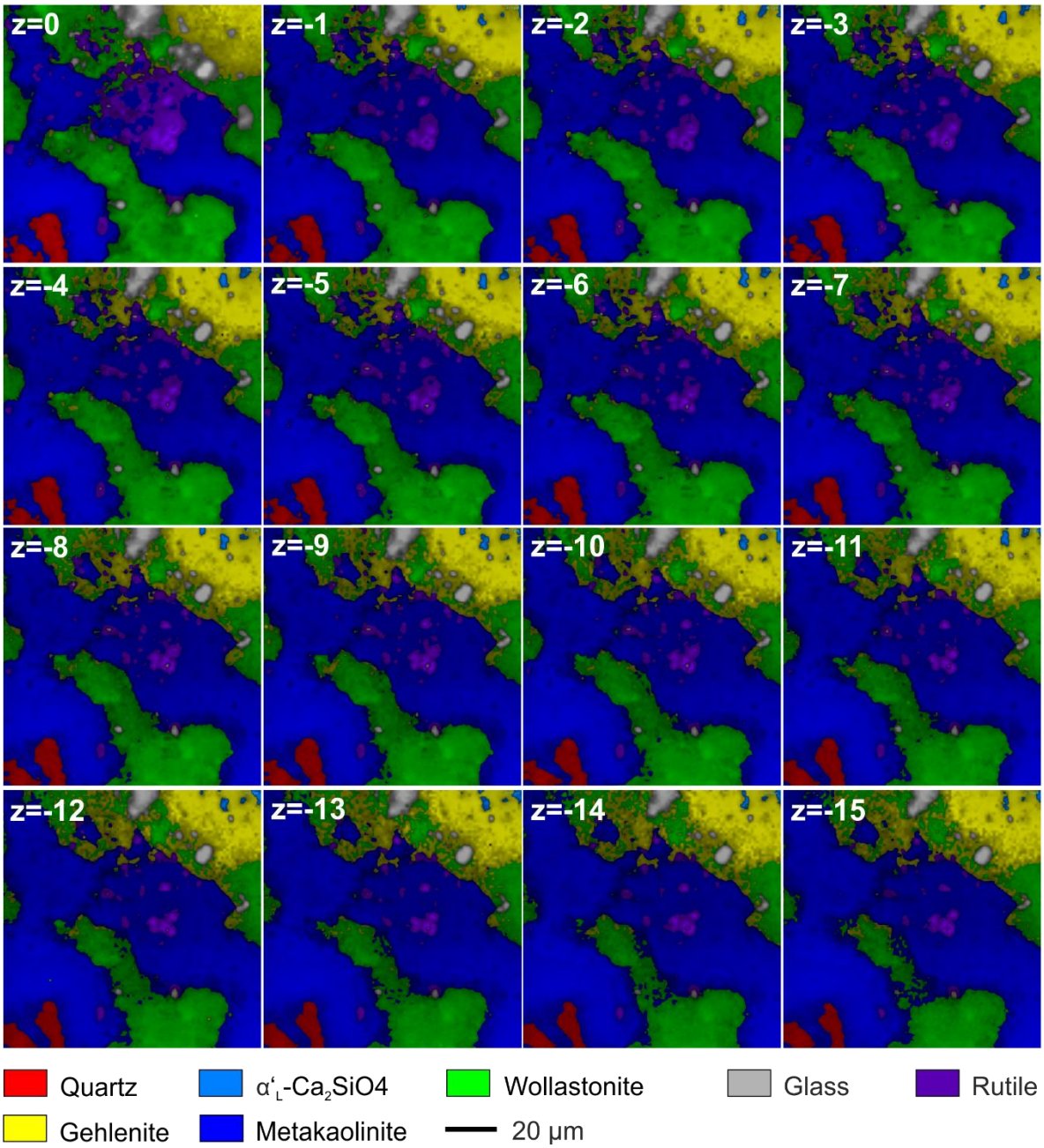

Figure 3.11: A series of 16 hyperspectral Raman images of a fired ceramic that were recorded with a focus between z = 0 (focus at the surface) and z = -15 µm (focus 15 µm below the surface). Note that despite the significant offset of the focus all images exhibit the same relative phase proportions and main morphological details.

3. Applications

3.1. Mineral reactions during firing and cooling

The occurrence or non-occurrence of certain mineral phases or mineral proportions are often used, for instance, to (i) determine the firing temperature of ancient ceramics, (ii) to devide ancient ceramics into groups for provenance studies [70], (iii) to estimate the formation temperature of natural rocks [69], and (iv) to determine the firing temperature of brown coal ashes burnt in a power plant[146]. The difficulty here is that it is not always obvious whether a mineral formed during firing or during cooling. Tschegg and coworkers [70], for example, could not solve the question whether large sparitic carbonate inclusions, observed in Cypriot Bronze-age plain white ceramics, represent incompletely decomposed or newly formed carbonate grains that were formed by a recarbonation process after firing. Such questions can principally be answered by *in situ* experiments [59].

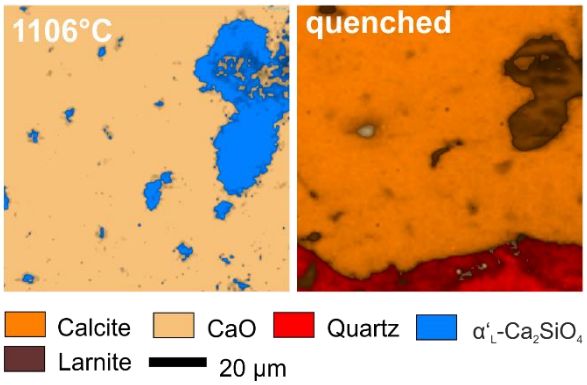

Figure 3.12 Raman images of sample composed of quartz and calcite fired to the last temperature step of 1106°C (a) and quenched to RT (b). At 1106°C calcite is decomposed to CaO and CO2 and quartz is completely reacted to α'L-Ca2SiO4 (a). After cooling with a cooling rate of 10°C/min to RT lime has reacted with atmospheric CO2 to calcite (b). During cooling α'L-Ca2SiO4 has transformed to β-Ca2SiO4 (larnite). Note the slight offset and grain boundary shifts, which is due to differential shrinkage of the sample during cooling.

To study the decarbonation and possible recarbonation process, i.e., the influence of cooling on the final product, a sample composed of quartz and calcite (mass ratio 1:1.03) was fired with a heating rate of 10°C/min and 50°C temperature steps from 660°C to 1106°C. At each temperature step two hyperspectral Raman images (100 x 100 µm^2, 1 µm step size, SWIFT 1.6 µm/s) were successively recorded within a dwell time of four hours. After recording the last hyperspectral Raman image at the maximum temperature of 1106°, the sample was cooled to RT with a cooling rate of 10°C/min.

At 839°C calcite gradually decomposes to CaO (images not shown here, but see Figure 3.1). Calcium oxide has no first order Raman-active modes [73] and Raman features of processes higher than first order are rarely used for Raman imaging so far [143]. However, CaO could be identified by Raman features near 540, 670,740, and 900 cm^{-1} and house-intern reference spectra of CaO were successfully used for data processing.

With increasing temperature α'_L-Ca_2SiO_4 formed from a reaction between lime and quartz. During cooling α'_L-Ca_2SiO_4 transformed to β-Ca_2SiO_4 that remained metastable at RT. Importantly, during cooling calcite recrystallized from a reaction of lime with atmospheric CO_2 which is released by the calcite decomposition during heating and partially trapped in the heating stage. This is noticed when comparing the *in situ* Raman image recorded at 1106°C with that recorded at RT, clearly showing that the calcite within the imaged area has fully decomposed to CaO and CO_2 at 1106°C (Figure 12). However, without this *in situ* information one could come to the conclusion that the calcite grains observed in the burnt ceramic represent remnant, precursor calcite grains. It follows that ex situ quench experiments are not necessarily sufficient to fully investigate mineral reactions at high temperatures during firing and subsequent cooling. However, it should be noted that only the sample surface is analyzed by Raman imaging. Therefore, based on the Raman data alone, it cannot be ruled out that only CaO from the first few micrometer recrystallizes to calcite, because CO_2 cannot reach the interior of the ceramic body.

3.2. Isothermal mineral reactions and grain growth

Understanding the kinetics of sintering reactions is necessary to systematically control the manufacturing process of a ceramic, but also to understand metamorphic rock forming processes in nature. Even if a mineral transformation is thermodynamically favored, it is not guaranteed that the transformation will occur at any measurable rate. The reaction rate strongly depends on the mechanisms involved in the reaction process and can change with time and temperature. Grain boundaries move and rearrange so as to increase the average size and decrease the grain boundary area per unit volume [75]. Here, isothermal *in situ* experiments were performed to study the effect of time on the formation of calcium silicates and grain growth during firing. One major advantage over conventional quench experiments is that the same sample position/material is continuously investigated without the need of quenching a new samples at each time step. For the experiment, a mixture of quartz and CaO (mass ratio 1:1) was fired with a heating rate of 10°C to 848°C and 12 hyperspectral Raman images (100 x 100 µm,

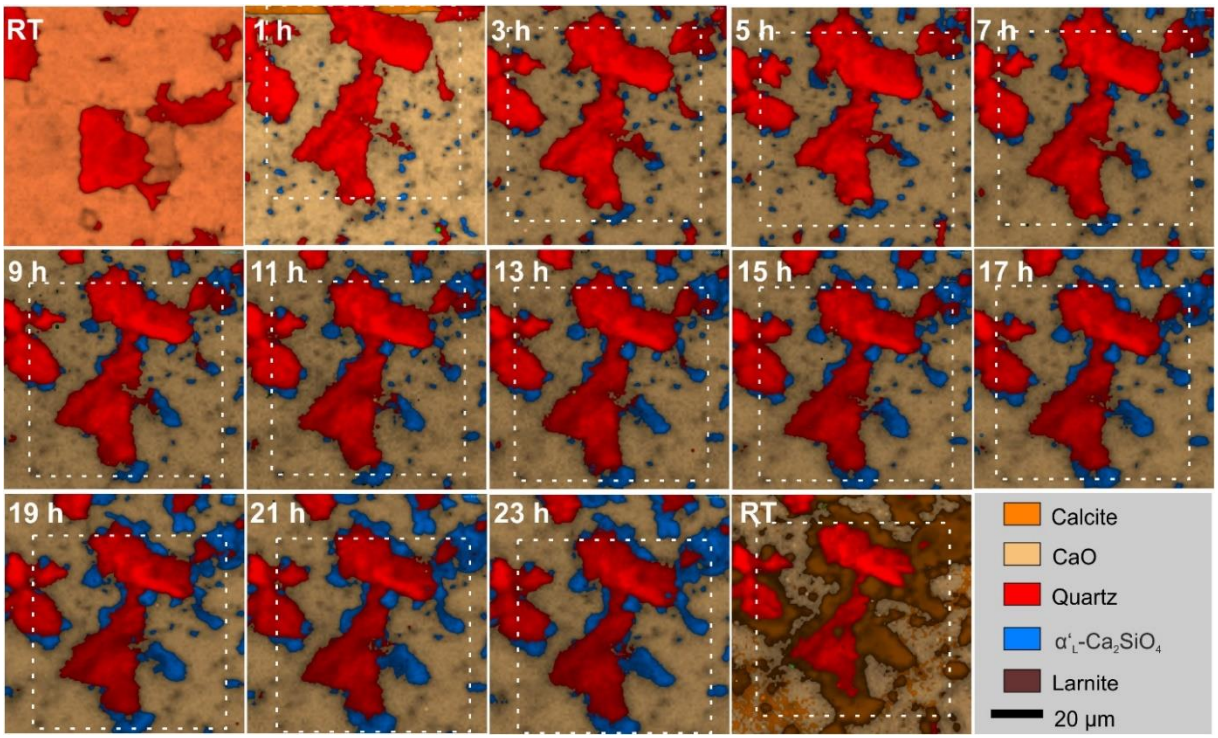

Figure 3.13: Hyperspectral Raman images of a green body composed of a mixture of quartz and CaO (mass ratio 1:1). The sample was fired with a heating rate of 10°C to 848°C and 12 hyperspectral Raman images (100 x 100 µm, 1 µm step size, SWIFT 1.6 µm/s) were subsequently recorded within a dwell time of about 24 h to follow the isothermal reaction kinetics. Calcite still decomposed during recording the first Raman image. Simultaneously, α'$_L$-Ca_2SiO_4 formed from CaO and quartz. With increasing sintering time, the content of α'$_L$-Ca_2SiO_4 increased. During cooling α'$_L$-Ca_2SiO_4 transformed to larnite and remained metastably at RT. White rectangles mark the areas used for semi quantitative determination of the phase composition (see text).

1 µm step size, SWIFT 1.6 µm/s) were recorded step by step within a dwell time of about 24 h. After the last hyperspectral Raman image had been taken, the sample was cooled to RT with a cooling rate of 10°C/min.

During the first 10 hours the sample has significantly shrunk, which is reflected by a shift of the imaged area (Figure 3.13).

Lin and co-authors also observed an increased shrinkage within the first 10 hours of isothermal sintering of $CaSiO_3$ at 1100 °C and explained this phenomenon by incomplete densification and increased porosity of the samples during the first few hours [147]. In order to semi quantify the apparent mineral content and grain size distribution over time, an area of 80 x 80 µm^2 was selected, which is more or less present in each image (white dotted squares Figure 3.13). For quantification, the marked area was used. Note that due to the three-dimensional shrinking of the sample, no complete match can be achieved. During recording of the first hyperspectral Raman image at 848°C calcite was still decomposing to CaO and CO_2 (Figure 3.13). Note that in this case the decomposition reaction was significantly faster than the image recording time (cf. Figure 3.2), reflected by the observation that calcite is still visible within the first rows of the image, but is not detected anymore afterwards. At the same time, α'$_L$-Ca_2SiO_4 formed from a solid-state reaction between lime and quartz, which transformed to larnite during cooling (cf. RT image in Figure 3.13). The fraction of α'$_L$-Ca_2SiO_4 increased linearly with time, while simultaneously the fractions of the CaO and quartz decreased also linearly (Figure 3.14).

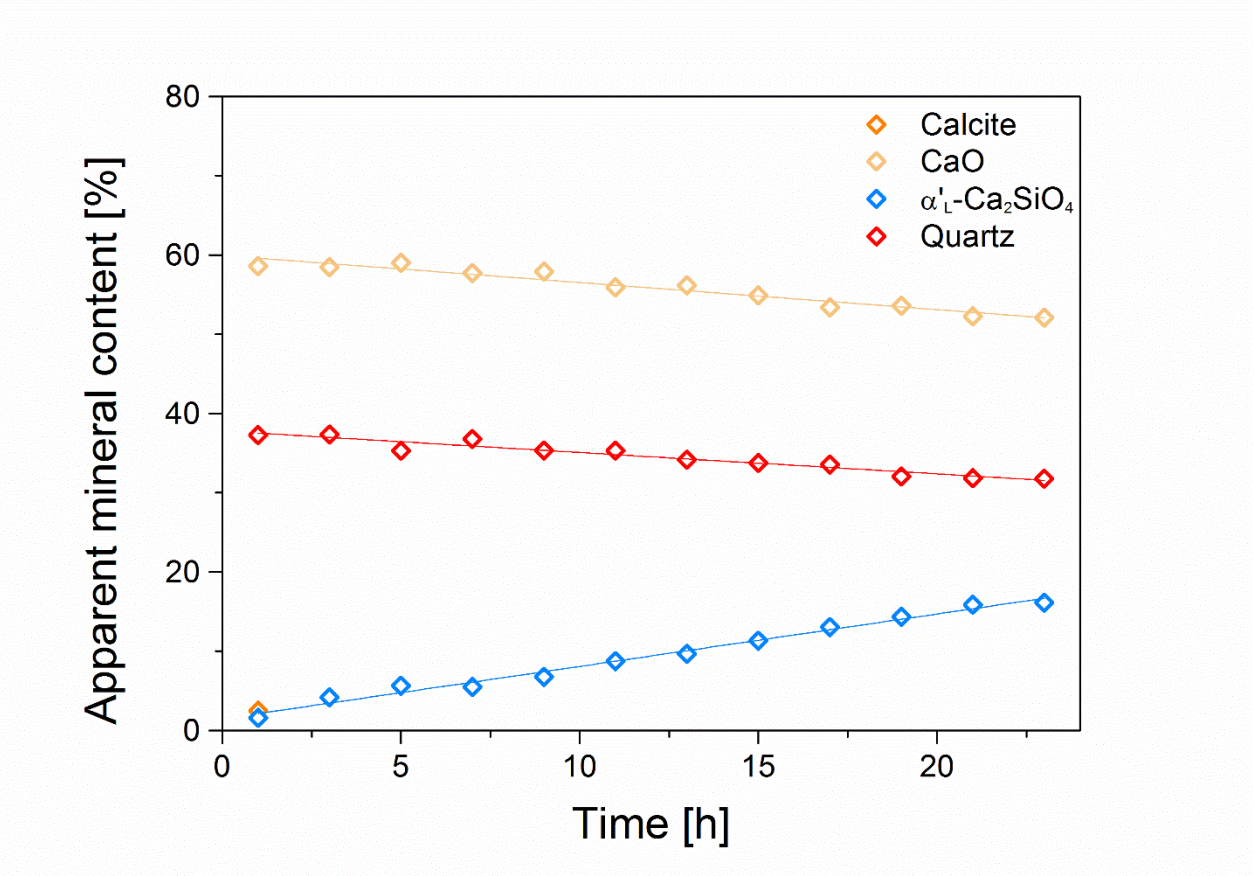

Figure 3.14: The evolution of the mineral fractions as function of time during isothermal sintering of a quartz-calcite (mass ratio 1:1) green body at 848°C obtained by the binary images of the single phases. The colored lines represent a linear fit to the data over the whole time interval.

The linear decrease of the reactant fractions with time suggests a zero-order kinetics, which, however, is always a result or a kind of artifact of the conditions under which the reaction is carried out. For this reason, reactions that follow zero-order kinetics are often referred to as pseudo-zero-order reactions. A pseudo-zero order behavior principally suggests that either only a small fraction of the reactants was able to react, which is continually replenished, or that the concentration of one reactant was much larger than those of the others. In our case, the latter explanation is more likely since the investigated area is dominated by lime that occurs with a volume fraction of about 60% in our experiment. Note that such a zero-order process cannot continue after one reactant has been exhausted or is protected against reactants by a solid reaction rim. If this point is reached, the reaction will change to another rate law such, for instance, the Avrami law [148]used to describe the isothermal kinetics of phase and microstructure transformations instead of falling directly to zero. In our experiments, this point was not reached within 24 hours of sintering.

In addition, Raman imaging also enables monitoring single grain growth during ceramic firing. Understanding grain growth is important to nearly every engineered material as porosity and grain size affect the strength of polycrystalline ceramics in a similar manner [149]. The strength of ceramics decreases with an increase in porosity and grain size [147] and therefore a stable small grain size is desirable for materials that rely on strength, toughness, or formability [75]. For grain size analyses, an area was selected, where newly formed α'_L-Ca_2SiO_4 is present. By using a color threshold, these image areas were converted into binary images with the aid of the graphics program ImageJ [150], which were then used to quantify the evolution of grain size of α'_L Ca_2SiO_4 as a function of time (data not shown here) by applying the "Analyze Particles" tool from ImageJ. With increasing sintering time, the grains of α'_L-Ca_2SiO_4 have grown and small

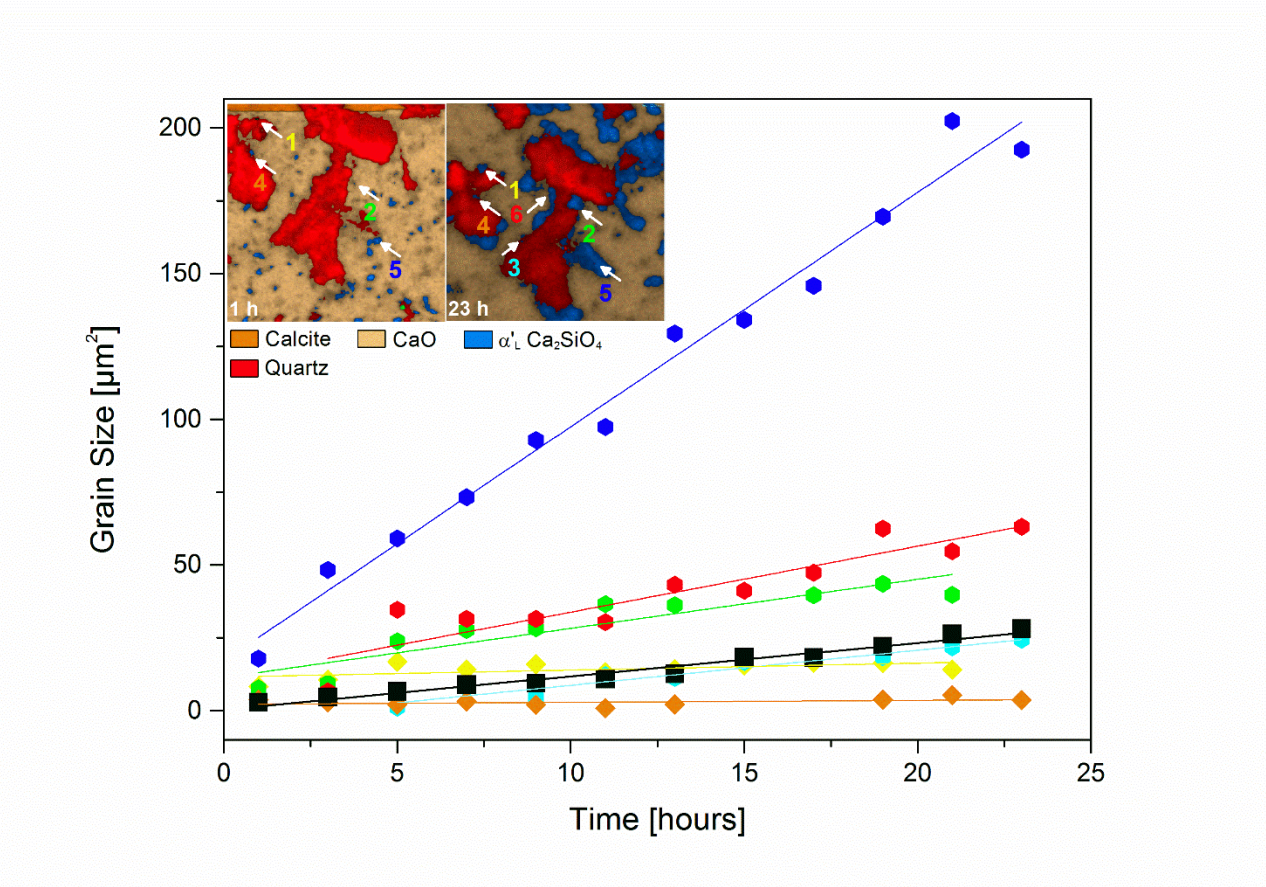

Figure 3.15 The growth of individual grains as a function of time. The average grain size (black squares) increases linearly with increasing sintering time which corresponds to a pseudo zero- order behavior. Also, the size of most single grains (colored hexahedron, grain 2, 3, 5, 6) increases linearly with time. The lines represent linear least-squares fits to the data. Image size in the inset is 100 x 100 µm².

grains have coalesced, whereby the average grain size (Figure 3.15, black squares) increased linearly over time, also indicating a pseudo zero-order behavior. This supports the interpretation that the pseudo zero-order behavior is due to the fact that the concentration of one reactant (CaO) was much greater than that of the others (quartz). Also, the size of most single grains (e.g., grain 2, 3, 5, 6 in Figure 3.15) have increased linearly with time, whereas some grains (e.g., grains 1 and 4 in Figure 3.15) did not significantly grow at all. These grains must have been separated from a continuous flux of SiO_2 or CaO for some reasons and therefore could not grow further. The growth of grain 5, however, was not limited, since several small quartz grains were surrounded by a CaO matrix and thus the contact surfaces between CaO and SiO_2 were very large.

This example demonstrates that the growth of distinct grains can be investigated at each time step without the need to use a new sample for each time step, which is a major advantage over conventional quench experiments. This enables studying the mechanism(s) of nucleation and growth, the quantification of grain growth rates, the identification of rate-limiting factors, and potentially activation energies from isochronal heating experiments.

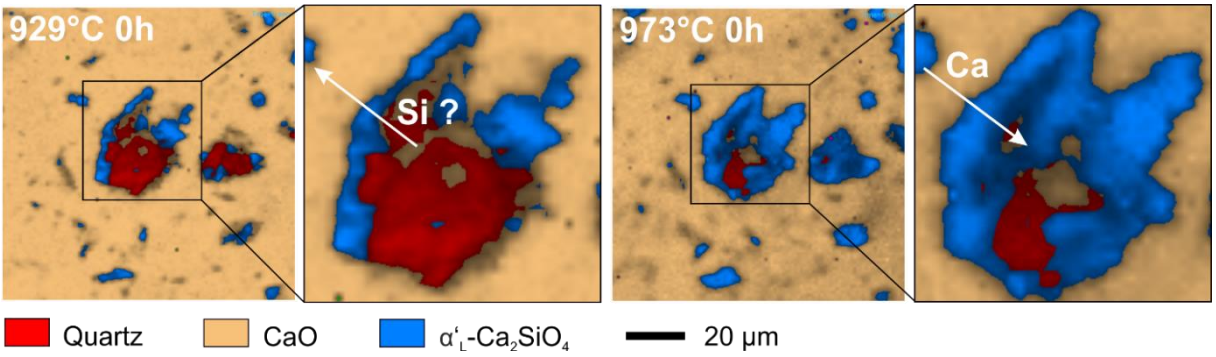

Figure 3.16 Hyperspectral Raman images from a sintering experiment with quartz and lime (CaO), showing grain boundary migration during the solid-state reaction between both reactants. Above 884°C the dicalcium silicate α'L-Ca2SiO4 formed by the direct reaction between lime and quartz as seen in the image taken at 929°C. At the beginning of the reaction, dicalcium silicate rims seems to have grown around the quartz grains, whereas with increasing temperature (and time) the reaction direction turned over and the dicalcium silicate replaced the quartz grain.

3.3. In situ observations of the migration of solid-solid reaction fronts

Reaction rims and corona textures are common non-equilibrium features in many metamorphic rocks [52,84] and ancient ceramics [70]. Because the reactant and product phases have different compositions, interlayer growth requires chemical mass-transfer which, in the absence of melts and fluids, can occur by diffusion only. At the same time, localized reactions must proceed at the 'reaction interfaces', which divide the growing layers on either side [84]. Both processes may be rate limiting, and the coupling between the two processes determines the overall reaction kinetics [84]. Two approaches are possible to identify the rate-limiting component and to identify the direction of the migration front: (i) the rim growth approach and (ii) experiments with isotopically doped reactants [51,52,85].

To study the solid-state reaction between quartz and lime at the grain scale at high temperatures, a mixture of quartz and CaO (mass ratio 0.93:1) was fired with a heating rate of 10°C/min stepwise (50°C steps) from 660°C to 1106°C. At each temperature step two hyperspectral Raman images (100 x 100 µm, 1 µm step size, SWIFT 1.6 µm/s) were subsequently recorded within a dwell time of four hours.

Above 884°C, dicalcium silicate α'_L-Ca_2SiO_4 crystallized by the solid-state reaction between CaO and quartz, which was already observed in experiments with calcite instead of lime (cf. Sec. 3.2). In both experiments α'_L-Ca_2SiO_4 did not only nucleate and grow at visible grain boundaries with quartz grains (cf. Figure 3.13), but also popped up as many small grains within the CaO matrix. Most likely SiO_2 needed for the formation of dicalcium silicate derived from small invisible quartz particles that are more reactive than the larger ones due to their larger surface area. With increasing time (sec. 3.2) or temperature (sec. 3.3) dicalcium silicate rims have increasingly grown around larger quartz grains (Figs. 3.13 and 16). However, with further increasing temperature (and time) the reaction direction seems to turn over and the dicalcium silicate phase clearly migrated inwards into the quartz grain and replaced it (Figure 3.16). This turn over can only be explained by a change in the mechanism of formation.

4. Further perspective

The potential of Raman spectroscopy for *in situ* investigation of sintering reactions is even further expanded by the possibility to image the distribution of ^{18}O within and among different phases at the micrometer scale when using ^{18}O-labeled precursor reactants. For instance, future experiments are planned in which the reactants are labeled with ^{18}O in order to find out why the mechanism of the reaction between quartz and lime apparently changed during the experiment (Figure 16). The principle behind analyzing the ^{18}O content in condensed matter by vibrational

spectroscopy is that the energies or frequencies associated with vibrational motions are dependent on the masses of the vibrating atoms [151]. In the simple harmonic approximation, the vibrational frequency shift is proportional to the square root of the mass ratio between the atoms involved in the vibration [151]. Light stable isotopes therefore cause larger isotope effects than heavy isotopes. This mass-dependent frequency of vibrational modes involving the motion of oxygen was already used to semi-quantify the ^{18}O content in oxides and silicates such as pyrochlore [152], amorphous silica [153], and feldspar [32] which formed in ^{18}O-labeled aqueous solutions as replacement or alteration product [33]. The oxygen isotope ^{18}O can potentially also be used as *in situ* tracer to gain insights into mechanistic and dynamic (*e.g.*, transport of matter, crystal growth) aspects of solid state sintering reactions. For instance, using ^{18}O-enriched calcite or quartz, the involvement of these phases in certain sintering reactions can be recognized by visualizing the distribution of ^{18}O among the distinct phases. For this purpose, however, the isotope mass-related frequency shift of a vibrational mode has to be separated from the temperature-related as well as from a defect-related (chemical) frequency shift in order to correctly estimate the ^{18}O content in a mineral at higher temperatures, which adds uncertainty to the quantification of ^{18}O [32,152].

5. Conclusion

In situ hyperspectral Raman imaging provided promising results to *in situ* study solid-solid phase transitions at high temperatures at a micrometer scale and in real time. This allows the detection of metastable phases and the identification of reverse reactions such as the decomposition of calcite. In addition, the migration of a solid-solid reaction front could be observed *in situ*, which allowed the observation of a turn-over of the reactive direction during the formation of α'_L-Ca_2SiO_4 from CaO-quartz and thus a change in reaction mechanism. The same reaction was followed during isothermal sintering at about 850° C for 24 hours. A linear increase of α'_L-Ca_2SiO_4 over time was observed. Accordingly, the fraction of the educts CaO and quartz also decreased linearly. Over time, the average grain size of the newly formed α'_L-Ca_2SiO_4 grains also increased linearly. A pseudo-zero order behavior of mineral growth was observed in the system, which is most likely due to a CaO excess. The here presented high temperature Raman imaging approach has a high potential to provide entirely new insights into transport and solid-solid or solid-melt reaction processes during high-temperature sintering and may thus help to monitor and control important technical properties of ceramic materials, including advanced and refractory ceramics, such as densification and grain growth during sintering.

Supplementary Materials: The following are available online at www.mdpi.com/xxx/s1, Figure S1: title, Table S1: title, Video S1: title.

Author Contributions: Conceptualization: K.H. and T.G.; Funding acquisition: T.G.; Investigation: K.H., J.K., N.B., and S.Z.; Methodology, K.H., N.B., S.Z., and T.G.; Supervision: T.G.; Visualization: K.H. and J.K.; Writing – original draft: K.H. and T.G.; Writing – review & editing: J.K., N.B., and S.Z.

Funding: This research was funded by the deutsche Forschungsgemeinschaft (DFG), grant number GE1094/22-1

Acknowledgments: Many thanks go to T. Schulz and D. Lülsdorf for the technical support with the heating stage. The financial support of the deutsche Forschungsgemeinschaft (grant DFG GE1094/22-1) is highly acknowledged.

Conflicts of Interest: The authors declare no conflict of interest.

References

1. Heimann, R. B. & Maggetti, R. B. H. M. *Ancient and Historical Ceramics*. (2014).

2. Vandiver, P., Klima, B., Svoboda, J. & Soffer, O. Linked references are available on JSTOR for this article : The Origins of Ceramic Technology at Dolni Vestonice , Czechoslovakia. *Science (80-.).* **246**, 1002–1008 (2016).

3. Wu, X. *et al.* Early pottery at 20,000

years ago in Xianrendong Cave, China. *Science (80-.).* **336**, 1696–1700 (2012).

4. Carter, C. B. & Norton, G. *Ceramic Materials: Science and Engineering*. *SpringerLink : Bücher* (2013). doi:10.1007/978-1-4614-3523-5.

5. Riedel, H. & Blug, B. A Comprehensive Model for Solid State Sintering and Its Application to Silicon Carbide. *Multiscale Deform. Fract. Mater. Struct.* 49–70 (2005) doi:10.1007/0-306-46952-9_4.

6. Tite, M. S. Ceramic production, provenance and use - A review. *Archaeometry* **50**, 216–231 (2008).

7. Elert, K., Cultrone, G., Rodriguez Navarro, C. & Sebastián Pardo, E. Durability of bricks used in the conservation of historic buildings - Influence of composition and microstructure. *J. Cult. Herit.* **4**, 91–99 (2003).

8. Traoré, K., Kabré, T. S. & Blanchart, P. Gehlenite and anorthite crystallisation from kaolinite and calcite mix. *Ceram. Int.* **29**, 377–383 (2003).

9. Chen, Y. F., Wang, M. C. & Hon, M. H. Phase transformation and growth of mullite in kaolin ceramics. *J. Eur. Ceram. Soc.* **24**, 2389–2397 (2004).

10. Cultrone, G., Sebastián, E. & De La Torre, M. J. Mineralogical and physical behaviour of solid bricks with additives. *Constr. Build. Mater.* **19**, 39–48 (2005).

11. Saboya, F., Xavier, G. C. & Alexandre, J. The use of the powder marble by-product to enhance the properties of brick ceramic. *Constr. Build. Mater.* **21**, 1950–1960 (2007).

12. Trindade, M. J., Dias, M. I., Coroado, J. & Rocha, F. Mineralogical transformations of calcareous rich clays with firing: A comparative study between calcite and dolomite rich clays from Algarve, Portugal. *Appl. Clay Sci.* **42**, 345–355 (2009).

13. Shoval, S., Boudeulle, M. & Panczer, G. Identification of the thermal phases in firing of kaolinite to mullite by using micro-Raman spectroscopy and curve-fitting. *Opt. Mater. (Amst).* **34**, 404–409 (2011).

14. Sokolář, R., Vodová, L., Grygarová, S., Štubňa, I. & Šín, P. Mechanical properties of ceramic bodies based on calcite waste. *Ceram. Int.* **38**, 6607–6612 (2012).

15. Aras, A. The change of phase composition in kaolinite- and illite-rich clay-based ceramic bodies. *Appl. Clay Sci.* **24**, 257–269 (2004).

16. Stange, K. Investigations into the methodology of in situ and real-time hyperspectral Raman imaging of phase transformation reactions during thermal annealing of ceramic materials. (Rheinische Friedrich-Wilhelms-Universität Bonn, 2015).

17. McMillan, P. A Raman spectroscopic study of glasses in the system CaO-MgO-SiO_2. *Am. Mineral.* **69**, 645–659 (1984).

18. Swamy, V. & Dubrovinsky, L. S. Thermodynamic data for the phases in the CaSiO<inf>3</inf> system. *Geochim. Cosmochim. Acta* **61**, (1997).

19. Richet, P., Mysen, B. O. & Ingrin, J. High-temperature X-ray diffraction and Raman spectroscopy of diopside and pseudowollastonite. *Phys. Chem. Miner.* **25**, 401–414 (1998).

20. Bouhifd, M. A., Gruener, G., Mysen, B. O. & Richet, P. Premelting and calcium mobility in gehlenite (Ca2Al2SiO7) and pseudowollastonite (CaSiO3). *Phys. Chem. Miner.* **29**, 655–662 (2002).

21. Khoo, T. C. *et al.* Quantitative label-free imaging of iron-bound transferrin in breast cancer cells and tumors. *Redox Biol.* **36**, 101617 (2020).

22. Brun, N. *et al.* In situ monitoring of styrene polymerization using Raman spectroscopy. Multi-scale approach of

homogeneous and heterogeneous polymerization processes. *J. Raman Spectrosc.* **44**, 909–915 (2013).

23. Wulfman, C., Djaker, N., Sadoun, M. & Lamy De La Chapelle, M. 3Y-TZP in-depth phase transformation by raman spectroscopy: A comparison of three methods. *J. Am. Ceram. Soc.* **97**, 2233–2240 (2014).

24. Hemberger, Y., Wichtner, N., Berthold, C. & Nickel, K. G. Quantification of yttria in stabilized zirconia by Raman spectroscopy. *Int. J. Appl. Ceram. Technol.* **13**, 116–124 (2016).

25. Wulfman, C. *et al.* Raman spectroscopy evaluation of subsurface hydrothermal degradation of zirconia. *J. Am. Ceram. Soc.* **95**, 2347–2351 (2012).

26. M. Becker; H. P. Strunk, S. C. Raman imaging of grain orientation, strain, crystallinity and doping levels in solar silicon. in *Raman Imaging:Techniques and Applications* (ed. Zoubir, A.) 256–299 (Springer Series in Optical Sciences, 2012).

27. Pasteris, J. D. & Beyssac, O. Welcome to Raman spectroscopy: Successes, challenges, and pitfalls. *Elements* **16**, 87–92 (2020).

28. Yaseen, T., Sun, D. & Cheng, J. Raman imaging for food quality and safety evaluation : Fundamentals and applications. *Trends Food Sci. Technol.* **62**, 177–189 (2017).

29. Qin, J., Chao, K. & Kim, M. S. *Introduction to Raman Chemical Imaging Technology*. *Computer Vision Technology for Food Quality Evaluation: Second Edition* (Elsevier Inc., 2016). doi:10.1016/B978-0-12-802232-0.00006-2.

30. Everall, N. Depth profiling with confocal Raman microscopy, part I. *Spectroscopy* **19**, 22–28 (2004).

31. Geisler, T., Dohmen, L., Lenting, C. & Fritzsche, M. B. K. Real time in situ observations of reaction and transport phenomena during silicate glass corrosion by fluid-cell Raman spectroscopy. *Nat. Mater.* in press (2019) doi:10.1038/s41563-019-0293-8.

32. Hövelmann, J., Putnis, A., Geisler, T., Schmidt, B. C. & Golla-Schindler, U. The replacement of plagioclase feldspars by albite: Observations from hydrothermal experiments. *Contrib. to Mineral. Petrol.* **159**, 43–59 (2010).

33. King, H. & Geisler, T. Tracing mineral reactions using confocal Raman spectroscopy. *Minerals* **8**, 158 (2018).

34. Daniel, I., Gillet, P., Poe, B. T. & McMillan, P. F. In-situ high-temperature Raman spectroscopic studies of aluminosilicate liquids. *Phys. Chem. Miner.* **22**, 74–86 (1995).

35. Borer, W. J., Mitra, S. S. & Namjoshi, K. V. Line shape and temperature dependence of the first order Raman spectrum of diamond. *Solid State Commun.* **9**, 1377–1381 (1971).

36. Liu, M. S., Bursill, L. A., Prawer, S. & Beserman, R. Temperature dependence of the first-order Raman phonon line of diamond. *Phys. Rev. B - Condens. Matter Mater. Phys.* **61**, 3391–3395 (2000).

37. Hirata, T. & Ohuchi, F. . Temperature dependence of the Raman spectra of ZrO2. *J. Am. Ceram. Soc.* **117**, 361–364 (2001).

38. Cuscó, R. *et al.* Temperature dependence of Raman scattering in <math display="inline"> <mrow> <mi>ZnO</mi> </mrow> </math>. *Phys. Rev. B* **75**, 165202 (2007).

39. Menéndez, J. & Cardona, M. Temperature dependence of the first-order Raman scattering by phonons in Si, Ge, and -Sn: Anharmonic effects. *Phys. Rev. B* **29**, 2051–2059 (1984).

40. Hart, T., Aggarwal, R. & Lax, B. Temperature Dependence of Raman Scattering in Silicon. *Phys. Rev. B* **1**,

638–642 (1970).

41. Ohsaka, T. Temperature Dependence of the Raman Spectrum in Anatase TiO2. *J. Phys. Soc. Japan* **48**, 1661–1668 (1979).

42. Herchen, H. & Cappelli, M. A. First-order Raman spectrum of diamond at high temperatures. *Phys. Rev. B* **43**, 11740–11744 (1991).

43. Gillet, P., Biellmann, C., Reynard, B. & Mcmillan, P. Raman-Spectroscopic Studies of Carbonates .1. High-Pressure and High-Temperature Behavior of Calcite, Magnesite, Dolomite and Aragonite. *Phys. Chem. Miner.* **20**, 1–18 (1993).

44. Daniel, I., Gillet, P., McMillan, P. F. & Richet, P. An In-situ High-Temperature Structural Study of Stable and Metastable CaAl2Si2O8 Polymorphs. *Mineral. Mag.* **59**, 25–33 (1995).

45. Shoval, S., Boudeulle, M., Yariv, S., Lapides, I. & Panczer, G. Micro-Raman and FT-IR spectroscopy study of the thermal transformations of St. Claire dickite. *Opt. Mater. (Amst).* **16**, 319–327 (2001).

46. McKeown, D. A. Raman spectroscopy and vibrational analyses of albite: From 25 °C through the melting temperature. *Am. Mineral.* **90**, 1506–1517 (2005).

47. Boussois, K., Tessier-Doyen, N. & Blanchart, P. Anisotropic kinetic of the kaolinite to mullite reaction sequence in multilayer ceramics. *J. Eur. Ceram. Soc.* **33**, 243–249 (2013).

48. L'vov, B. V. Mechanism and kinetics of thermal decomposition of carbonates. *Thermochim. Acta* **386**, 1–16 (2002).

49. Maximenko, A. L. & Olevsky, E. A. Effective diffusion coefficients in solid-state sintering. *Acta Mater.* **52**, 2953–2963 (2004).

50. Djohari, H. & Derby, J. J. Transport mechanisms and densification during sintering: II. Grain boundaries. *Chem. Eng. Sci.* **64**, 3810–3816 (2009).

51. Milke, R., Wiedenbeck, M. & Heinrich, W. Grain boundary diffusion of Si, Mg, and O in enstatite reaction rims: A SIMS study using isotopically doped reactants. *Contrib. to Mineral. Petrol.* **142**, 15–26 (2001).

52. Milke, R. & Heinrich, W. Diffusion-controlled growth of wollastonite rims between quartz and calcite: Comparison between nature and experiment. *J. Metamorph. Geol.* **20**, 467–480 (2002).

53. Cultrone, G., Rodriguez-Navarro, C., Sebastian, E., Cazalla, O. & De La Torre, M. J. Carbonate and silicate phase reactions during ceramic firing. *Eur. J. Mineral.* **13**, 621–634 (2001).

54. Raith, M. M., Hoffbauer, R., Spiering, B., Shinoto, M. & Nakamura, N. Melting behaviour of feldspar clasts in high-fired Sue ware. *Eur. J. Mineral.* **28**, 385–407 (2016).

55. Salmag & Scholze. *Keramik*. (Springer, 2007).

56. Nkou Bouala, G. I. *et al.* From in Situ HT-ESEM Observations to Simulation: How Does Polycrystallinity Affects the Sintering of CeO2Microspheres? *J. Phys. Chem. C* **120**, 386–395 (2016).

57. Podor, R. *et al.* Dynamic aspects of cerium dioxide sintering: HT-ESEM study of grain growth and pore elimination. *J. Eur. Ceram. Soc.* **32**, 353–362 (2012).

58. Zhang, J., Huang, F. & Lin, Z. Progress of nanocrystalline growth kinetics based on oriented attachment. *Nanoscale* **2**, 18–34 (2010).

59. Stange, K., Lenting, C. & Geisler, T. Insights into the evolution of carbonate-bearing kaolin during sintering revealed by in situ hyperspectral Raman imaging. *J. Am. Ceram. Soc.* **101**, 897–910 (2018).

60. Hauke, K., Kehren, J., Böhme, N., Zimmer, S. & Geisler, T. In situ Hyperspectral Raman Imaging: A new Method to investigate Sintering Processes of Ceramic Material at High Temperature. *Appl. Sci.* submitted (2019) doi:10.3390/app9071310.

61. Stewart, S., Priore, R. J., Nelson, M. P. & Treado, P. J. Raman imaging. *Annu. Rev. Anal. Chem.* **5**, 337–360 (2012).

62. Hibbert, R., Price, M. C., Kinnear, T. M., Cole, M. J. & Burchell, M. J. The effects of temperature on the Raman spectrum of high purity quartz crystals. in *46th Lunar and Planetary Science Conference* 2–3 (The Woodlands, TX, USA, 16–20 March 2015, 2015).

63. Swamy, V., Dubrovinsky, L. S. & Tutti, F. High-Temperature Raman Spectra and Thermal Expansion of Wollastonite. *J. Am. Ceram. Soc.* **80**, 2237–2247 (1997).

64. Sharma, S. K., Simons, B. & Yoder, H. S. Raman study of anorthite, calcium Tschermak's pyroxene, and gehlenite in crystalline and glassy states. *Am. Mineral.* **68**, 1113–1125 (1983).

65. Daniel, I., Gillet, P., McMillan, P. F. & Richet, P. An in-situ high-temperature structural study of stable and metastable CaAl 2 Si 2 O 8 polymorphs . *Mineral. Mag.* **59**, 25–33 (1995).

66. Kieffer, S. W. Thermodynamics and lattice vibrations of minerals: 5. Applications to phase equilibria, isotopic fractionation, and high-pressure thermodynamic properties. *Rev. Geophys.* **20**, 827–849 (1982).

67. Gale, J. D. & Rohl, A. L. The General Utility Lattice Program (GULP). *Mol. Simul.* **29**, 291–341 (2003).

68. Richet, P., Robie, R. A. & Hemingway, B. S. Thermodynamic properties of wollastonite, pseudowollastonite and CaSiO3 glass and liquid. *Eur. J. Mineral.* **3**, 475–484 (1991).

69. Seryotkin, Y. V., Sokol, E. V. & Kokh, S. N. Natural pseudowollastonite: Crystal structure, associated minerals, and geological context. *Lithos* **134**–**135**, 75–90 (2012).

70. Tschegg, C., Ntaflos, T. & Hein, I. Thermally triggered two-stage reaction of carbonates and clay during ceramic firing - A case study on Bronze Age Cypriot ceramics. *Appl. Clay Sci.* **43**, 69–78 (2009).

71. Shoval, S. Using FT-IR spectroscopy for study of calcareous ancient ceramics. *Opt. Mater. (Amst).* **24**, 117–122 (2003).

72. Shoval, S., Yofe, O. & Nathan, Y. Distinguishing between natural and recarbonated calcite in oil shale ashes. *J. Therm. Anal. Calorim.* **71**, 883–892 (2003).

73. Schmid, T. & Dariz, P. Shedding light onto the spectra of lime: Raman and luminescence bands of CaO, Ca(OH)2 and CaCO3. *J. Raman Spectrosc.* **46**, 141–146 (2014).

74. Putnis, A. *Introduction to mineral sciences*. vol. 5 (Cambridge University Press, 2003).

75. Holm, E. A. & Foiles, S. M. How grain growth stops: A mechanism for grain-growth stagnation in pure materials. *Science (80-.).* **328**, 1138–1141 (2010).

76. Geisler-wierwille, T., Schaltegger, U. & Tomaschek, F. Re-equilibration of Zircon in Aqueous Fluids and Melts. (2007) doi:10.2113/gselements.3.1.43.

77. Putnis, A. Mineral replacement reactions: from macroscopic observations to microscopic mechanisms. *Mineral. Mag.* **66**, 689–708 (2002).

78. Johannes, W., Koepke, J., Behrens, H. & Hannover, D. Partial melting reactions of plagioclases and plagioclase-bearing systems. in *Feldspars and their Reactions* (ed. Parson, I.) 161–194 (Springer, Dordrecht, 1994).

79. Geisler, T., Burakov, B. E., Zirlin, V.,

Nikolaeva, L. & Pöml, P. A Raman spectroscopic study of high-uranium zircon from the Chernobyl 'lava'. *Eur. J. Mineral.* **17**, 883–894 (2005).

80. Van Nguyen, C. *et al.* A comparative study of different sintering models for Al2O3. *J. Ceram. Soc. Japan* **124**, 301–312 (2016).

81. German, R. M. Critical Overview of Sintering Computer Simulations. *V. Arnhold, C.L. Chu, W.F. Jandeska, H.I. Sanderow (Eds.), Adv. Powder Metall. 6 Part. Mater.* **9**, 1–15 (2002).

82. Böhme, N., Hauke, K., Neuroth, M. & Geisler, T. In situ Raman imaging of high-temperature solid-state reactions in the CaSO 4 – SiO 2 system. *Int. J. Coal Sci. &Technology* **6**, (2019).

83. Böhme, N., Hauke, K., Neuroth, M. & Geisler, T. In Situ Hyperspectral Raman Imaging of Ternesite Formation and Decomposition at High Temperatures. *Minerals* **10**, 287 (2020).

84. Gaidies, F., Milke, R., Heinrich, W. & Abart, R. Metamorphic mineral reactions: Porphyroblast, corona and symplectite growth. *EMU Notes Mineral.* **16**, 469–540 (2017).

85. Abart, R., Kunze, K., Milke, R., Sperb, R. & Heinrich, W. Silicon and oxygen self diffusion in enstatite polycrystals: The Milke et al. (2001) rim growth experiments revisited. *Contrib. to Mineral. Petrol.* **147**, 633–646 (2004).

86. Tzvetanova, Y., Kadyiski, M. & Petrov, O. Parawollastonite (wollastonite-2M polytype) from the skarns in Zvezdel pluton, Eastern Rhodopes - A single crystal study. *Bulg. Chem. Commun.* **44**, 131–136 (2012).

87. Remy, C., Reynard, B. & Madon, M. Raman Spectroscopic Investigations of Dicalcium Silicate: Polymorphs and High-Temperature Phase Transformations. *J. Am. Ceram. Soc.* **80**, 413–423 (1997).

88. Hoy, C. & Luidold, S. Das Dreistoffsystem Al2O3-CaO-SiO2 – ein Vergleich von berechneten und gemessenen Daten. *BHM Berg- und Hüttenmännische Monatshefte* **157**, 7–13 (2012).

89. Gou, Z. & Chang, J. Synthesis and in vitro bioactivity of dicalcium silicate powders. *J. Eur. Ceram. Soc.* **24**, 93–99 (2004).

90. Gou, Z., Chang, J. & Zhai, W. Preparation and characterization of novel bioactive dicalcium silicate ceramics. *J. Eur. Ceram. Soc.* **25**, 1507–1514 (2005).

91. Hazar, A. B. Y. Preparation and in vitro bioactivity of CaSiO3 powders. *Ceram. Int.* **33**, 687–692 (2007).

92. Groves, G. W. Phase transformations in dicalcium silicate. *J. Mater. Sci.* **18**, 1615–1624 (1983).

93. Liu, X., Morra, M., Carpi, A. & Li, B. Bioactive calcium silicate ceramics and coatings. *Biomed. Pharmacother.* **62**, 526–529 (2008).

94. Hench, L. L. & Thompson, I. Twenty-first century challenges for biomaterials. *J. R. Soc. Interface* **7 Suppl 4**, S379-91 (2010).

95. Wu, C. & Chang, J. A review of bioactive silicate ceramics. *Biomed. Mater.* **8**, (2013).

96. Lee, K. Y. *et al.* Ceramic bioactivity: Progresses, challenges and perspectives. *Biomed. Mater.* **1**, (2006).

97. Ou, J. *et al.* Preparation and in vitro bioactivity of novel merwinite ceramic. *Biomed. Mater.* **3**, (2008).

98. Zhong, H. *et al.* Mechanical properties and bioactivity of β-Ca2SiO4ceramics synthesized by spark plasma sintering. *Ceram. Int.* **37**, 2459–2465 (2011).

99. Zhao, W., Chang, J., Wang, J., Zhai, W. & Wang, Z. In vitro bioactivity of novel tricalcium silicate ceramics. *J. Mater. Sci. Mater. Med.* **18**, 917–923 (2007).

100. Abramczyk, H. & Brozek-pluska, B. Raman imaging in biochemical and biomedical applications . Diagnosis and treatment of breast cancer. *Chem. Rev.* **113**, 5766–5781 (2012).

101. Toporski, J. *Confocal Raman microscopy*. vol. 66 (Springer Series in Surface Sciences, 2018).

102. Geisler, T., Burakov, B. E., Zirlin, V., Nikolaeva, L. & Pöml, P. A Raman spectroscopic study of high-uranium zircon from the Chernobyl 'lava'. *Eur. J. Mineral.* **17**, 883–894 (2005).

103. Geisler, T., Popa, K. & Konings, R. J. M. Evidence for lattice strain and non-ideal behavior in the (La1−xEux)PO4 solid solution from X-ray diffraction and vibrational spectroscopy. *Front. Earth Sci.* **4**, (2016).

104. Klemens, P. G. Anharmonic decay of optical phonon in diamond. *Phys. Rev. B* **11**, 3206–3207 (1975).

105. Huang, F. *et al.* Temperature dependence of the Raman spectra of carbon nanotubes. *J. Appl. Phys.* **84**, 4022–4024 (1998).

106. Richet, P., Ingrin, J., Mysen, B. O., Courtial, P. & Gillet, P. Premelting effects in minerals: an experimental study. *Earth Planet. Sci. Lett.* **121**, 589–600 (1994).

107. Malfait, W. J. & Halter, W. E. Structural relaxation in silicate glasses and melts: High-temperature Raman spectroscopy. *Phys. Rev. B - Condens. Matter Mater. Phys.* **77**, 1–6 (2008).

108. Neuville, D. R. & Mysen, B. O. Role of aluminium in the silicate network: In situ, high-temperature study of glasses and melts on the join SiO2-NaAlO2. *Geochim. Cosmochim. Acta* **60**, 1727–1737 (1996).

109. Voron'ko, Y. K., Sobol', A. A., Ushakov, S. N., Jiang Guochang & You Jinglin. Phase transformations and melt structure of calcium metasilicate. *Inorg. Mater.* **38**, 825–830 (2002).

110. Gillet, P. Raman spectroscopy at high pressure and high temperature. Phase transitions and thermodynamic properties of minerals. *Phys. Chem. Miner.* **23**, 263–275 (1996).

111. Osipov, A. A. & Osipova, L. M. Raman scattering study of barium borate glasses and melts. *J. Phys. Chem. Solids* **74**, 971–978 (2013).

112. Saloman, E. B. Wavelengths, energy level classifications, and energy levels for the spectrum of neutral mercury. *J. Phys. Chem. Ref. Data* **35**, 1519–1548 (2006).

113. von Salje, E. Experimentelle Untersuchung der Ramanstreuung an Kristallpulvern (experimental investigation of Raman scattering of crystall powder). *J. Appl. Cryst.* **6**, 442–446 (1973).

114. Linkam Scientific Instruments TS1500. Linkam Scientific Instruments TS1500. (2018).

115. Neuville, D. R., de Ligny, D. & Henderson, G. S. Advances in Raman spectroscopy applied to earth and material sciences. *Rev. Mineral. Geochemistry* **78**, 509–541 (2014).

116. Vajna, B. *et al.* Comparison of chemometric methods in the analysis of pharmaceuticals with hyperspectral Raman imaging. *J. Raman Spectrosc.* **42**, 1977–1986 (2011).

117. Nasdala, L., Beyssac, O., Schopf, J. W. & Bernd Bleisteiner. Application of Raman-based images in the Earth Sciences. in *Raman Imaging:Techniques and Applications* 145–189 (Springer Series in Optical Sciences, 2012).

118. Kramida, A., Ralchenko, Yu., Reader, J. and N. A. T. (20l6). NIST: Atomic Spectra Database - Version History. *National Institute of Standards and Technology* (2016).

119. Tian, H., Wachs, I. E. & Briand, L. E. Comparison of UV and visible Raman

spectroscopy of bulk metal molybdate and metal vanadate catalysts. *J. Phys. Chem. B* **109**, 23491–23499 (2005).

120. Zouboulis, E., Renusch, D. & Grimsditch, M. Advantages of ultraviolet Raman scattering for high temperature investigations. *Appl. Phys. Lett.* **72**, 1–3 (1998).

121. Hope, G. A., Woods, R. & Munce, C. G. Raman microprobe mineral identification. *Miner. Eng.* **14**, 1565–1577 (2001).

122. Hopkins, J. B. & Farrow, L. A. Raman microprobe determination of local crystal orientation. *J. Appl. Phys.* **59**, 1103–1110 (1986).

123. Chaigneau, M., Picardi, G., Girard, H. A., Arnault, J. C. & Ossikovski, R. Laser heating versus phonon confinement effect in the Raman spectra of diamond nanoparticles. *J. Nanoparticle Res.* **14**, (2012).

124. Bersani, D., Lottici, P. P. & Ding, X. Phonon confinement effects in the Raman scattering by TiO 2 nanocrystals. *Appl. Phys. Lett.* **72**, 72–75 (1998).

125. Swamy, V. *et al.* Finite-size and pressure effects on the Raman spectrum of nanocrystalline anatase Ti O2. *Phys. Rev. B - Condens. Matter Mater. Phys.* **71**, 15–17 (2005).

126. Swamy, V. Size-dependent modifications of the first-order Raman spectra of nanostructured rutile TiO2. *Phys. Rev. B - Condens. Matter Mater. Phys.* **77**, 15–18 (2008).

127. Namba, Y., Heidarpour, E. & Nakayama, M. Size effects appearing in the Raman spectra of polycrystalline diamonds Size effects appearing in the Raman spectra of polycrystalline. *J. Appl. Phys.* **1748**, 1–5 (2012).

128. Yoshikawa, M. *et al.* Raman scattering from nanometer-sized diamond Raman scattering from nanometer-sized diamond. *Appl. Phys. Lett.* **694**, 5–8 (2008).

129. Zhao, X. Z., Cherian, K. A., Roy, R. & White, W. B. Downshift of Raman peak in diamond powders. *J. Mater. Res.* **13**, 1974–1976 (1998).

130. Polsky, C. H., Smith, K. H. & Wolf, G. H. Effect of pressure on the absolute Raman scattering cross section of SiO2 and GeO2 glasses. *J. Non. Cryst. Solids* **248**, 159–168 (1999).

131. Quittet, A. M. & Lambert, M. Temperature dependence of the Raman cross section and light absorption in cubic BaTiO3. *Solid State Commun.* **12**, 1053–1055 (1973).

132. Demos, S. G. *et al.* Measurement of the Raman scattering cross section of the breathing mode in KDP and DKDP crystals. *Opt. Express* **19**, 21050 (2011).

133. Rappoport, D. Berechnung von Raman-Intensitäten mit zeitabhängiger Dichte-Funktionaltheorie. (Universitätsverlag Karlsruhe, 2007).

134. Neuville, D. R., Cormier, L. & Massiot, D. Al coordination and speciation in calcium aluminosilicate glasses: Effects of composition determined by27Al MQ-MAS NMR and Raman spectroscopy. *Chem. Geol.* **229**, 173–185 (2006).

135. Neuville, D. R. Viscosity, structure and mixing in (Ca, Na) silicate melts. *Chem. Geol.* **229**, 28–41 (2006).

136. Guerette, M. & Huang, L. A simple and convenient set-up for high-temperature Brillouin light scattering. *J. Phys. D. Appl. Phys.* **45**, 1–7 (2012).

137. Behrens, H., Roux, J., Neuville, D. R. & Siemann, M. Quantification of dissolved H2O in silicate glasses using confocal microRaman spectroscopy. *Chem. Geol.* **229**, 96–112 (2006).

138. Everall, N. J. Confocal Raman microscopy: Why the depth resolution and spatial accuracy can be much worse than you think. *Appl. Spectrosc.*

54, 1515–1520 (2000).

139. Everall, N. J. Depth Profiling with confocal Raman microscopy, part II. *Spectroscopy* **19**, 16–27 (2004).

140. Everall, N. J. Confocal Raman microscopy: common errors and artefacts. *Analyst* **135**, 2512 (2010).

141. Presser, V., Keuper, M., Berthold, C. & Nickel, K. G. Experimental determination of the Raman sampling depth in zirconia ceramics. *Appl. Spectrosc.* **63**, 1288–92 (2009).

142. Everall, N. Optimising image quality in 2D and 3D confocal Raman mapping. *J. Raman Spectrosc.* **45**, 133–138 (2014).

143. Zoubir, A. *Raman Imaging: Techniques and Applications*. *Springer Series in Optical Sciences* vol. 168 (Springer Series in Optical Sciences, 2012).

144. Everall, N. J. Modeling and measuring the effect of refraction on the depth resolution of confocal Raman microscopy. *Appl. Spectrosc.* **54**, 773–782 (2000).

145. Juang, C. B., Finzi, L. & Bustamante, C. J. Design and application of a computer-controlled confocal scanning differential polarization microscope. *Rev. Sci. Instrum.* **59**, 2399–2408 (1988).

146. Nankervis, J. C. & Furlong, R. B. Phase changes in mineral matter of North Dakota lignites caused by heating to 1200 °C. *Fuel* **59**, 425–430 (1980).

147. Lin, K. *et al.* Study of the mechanical property and in vitro biocompatibility of CaSiO3ceramics. *Ceram. Int.* **31**, 323–326 (2005).

148. Avrami, M. Kinetics of phase change. I: General theory. *J. Chem. Phys.* **7**, 1103–1112 (1939).

149. Knudsen, F. P. Dependence of mechanical strength of brittle polycrystalline specimens on porosity and grain size. *J. Am. Ceram. Soc.* **42**, 376–387 (1959).

150. Schneider, C. A., Rasband, W. S. & Eliceiri, K. W. NIH Image to ImageJ: 25 years of image analysis. *Nat. Methods* **9**, 671–675 (2012).

151. Herzberg, G. *Atomic Spectra and Atomic Structure*. (Dover puplications, 1944).

152. Geisler, T., Pöml, P., Stephan, T., Janssen, A. & Putnis, A. Experimental observation of an interface-controlled pseudomorphic replacement reaction in a natural crystalline pyrochlore. *Am. Mineral.* **90**, 1683–1687 (2005).

153. King, H. E., Plümper, O., Geisler, T. & Putnis, A. Experimental investigations into the silicification of olivine: Implications for the reaction mechanism and acid neutralization. *Am. Mineral.* **96**, 1503–1511 (2011).

154. Pan, X., Zhang, D., Wu, Y. & Yu, H. Synthesis and characterization of calcium aluminate compounds from gehlenite by high-temperature solid-state reaction. *Ceram. Int.* **44**, 13544–13550 (2018).

155. Ptáček, P., Opravil, T., Šoukal, F., Havlica, J. & Holešinský, R. Kinetics and mechanism of formation of gehlenite, Al-Si spinel and anorthite from the mixture of kaolinite and calcite. *Solid State Sci.* **26**, 53–58 (2013).

156. Majerová, M. *et al.* Crystallization kinetics of gehlenite glass microspheres. *J. Therm. Anal. Calorim.* (2020) doi:10.1007/s10973-020-09305-7.

157. Jia, D., Kim, D. & Kriven, W. M. Sintering behavior of gehlenite. Part I: Self-forming, macro-/mesoporous gehlenite - Pore-forming mechanism, microstructure, mechanical, and physical properties. *J. Am. Ceram. Soc.* **90**, 1760–1773 (2007).

158. Abràmoff, M. D., Magalhães, P. J. & Ram, S. J. Image processing with imageJ. *Biophotonics Int.* **11**, 36–41 (2004).

159. Dvořáková, P., Kloužková, A., Kohoutková, M. & Kolářová, M. Moisture expansion of Ca-rich ceramic body. *IOP Conf. Ser. Mater. Sci. Eng.* **1050**, 012004 (2021).

160. Klosek-Wawrzyn, E., Malolepszy, J. & Murzyn, P. Sintering behavior of kaolin with calcite. *Procedia Eng.* **57**, 572–582 (2013).

161. Freundlich, H. *Kapillarchemie: Eine Darstellung der Chemie der Kolloide und verwandter Gebiete [Capillary Chemistry: A presentation of colloid chemistry and related fields]*. (Akademische Verlagsgesellschaft, 1909).

162. Mugnaioli, E. *et al.* Electron Diffraction on Flash-Frozen Cowlesite Reveals the Structure of the First Two-Dimensional Natural Zeolite. *ACS Cent. Sci.* **6**, 1578–1586 (2020).

163. Tsai, Y. L. *et al.* Raman spectroscopic characteristics of zeolite group minerals. *Minerals* **11**, 1–14 (2021).

164. Allegretta, I., Pinto, D. & Eramo, G. Effects of grain size on the reactivity of limestone temper in a kaolinitic clay. *Appl. Clay Sci.* **126**, 223–234 (2016).

165. Redaoui, D., Sahnoune, F., Heraiz, M., Belhouchet, H. & Fatmi, M. Thermal decomposition kinetics of Algerian Tamazarte kaolinite by thermogravimetric analysis. *Trans. Nonferrous Met. Soc. China (English Ed.* **27**, 1849–1855 (2017).

166. Fabbri, B., Gualtieri, S. & Leonardi, C. Modifications induced by the thermal treatment of kaolin and determination of reactivity of metakaolin. *Appl. Clay Sci.* **73**, 2–10 (2013).

167. Cheng, H., Liu, Q., Yang, J., Ma, S. & Frost, R. L. The thermal behavior of kaolinite intercalation complexes-A review. *Thermochim. Acta* **545**, 1–13 (2012).

168. Saraya, M. E. I. & Sayed, M. Characterization and Evaluation of Natural Zeolite As a Pozzolanic Material. *Al-Azhar Bull. Sci.* **29**, 17–34 (2018).

169. Heimann, R. B. *Classic and Advanced Ceramics: From Fundamentals to Applications*. (WILEY-VCH Verlag GmbH & Co. KGaA, 2010).

170. Zimmer, S. In Situ Hyperspectral Raman Imaging of High Temperature Solid-solid Reactions in the System Al 2 O 3 - SiO 2 -CaO. (2019).

171. Lafuente, B., Downs, R. T., Yang, H. & Stone, N. RRUFF^{TM} Project. *power databases RRUFF Proj. Highlights Mineral. Crystallogr. T Armbruster R M Danisi, eds.* 1–30 (2015).

172. Gualtieri, A., Bellotto, M., Artioli, G. & Clark, S. M. Kinetic study of the kaolinite-mullite reaction sequence. Part II: Mullite formation. *Phys. Chem. Miner.* **22**, 215–222 (1995).

173. Bellotto, M., Gualtieri, A., Artioli, G. & Clark, S. M. Kinetic study of the kaolite-mullite reaction sequence-Part_1_kaolinite dehydroxylation. *Phys. Chem. Miner.* **22**, 207–214 (1995).

174. Frost, R. A. Y. L. & Vassallo, A. M. The dehydroxylation of kaolinite clay minerals using infrared emission spectroscopy. **44**, 635–651 (1996).

175. Frost, R. L. & Van Der Gaast, S. J. Kaolinite Hydroxyls-A Raman Microscopy Study. *Clay Miner.* **32**, 471–484 (1997).

176. Sperinck, S., Raiteri, P., Marks, N. & Wright, K. Dehydroxylation of kaolinite to metakaolin - A molecular dynamics study. *J. Mater. Chem.* **21**, 2118–2125 (2011).

177. Gasparini, E. *et al.* Thermal dehydroxylation of kaolinite under isothermal conditions. *Appl. Clay Sci.* **80–81**, 417–425 (2013).

178. Traoré, K., Kabré, T. & Blanchart, P. Low temperature sintering of clay for

pottery from Burkina Faso. *Appl Clay Sci.* **17**, 279–292 (2000).

179. Ptáček, P. *et al.* The kinetics and mechanism of kaolin powder sintering I. The dilatometric CRH study of sinter-crystallization of mullite and cristobalite. *Powder Technol.* **232**, 24–30 (2012).

180. Ptáček, P. *et al.* The influence of structure order on the kinetics of dehydroxylation of kaolinite. *J. Eur. Ceram. Soc.* **33**, 2793–2799 (2013).

181. Dion, P. Kinetic Study by Controlled-Transformation Rate Thermal Analysis of the Dehydroxylation of Kaolinite. *Clay Miner.* **33**, 269–276 (1998).

182. Dubois, J., Murat, M., Amroune, A., Carbonneau, X. & Gardon, R. High-temperature transformation in kaolinite: the role of the crystallinity and of the firing atmosphere. *Appl. Clay Sci.* **10**, 187–198 (1995).

183. Ptáček, P. *et al.* Isothermal kinetic analysis of the thermal decomposition of kaolinite: The thermogravimetric study. *Thermochim. Acta* **501**, 24–29 (2010).

184. Piga, L. thermochimica acta Thermogravimetry of a kaolinite-alunite ore. *Thermochim. Acta* **265**, 177–187 (1995).

185. Gualtieri, A. & Bellotto, M. Modelling the structure of the metastable phases in the reaction sequence kaolinite-mullite by X-ray scattering experiments. *Phys. Chem. Miner.* **25**, 442–452 (1998).

186. De Noni, A., Hotza, D., Soler, V. C. & Vilches, E. S. Influence of composition on mechanical behaviour of porcelain tile. Part I: Microstructural characterization and developed phases after firing. *Mater. Sci. Eng. A* **527**, 1730–1735 (2010).

187. Heimann, R. B. Mineralogy and Chemistry of the Ceramic Firing Process. *Class. Adv. Ceram.* 99–118 (2010) doi:10.1002/9783527630172.ch4.

188. Bost, N., Duraipandian, S., Guimbretière, G. & Poirier, J. Raman spectra of synthetic and natural mullite. *Vib. Spectrosc.* **82**, 50–52 (2016).

189. Santana, L. N. L. *et al.* Mullite formation from bentonites containing kaolinite: Effect of composition and synthesis parameters. *Appl. Clay Sci.* **87**, 28–33 (2014).

190. Sun, J., Wu, Z., Cheng, H., Zhang, Z. & Frost, R. L. A Raman spectroscopic comparison of calcite and dolomite. *Spectrochim. Acta - Part A Mol. Biomol. Spectrosc.* **117**, 158–162 (2014).

191. Osborn, E. F. & Schairer, J. F. The ternary system pseudowollastonite-akermanite-gehlenite. *Am. J. Sci.* **239**, 715–763 (1941).

192. Rodriguez-Navarro, C., Ruiz-Agudo, E., Luque, A., Rodriguez-Navarro, A. B. & Ortega-Huertas, M. Thermal decomposition of calcite: Mechanisms of formation and textural evolution of CaO nanocrystals. *Am. Mineral.* **94**, 578–593 (2009).

193. Ewing, J., Beruto, D. & Searcy, A. W. The Nature of CaO Produced by Calcite Powder Decomposition in Vacuum and in CO2. *J. Am. Ceram. Soc.* **62**, 580–584 (1979).

194. Beruto, D. & Searcy, A. W. Calcium oxides of high reactivity. *Nature* **263**, 221–222 (1976).

195. Wieczorek-Ciurowa, K., Paulik, J. & Paulik, F. Influence of foreign materials upon the thermal decomposition of dolomite, calcite and magnesite Part 1. *Thermichimica Acta* **38**, 157–164 (1980).

196. Kehren, J. The Formation of Calcium Silicates in the CaO-SiO2-System studied by In situ Hyperspectral Raman Imaging. (Rheinische Friedrich-Wilhelms-Universität Bonn, 2018).

197. Beruto, D. T., Searcy, A. W. & Kim, M. G. Microstructure, kinetic, structure, thermodynamic analysis for calcite decomposition: Free-surface and powder bed experiments. *Thermochim. Acta* **424**, 99–109 (2004).

198. Beruto, D., Barco, L. & Searcy, A. W. Rearrangement of Porous CaO Aggregates During Calcite Decomposition in Vacuum. *J. Am. Ceram. Soc.* **66**, 893–896 (1983).

199. Zhong, Q. & Bjerle, I. Calcination kinetics of limestone and the microstructure of nascent CaO. *Thermochim. Acta* **223**, 109–120 (1993).

200. Shoval, S., Gaft, M., Beck, P. & Kirsh, Y. Thermal behaviour of limestone and monocrystalline calcite tempers during firing and their use in ancient vessels. *J. Therm. Anal.* **40**, 263–273 (1993).

201. Shoval, S. Mineralogical changes upon heating calcitic and dolomitic marl rocks. *Thermochim. Acta* **135**, 243–252 (1988).

202. Kehren, J., Zimmer, S., Hauke, K. & Geisler, T. The Formation of Calcium Silicates in the CaO-SiO2-System studied by In situ Hyperspectral Raman Imaging (HSRI). in *62nd International Colloquium on Refractories 2019 – Supplier Industries enabling REFRACTORIES* 111–114 (2019).

203. Kehren, J., Hauke, K., Zimmer, S. & Geisler, T. Hyperspectral Raman Imaging : A Powerful Tool for Time- , Space- , and Temperature-Resolved In Situ Studies Using the Example of the. in *United International Technical Conference of Refractories* 10–13 (2019).

204. Abd Rashid, R., Shamsudin, R., Abdul Hamid, M. A. & Jalar, A. Low temperature production of wollastonite from limestone and silica sand through solid-state reaction. *J. Asian Ceram. Soc.* **2**, 77–81 (2014).

205. Adylov, G. T. *et al.* Use of wollastonite from the Koitashskoe deposit in the production of ceramics and refractory materials. *Refract. Ind. Ceram.* **43**, 359–361 (2002).

206. Deer, W. A., Howie, R. A. & Zussman, J. Rock-forming minerals Single-Chain Silicates. 668 (1997).

207. Diella, V., Adamo, I., Pagliari, L., Pavese, A. & Francescon, F. Effects of particle size distribution and starting phase composition in Na-feldspar/kaolinite system at high temperature. *J. Eur. Ceram. Soc.* **35**, 1327–1335 (2015).

208. Vichaphund, S., Kitiwan, M., Atong, D. & Thavorniti, P. Microwave synthesis of wollastonite powder from eggshells. *J. Eur. Ceram. Soc.* **31**, 2435–2440 (2011).

209. Mazzucato, E. & Gualtieri, a. F. Wollastonite polytypes in the CaO-SiO 2 system. *Phys. Chem. Miner.* **27**, 565–574 (2000).

210. Zhao, C. & Wang, G. The melting reaction mechanism of NaOH in decomposing Ca2SiO4. *Miner. Process. Extr. Metall. Rev.* **36**, 385–390 (2015).

211. Adamo, I., Diella, V., Pavese, A., Vignola, P. & Francescon, F. Na-feldspar (F) and kaolinite (K) system at high temperature: Resulting phase composition, micro-structural features and mullite-glass Gibbs energy of formation, as a function of F/K ratio and kaolinite crystallinity. *J. Eur. Ceram. Soc.* **33**, 3387–3395 (2013).

212. Kalampounias, A. G. IR and Raman spectroscopic studies of sol – gel derived alkaline-earth. **34**, 299–303 (2011).

213. Fintor, K., Park, C., Nagy, S., Pál-Molnár, E. & Krot, A. N. Hydrothermal origin of hexagonal CaAl2Si2O8 (dmisteinbergite) in a compact type A CAI from the Northwest Africa 2086 CV3 chondrite. *Meteorit. Planet. Sci.* **49**, 812–823 (2014).

214. Zolotarev, A. A., Krivovichev, S. V.,

Gurzhiy, T. L. P. V. V., Bocharov, V. N. & Rassomakhin, M. A. Dmisteinbergite, CaAl2Si2O8, a Metastable Polymorph of Anorthite: Crystal-Structure and Raman Spectroscopic Study of the Holotype Specimen. *Minerals* **9**, 1–12 (2019).

215. Fritz, J. *et al.* Donwilhelmsite, [CaAl4Si2O11], a new lunar high-pressure Ca-Al-silicate with relevance for subducted terrestrial sediments. *Am. Mineral.* **105**, 1704–1711 (2020).

216. Kimura, M. *et al.* Kushiroite, CaAlAlSiO6: A new mineral of the pyroxene group from the ALH 85085 CH chondrite, and its genetic significance in refractory inclusions. *Am. Mineral.* **94**, 1479–1482 (2009).

217. Roskosz, M., Toplis, M. J., Besson, P. & Richet, P. Nucleation mechanisms: A crystal-chemical investigation of phases forming in highly supercooled aluminosilicate liquids. *J. Non. Cryst. Solids* **351**, 1266–1282 (2005).

218. Hofmeister, A. M., Wopenka, B. & Locock, A. J. Spectroscopy and structure of hibonite, grossite, and CaAl2 O4: Implications for astronomical environments. *Geochim. Cosmochim. Acta* **68**, 4485–4503 (2004).

219. Brohsonn, N. High temperature Raman spectroscopy of wollastonite. (Rheinische Friedrich-Wilhelms-Universität Bonn, 2017).

Annotations

This chapter is published in *Applied Sciences*[60]. The conceptualization is done by T. Geisler and myself. The Raman measurements are performed by S. Zimmer, J. Kehren and myself. S. Zimmer, J. Kehren, N. Böhme and T. Geisler contributed to the interpretation. T. Geisler and I wrote the manuscript and I produced all figures. S. Zimmer, J. Kehren and N. Böhme reviewed and edited the manuscript.

4 In-operando evidence for the formation of an undescribed Ca aluminosilicate phase during sintering of a kaolinite-calcite mixture by in situ Raman spectroscopy

Abstract

The kinetics of gehlenite nucleation and growth from a kaolinite-calcite mixture were studied *in operando* by *in situ* Raman imaging. The green bodies were fired in air to six different temperatures between 803°C and 1020°C. During a dwell time of about 48 hours, 24 high-temperature Raman images were subsequently recorded from which the phase evolution as a function of temperature and time could be quantified. Using isoconversional, model-free time-to-a-given-fraction method, an empirical activation energy of 107 ± 19 kJ/mol was determined for nucleation and growth of gehlenite in the temperature range between 803 and 880 ± 5°C. Above 880°C the activation energy changed to 633 ± 31 kJ/mol. This large change in the kinetics was also reflected by a change in grain size distribution of gehlenite in the same temperature range. Moreover, a previously undescribed intermediate hydrous calcium aluminosilicate phase (main Raman band near 560 cm^{-1}) was identified during firing which seems to affect the kinetics and mechanism of gehlenite formation.

1. Introduction

Gehlenite ($Ca_2Si_2O_7$) is an important target product and intermediate phase based on the CaO-Al_2O_3-SiO_2 system[154]. The sorosilicate (silicate with an isolated group of tetrahedra) is part of the family of melilites, which belongs to the space group $P\bar{4}2_1m$[154]. In nature, gehlenite is formed in the contact zone of a magma with calcite-bearing rocks[155]. It is used as a regular constituent of (building) ceramic materials and cookware. Gehlenite glass can be used for the synthesis of bio-soluble glass fibers and glass ceramics[156]. The desired properties like significant strain, a specific grain shape[8] or a special porous network structure[157] can only be achieved if the ceramic process is understood. The high temperature, low-pressure mineral trans-formations occurring during ceramic firing are influenced by many factors like the chemical and mineralogical composition of the original clay, its grain-size distribution, the maximum heating temperature, heating rate, duration of firing and kiln redox atmosphere[12]. Little is known about the transformation reactions between silicate and carbonate phases at the reaction interfaces. In particular, the transport mechanisms of reactants (diffusion vs. mass transport/viscous flow) and the transformation processes involved at high-T (solid-state reactions vs. crystallization from a melt) are not yet fully understood[53].

In samples of high Ca content, the stability field of gehlenite is relatively small (approximately between 800 and 1000°C) which makes it useful to utilize it as a temperature sensor in ancient ceramics or natural rock samples of high-temperature metamorphism. Here, six samples of a kaolinite-calcite mixture were fired to temperatures between 803 and 1020 ± 5°C to study the nucleation and grain growth kinetics of gehlenite in this temperature range. High-temperature Raman imaging enables the investigation of textural and mineralogical changes *in situ* and *in operando* and thereby spatially resolved. Within a dwell time of 48 hours, 24 Raman images (about two hours exposure time per image) were recorded. A semi-quantitative mineral content was obtained from the Raman images and the isoconversional, model-free 'time-to-a-given fraction'-method was used to determine the activation energy of gehlenite nucleation and growth. With the help of the graphical program imageJ[150,158] the grain growth of gehlenite was quantified as a function of time and temperature. The high sensitivity of high-temperature Raman imaging for minor changes in mineralogy and texture enabled the observation of a previously undescribed Ca

aluminosilicate phase that influenced the kinetics of gehlenite nucleation and growth.

2 Materials and Methods

2.1 Materials

The green bodies were prepared from a mixture of kaolinite from Carl Jäger Tonindustriebedarf and calcite from Alfa Aesar. Details on particle size and level of purity of the precursor material are given elsewhere[60]. The powdered precursor material (dried at 100°C for 24 hours) was blended and homogenized in a ratio of 1:1. Six samples were produced by compacting about 4.3 mg of the material into cylinders (3 x 2.7 mm^2) at a pressure of 0.01 MPa, which resulted in a flat sample surface.

2.2 Hyperspectral Raman imaging

All sintering experiments were carried out with a Linkam stage TS1500 (Linkam Scientific Instruments, Surrey, UK) that was placed under an Olympus BX41 microscope of a Horiba Scientific HR 800 Vis confocal Raman spectrometer. The spectrometer is equipped with a frequency-doubled, solid state Nd:YAG laser (532 nm) with a maximum power of 2 W and an electron multiplying charge-coupled device (EM-CCD) detector. A 50x long-working distance (LWD) objective with a numerical aperture (NA) of 0.5 and a working distance of 10.6 mm was used for all experiments. With a grating of 600 groves/mm the spectral resolution was about 3.5 cm^{-1}, as given by the width of the intense Ne line at 1707.06 cm^{-1}. The Ne lamp was placed into the beam path of the scattered light to correct for any spectrometer shifts occurring during long-time measurements.

At first of each experiment, Raman images were recorded at RT to select a representative area. Subsequently, the sample was fired with a heating rate of 10 °C/min to the target temperature. During a dwell time of about 48 hours 24 Raman images (1 hour 53 min per image) were recorded in a row. The sample was then cooled down with a cooling rate of 10° C/min before recording the last image at RT. Depth profiles were acquired using the auto-focus function (depth profiling) before recording each Raman image to obtain an optimal signal-to-noise ratio and to monitor reaction- and temperature-related shrinking or expansion effects. The “tilt at limits” mode acquires depth profiles of the image center and the four corners and determines the best focus regarding the reflection of the laser from the sample surface, from which the focus at each position (pixel) of the image is interpolated. Raman spectra were collected during continuous x-y stage movement with a speed of 1.6 m/s (SWIFT© mode). During movement, Raman intensities were recorded for 0.6 s in the wavenumber range from 100 to 1750 cm^{-1}. All recorded images comprised an area of 100 x 100 μm^2 in size. The step size was 1 µm, yielding 10,000 spectra per image. Despite the short acquisition time per spectrum, the total exposure time was still about two hours for a single image. Hence, an image is never an accurate snapshot, because processes may still run while recording the image. For fast reactions, this may easily be recognized by image distortions[60], but should in general be considered when interpreting the hyperspectral Raman images.

All spectra were corrected for (i) the wavelength-dependent instrumental sensitivity (white light correction), (ii) a possible spectrometer shift by calibrating the spectrum using the intense Ne line at 1707.06 cm^{-1}, (iii) cosmic spikes, and (iv) background contributions that, at high temperatures, are mainly composed of black body radiation and in some cases of continuous fluorescence signals. More details can be found elsewhere[60].

To determine the phase proportions at each pixel of an image the classical least squares (CLS) fitting procedure was used. This method assumes that a spectrum of a polyphase material is a linear mixture of the spectra of the pure phases. Within the multidimensional spectral array, the CLS fitting procedure finds a linear combination of reference spectra of the pure phases, which fits best with respect to the raw spectrum at each position (pixel). In-house

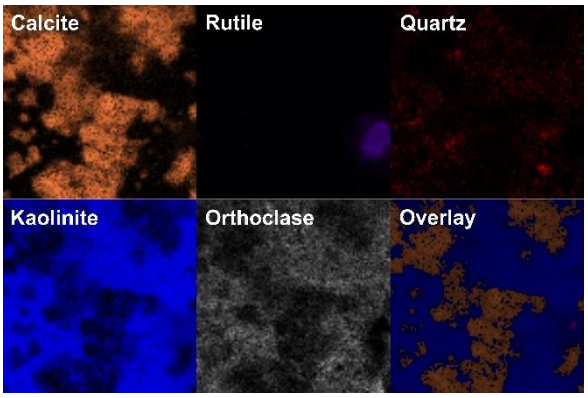

Figure 4.1: False-colored Raman images showing the distribution of calcite, rutile, quartz, kaolinite, and orthoclase compared with the overlay image which is composed of the single-phase images.

high-temperature reference spectra were used for the fitting procedure. The procedure is explained in more detail elsewhere[59,60]. The false-colored hyperspectral Raman images are composed of the images of the pure phases (Figure 4.1). Each pixel is colored in the color of the phase that dominates in the Raman spectrum and the brightness of the color reflects the intensity of the spectrum at this pixel. While a dark color represents low intensity, a bright color signifies high intensity.

When the Raman cross sections of the phases that contribute to the Raman spectra differ widely, the image appears to be black apart from small bright dots where phases (e.g., anatase) with a high Raman cross section is located (Figure 4.2, not normalized). This is the case, because here the intensity of the Raman spectrum is extremely high in contrast to all other spectra in which the dominant phases have lower Raman intensities. Therefore, the Raman CLS images were normalized to 100 % for each pixel.

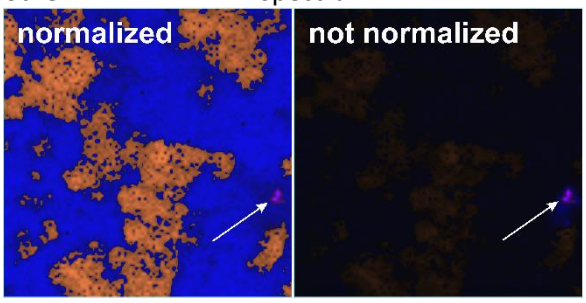

Figure 4.2: Example of a normalized CLS image compared to a non-normalized CLS image. The arrow points to an anatase grain whose Raman intensities are very intense compared to all other phases.

For millerite and an unknown phase with a main Raman band near 560cm^{-1} that were identified in the experiments high-temperature reference spectra were not available. We therefore used synthetic spectra for the fitting procedure as described in Chapter 2[59]. In this case, the Raman scattering cross section cannot be considered and the amount of these phases might therefore be over- or underestimated.

Due to shrinkage and densification or volume gain by the sintering reactions the sample moved during an experiment lasting 48 hours. To quantify the evolution of the semi-quantitative phase content as a function of time and temperature and thus the crystallization kinetics of the calcium silicates, it was important to always analyze the same sample area (volume) during one experiment. Therefore, the plugins TrakEM2 and Manual Tracking of the software ImageJ were used to align the images of each experiment. Here, two images are compared with each other and the position of one image is shifted according to the position of the second image. In the end, the area is chosen which occurs in all pictures (Figure 4.3). The disadvantage of this method is that the analyzed area (volume) is reduced (Table 4.1). In four out of six experiments the sample area was reduced to about one half (Exp. T843, T880, T931, and T1020). In the experiment with the lowest firing temperature (T803) 83 % of the sample area could be used for the semi-quantitative analysis, whereas in experiment T971 only 35 % could be used for quantification.

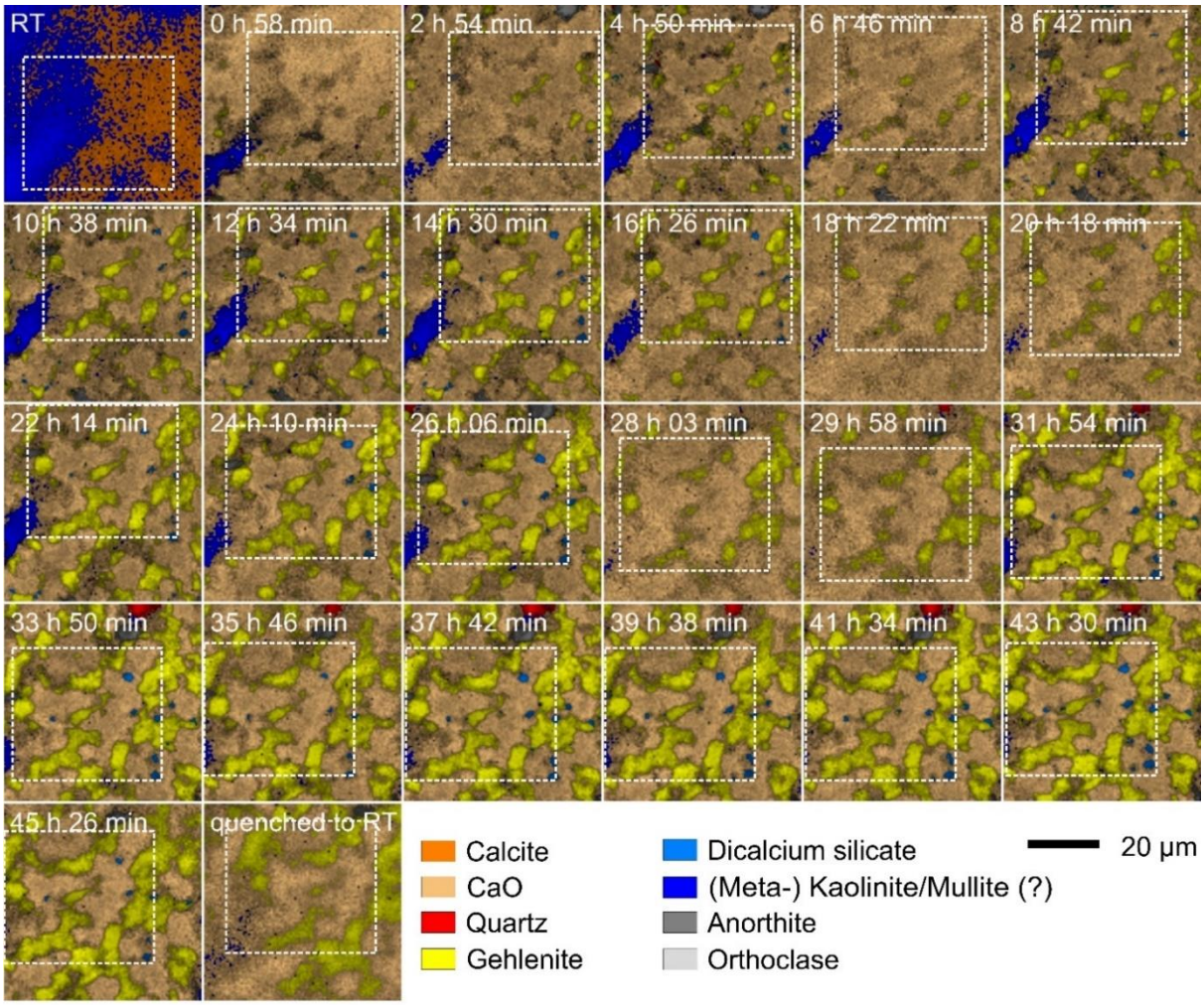

Figure 4.3: False-colored, hyperspectral Raman images (overlay) of Exp. T880. To study the crystallization kinetics, it is important to always analyze the same area (volume) of the sample during the experiment. Therefore, the images of each experiment are aligned. The white dashed rectangles mark the area used for quantification of the phase composition in this experiment.

2.3 Determination of the relative expansion and shrinkage and phase quantification

The relative expansion/shrinkage of the green body during the experiments is influenced by several processes. On the one hand, the sample expands due to thermal expansion. The sample may also gain in volume by the formation of new mineral phases with a higher molar volume. On the other hand, the sample shrinks due to densification because the pore volume is decreasing or because of the formation of new phases with a smaller molar volume. The relative expansion was obtained by the autofocus function implemented in the Labspec software. It was calculated by using the original sample height of the green body and the sample height measured by the autofocus before each Raman image was recorded. It must be considered that only a small area of 100 x 100 µm was measured. The significance of these values depends on the heterogeneity of the sample surface that can vary from experiment to experiment. On the other hand, the internal precision of the

Table 4.1: Size of the area that was used for phase quantification.

Exp.	x (µm)	y (µm)	map size (pixel)
T803	91	91	8281
T843	81	60	4860
T880	75	68	5100
T931	68	73	4964
T971	61	58	3538
T1020	89	59	5251

obtained values for the relative expansion as a function of time is in the order of one percent.

To minimize the error caused by a shifted image area, due to expansion and shrinkage or densification, the aligned images were used for the quantification. We note that, when using the data for each phase from all pixel. The mineral content was quantified from the matrix behind the unnormalized images of all end members of the CLS fit. The relative mineral fractions are different to those deduced from the 2-dimensional hyperspectral Raman images. This is because in the hyperspectral Raman images, a pixel was colored in the color of the pure phase that was dominating in the CLS fit of this pixel and the Raman CLS images were normalized (see chapter 2.1). In contrast to that the unnormalized data were used to quantify the mineral content. Every CLS Raman image is an overlay of the Raman images of the single phases. Behind these images there are matrices of the content of the respective phase in every pixel. In difference to the Raman image overlay, the content of the respective phase in all CLS fits (pixels) is considered, even when the phase is not the dominant one of a single pixel. Using this approach, the evolution of the mineral content as a function of time and temperature could be studied, at least semi-quantitatively.

2.4 Determination of gehlenite nucleation and growth kinetics

The growth of gehlenite grains during firing was quantified form the single-phase Raman images of gehlenite. When compared to the overlay images in which all phases are displayed, the single-phase images have the advantage that all Raman signal are used for quantification. By using a color threshold, these images were converted into binary images with the aid of the graphic program ImageJ[150]. These binary images were then used to apply the “Analyze Particles” tool provided by ImageJ. The grain size was given by the software as a specific area (pixels). Because a common assumption is that the grain morphology is spherical, the particle radius (µm) was calculated from the area. Since there is no significant difference among the different particle parameters, we here use the radius to characterize the grain size.

To evaluate the activation energy of gehlenite formation, the isoconversional, model-free “time-to-a-given-fraction method” was used. For this purpose, the fraction of gehlenite as a function of time was examined. Especially with respect to the higher temperatures a significant amount of gehlenite was already formed during heating to the target temperature. The time *t(f)*, needed to reach the gehlenite fraction f = 0.02, 0.025, 0.04, 0.075, 0.1, 0.125, 0.15, and 0.175 within the temperature range between 803 and 880 ± 5°C was determined by linear interpolation between two consecutive data points. Within the temperature range between 880 and 971°C the time *t(f)*, to reach a gehlenite fraction f = 0.2, 0.225, 0.25, 0.275, and 0.31 was additionally be determined. With this selection, the extrapolation of the low-T experiments to longer times was avoided. Obvious fluctuations of the data due to technical problems were excluded and *t(f)* was determined by a linear interpolation between two more reliable data values that are indicated in Figure 4.8. A plot of ln t(f) against $1/T$ is linear if E_a is independent of T. A linear arrangement over the entire temperature range indicates that the activation energy remained constant during the nucleation and growth process.

3 Results

3.1 Expansion and shrinking of the green body during sintering

The relative expansion curve of four out of six experiments (T880, T931, T971, and T1020) was similar (Figure 4.4 A). During the first eight hours the relative expansion curve rose sharply, then flattened out and showed an asymptotic trend after 30 hours. During cooling to RT all samples shrunk. The sample fired at the lowest temperature (T803) showed no shrinkage or expansion at all during the dwell time of 48 hours. T843 is the only sample that shrunk with time (Figure 4.4) and in which the height of the last map at HT was (6 %) lower than that of the green body. At 880°C and after a dwell time of 45.5 hours the relative expansion was 8.5 %. Up to 971°C the relative expansion decreased with increasing firing temperature. At the highest firing temperature, the relative expansion was the highest with 8.7 %.

3.2 Phase evolution during sintering

The 24 Raman images recorded during the dwell time of about 48 hours and the additional RT images of the green body and the quenched sample for all six experiments are given in the Supplement (V.VII Figures S1-S6). The semi-quantitative mineral content was obtained from the matrices behind the unnormalized images of all 13 pure phases (end members) of the CLS fit (Figure 4.5).

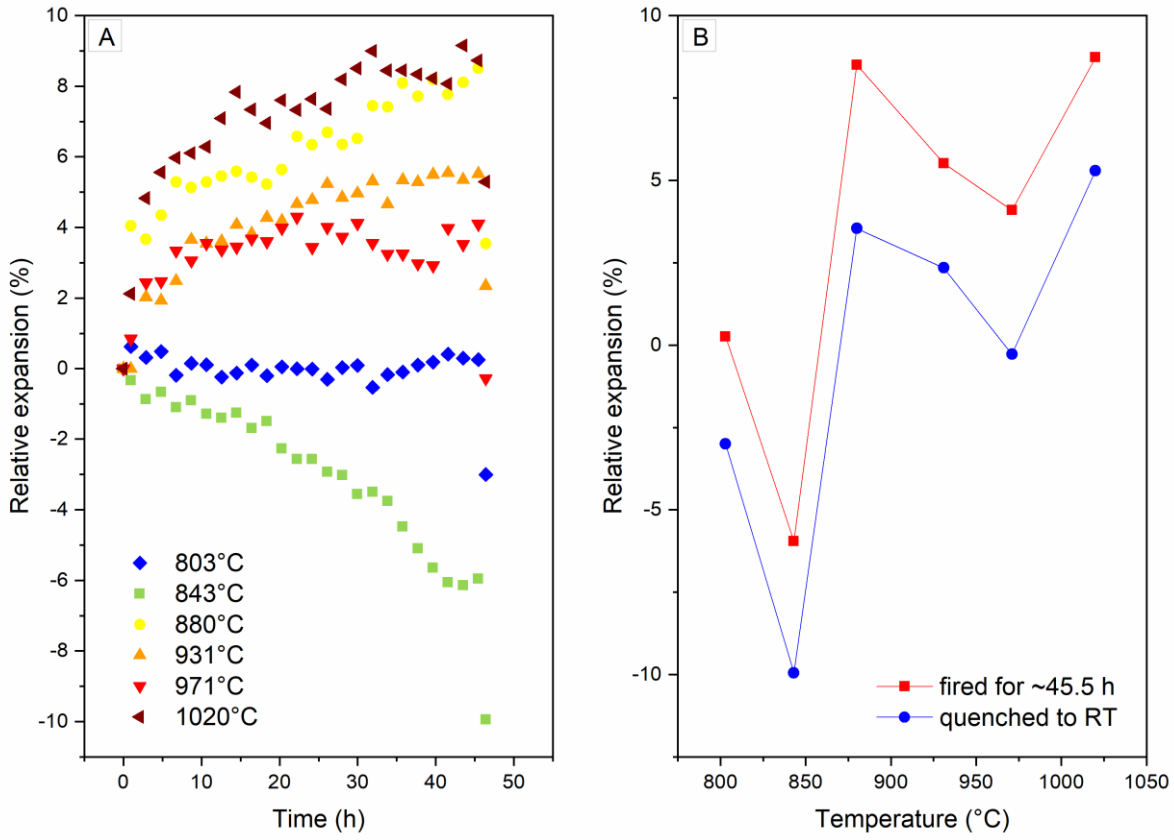

Figure 4.4: The relative expansion as a function of time at the six sintering temperatures (A). The error bars lie within the region of the data point symbols. The relative expansion as a function of the firing temperature of the last map at HT (starting time of the last image ~45.5 hours, red squares) and the sample quenched to RT (blue squares) (B).

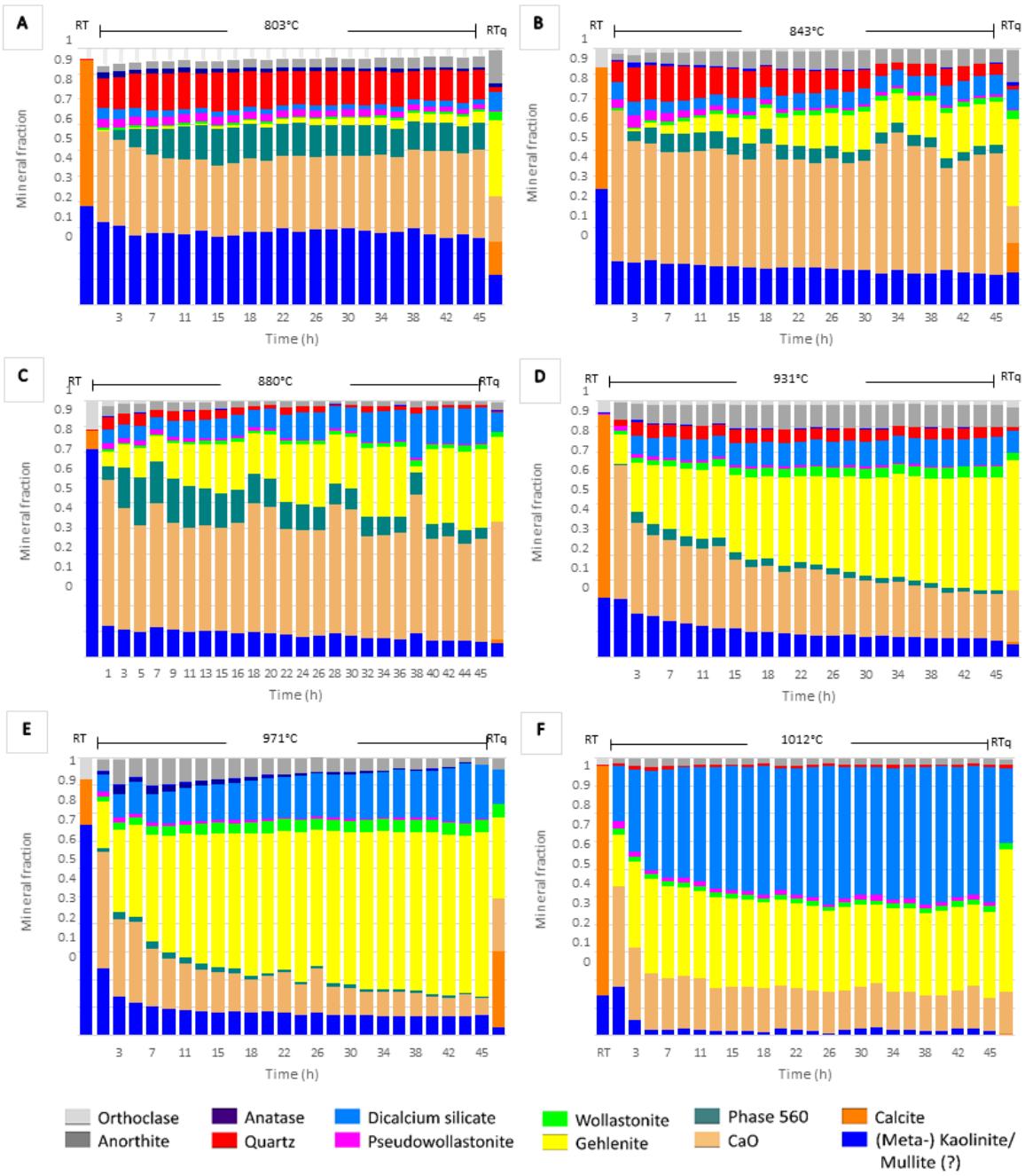

Figure 4.5: Semi-quantitative mineral content obtained by hyperspectral Raman imaging of a kaolinite-calcite mixture fired at six different temperatures for about 48 hours. The data were taken from the matrices behind the unnormalized CLS images of the single phases. RT=room temperature image of the green body. RT^q = image recorded after cooling the sample down to room temperature.

For more details see Figures V.VII S7 to S19 in which the respective content of each mineral phase of all six experiments was plotted against the dwell time. Some fluctuations in the phase content were due to technical reasons resulting from auto-focus problems during automated acquisition. This occurred especially in experiment T880 and is well documented in the false-color hyperspectral Raman images (Figures V.VII S1-S6). In the RT images of all experiments calcite and kaolinite were the major phases (Figure 4.5). Accessory phases of the kaolinite precursor material were orthoclase (in all experiments), anatase (Exp. T931), and quartz (Exp. T803-T931).

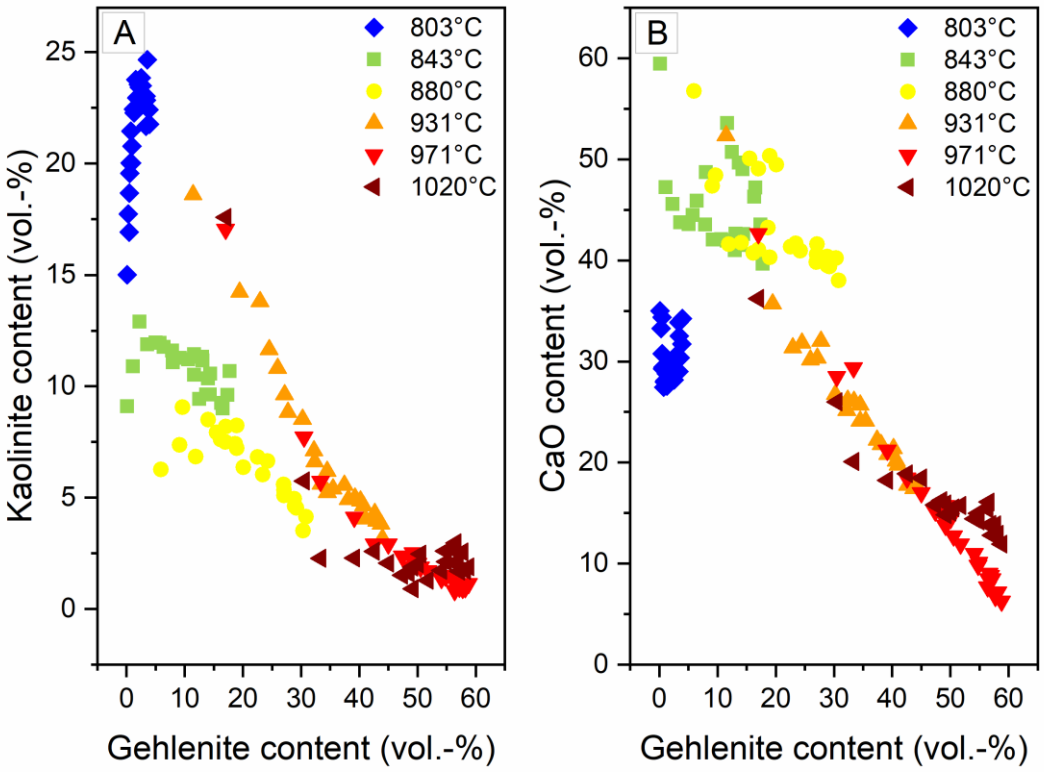

Figure 4.6: The contents of kaolinite (A) and CaO (B) as a function of the gehlenite content at the six firing temperatures.

During firing to the sintering temperature calcite was decomposed to CaO and CO_2 and kaolinite was dehydroxylated to metakaolinite. In all experiments new calcium (aluminum) silicates formed. These are mainly gehlenite, dicalcium silicate, wollastonite, and a still unknown phase that is characterized by a broad Raman band near 560 cm^{-1}. In general, the amount of these phases increased with time, whereas the amount of kaolinite and CaO decreased. Gehlenite was formed in all six experiments. In general, the gehlenite content increased with time. Up to 971°C the higher the sintering temperature, the higher the gehlenite content was. In T971 the amount of gehlenite was up to 60 vol.-% after a dwell time of 48 hours. In T1020 the gehlenite content increased only during the first six hours. Afterwards, it decreased slightly with time. Gehlenite was previously reported to crystallize from metakaolinite and calcium[8,155]. This is corroborated by the (partly linear) correlation between the fraction of kaolinite and CaO as a function of the gehlenite content at temperatures above 880°C (Figure 4.6). Especially for CaO this correlation was much less significant in the low temperature range up to 880°C.

Dicalcium silicate also increased as a function of time in experiment T843. In T1020 the increase of dicalcium silicate was the highest to about 49 vol.-% after 48 hours. The content of the unknown phase escalated in the beginning of the dwell time. After a maximum was reached, it decreased as a function of time. The higher the content of the unknown phase, the lower was the sintering temperature. It was not detected in the experiment with the highest sintering temperature of 1020°C. In general, the content of the unknown phase increased fast during the first hours and then slowly decreased again. The unknown phase disappeared during cooling and was not detected in any room temperature map. The anorthite content behaved very differently in the experiments. In T803 anorthite seemed to

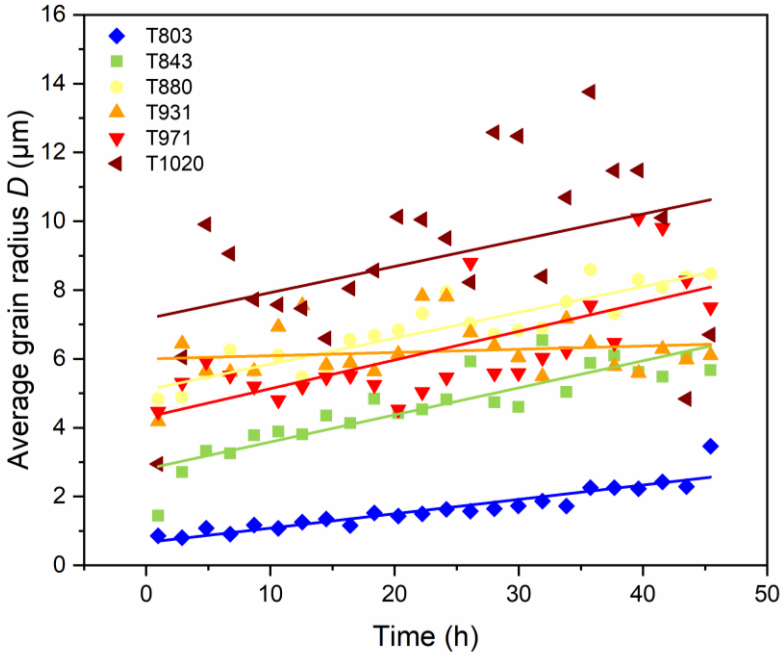

Figure 4.7: The average grain radius (µm) as a function of time for the six firing temperatures between 803 and 1020 ± 5°C.

increase linearly with time. In T843 and T931 the anorthite content increased with a maximum at a dwell time of 24 hours. Afterwards, it decreased slightly. In T931 the highest amount of anorthite had formed after a dwell time of 48 hours. In T880 and T1020 anorthite did not increase as a function of time. In T971 it increased during the first eight hours and then decreased. Wollastonite and pseudowollastonite were formed only in little quantities under 5 vol.-%. Up to a sintering temperature of 931°C the wollastonite content increased linearly with time. In T931°C there was the highest amount of wollastonite. Quartz, orthoclase, and anatase were accessory minerals within the kaolinite precursor material. Quartz occurred in different proportions up to 15 vol.-% in the experiments and orthoclase up to 8 vol.-%. In most experiments the content of both minerals remained the same or slightly decreased. Anatase occurred in little proportions under 2.5 vol.-% in all experiments. With time it seemed to decrease or remained stable during the dwell time. It must be considered that an increase of mineral A is always related to a decrease of a mineral B, due to the normalized representation.

3.3 Kinetics of gehlenite nucleation and growth

3.3.2 Gehlenite grain size distribution

The average grain size of gehlenite increased linearly with time (Figure 4.7). In general, the average grain size was larger, the higher the firing temperature. It is also noted that the higher the firing temperature, the higher the scatter of the data.

At low firing temperatures most of the gehlenite grains were small. The grains grew larger at higher temperatures (Figure 4.8 A). At 803°C all identified and counted grains were smaller than 5 µm and most of the grains were smaller than 1 µm in size. The grain size distribution was observed to be log normal with a mean grain radius D_{mean} of 1,57 µm (Figure 4.8 B). In experiment T880 and T931 the number of small grains smaller 3 µm was significantly lower than in experiment T803 and T843. Instead, more grains were between 5 and 15 µm in size. With increasing temperature, a second maximum occurred which shifted towards higher grain sizes with increasing temperature and the distribution of the grain size became rather bimodal (Fig. 4.8 A). The mean grain radius of gehlenite increased to

D_{mean}= 3,33 µm at 880°C. After that, the mean grain radius decreased again with increasing temperature. The D_{mean} was the highest at 1020°C (Figure 4.8 B).

3.3.1 Activation energy for gehlenite nucleation and growth

The activation energy E_a of the crystallization of gehlenite was determined by the isoconversional and model-free 'time-to-a-given-fraction'-method. For the temperature range of 803 to 880 ± 5°C the time needed to reach a certain gehlenite fraction *t(f)* were determined for fractions, *f*, between 0.02 and 0.175. For the high temperature range (880 - 971 ± 5°C) five further gehlenite fractions of up to 0.31 were selected and the time determined that was needed to reach that fraction (Figure 4.9). A plot of ln(*t(f)*) against 1/*T* is linear if E_a does not change with temperature (Figure 4.10). This applies to the upper temperature range above 880°C. However, for all small fractions of up to 0.175 the linear trend seems to be split up in two linear trends with a different slope. For these data both possibilities are plotted, i.e., one linear trend (light grey) and two linear trends with different slopes for the low (dark blue) and the high temperature range (dark red) (Figure 4.10). From the slopes of the ln(*t(f)*) vs. 1/*T* graphs, empirical activation energies, E_A, were calculated and plotted in Figure 4.11 as a

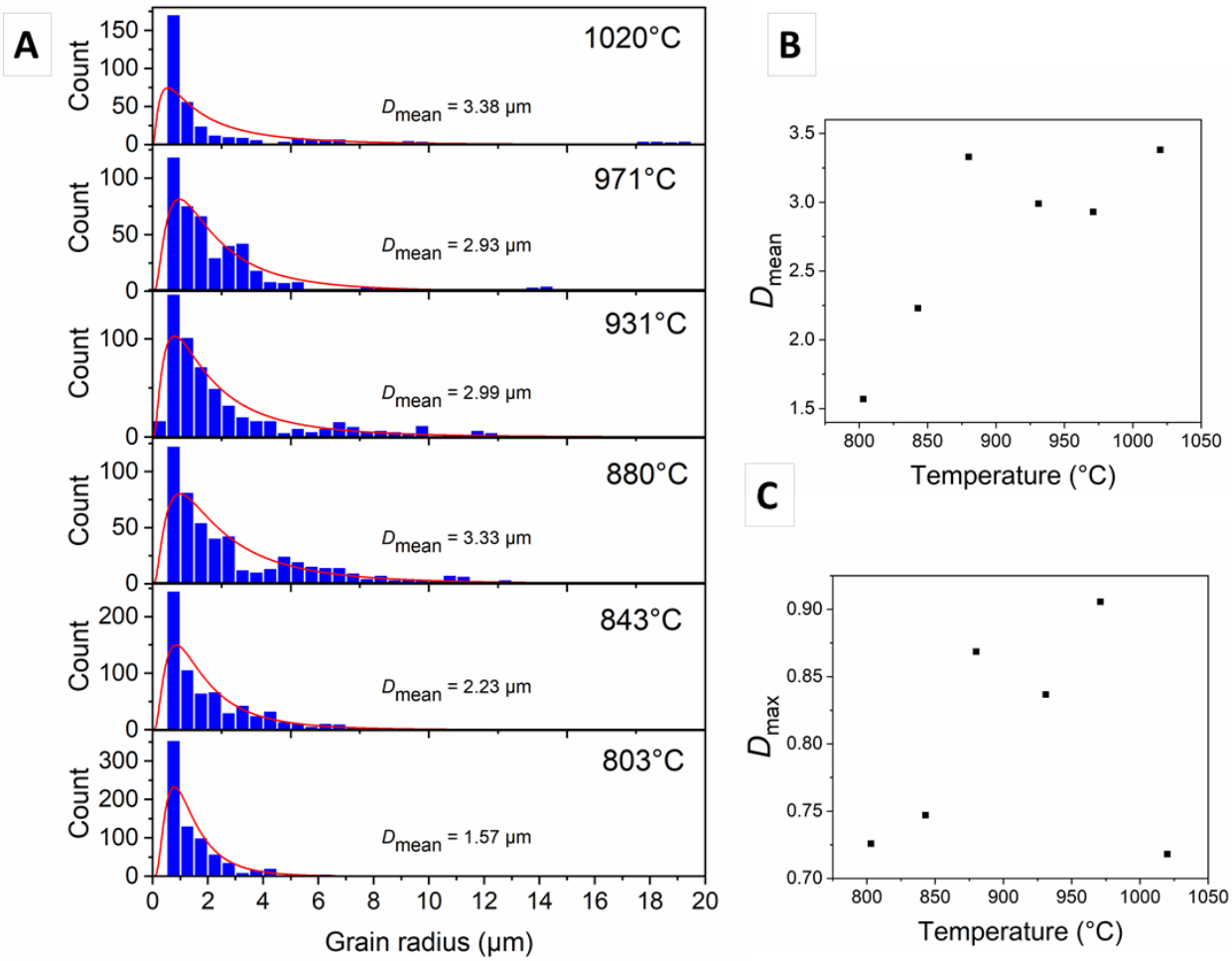

Figure 4.8: Grain size distribution of gehlenite along with the log normal fit for the six firing temperatures (A). D_{mean} *(B) and* D_{max} *(C) of the log normal grain size distribution as a function of the firing temperature.*

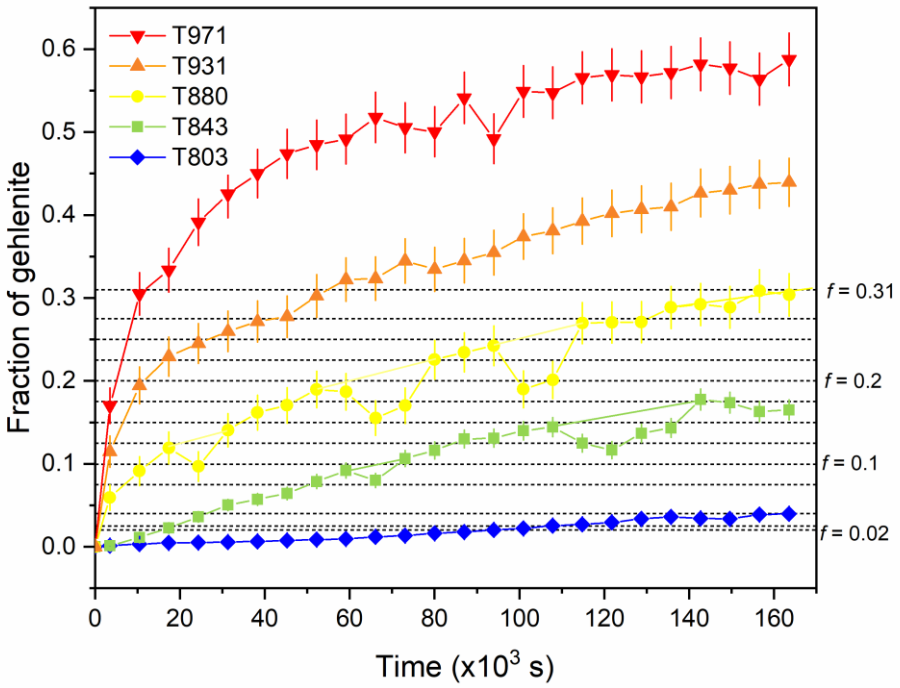

Figure 4.9: The fraction of gehlenite f_{Gh} crystallized during firing of a mixture of kaolinite and calcite as a function of time at five temperatures between 803 and 971°C. Obvious fluctuations of the data due to technical problems were equalized by doing a linear interpolation between two values.

function of *f*. The empirical activation energy was obtained from the slope(s) of Figure 4.10. Linear fits to all twelve ln(*t(f)*) values yielded an activation energy of 336 ± 11 kJ/mol. For the small fractions of $f_{0.025}$ to $f_{0.2}$ a division into two linear functions for a low temperature range of 803°C to 880 ± 5°C and a high temperature range of 880 to 971 ± 5°C yielded an activation energy of 107 ± 19 kJ/mol and 663 ± 31 kJ/mol, respectively.

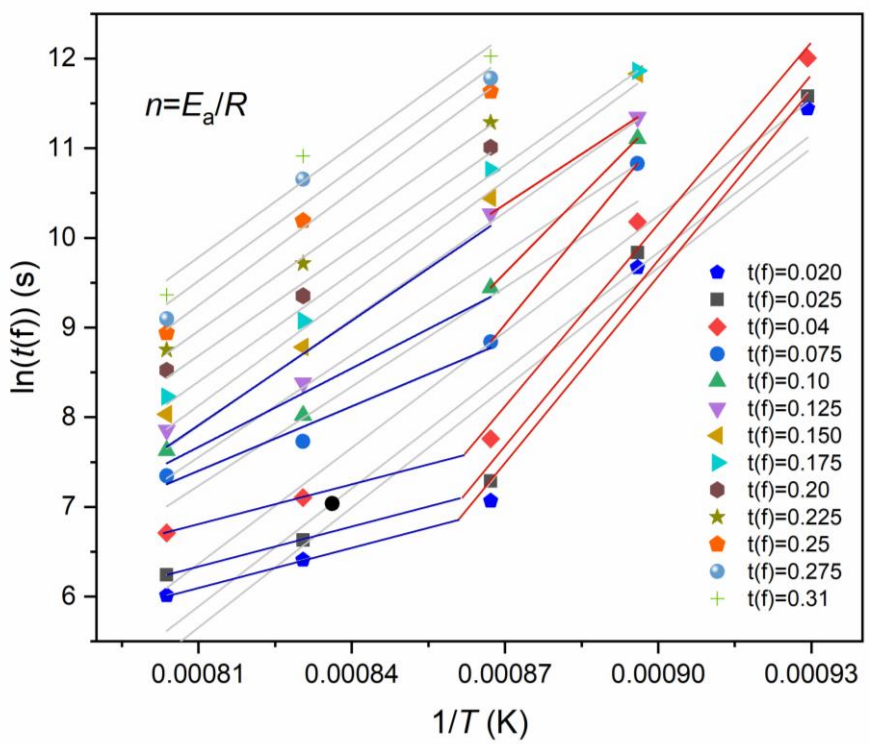

Figure 4.10: The logarithm of the time needed to reach a gehlenite fraction, t(f) *(s), for fractions between of 2 and 31 vol.% gehlenite, as a function of 1/*T *(K). Two different slopes for* f *= 0.020 to 0.2 indicates a change in the activation energy near 880°C. A linear step function was fitted to these data.*

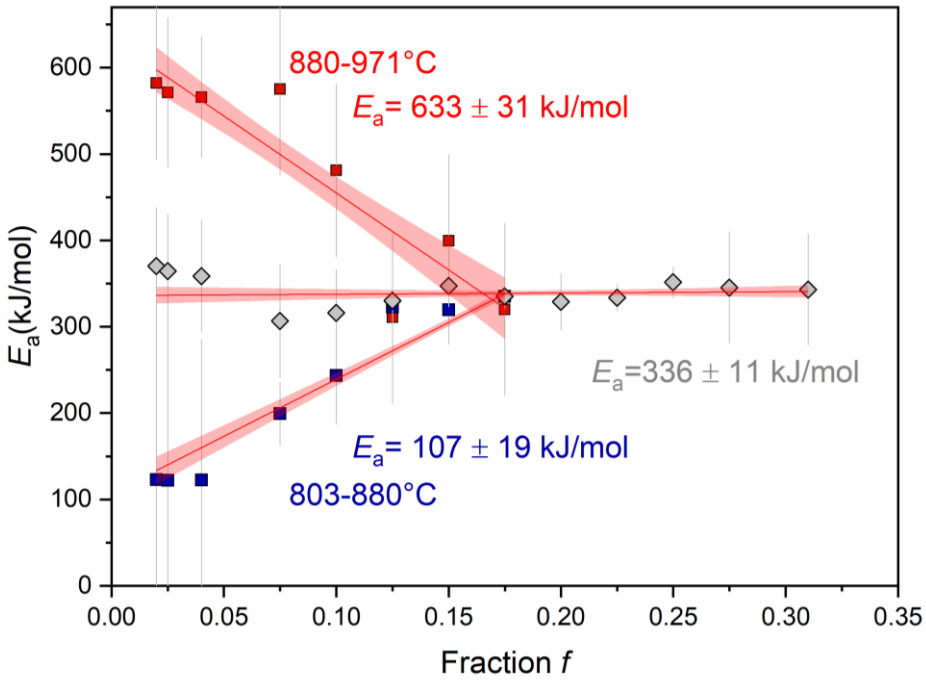

Figure 4.11: Empirical activation energies E_a*, obtained with the model free 'time-to-a-given-fraction' method, as a function of the gehlenite fraction* f*. A linear fit for all twelve values for* $\ln(t_f)$ *as a function of time (Figure 4.10) yielded an activation energy of 336 ± 11 kJ/mol. A fit of two linear functions in the Arrhenius diagram, shown in Figure 4.9, yielded two activation energies for different gehlenite fractions of 107 ± 19 kJ/mol for the low temperature range between 803 and 880 ± 5°C and 663 ± 31 kJ/mol for the high temperature range (880 to 971 ± 5°C).*

4 Discussion

In all six experiments the precursor material kaolinite lost its chemically bound water and metakaolinite was formed during heating from RT to the target temperature (e.g., Ref. 59). During heating calcite was decomposed to CaO and CO_2. Firing at 803 ± 5°C revealed only a slight change in the phase content. This was also reflected by an insignificant relative expansion during the dwell time of 48 hours (Figure 4.4) and only slight movement of the sample (e.g., the large area of 83% that is present in all 24 HT Raman images, Table 4.1). Ptáček and colleagues reported that the dehydroxylation of kaolinite to metakaolinite and the formation of lime from calcite are linked with a mass reduction of up to 7.0 ± 0.4 and 20.0 ± 0.6 wt.%, respectively[155]. Here this effect seemed to be superimposed by the thermal expansion. At 803 ± 5°C small amounts of gehlenite and dicalcium silicate were formed and their fraction linearly increased with time. Additionally, an unknown phase strongly increased during the first 15 hours and afterwards decreased linearly with time. Dvoáková and colleagues discovered that initial sintering and significant shrinkage of Ca-rich ceramic bodies occur above 850°C[159]. This is in good agreement with the observation that T843 was the only experiment in which the green body shrunk during sintering (Figure 4.4). It is also the only experiment in which the height of the last image at HT is lower (= 6%) than that of the original green body. Dvoáková and coworkers associated an observed significant volume increase with the crystallization of gehlenite and wollastonite. The samples fired above 880°C showed a relative expansion between 4 and 8.7 % and an increase of gehlenite and wollastonite, but the relative expansion does not correlate with the increase of the gehlenite and wollastonite fractions. This might be associated with densification processes that occurred at the same time. This was observed by Klosek-Wawrzyn and colleagues who reported a length reduction of the calcite bearing kaolin sample of about 1 % between 935 and 1000°C[160]. In all experiments above 843°C the relative expansion increased strongly during the first couple of hours and then the increase became less pronounced (Figure 4.4). This pattern fits to the formation of new calcium (alumo-)silicates. In all six experiments the height of the quenched sample was lower than at HT. The difference of up to 5 % was probably caused by the reduction of the molar volume of the minerals related to the decreasing temperature. Influences of the mineral reactions that occurred during cooling were also possible (Figure 4.5).

The main phase that was formed during firing of the kaolinite-calcite mixture was gehlenite. Up to 971°C the gehlenite content increased with time and increasing firing temperature (Figure 4.5), while at a firing temperature of 1020°C less gehlenite was detected. After a strong increase during the first six hours of firing, the gehlenite content decreased linearly with time (V.VII S10). This observation agrees with the study of Cultrone and colleagues in which gehlenite was found to appear at 800°C and to break down above 1000°C[53].

The semi-quantitative mineral content and the grain size did not behave similarly. In all experiments besides experiment T931 the grain size of gehlenite increased linearly with time (Figure 4.7). Only in experiment T803 the semi-quantitative gehlenite content also increased linearly with time. Above 880°C the data began to scatter which increased with increasing temperature. In the other experiments the semi-quantitative gehlenite content increased sharply during the first hours of firing and then increased at a slower rate. The grain size distribution was observed to be log normal (Figure 4.8 A). With increasing temperature, a second maximum occurred which shifted towards higher grain sizes with increasing temperature and the distribution of the grain size became bimodal (Fig. 4.8 A). This was also reflected by the increase of the mean grain radius of D_{mean} up to 880°C and a shift of

the maximum of the log normal function D_{max} to higher values (4.8 B and C). With further increase of the firing temperature this second population of medium sized grains decreased again. Small and medium sized grains partly coalesced and a new population of large grains occurred around 14 and 18 µm, respectively (Figure 4.8 A). Oswald ripening effects may also have occurred, a phenomenon which describes how surface tension causes small particles to dissolve and larger ones to grow[161].

Besides the change in the grain size distribution around 880°C, a change in the activation energy was observed in the same temperature range. For the low temperature range of 803°C to 880°C, an activation energy of 107 ± 19 kJ/mol was obtained. The low value indicates that the reaction is far from equilibrium. With increasing gehlenite content and in closer proximity to equilibrium the activation energy was higher. The activation energy of 663 ± 31 kJ/mol obtained for the temperature range between 880°C and 971°C is in good agreement with the published values ranging from 411 to 740 ±5 kJ/mol (Table 4.2). These data were all obtained from temperatures above 900°C, which explains that a change in the activation energy was never described before.

The kinetics of gehlenite formation seemed to be divided into two temperature stages, a low temperature stage up to 880°C and a high temperature stage between 880°C and 971°C. This is reflected by the change in the activation energy appearing at 880°C and the second maximum of medium sized grains at this temperature. The kinetics of the gehlenite crystallization in the low temperature range seemed to be influenced by the appearance of the unknown phase. A nearly lognormal correlation was observed between the fraction of the unknown phase and gehlenite for all five firing temperatures at which the unknown phase was observed. With increasing temperature, the maxima of the log normal correlation shifted to higher gehlenite contents.

At a specific ratio of the unknown phase and gehlenite (i.e., at a specific time) gehlenite seemed to form at the expense of the unknown phase. With increasing temperature this point, i.e, Gh_{max}, was shifted towards higher gehlenite contents. The time at which the unknown phase became unstable and broke down decreased with increasing temperature (Fig. 4.12).

Table 4.2: Overview of published kinetics of gehlenite formation along with the respective temperature range and a short description of materials and the method that was used to obtain the activation energy.

Temperature range (°C)	**E_a (kJ mol $^{-1}$)**	**Description**	**Reference**
~ 950-980	411 ± 5	Mixture of kaolinite and calcite, Kissinger method	2
~ 930-955	604	Mixture of kaolinite and calcite, Kissinger method	12
	722 ± 3	Crystallization kinetics of gehlenite glass microspheres from SiO_2, Al_2O_3 and $CaCO_3$, Avrami equation	3
~1200-1260	740	Devitrification of pure gehlenite glass, Avrami equation.	13
~1200-1300	645, 670, 680 and 800	Devitrification of pure and doped Eu, Th, Co, Eu gehlenite glass, Avrami equation	13
803-880 ± 5	107 ± 19	Mixture of kaolinite and calcite, 'Time-to-a-given-fraction'-method	This study
880-971 ± 5	663 ± 31	Mixture of kaolinite and calcite, 'Time-to-a-given-fraction'-method	This study
803-971 ± 5	336 ± 11*	Mixture of kaolinite and calcite 'Time-to-a-given-fraction'-method.	This study

*Averaged over the whole temperature range.

4.2 The formation of an unknown Ca aluminosilicate phase

The unknown phase was formed at temperatures between 803°C and 971°C. In general, the lower the sintering temperature was, the higher the content of the unknown phase. In contrast to all other minerals the amount of this phase increased during the first couple of hours and then decreased again with increasing dwell time (Figure S4.12). The unknown phase had one characteristic Raman band near 540 cm^{-1} (at 803°C) (Figure 4.13). The Raman spectra of none of the calcium alumina silicates match the spectra of the unknown phase (c.f., Table 2) even if it is considered that the bands of the unknown phase were most likely shifted to lower wavelengths due to the increased temperature. The identification of this phase with other analytical methods such as XRD or EBSD was not possible so far, because the unknown phase disappeared during cooling and did not remain (metastable) at RT.

The only mineral that matches to the spectrum of the unknown phase is cowlesite $Ca(Si_3Al_2)O_{10} \cdot 5\text{-}6H_2O$ which is a natural Ca-rich zeolite (Table S1). In cowlesite, rigid 2D zeolitic layers are loosely connected by water and Ca ions which is similar to minerals like vermiculite and explains why its properties are similar to the properties of clays[162]. Cowlesite does not belong to any of the zeolite structural groups and at RT has only two week Raman bands at 325 and 393 cm^{-1} and one intense characteristic band at 534 cm^{-1} [163](Table S1). Zeolites crystallize under hydrothermal conditions. Locally at the sample surface and for a limited amount of time, the conditions during the firing process may be similar to those of hydrothermal events. Most of the hydrated phases and carbonates in the clay

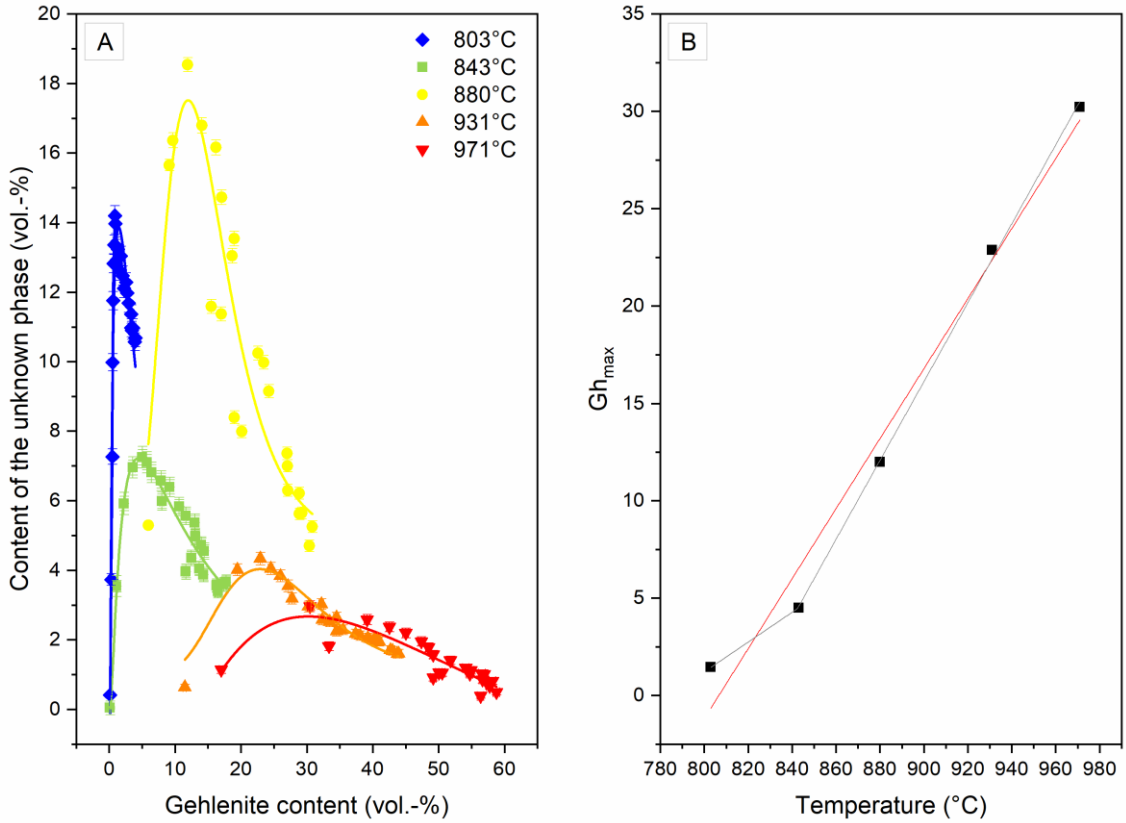

Figure 4.12: The content of the unknown phase as a function of the gehlenite content for all five temperatures at which the unknown phase occurred (A). The correlation between the contents of the unknown phase and gehlenite (Gh_{max}) appeared to be log normal. The function Gh_{max} correlates linearly with the firing temperature (B).

body decompose and recrystallize through different reaction paths during firing without necessarily attaining thermodynamic equilibrium con-sidering the coexistence of low- and high-temperature phases[164]. Previous work has shown that the temperature range for kaolinite dehydroxylation is between about 400 and 700°C[165–167]. Because the heating stage was not flushed with argon or nitrogen, the water from the kaolinite dehydroxylation was possibly not removed quickly from the sample surface, which locally may have led to hydrothermal-like conditions. Saraya and Sayad performed DSC (*differential scanning calorimetry)* analyses of natural cowlesite and obtained endothermic signals at 302°C and 520°C that the authors assigned to distortions of the framework structure of cowlesite due to the dehydration process[168]. Mugnaioli and colleagues performed an *in situ* powder XRD study and found a very sharp phase transition at 125°C, corresponding to the change from the hydrated to the dehydrated form. When they cooled the dehydrated cowlesite to RT, a peak shift and decay along with the growth of a broad diffraction peak was observed which suggests that this form is unstable and slowly rehydrate even at mild ambient humidity[162]. The hydrated form seems to be the more stable form, so possibly, the presence of water at the sample surface from the kaolinite dehydroxylation stabilized the hydrated cowlesite even at temperatures of up to 970°C. After a couple of hours, the fraction of the unknown phase decreased again with increasing dwell time. Most likely the water concentration at the sample surface had been decreased at this stage, because the water slowly escaped the sample and heating stage. We recall that the content of gehlenite and the unknown phase seemed to be closely associated, suggesting that gehlenite indeed also formed by the breakdown cowlesite (Figure 4.12) according to following reaction:

$$Ca_6(Si_{18}Al_{12})O_{30} \cdot 36\ H_2O \rightarrow 3\ Ca_2Al(AlSi)O_7 + 3\ Al_2O_3 + 15\ SiO_2 + 36\ H_2O$$

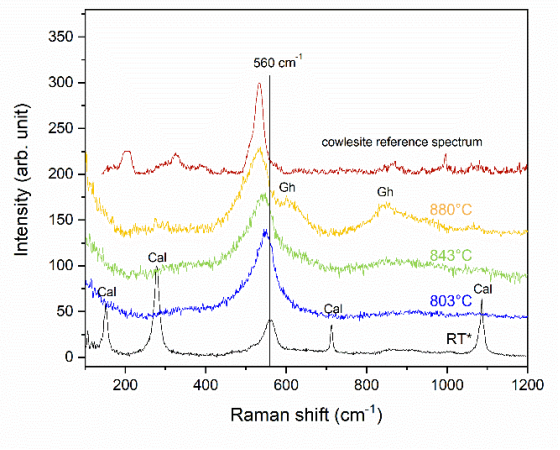

Figure 4.13: Average spectra (9 pixel) of the unknown phase at 803 ± 5°C, 843 ± 5°C, 880 ± 5°C, an average spectrum from a Raman image recorded from a quenched sample that was fired at 750°C (data from Ref.[170]), and a reference spectra of cowlesite[171].

In nature gehlenite dissolves under humid conditions in contact with soil solutions and transforms to zeolites[169]. Possibly, in this case the inverse reaction occurred.

4.4 Interpretation of Raman images and possible sources of quantification errors

There are two primary sources of errors that must be considered with respect to the interpretation of the semi-quantitative mineral content. The first source is the sampling area and the second the CLS fit of the Raman spectra. The sampling area analyzed in the experiments was only a 100 x 100 µm small area of a sample with a diameter of 3 mm. Despite a careful mixture of the precursor material a certain degree of heterogeneity could not be avoided. Thus, the quantity in which a mineral was formed could have been influenced by the availability of the educts. A small grain size of the precursor material[60] was chosen to minimize this source of error. However, the small sampling area also affects the internal reproducibility, because processes like shrinkage, densification, crack formation, and mineral formation can led to a misalignment of the sample area. To quantify the mineral content and grain size distribution over time, an area was selected which was – to a different degree – present in each image. For quantification, only this area was used at the expense of sampling size. However, due to

three-dimensional shrinking of the sample, a complete match could not be achieved, which likely explains the scatter in the gehlenite fraction *versus* time series (Figure 4.3).

The other source of errors is the CLS fit of the Raman spectra. One problem was that in the studied system phases occurred which are highly crystalline with sharp Raman bands like dicalcium silicate or gehlenite, but also phases with broad Raman signals like metakaolinite that has an amorphous structure or CaO that has only a second-order Raman spectrum. Due to a high background signal and a low signal-to-noise ratio in high-temperature Raman spectra, phases with broad bands like CaO can be overestimated in the CLS fit. Furthermore, it has to be considered that the Raman scattering cross section is specific for every mineral phase. This was partly considered, because the in-house reference spectra used for the CLS fitting were acquired under the same conditions and the intensities of the reference spectra were not normalized. However, the (relative) intensities can vary due to (i) the roughness of the sample surface or (ii) orientation effects. For more detail see Hauke et al. 2019[60]. Therefore, only a semi-quantitative mineral content can be estimated from the high-temperature Raman images. Nevertheless, within one experiment the semi-quantitative mineral content is usually well-reproducibly and could be used to determine kinetic parameters with a reasonable precision between about 3 and 20 %.

It is noteworthy that with confocal Raman spectroscopy the upper few micrometers of the sample surface are analyzed. After sintering, the obtained quantitative mineral content does not necessarily represent the mineral content of the whole sample body, because of (1) a temperature gradient of about 50°C within the ~2.7 mm height of the sample body[59] and (2) longer transport routes for gases such as CO_2 and H_2O[60]. One great difference between the sample surface and the center of the sample is that at the surface gas exchange with the environment is less limited by long-distance mass transport. This may have an impact on the observed reaction rates, which has to be considered when comparing reaction rates obtained from surface reaction with those obtained from bulk reactions that were studied by bulk techniques such as differential thermal analysis and *in situ* X-ray diffraction. However, if proven correct, the formation of an intermediate, hydrous calcium aluminosilicate suggests that at least locally the exchanged of water between samples surface and the furnace atmosphere was slow enough to stabilize a hydrous phase at high temperatures.

5 Conclusion

Gehlenite formed from a kaolinite-calcite mixture during isothermal firing for 48 hours at all six sintering temperatures between 803 and 1020°C. The gehlenite content increased with increasing firing temperature, while less gehlenite crystallized at temperatures above 971°C. The average grain size of gehlenite increased linearly with time. At a firing temperature of 803°C the grain size distribution can be well described by a lognormal function (Figure 4.7A). With increasing temperature, a second maximum of medium-sized grains crystallized which decreased again above 931°C. An estimation of the phase proportions only by a simple visual inspection of the images was difficult. Therefore, the semi-quantitative mineral fractions were obtained from the matrices of the CLS fit of the Raman images. At 971°C gehlenite reached about 60 vol.-% after firing the sample for 48 hours. The isoconversional and model-free 'time-to-a-given-fraction' method yielded an activation energy of 665 ± 31 kJ/mol for gehlenite nucleation and growth far from equilibrium within a temperature range between 880 und 971°C. These values agree well with the results of previous studies in which a similar temperature range was investigated (Table 4.3)[155,156]. The Raman images and plots of the contents of lime and kaolinite as a function of the gehlenite content show that gehlenite was formed by the

reaction between lime (formerly calcite) and metakaolinite (formerly kaolinite). For the low temperature range between 803 and 800°C a much lower activation energy of 107 ± 19 kJ/mol was obtained. The change in the activation energy and the grain size distribution correlated with the appearance of a previously undescribed Ca aluminosilicate phase. This unknown phase seems to be a metastable hydrous calcium alumosilicate, possibly cowlesite, which seems to be another precursor phase for the formation of gehlenite.

5 High-temperature Raman spectroscopy on ceramic phases in the CaO-SiO_2-Al_2O_3 system

5.1 Introduction

The position of the Raman modes and their widths are temperature-dependent due to thermal expansion and anharmonic effects. For most of the relevant ceramic phases the temperature-dependent mode behavior has already been investigated, as for the kaolinite-mullite reaction series[13], calcite and dolomite[43], and wollastonite[63]. However, the spectra are not available to the public and the experiments were performed with different instruments and different experimental conditions (for example larger temperature steps). Therefore, high-temperature Raman spectra of more than 20 relevant ceramic phases were recorded to

(a) identify individual high-temperature phases in mixed spectra,

(b) to improve the CLS fitting results,

(c) to estimate relative Raman cross sections to more accurately determine the relative phase proportions from a mixed Raman spectrum, and

(d) to use the dependence of band positions on temperature as a local mineral thermometer.

A complete list of all experiments that were carried out within the framework of this thesis, including the single phase experiments, is given in Table V.V.II.

5.2 Methods

The experiments were performed either with single crystals or flat cylinders of 3 mm Ø and >1mm height of the powdered sample material. The flatter the sample, the lower the deviation of the set temperature to the real temperature at the sample surface, caused by the temperature gradient within the heating stage. The samples were fired with a heating rate of 10°C/min in 10°C steps to the respective maximum temperature of up to 1400°C (for more details see table V.VII). The spectra covered a spectral range between 100 and 1720 cm^{-1}. For minerals like CaO and kaolinite, in which cases OH or H_2O bands were expected, a spectral range of 100-4000 cm^{-1} was investigated. A Raman spectrum with a total acquisition time of 100 s was recorded for each spectral range. At each temperature step, depth profiles were acquired with the auto-focus function after an equilibration time of 300 s to obtain an optimal signal-to-noise ratio and a measure of reaction- and temperature-related shrinking or expansion effects. For an optimal comparison the experimental setup was the same for all mineral phases (Table V.VII). The raw data were treated as described in detail in Chapter 3 “In Situ Hyperspectral Raman Imaging: A New Method to Investigate Sintering Processes of Ceramic Material at High-temperature” and further summarized in Chapter 8.1.2 (Data reduction). Some of the single-phase experiments already included reactions like decarbonation processes, dehydroxylation, or polymorphic phase transitions. The most striking findings are briefly outlined in the following.

5.3 Results and Discussion

5.3.1 The kaolinite-mullite reaction series

Kaolinite is one of the most important natural ceramic raw material with hydro-aluminosilicate composition and platy micro-crystals about 2 µm in size[13]. During ceramic firing three thermal phases are reported to be stable at different temperatures as there are: metakaolinite, a spinel-type phase, and mullite[13]. Due to the importance for ceramic industry the kaolinite-mullite reaction series was subject of many studies[13,165,172–175].

To investigate the dehydroxylation, a kaolinite powder (more details in Chapter 3[60]), was fired with a heating rate of 10°C/min to 600°C with

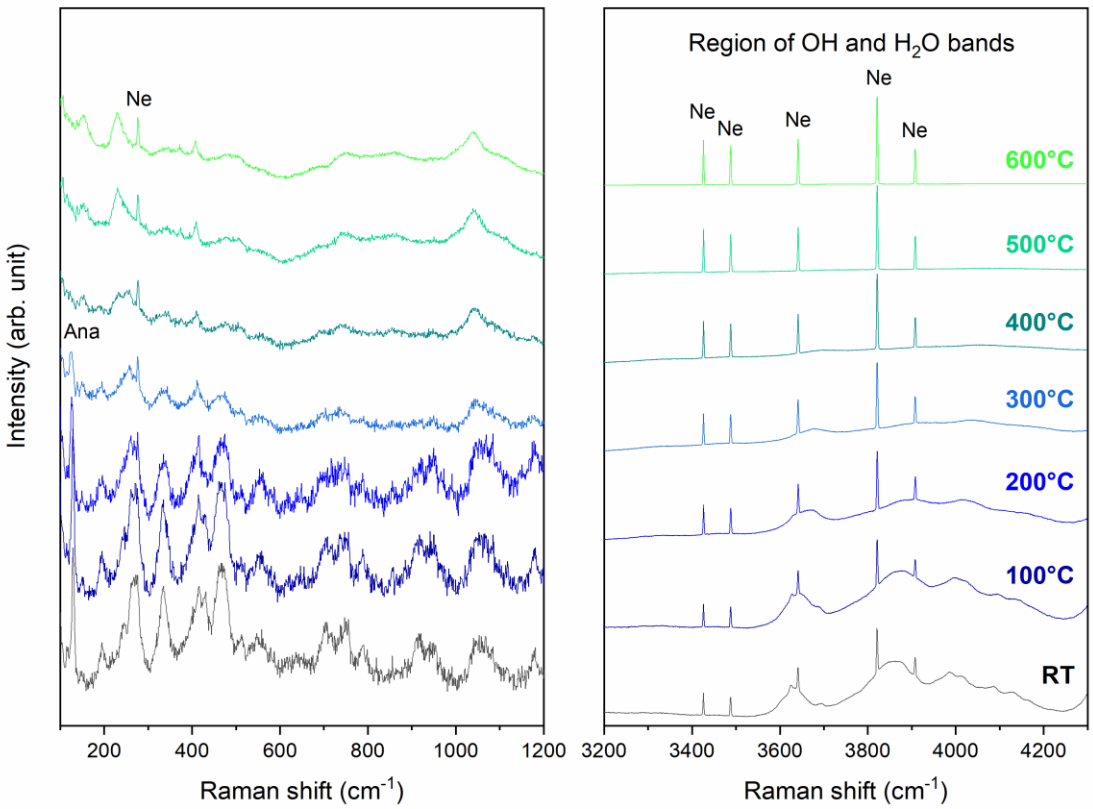

Figure 5.1: Heating study (experiment 1-8-4a) of pure kaolinite. The sample was fired up to 600°C in 100°C-steps. The Raman spectrum of kaolinite contained the sharp Ne lines that are used as an internal standard and additional bands of anatase (Ana). The spectra are baseline-corrected (2nd order polynomial).

temperature steps of 100°C (Exp. 1-8-4a). In addition to the usual spectral range of 100 to 1200 cm^{-1}, a second spectrum between 3200 and 4200 cm^{-1} was recorded at each temperature step to follow the development of the H_2O bands. The dehydroxylation of kaolinite was completed at 500°C at the sample surface, which could be seen by the complete disappearance of the H_2O bands between 3600 and 4200 cm^{-1} (Figure 5.1). Note that Raman spectroscopy probes the sample surface, where diffusion and transport limitations of water are less important, and thus the direct kinetics of the structural breakdown.

In general, the fundamental Raman bands of disordered, powdered kaolinite are not easy to detect with a significant signal-to-noise ratio due to weak Raman bands and severe fluorescence emission when using a green laser excitation[175]. The same is valid for metakaolinite which exhibits only weak bands near 812 cm^{-1} and 995 cm^{-1} [13]. In the spectrum of kaolinite additional bands of anatase (An) and millerite (phase 240) occurred that were accessory minerals of the kaolinite powder (Figure 5.1). According to Sperinck and colleagues[176] the dehydroxylation follows the reaction:

$$\underset{Kaolinite}{Al_4Si_4O_{10}(OH)_8} \rightarrow \underset{Metakaolinite}{2Al_2Si_2O_7} + 4H_2O\uparrow$$

In general, the dehydroxylation of clay minerals occurs at various temperatures depending on the specific mineral. In literature a wide temperature range for dehydroxylation can be found. The stated temperatures all lie between 450 and 900°C[13,53,177,178]. This is not surprising, as the decomposition temperature is affected by many parameters such as particle size, shape and morphology, defect concentration,

accessory minerals, heating rate, pressure, and partial water vapor[155,177,179–182]. Dehydroxylation causes a collapse and transformation of the crystal structure due to the release of water and subsequently to the formation of meta-kaolinite[181]. The dehydroxylation of kaolinite causes a mass loss between about 11 and 14 wt.-%[183,184].

Dehydroxylation could be followed by the disappearance of kaolinite bands at 245, 336, 431, 467, 746, 792 and 916 cm^{-1} and the bands that are related to the OH-groups between 3200 and 4200 cm^{-1} (Figure 5.1). The Raman bands of kaolinite became broader with increasing temperature and some bands, e.g., those near 457 cm^{-1}, disappeared. Distinct Raman bands of metakaolinite could not be detected in the Raman spectra of this study.

In a second heating study, the sample was fired at temperatures between 600 and 1400 °C in 50°C steps (Figure 5.2). Although the firing temperatures significantly exceeded the temperature for complete dehydroxylation of kaolinite proposed in previous studies, again distinct Raman bands that could be assigned to metakaolinite could not be detected. Shoval and colleagues assigned broad bands at 812 cm^{-1} and 995 cm^{-1} to metakaolinite[13], which, however, were not detected in this study. However, between about 250 and 900°C a new Raman band appeared near 469 cm^{-1}. It is thus conceivable that this band can be assigned to metakaolinite.

According to previous studies firing of kaolinite to higher temperatures results in the transformation of metakaolinite into a defect spinel-type phase[180,185] that is also described as γ-Al_2O_3 or Al-Si-spinel[185]. However, the existence of such a spinel phase is still highly debated. The spinel is reported to form according to the reaction[155]:

$$\underset{metakaolinite}{2\,AL_2Si_2O_7} \rightarrow \underset{Al-Si-spinel}{Al_4Si_3O_{12}} + \underset{silica}{SiO_2}$$

Shoval and colleagues assigned a broad band at 803 cm^{-1} to spinel and found bands of amorphous silica at 455, 487, and 620 cm^{-1} in Raman spectra recorded between 940 and 1000°C[13]. However, neither this Raman band nor any other band that could be assigned to a spinel-type phase or amorphous silica were detected.

It has been suggested that at temperatures the spinel transforms into mullite and silica according to following reaction[180]:

$$\underset{Al-Si-spinel}{3Al_4Si_3O_{12}} \rightarrow \underset{mullite}{2Al_6Si_2O_{13}} + \underset{silica}{5SiO_2}$$

However, like the dehydroxylation temperature of kaolinite, an exact formation temperature of mullite has also not yet been clearly defined. The proposed temperatures of previous studies vary between 950 and 1150°C[13,177,185–187]. Shoval and colleagues identified mullite bands at 304, 342, 408, 476, 607, 724, 777, 882, 965, 1023, 1082, 1136 and 1773 cm^{-1}. Some of these bands were also detected in the heating study (Exp. 1-8-3) after cooling the sample to RT (Figure 5.2). However, not all Raman bands reported in the literature were detected, which most likely reflects the

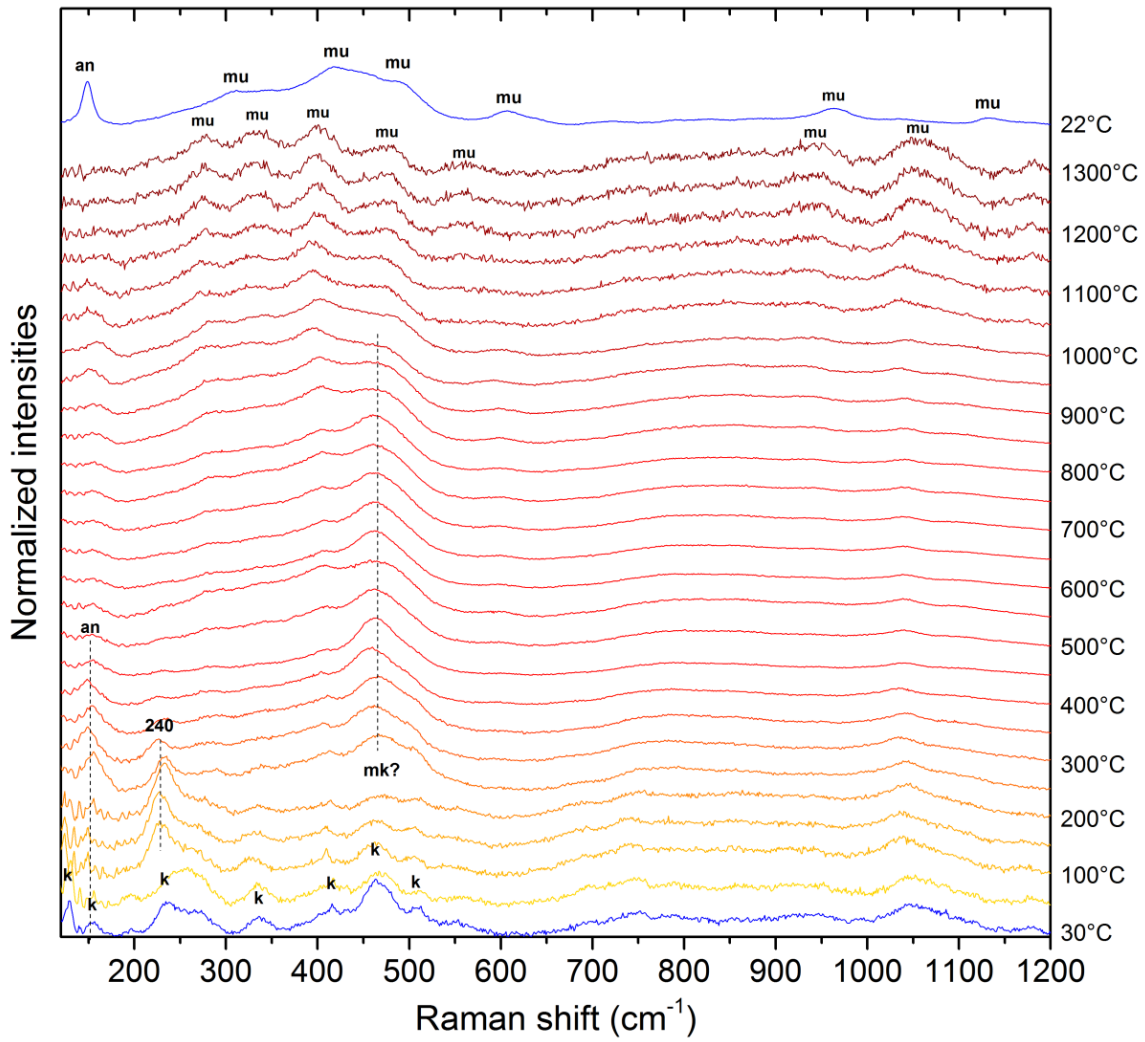

Figure 5.2: Heating of pure kaolinite powder (Exp. 1-8-3). Kaolinite was fired to 1300°C and after each 50°C-step a Raman spectrum was recorded. Abbreviations: an: anatase; k: kaolinite; mk: metakaolinite; 240: phase 240; mu: mullite[170].

fact that the structure and Si-Al ratio of mullite dramatically affects the Raman spectrum[188].

Neither an Al-Si spinel phase nor mullite, which are assumed to form from metakaolinite at temperatures greater than 950°C[9,189], were detected in the heating ramp experiments or isothermal experiments. Therefore, there is no (color-) distinction between kaolinite and its high-temperature forms in this study. Above 650°C the amount of the CLS fit which corresponds to the reference spectra of the kaolinite-mullite series is ascribed to metakaolinite.

In future, however, the investigation of an area instead a single-point in combination with larger acquisition times of a pure kaolinite sample could reveal more information about the structure of metakaolinite and the existence or non-existence of an Al-Si spinel phase.

5.3.2 The decarbonation of calcite

The occurrence or non-occurrence of certain mineral phases and their relative proportions are often used, for instance, to determine the firing temperature of ancient ceramics or to estimate the formation temperature of natural rocks[69]. As an example, Tschegg and colleagues[70] could not solve the question whether large sparitic carbonate inclusions observed in Cypriot Bronze-age plain white ceramics represent incompletely decomposed or secondary calcites that were formed by a

recarbonation process after firing. It has been suggested that under ambient conditions calcite may crystallize from non-reacted lime[71,72]. It is assumed that during this process, the hygroscopic lime may picks up moisture from the air, forming portlandite, $Ca(OH)_2$. The portlandite then may slowly reacts with atmospheric CO_2 to calcite. This hypothesis can be tested using the advantages of *in situ* and real-time hyperspectral Raman imaging. In particular, since portlandite is a good Raman scatterer, its Raman bands can easily be detected, including its sharp and intense Raman ν_s(OH) band near 3620 cm^{-1} [73]

Calcite has five characteristic Raman bands at 157, 278, 715, 1088, and 1361cm^{-1} [190]. In experiment 1-1-5 calcite was fired to 1100°C (Table 8.5). With increasing temperature, the Raman bands shifted to lower wavenumbers and became broader (Figure 5.3). The decarbonation of calcite to CaO (lime) and CO_2 took place between 700 and 950°C, which can also be monitored by the shrinkage of the sample. Above 813°C, calcite at the sample surface was fully decomposed to CaO. Lime crystallizes in the halite structure and thus does not give a first-order Raman spectrum[73]. However, the broad second-order bands of CaO (Figure 5.3, inset) can be used for identification and quantification. After cooling the sample to RT, the broad Raman bands of CaO had completely disappeared, because calcite formed by the reaction of lime with the CO_2 that was trapped in the heating stage. A reaction of unreacted lime and moisture from the air to portlandite, as reported by Shoval and colleagues[72], could not be observed.

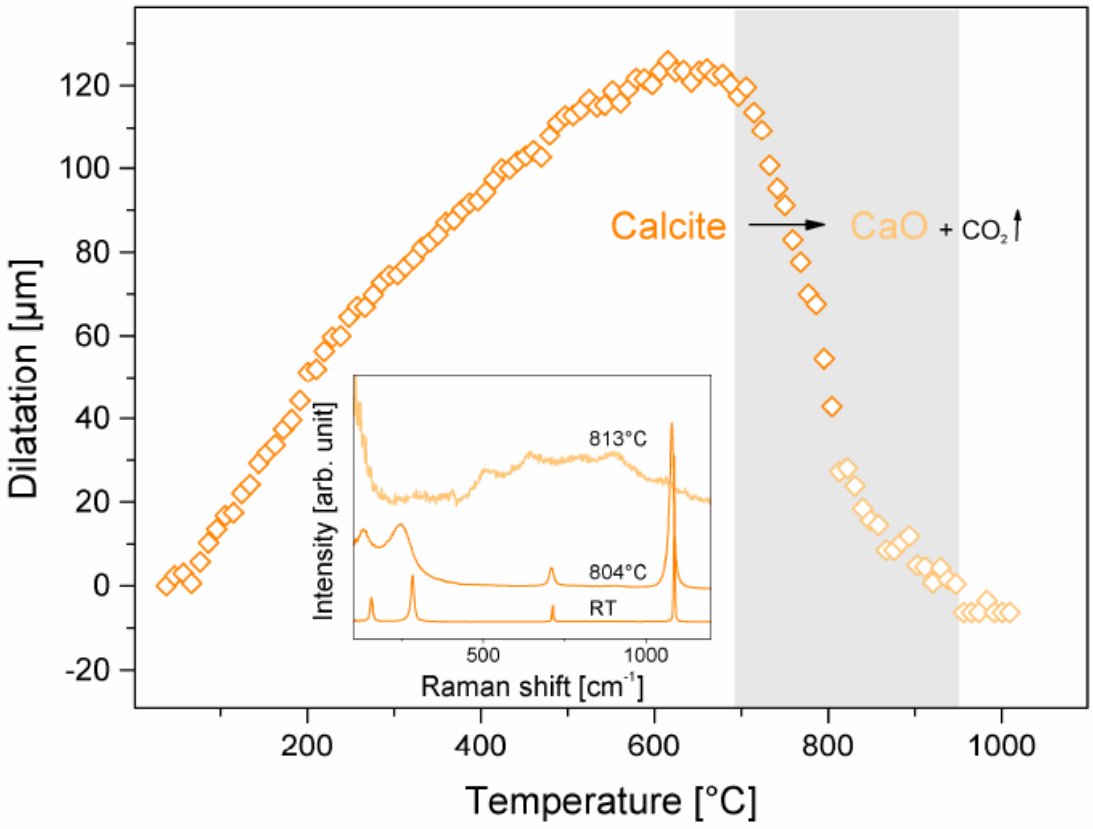

Figure 5.3: Dilatation of a pellet composed of calcite powder as a function of temperature. The dilatation was measured during the automated measurements by depth profiling. The dramatic shrinkage above 740°C is due to the decarbonation of calcite. The decarbonation took place between 700 and 950°C, which can be followed by the shrinkage of the sample. At 804°C the calcite bands broadened and were shifted to lower wavenumbers (inset). Above 813°C calcite at the sample surface was fully decomposed to CaO (lime) which only shows a second order Raman spectrum. It is important to note, that the Raman spectra were recorded at the sample surface[60].

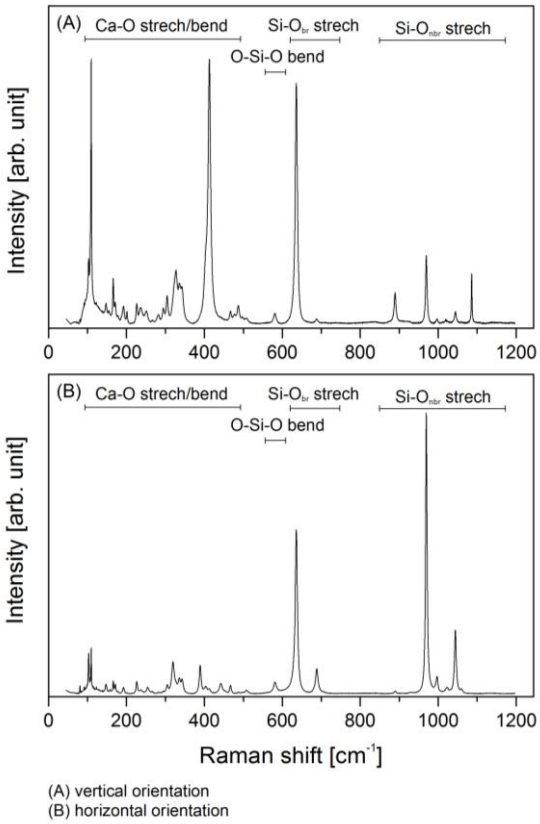

Figure 5.4: Unpolarized Raman spectra of natural wollastonite at RT in vertical (A) and horizontal (B) orientation in respect to the c-axis.

Therefore, the direct reaction of lime with CO_2 to calcite seems to be the preferred reaction when CO_2 is present.

5.3.3 Polymorphism of monocalcium silicate

Wollastonite ($CaSiO_3$) is an important mineral in ceramic and cement industries with industrial importance worldwide. Favorable properties such as low shrinkage, good mechanical strength, lack of volatile constituents, body permeability, good fluxing characteristics, whiteness, and acicular shape render it useful in several ceramic materials and for other applications[63]. The natural occurrence of wollastonite is subjected to high temperature and pressure and sometimes related to the presence of silica-bearing fluids as observed in metasomatic and metamorphic rocks such as, for instance, skarns.

Under ambient conditions the 1T [polytype notation wollastonite-IA] (P-1) is the stable form[18]. Wollastonite has three prominent Raman bands (in horizontal orientation in respect to the c-axis) at 636, 968, and 1046 cm^{-1} (Figures 5.4 and 5.5). At 1125°C the common triclinic wollastonite transforms to pseudowollastonite (triclinic/ pseudo monoclinic)[191]. Swamy and Dubrovinsky reported subtle discontinuities of the frequency, width, and intensity of Ca−O stretching and Si−O bending modes of wollastonite in the temperature range between 677 and 707°C with no corresponding changes in the temperature dependencies of the lattice parameters[18].

Currently, it is not fully clear whether these discontinuities reflect (a) a minor displacive transformation, (b) premonitory behavior, leading to a first-order phase transition at 722 ± 10°C which is indicated by the results of drop colorimetric measurements[68], or (c) ordering of polytypic stacking faults, the latter of which is the preferred explanation by Swamy and Dubrovinsky[18].

In general, the Raman bands of wollastonite shifted to lower wavenumbers with increasing temperature. The bands became broader and their intensities decreased (Figure 5.5). Below 600°C the Raman band near 581 cm^{-1} (Figure 5.6) linearly shifts to lower wavenumbers with increasing temperature. Between 600 and wavenumbers before decreasing again to lower wavenumbers with a steeper slope. At 750°C, however, the band shifted to higher wavenumbers.

This shift to higher wavenumbers may suggest premonitory behavior leading to the transition, which was proposed to take place at 720°C[63]. At 1130°C a dramatic shift of around 10 wavenumbers occurred, which can be related to the transition of wollastonite to pseudowollastonite (Figure 5.6). The Raman band near 689 cm^{-1} also shifted to lower wavenumbers with increasing temperature. At 720°C, a small kink occurred. The band disappeared at 1130°C due to the wollastonite-pseudowollastonite phase transition. The sharp disappearance of this band at the published transition temperature of 1125°C

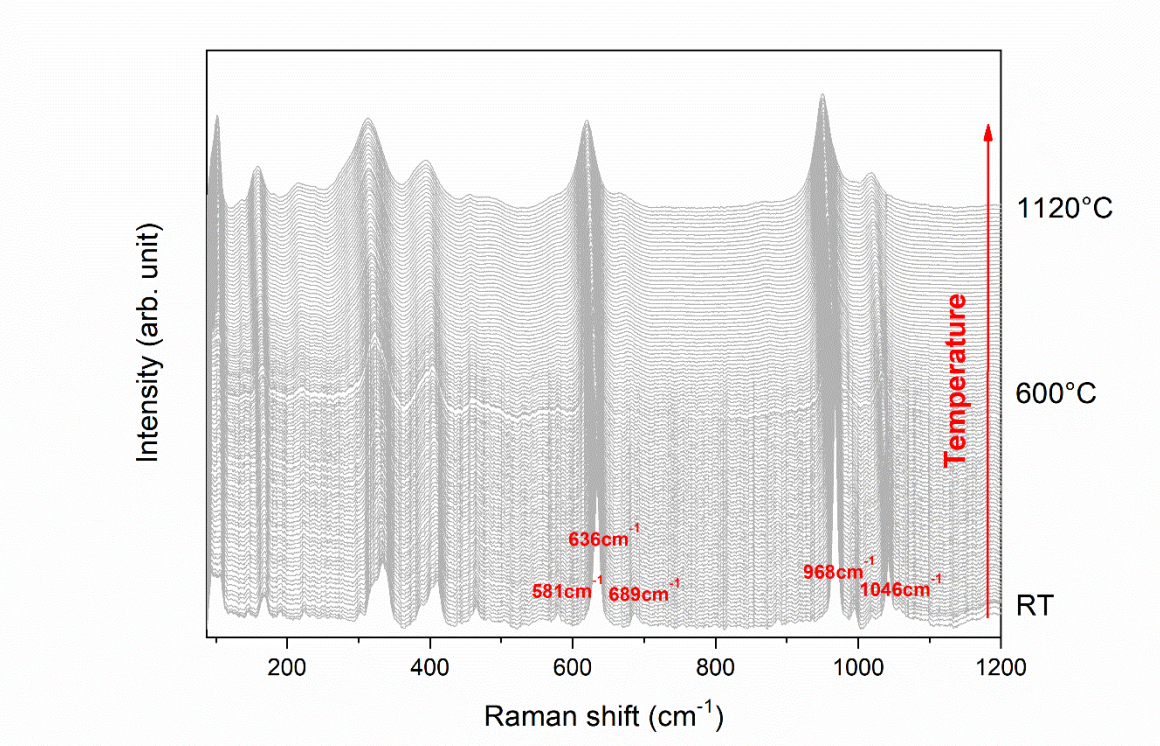

Figure 5.5: Heating study of wollastonite from RT to 1200°C (Exp. 1-3-1). Here, only the Raman spectra up to 1120°C are shown. Raman spectra were recorded every 10°C and were baseline corrected. With increasing temperature, the Raman bands shifted to lower wavenumbers and broaden.

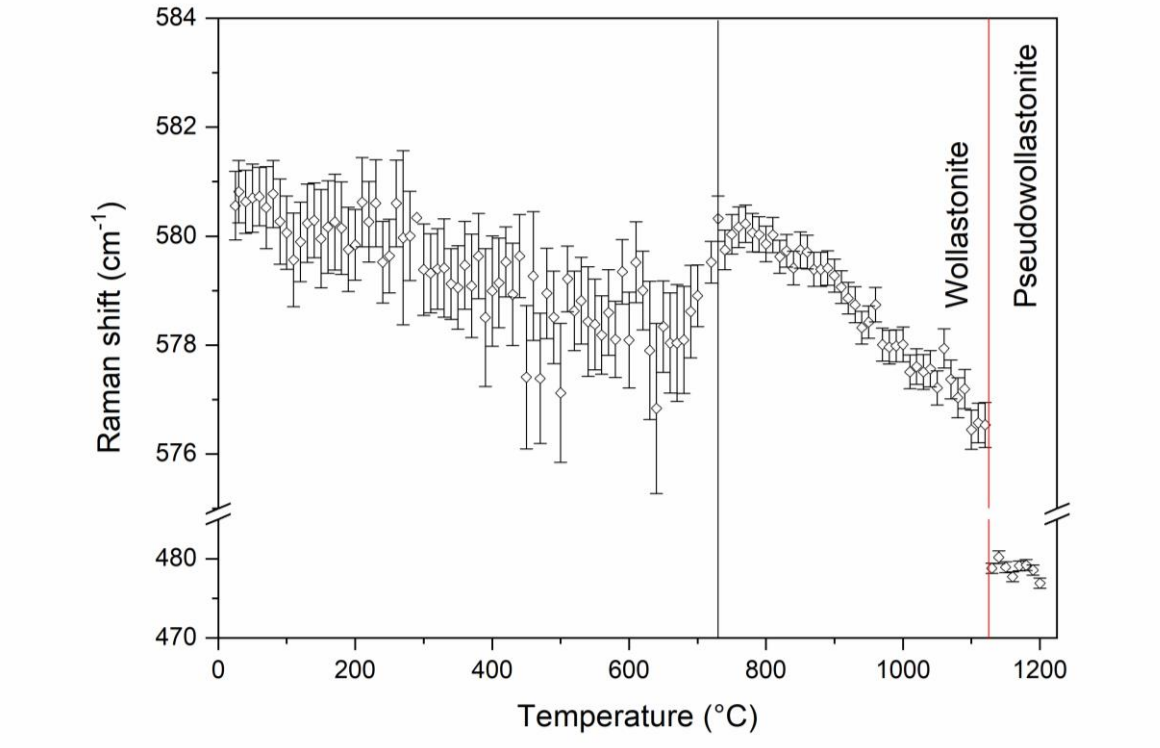

Figure 5.6: The Raman shift of the band near 581 cm-1 as a function of temperature (Exp. 1-3-9). Around the first-order phase transition (720°C marked by a black line) a shift to higher wavenumbers occurred. At 1130°C a shift of around 10 wavenumbers occurred due to the transition of wollastonite into pseudowollastonite.

demonstrates a very good accuracy of the temperature in the heating stage.

Swamy and colleagues proposed that the relatively smooth temperature dependencies of the Si−O−Si and O−Si−O stretching modes (those >500 cm^{-1}) and more dramatic temperature variations in the Ca−O stretching and Si−O bending modes (those in the region below ∼500 cm^{-1}) can be related to structural changes in response to heating that occur mainly in the CaO_6 polyhedra, affecting the Si−O−Si angles, but only little the Si−O bond lengths[63]. However, the high-precision data of this study revealed that also the Si-O-Si and O-Si-O stretching modes show dramatic temperature variations around 720°C (Figure 5.6 and 5.7).

5.3 Summary and conclusion

Single-phase experiments of more than 20 mineral phases were performed to identify individual high-temperature phases in mixed spectra and to improve the CLS fitting results which are the basis for image generation. Beyond that, each heating study reveals new insights about, for instance, dehydroxilation processes, decarbonation processes, or phase transitions. The high precision of the measurements allowed studying smallest changes of the mode frequencies, even of low-intensity vibrations such as those associated with the wollastonite bands near 581 and 689 cm^{-1}. Finally, it is noted that a detailed investigation of the Raman spectra of all single-phase experiments is planned for future work but was far beyond the objectives of this thesis.

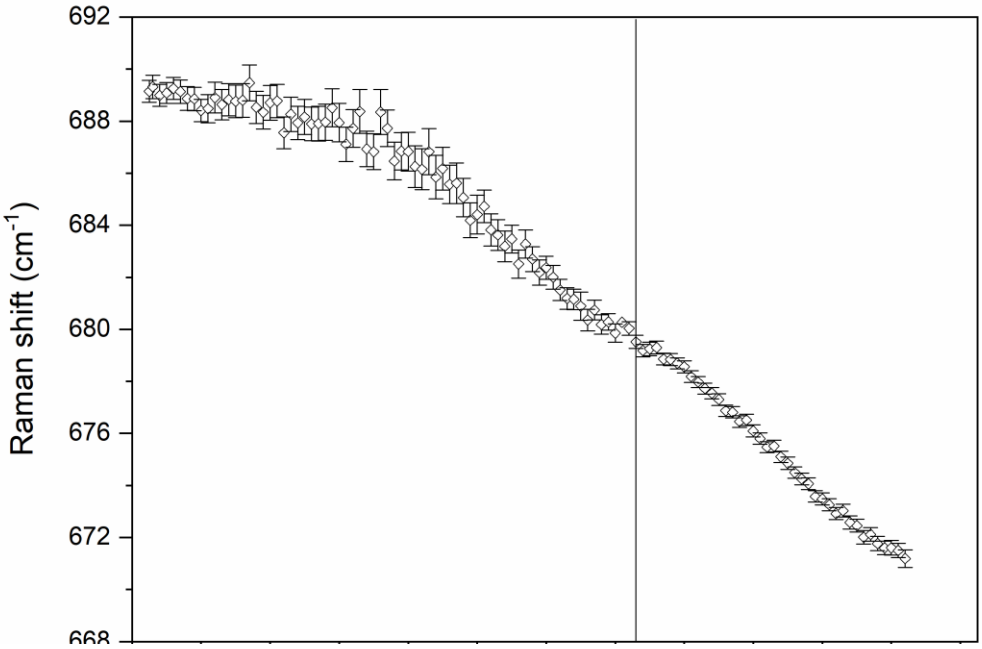

Figure 5.7: The Raman band at 689 cm^{-1} shifted to lower wavenumbers with increasing temperature (Exp. 1-3-9). At 720°C a small but significant decrease in the wavenumbers occurred.

6 Calcite decomposition and recrystallization studied by *in situ* Raman imaging

6.1 Introduction

The thermal decomposition of calcium carbonate is an important process in several geologic settings and technological implications. In nature the decomposition of calcite occurs during pyrometamorphism, high-grade metamorphism and at subduction zones[192]. The thermal decomposition of calcite to burnt lime or quicklime (CaO), commonly called calcining or calcination, has been the subject of extensive research over the last 100 years, because of its use in many technical applications (e.g., for construction materials such as concrete, motar, and plaster and for flue-gas desulfurization and the desulfurization of iron melts)[48,192–195]. The accurate control of thermal decomposition of calcium carbonate is necessary to achieve a high-quality product possessing all required properties. Moreover, the decarbonation temperature is an important temperature marker of ancient ceramics.

6.2 Materials and Methods

Heating experiments were carried out with powdered calcite precursor material, obtained from Alfa Aesar, that was dried at 100°C for 24 h. Details regarding the level of purity and the particle size are given elsewhere[60]. For each green body 4.3 g of the sample material was pressed with 0.01 MPa into cylinders of 3 x ~2.7 mm^2 to obtained flat surfaces for high-quality Raman images.

After selecting a representative area of the sample surface, a hyperspectral Raman image was first recorded at RT. The sample was then fired with a heating rate of 10 °C/min to 659 ± 5°C, where two images were subsequently recorded before heating the sample to the next temperature step. After having recorded the last high-temperature image at 1104 ± 5°C the sample was cooled to RT with a cooling rate of 10 °C/min and a final image was taken. All Raman images comprised an imaging area of 100 x 100 µm with a step size of 1 µm. Raman spectra were collected during continuous x-y stage movement with a speed of 1.6 µm/s (SWIFT© mode) which results in a total imaging time of 1 h and 53 min per image. Hence, an image is never an accurate snapshot, because processes may still run while recording the image. This must be considered when interpreting the hyperspectral Raman images.

All Raman spectra were corrected for any temperature shift that could potentially occur within the Raman laboratory during long-time measurements, baseline-corrected, and the spectra were reduced to the spectral range between 100 and 1200°C. For more details regarding the data reduction and image visualization see Chapters 8.1.2 and 8.1.3. In the following, only parts of the experimental data set, that was collected within the frame work of this project, are shown and the main results are presented and briefly discussed. However, all Raman images of the CaO-SiO_2 heating ramp experiments were published along with a detailed analysis and interpretation in the Master thesis of Johannes Kehren[196].

6.3 Results and discussion

6.3.1 Influence on the calcite decomposition temperature

Calcite started to decompose to lime and CO_2 at 793°C (Figure 6.1 A). In all four heating ramp experiments with a mixture of calcite and quartz, calcite always decomposed between 793 and 838°C[196]. The same is valid for a mixture in which quartz was replaced by fused silica[196]. This corresponds to the results found in the single-phase heating study of calcite in which the decomposition started near 750°C (5.3.2 The decarbonation of calcite).

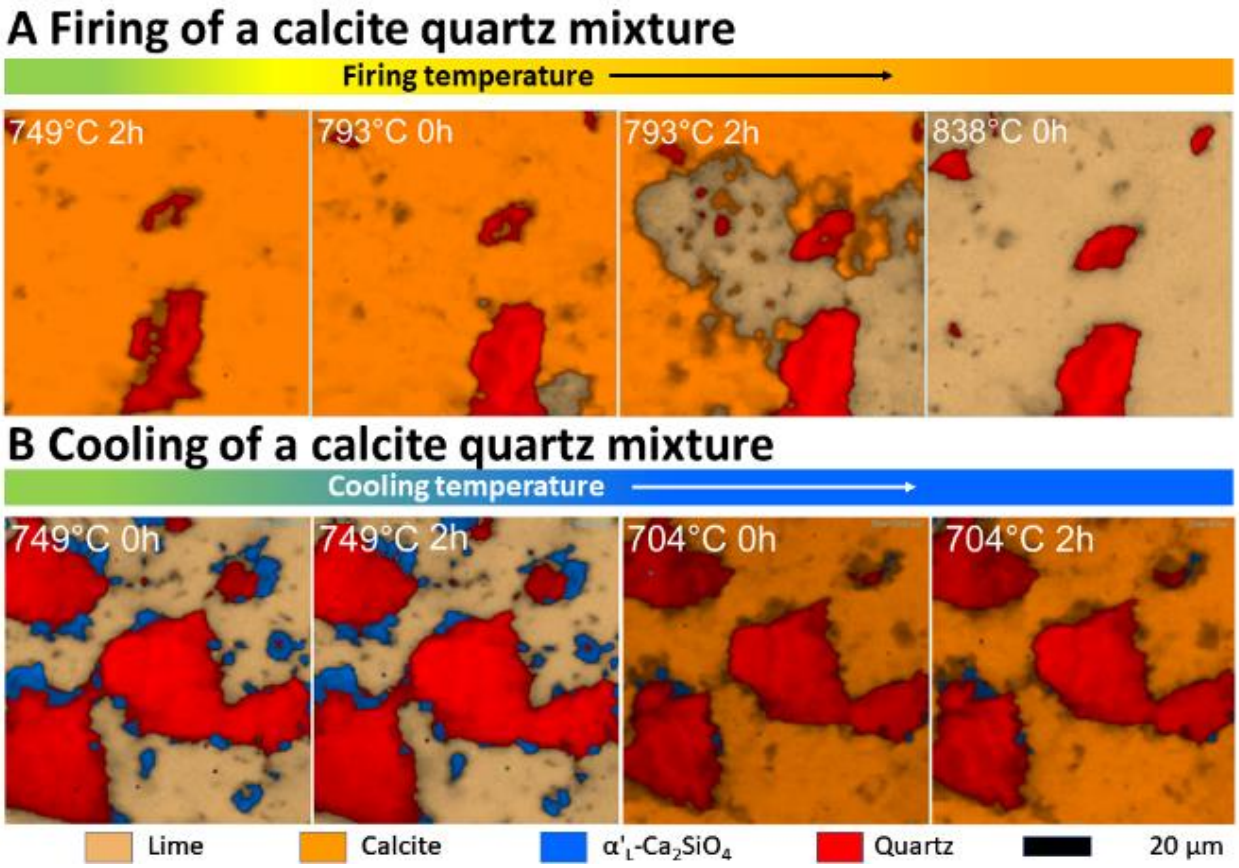

Figure 6.1: A) Heating ramp experiment of calcite and quartz (Exp. 2-4-8) The decomposition of calcite started at 793°C and was completed at 838°C. B) Cooling ramp experiment of calcite and quartz. Calcite and quartz in a mass ratio of 1:1 were fired to 927°C and successively cooled down to 387°C in 50°C-steps. Calcite was decomposed completely during firing to 927 °C and only CaO was present. During cooling from 749°C to 704°C calcite suddenly recrystallized from CaO and CO_2 trapped in the heating stage.

The thermal decomposition of calcite is known to be topotactic and pseudomorphic[192]. Furthermore, the {1014} rhombohedron and its external shape is preserved during the thermal decomposition of calcite single crystals[192]. CO_2 can diffuse outside of the reactant-product interface and allows the interface to move forward into the crystal following specific crystallographic directions[192,197]. In vacuum, about 98 ± 2 % of the original volume of a calcite crystal are replaced by CaO aggregates[198]. After the conversion and full release of CO_2 the porosity reaches a theoretical maximum of 54 %[198,199]. Rodriguez-Navarro and co-authors[192] measured a porosity of 53 vol.-% at 900°C in air, which decreased to 47 vol.-% during firing to 1150°C as a result of sintering and associated shrinking of the sample. Even after two days of firing a mixture of kaolinite and calcite at 971°C and 1020°C respectively, clusters of unreacted lime were preserved at the sample surface (Figure 6.2, A and B). These CaO clusters were most likely relicts of former calcite grains. A completed conversion of the educts was not reached, because the educts did not come into contact to each other and/or one of the educts was fully consumed. This information could not be gained from a simple analyzation of the bulk composition.

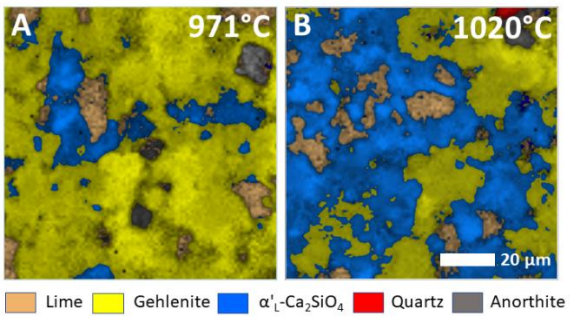

Figure 6.2: Raman images of an area from the surface of a mixture of calcite and kaolinite that was fired for about 48 hours at 971°C (A Exp. 2-3-24) and 1020°C (B Exp. 2-3-25-2). Clusters of unreacted lime were still preserved, which are most likely relicts of former calcite grains.

Tschegg and colleagues claim that a favored firing temperatures for highly calcareous materials falls within the temperature range between about 700 and 800°C, because the calcite decomposition at higher temperatures could cause the formation of defects in the created pots[70]. To avoid crack-development due to a volume increase within portlandite recarbonation, it is common practice to immersed carbonate containing bricks in water to dissolve and eliminate existing CaO or $Ca(OH)_2$[53].

In experiments in which quartz was substituted by kaolinite, calcite decomposition occurred at noticeable lower temperatures. In an *in situ*/quench experiment of calcite and kaolinite, calcite was decomposed while recording the Raman image at 660°C (Exp. 2-3-7-2)[170]. In a multi-phase heating ramp experiment (Figure 6.3, B, Exp. 3-1-1) of kaolinite, quartz, and calcite, the calcite decomposition was already completed when reaching the first temperature step at 669°C, which indicates that the dehydration of kaolinite catalyzes the decomposition of calcite.

According to Rodriguez-Navarro and co-authors the thermal decomposition is not affected by parameters like grain size or CO_2 pressure. However, other authors found a dependence of particle size and shape[197], crystallinity[200], and the chemical composition[53,201] on the sintering rate and decomposition temperature. Additionally, an influence of CO_2 pressure has been observed by Zhong and Bjerle[199] as well as Beruto and co-authors[197]. These authors stated that the CO_2 pressure acts as a catalyst and increases the sintering rate with a higher CO_2 pressure value. The reaction kinetics of the calcite decomposition can change due to the addition of other minerals. The dehydroxylation of clay minerals can decrease the temperature of the calcite decomposition[71]. Firing a mixture of calcite and kaolinite resulted in a completion of

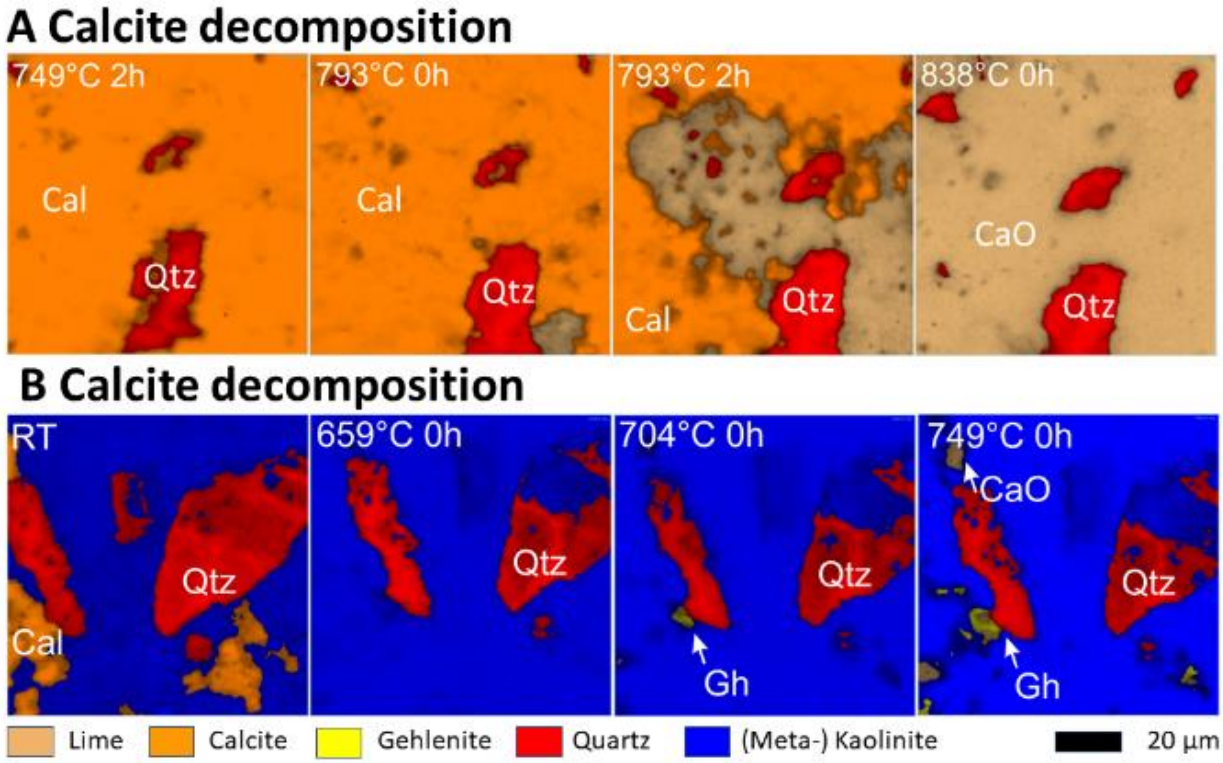

Figure 6.3: Raman images of calcite and quartz from a heating ramp experiment (A Exp. 2-4-8), calcite started to decompose at 793°C and was completed at 838°C. In a multi-phase heating ramp experiment (B Exp. 3-1-1) of kaolinite, quartz, and calcite, the calcite decomposition was already completed when reaching the first temperature step at 669°C. The dehydration of kaolinite catalyzes the decomposition of calcite. All Raman images of the Exp. 2-4-8) were published in the master thesis of Johannes Kehren[196]. Exp. 3-1-1 is unpublished so far.

the thermal decomposition at lower temperatures of 750°C[200].

In all heating ramp experiments calcite was recrystallized during cooling. To narrow the temperature range in which lime recrystallizes to calcite, an experiment with a cooling ramp was performed. Calcite and quartz in a mass ratio of 1:1 were fired to 927°C and successively cooled down to 387°C in steps of 50°C. Calcite was decomposed completely during firing to 927 °C and only CaO was present (Raman images not shown here, see Johannes Kehren)[196]. During cooling from 749 to 704°C calcite recrystallized from unreacted lime and CO_2 that was trapped in the heating stage[196,202]. In experiments in which calcite was replaced by CaO as precursor material, calcite was not observed in the quenched samples. This supports the assumption that the recrystallization only occurs because the CO_2 that was released by calcite decomposition was trapped in the heating stage and therefore available for recrystallization.

6.3.2 Calcite recrystallization during cooling

In contrast to the heating ramp experiments, calcite was not recrystallized at the sample surface in all isothermal firing experiments (Chapter 4). In the experiments at 803 and 843°C calcite was recrystallized from the unreacted lime and CO_2 that was trapped in the heating stage (Figure 6.4 A). At higher firing temperatures there was still unreacted lime at the sample surface after quenching the sample to RT (Figure 6.4 B). The lime did not recrystallize to calcite. However, this suggests that there was no CO_2 available for that reaction or the structure of lime did not allow a recrystallization anymore. Because the recrystallization took place in all heating ramp experiments after quenching the sample from about 1105°C and in the isothermal firing experiments this did not even happen after firing to 880°C, the determining factor appears to be time rather than temperature. It seems unlikely that CO_2 can leave the heating stage due to the firing at temperatures higher than 843°C for two days and there is no hint that CO_2 could be bound in another phase. Therefore, most likely the structure of lime has changed during firing at temperatures higher than 843°C for such a long dwell time. It is important to stress that with this technique only the sample surface could be investigated which does not necessarily have a significance for processes in the middle of the sample body. It is possible that the recrystallization of calcite only occurs in the first µm of the sample, because there are no channels where CO_2 can reach the CaO.

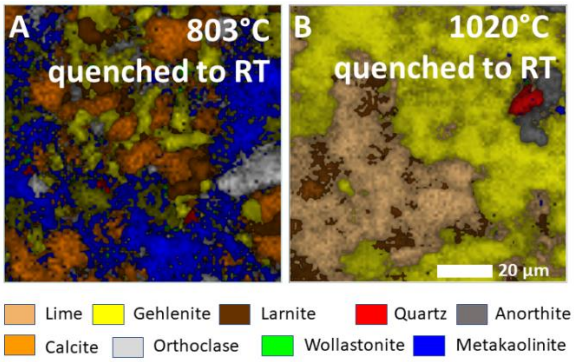

Figure 6.4: Raman images of the surface of a mixture of calcite and kaolinite that was fired for two days at 803°C and quenched (T803 Exp. 2-3-20) to RT. Calcite has recrystallized from unreacted lime and CO_2 that was trapped in the heating stage (A). After firing the same mixture for two days at 1020°C and quenching the sample (T1020 Exp. 2-3-25-2) to RT, there was still unreacted lime, suggesting that there was no CO_2 available for the reaction.

6.4 Conclusion

The decomposition of calcite was observed in the experiments at different temperatures depending on the presence or absence of kaolinite. This observation agrees with those of Wieczorek-Ciurowa, who found that the course of the decomposition depends on the experimental conditions and the presence of foreign substances[195]. Additionally, recrystallize-tion of calcite from unreacted lime and CO_2 during cooling to RT was observed in some experiments[60,170,196,202,203].

7 Formation of calcium silicates in the system SiO_2-CaO studies by *in situ* Raman imaging

7.1 Introduction

The mineral phases of the system CaO-SiO_2 are industrial materials that are often used in many industries. The most important applications of calcium silicates are in building materials such as glass, cement, bricks and tiles for roofs, fireproof ceilings and building board[204]. Wollastonite-containing material is used for production of special radioceramics, porcelain and faience, low-loss insulators, sanitary engineering components, lining brick, glaze, and flux[205]. Wollastonite added to glazes renders them more resistant to cracking, spalling, and other types of damage, and improves luster. The addition of wollastonite to ceramic mixtures also reduces the firing time, decreases the firing temperature, reduces shrinkage, and imparts strength to the material[205]. During the last decades the excellent bioactivity of some calcium silicate ceramics such as wollastonite, pseudowollastonite, and dicalciumsilicate powders was discovered. Biomaterials containing CaO–SiO_2 were found to bond to living bone and soft tissue[89].

Due to the simple stoichiometry of the reaction

$$\underset{Quartz}{SiO_2} + \underset{Calcite}{CaCO_3} \rightarrow \underset{Wollastonite}{CaSiO_3} + CO_2 \uparrow$$

and its importance in silicate ceramics[53] as well as in metamorphic rocks[52,206], this reaction was considered as a model reaction in the system CaO-SiO_2 to study two-phase solid-state reactions *in operando* at the mesoscopic scale.

7.2 Materials and methods

CaO, $CaCO_3$ and vitreous silica powders used in this study were purchased from Alfa Aesar and the quartz from Merck. Details regarding purity and particle size can be found elsewhere[60]. About 0.045 g of the precursor material were pressed with 0.01 MPa in a wolfram carbide press to a cylinder of 3 mm in diameter. The green bodies had a height of about 2.7 mm. Green bodies of different ratios of calcite (or CaO) and quartz (or fused silica) were produced. The used material, the composition, and the experimental details are summarized in Table V.VIII.

The samples 2-4-3, 2-4-4, 2-4-6, 2-4-9, and 2-4-14 were fired to temperatures between 659 and 1104 ± 5°C in nominal steps of 50°C. Exp. 2-4-7 was started already at 400°C. The samples were fired with a heating rate of nominal 10 °C/min to 387 or 659 ± 5°C, respectively, at which two images were subsequently recorded before heating the sample to the next temperature step. All Raman images comprised an imaging area of 100 x 100 µm with a pixel size of 1 µm. Raman spectra were collected during continuous x-y stage movement with a speed of 1.6 µm/s (SWIFT© mode) which results in a total imaging time of 1 h and 53 min per image. Two RT Raman images were recorded for each experiment. One image of the green body and one image after cooling the sample to RT. Details regarding data reduction and image visualization can be found in Chapters 9.1.2 and 9.1.3. In this thesis only parts of the experiments are shown. All Raman images of the experiments were published in the Master thesis of Johannes Kehren[196].

7.3 Results and discussion

7.3.1 The formation of calcium silicates

In the heating ramp experiments of calcite and quartz, wollastonite was firstly detected around 800°C, when calcite was decomposed. In experiments in which calcite was replaced by lime (Exp. 2-4-3, 2-4-4, 2-4-6, 2-4-7), wollastonite was already formed at temperatures around ~750°C[196]. However, in all these experiments another calcium silicate was formed preferentially and wollastonite occurred only in small amounts (Figure 6.5 A). Already at temperatures of 524°C small amounts of dicalcium silicate were formed in a heating ramp experiment with CaO and quartz (Exp. 2-4-7, data not shown here)[196]. Dicalcium silicate did not only nucleate and grow at

visible grain boundaries between lime and quartz grains (Figure 6.5 A), but also as many small grains within the CaO matrix. Most likely SiO_2 needed for the formation of dicalcium silicate derived from small invisible quartz particles that are more reactive than the larger ones due to their larger surface area. Such a grains size effect was also reported for feldspar by Diella and co-workers, who studied the effect of particle size distribution in Na-feldspar/kaolinite system[207]. It is consistent with Oswald ripening that is described by the Ostwald-Freundlich equation[161] in which surface tension causes small particles to dissolve and larger ones to grow. With increasing dwell time and temperature, the amount of dicalcium silicate increased and reaction rims have grown around larger quartz grains (Figure 7.1). While the amount of wollastonite seems to vary widely in the heating study experiments, the amount of dicalcium silicate seems to be relatively stable. A correlation between the amount of dicalcium silicate or the time and temperature when it was formed and the use of calcite or lime as a precursor cannot be found. Additionally, there was no correlation between the formation of calcium silicates and the mass ratio of calcite and quartz, or CaO and quartz, or the initial firing temperature. This stands in marked contrast to other studies in which the mass ratio does not only have a great influence on the overall amount of Ca-silicates[208], but also controls the type of Ca-silicate that is formed[204]. More experiments with different starting compositions are necessary to solve this contradiction.

7.3.2 Replacing quartz by amorphous silica

However, replacing quartz with fused silica has a major impact on the formation of Ca-silicates. When amorphous silica (fused silica) was used as a precursor material, a higher amount of mono- and dicalcium silicates was formed during firing (Figure 7.1 B). Especially the amount of wollastonite was increased considerably (Figure 7.1 B) and its formation temperature was decreased (in Exp. 2-4-14 wollastonite was already present in the first image recorded at 659°C). The different

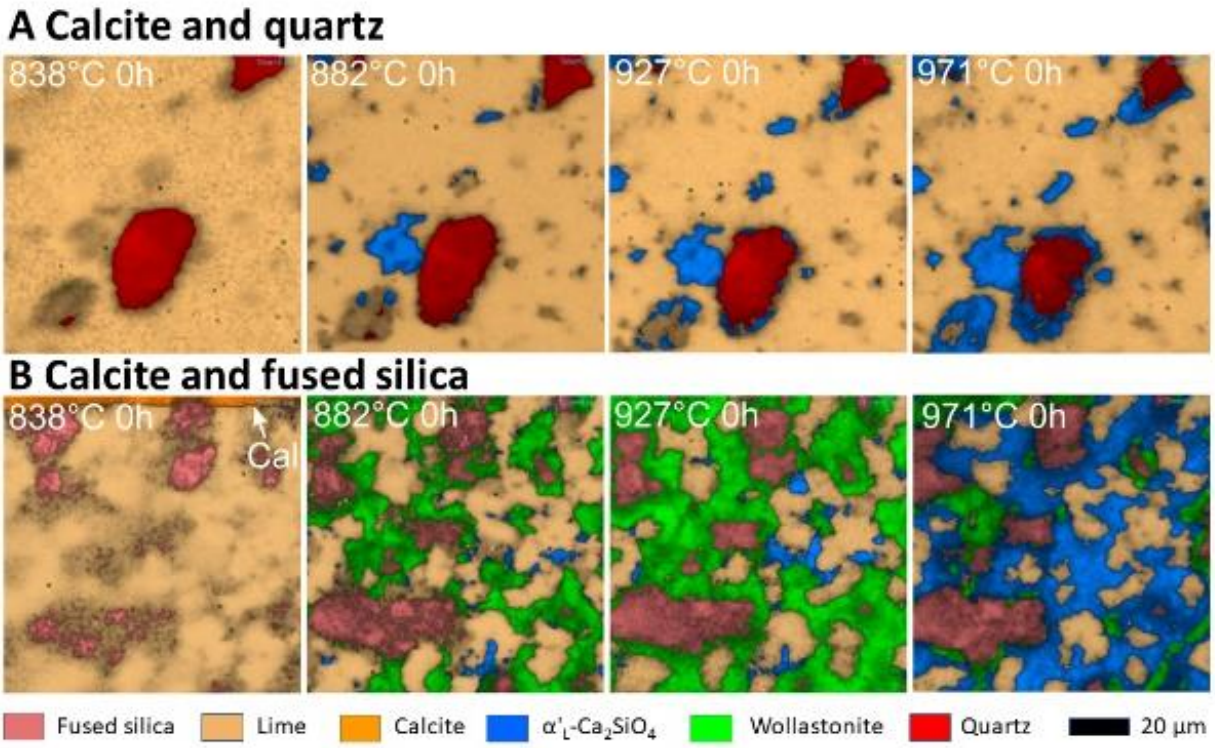

Figure 7.1: HT-Raman images of a mixture of calcite and quartz (A) and calcite and fused silica (B). Two experiments were performed under the same experimental conditions. The only difference is that in experiment A quartz was the SiO_2 source and in experiment B quartz was replaced by fused silica (A Exp. 2-4-6 and B Exp. 2-4-9).

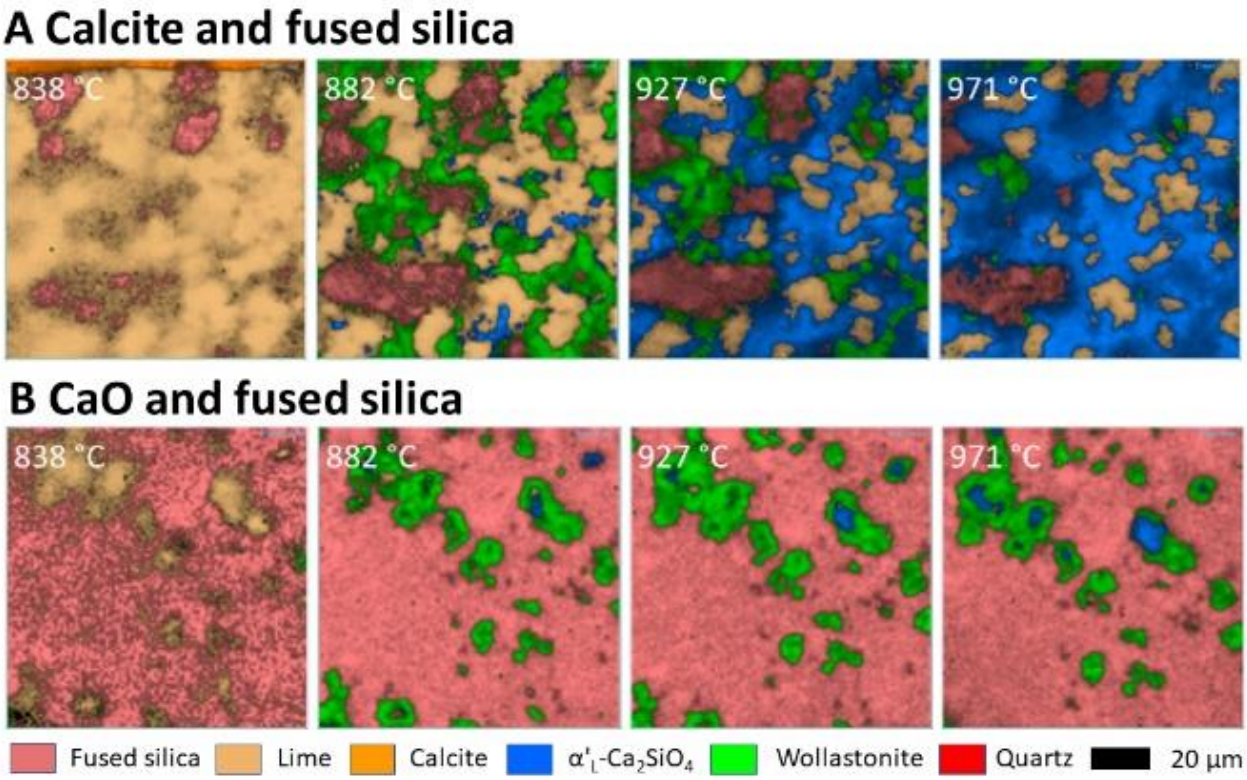

Figure 7.2: HT-Raman images of calcite and fused silica (A) and CaO and fused silica (B), illustrating the observation that the type of calcium silicate that formed depended on the local Ca content. In experiment 2-4-9 (A) the CaO to SiO_2 ratio in the investigated area is higher than that in Exp. 2-4-14 (B).

reactivity of quartz and amorphous silica is also evident from the amount of raw material that is still present after the experiments. In the experiments using quartz high amounts of unreacted calcite/lime and quartz remained after cooling to RT. When fused silica was used instead of quartz, most of the precursor material reacted to new mineral phases.

7.3.3 The local CaO supply

In an experiment (Exp. 2-4-9) in which the local CaO to SiO_2 ratio of the investigated area was relatively high the main phase at 971°C was dicalcium silicate (Figure 7.2 A). In contrast, in experiment 2-4-14 with a lower local CaO to SiO_2 ratio in the investigated area more wollastonite was formed (Figure 7.2 B), i.e., the higher the Ca supply, the higher is the content of the dicalcium silicate phase.

In some experiments, wollastonite was replaced by dicalcium silicate in the course of the experiment (Figure 7.3), according to the following reaction equation:

$$\underset{Wollastonite}{\beta-CaSiO_3} + \underset{Lime}{CaO} \rightarrow \underset{Dicalcium\ silicate}{\alpha'_L-Ca_2SiO_4}$$

In experiment 2-4-9 wollastonite was the major phase at 882 °C, but at 971 °C it was mostly replaced by a'_L-Ca_2SiO_4. The same was observed in experiment 2-4-7 (Figure 7.3). This contrasts with observations made by Mazzucato and Gualtieri, who proposed that wollastonite formation is a two-step process in which larnite (dicalcium silicate) appears in a first step and reacts in a second step with excess SiO_2 to wollastonite (β-wollastonite at lower temperature, α-wollastonite, the cyclo-silicate polymorph, at higher temperature)[209]. Zhao and Wang, on the other hand, calcinated wollastonite and CaO at 1200°C for five hours and observed the formation of dicalcium silicate[210].

7.3.4 The dicalcium silicate polymorphs

Within the firing experiments several phase transitions of dicalcium silicate were observed. In two heating-ramp experiments γ-Ca_2SiO_4

was already an accessory mineral of the lime precursor material. The irreversible γ→α'$_L$ transition was observed in two experiments, but at different critical temperatures. In Exp. 2-4-6, the phase transition took place between 838 and 882 ± 5°C and was clearly visible in the Raman spectra (Figure 7.4). At RT and from 659 to 838 ± 5°C

γ-Ca_2SiO_4 was observed. The polymorph was clearly identified by its main Raman band near 809 cm^{-1} (at RT), which shifts slightly to lower wavenumbers with increasing temperatures. During firing from 838 to 882 ± 5°C this main Raman band as well as most of the other bands at lower wavenumbers disappeared and a new Raman band at 843 cm^{-1} appeared. The new band was broader and can be assigned to the a'$_L$-phase. The phase transition also occurred in Exp. 2-4-7. However, in this experiment the transition was more sluggish and took place between 614 and 749 ± 5°C. This was also observed by Remy and colleagues[87], who reported a sluggish transition between 817 and 917°C. In all experiments in which dicalcium silicate was newly formed, the a'$_L$-phase occurred. During cooling of all experiments in which dicalcium silicate was formed, the a'$_L$ → β transition took place. In the cooling experiment (Exp. 2-4-10) the transition took place in the temperature range between 569 and 478 ± 5°C. At temperatures above 569 ± 5°C the spectrum of a'$_L$-Ca_2SiO_4 was like the spectrum observed in Exp. 2-4-7 with small differences in the band position of the main band. However, the determination of the exact band position was very difficult due to the broadness of the band. Between 569 and 524 ± 5°C the main Raman band started to separate in two bands and at 478 ± 5°C a new band at 858 cm^{-1} was clearly distinguishable. In addition, a new band at 844 cm^{-1} appeared. These observations, however, contrast with a study by Remy and colleagues, who described an abrupt shift between 714 and 686°C[87]. These differences may be a kinetic effect due to the slow cooling in the experiments of this study which was frequently stopped to take a Raman image. However, in the experiments of this study only β-Ca_2SiO_4 was present at RT and no γ-Ca_2SiO_4 was detected.

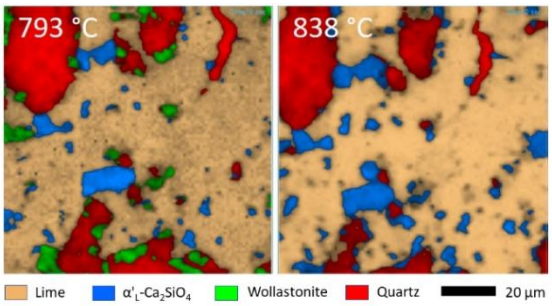

Figure 7.3: HT-Raman images of CaO and quartz. With increasing reaction time, wollastonite is replaced by dicalcium silicate (Exp. 2-4-7).

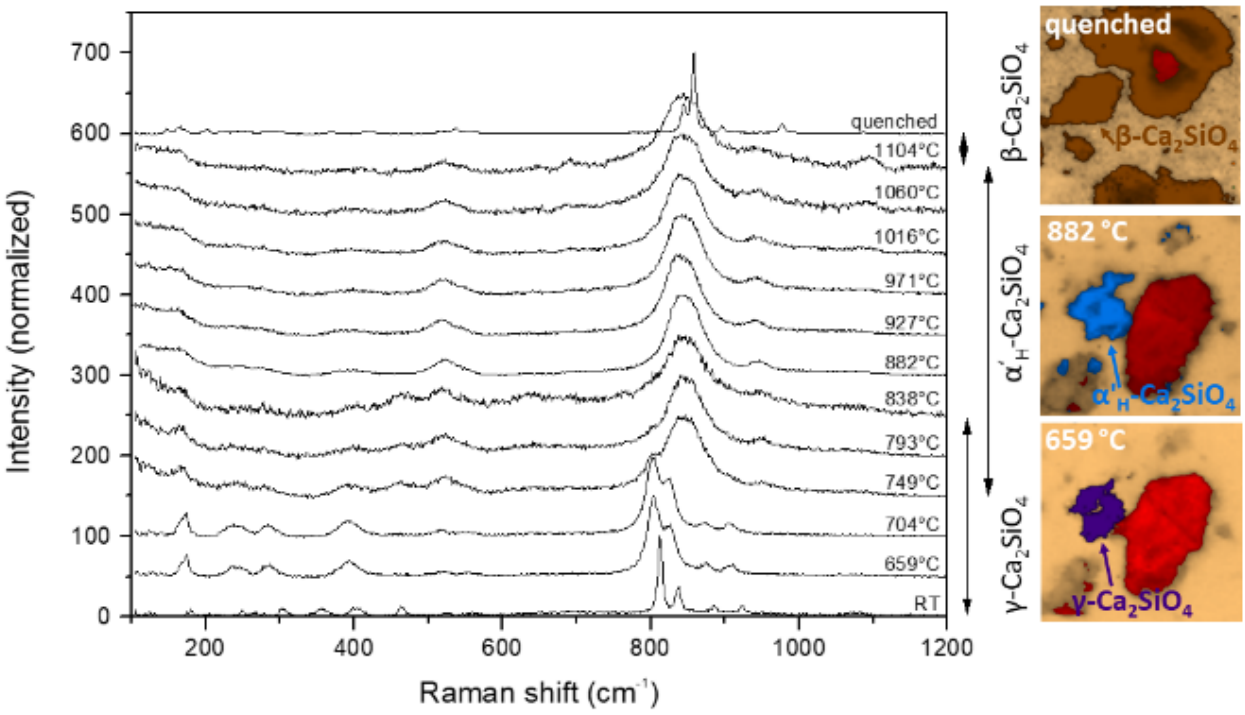

Figure 7.4: Average Raman spectra (9 pixels) of dicalcium silicate from the Raman images recorded between 659 and 1104 ± 5°C. Three polymorphs of dicalcium silicate occurred within one experiment (Exp. 2-4-6).

7.3.5 Conclusion

Calcium silicates are of great importance for many industries and frequently used as building material or bioactive material. In this study, the formation of Ca-silicates, such as wollastonite, pseudowollastonite, and dicalcium silicate in the two component system $CaO\text{-}SiO_2$ was investigated. Different precursor materials such as calcite/CaO and quartz/amorphous silica were used to determine the influence of the oxide source on the formation temperature and the mineral paragenesis. The decarbonation of calcite was observed in the temperature range between 749 and 838 ± 5°C and the carbonation between 749 and 704 ± 5 °C. Both processes are clearly recognizable by the appearance and disappearance of the symmetric stretching (A_{1g}) mode of [CO_3^{2-}] in calcite at 1086 cm^{-1}. Dicalcium silicate was formed for the first time at 524 ± 5°C and wollastonite at 749 ±5 °C. The amount of both phases increased rapidly in the temperature range from 838 to 927 ± 5°C. The replacement of quartz by fused silica dramatically increased the formation of calcium silicates due to the higher reactivity of amorphous silica compared to quartz. Replacing calcite with lime, on the other hand, had no significant effect on the amount of calcium silicates that was formed, but decreased the formation temperatures of dicalcium silicate. However, the most surprising discovery is the formation of pseudowollastonite at about 750 °C, which is about 375 °C below the critical temperature for the wollastonite to pseudo-wollastonite transition (1125 ± 10°C). Pseudo-wollastonite formed without wollastonite being present and contemporaneously and in contact with wollastonite (c.f., Chapter 2 “Insights into the evolution of carbonate-bearing kaolin during sintering revealed by in situ hyperspectral Raman imaging”). Multiple polymorphic phase transi-tions of dicalcium silicate were observed during firing. The γ to α'_L-transition took place during firing from 838 to 882 ± 5°C while the a'_L

to β-transition occurred during cooling between 569 and 478 ±5°C. The β-phase remained stable after the transition (even at RT) even without the use of stabilizers.

8 Summary discussion

In situ hyperspectral Raman imaging offers plenty of information about the firing process of silicate ceramics. The method facilitates the study of the firing process *in situ* at high temperatures and with a spatial resolution on a micrometer scale. The major aims of the project were

(1) to set up an experimental procedure, to develop a method for the data treatment, and to evaluate its possibilities and limits,

(2) to acquire high-temperature Raman spectra from relevant ceramic phases as references for (semi-)quantitative phase determination and to study single-phase transitions and de-composition reactions,

(3) to investigate the dependence of the textural and phase evolution on the starting phase composition during high-temperature sintering and cooling of ceramic systems,

(4) to investigate mesoscopic mechanisms of high-temperature, two-phase, solid-state sintering reactions, and

(5) to gain semi-quantitative information on the mineral content and to study crystallization kinetics and the evolution of the grain size during isothermal firing.

The following chapter shows which of the five overall goals could be achieved.

8.1 Experimental procedure and data treatment

8.1.1 Map programming

Within this project four major types of experiments were performed (1) *in situ* heating studies of single-phases, (2) *in situ* two-phase experiments, with (a) a heating ramp between about 650 and 1100°C, or (b) isothermal firing for several hours, (3) *in situ* multi-phase experiments, and (4) additional *ex situ* and *in situ* experiments to study the effect of experimental parameters on, for instance, the size of the confocal pinhole on the axial resolution. For the isothermal two-phase experiments an automatic measuring protocol was developed with the help of VBS codes and the "method" function implemented in the Labspec software. This protocol consists of the following steps:

(1) Acquisition of an RT image with 100 x 100 µm in 1 µm steps, (2) firing at a heating rate of 10°C/min to the respective temperature, (3) performing the "tilt at limits" autofocus procedure, (4) recording a Raman image, …repeating steps (3) and (4) for a further 23 times, (5) cooling to RT with a cooling rate of 10°C/min, and, finally, (6) recording a Raman image at RT. For more details regarding the experimental procedure and map programming see Chapters 2 to 4.

8.1.2 Data reduction

The data reduction was performed with the Labspec software. With the help of the implemented "methods" function an automatic data reduction protocol was programmed. This protocol comprises (1) a correction procedure to correct any spectrometer shift using the intense Ne line at 1707.06 cm^{-1} (with 532 nm excitation), (2) the subtraction of a baseline, fitted with a 2^{nd} degree polynomic function, to correct the spectrum for background contributions that at high temperatures are mainly composed of black body radiation and in some cases of continuous fluorescence signals, (3) a spike correction where all peaks smaller six pixels were removed, and (4) the reduction of the spectral range to 100 -1200 cm^{-1}. All hyperspectral Raman images and the reference spectra were evaluated and corrected using this protocol.

However, despite the spike correction in step (3), some cosmic spikes remained in all Raman images. They were manually removed, which dramatically improved the contrast of the

Raman images. The data prepared this way were eventually used for quantification and visualization.

8.1.3 Image visualization

Since there does not exist standardized data evaluation protocol for the creation of hyperspectral Raman images from a set of high-temperature Raman spectra in the literature, several different approaches were tested, and the method for data evaluation and quantification was further developed during the project. As a first approach to visualize the phase distribution and their textural relationship from a multi-dimensional hyperspectral Raman data set, three data reduction methods were tested [59]. In the main band method, only the intensity of one intense and characteristic Raman band of the identified phases was used to visualize their spatial distribution. The other methods were based on a CLS fitting method. The CLS method assumes that a spectrum of a polyphase material is a simple mixture of the spectra of the pure phases. Within the multidimensional spectral array, the CLS fitting procedure finds a linear combination of reference spectra of the pure phases, which best fits the raw spectrum at each position (pixel). The CLS fitting method 1 uses a representative background-corrected average Raman spectrum of 8 pixels as reference spectra. In the CLS fitting method 2 synthetic spectra are used as refence spectra. A spectrum is chosen in which the respective phase dominates, and all fitted Gauss-Lorentz functions that do not belong to this phase are deleted. The remaining functions are added together and saved as a synthetic spectrum of that phase. Drawback of all three methods was that some (weak) bands could not be assigned to the respective phase leaving high residuals or leading to an overestimation of minor phases.

In a second step, an in-house database of high-temperature spectra of over 20 mineral phases (the number is still increasing) that occur in the investigated systems was created. Since then the HT reference spectra are used for the CLS fitting procedure[60]. The resulting false-colored Raman image is composed of the images of the pure phases. Each pixel was colored in the color of the phase that dominated the CLS fit of this pixel. The brightness of the color expresses the intensity of the spectrum at that pixel. While a dark color represents a low intensity, a light color represents high intensity.

8.1.4 Image alignment

Due to various processes such as shrinkage and compaction the sample moved during the experiments. For kinetic studies it is essential (Chapters 3 and 4) to analyze the same area (volume) of the sample at each temperature and time step. As a first approach to semi-quantify the apparent mineral content and grain size distribution over time, an area (region of interest, ROI) that is present in all images was selected by eye (Chapter 3). For quantification, the ROI was used. The disadvantage of that method was that the analyzed area (volume) was usually reduced. To improve the image alignment, the plugins TrakEM2 and Manual Tracking of the freeware software ImageJ[150,158] were used to align the images of each experiment that is presented in Chapter 4. Two images were compared with each other and the position of one image was shifted according to the position of the second one. In the end, a ROI was chosen that occurs in all images. However, due to the three-dimensional movement of the sample, a complete match could not be achieved.

8.1.5 Semi-quantification of the mineral content

As a first attempt, a semi-quantification of the mineral content was obtained from the Raman images (Chapter 3, 3.2. Isothermal mineral reactions and grain growth). By using a color threshold the false-colored Raman images were converted into binary images with the help of the graphics program ImageJ[150,158]. One

binary image for each mineral phase was created and the proportion of the respective mineral phase was calculated by applying the "Analyze Particles" tool implemented in the ImageJ software. However, with this approach, only the areas in which the mineral phase was the dominant one is considered. Therefore, the quantification of the mineral content was improved by using the matrix behind the unnormalized images of all end members of the CLS fit. To minimize the error by a shifting mapping area due to shrinkage or densification, the aligned images were used for the procedure. Every CLS Raman image is an overlay of the Raman images of the single phases. Behind these images there are matrices of the content of the respective phase in every pixel. In contrast to the Raman image overlay which was used for the first attempt (Chapter 3) the content of the phase in all fits (pixels) was considered, even when the phase was not the dominant phase in a single pixel.

8.1.6 Investigation of the grain size

In the isothermal *in situ* experiments (Chapters 3 and 4) the effects of temperature and time on grain growth were studied using the example of one mineral, respectively. In chapter 3 the grain growth of dicalcium silicate and in chapter 4 the grain growth of gehlenite were investigated. One major advantage over conventional quench experiments is that the same sample position/material is continuously investigated without the need for quenching a new sample at each time step. In chapter 3 the grain size of dicalcium silicate was obtained from the binary images by the "Analyze Particles" tool of ImageJ. The binary image was constructed from the overlay-image by a color-threshold. The growth of six individual grains as a function of time as well as the average grain size were investigated. In both cases, the grain size increases linearly with time which corresponds to a pseudo-zero-order behavior[60]. In chapter 4, the grain size of gehlenite was obtained from a binary image which was based on the single-phase image of the phase. The "Analyze Particles" tool from ImageJ was also used. With the aid of the program Origin the distribution of the grain sizes as a function of time and temperature were investigated.

8.2 Textural and phase evolution during high-temperature sintering and cooling

In all experiments containing kaolinite as precursor material, the dehydroxylation of kaolinite was the first reaction that occurred. Already during firing to 660°C (the lowest investigated firing temperature) kaolinite lost its chemically bounded water and metakaolinite was formed. At temperatures greater than about 600°C this reaction was accompanied by the decarbonation reaction of calcite. The decomposition of calcite was observed in the experiments at different temperatures depending on the presence or absence of kaolinite. Depending on the firing temperature and time the recrystallization of calcite from unreacted lime and CO_2 during cooling to RT was observed. In experiments in which the sample was fired at temperatures higher than 843°C for two days the recrystallization of calcite was not observed.

Dicalcium silicate was the first calcium silicate which was formed during firing. Already at temperatures of 524°C small amounts of dicalcium silicate were formed in a heating ramp experiment with CaO and quartz as small grains within the CaO matrix. The SiO_2 needed was derived from small invisible quartz particles that are more reactive than larger ones due to their larger surface area. This is in good agreement with the observation of Diella and co-workers, who studied the effect of the particle size on sintering processes in the system Na-feldspar/kaolinite[211].

With increasing time (Section 3.3.2) or temperature (Section 3.3.3) dicalcium silicate rims have grown around larger quartz grains.

During isothermal firing of calcite and quartz at 848 ± 5°C the fraction of dicalcium silicate increased linearly with time, while simultaneously the fractions of the CaO and quartz decreased linearly. This suggests a

pseudo zero-order kinetics, which is always a result or a kind of artifact of the reaction conditions. This is most likely due to the domination of one reactant (60% CaO in the first high-temperature image). Such a zero-order process cannot continue after one reactant has been exhausted or is protected against reactants by a solid reaction rim. If this point is reached, the reaction will change to another rate law.

The formation of such a protective barrier can be observed in a heating ramp experiment of calcite and quartz. A tenth of micrometer thick dicalcium silicate rim was formed around the quartz grains. With increasing temperature (about 950°C) and time the reaction direction turned over and the dicalcium silicate replaced the quartz grain. This turn over can only be explained by a change of the formation mechanism. The reaction rim separated the educts by forming a barrier between lime and quartz. At this stage, new crystallization was only possible by diffusion of the smaller Ca^{2+} ions through the barrier layer, so the quartz grain could be replaced by dicalcium silicate.

Besides dicalcium silicate, wollastonite was formed at 749 ±5 °C. The amount of both phases increased rapidly in the temperature range from 838 to 927 ± 5°C. The replacement of quartz by fused silica as the SiO_2 precursor material dramatically increased the formation of calcium silicates due to its amorphous structure and the associated higher SiO_2 availability. Which calcium silicate was formed depended on the local CaO supply. However, the most surprising discovery is the formation of pseudowollastonite at about 750 °C, which is around 375 °C below the critical temperature for the wollastonite-pseudowollastonite transition (1125 ± 10°C). Pseudowollastonite formed without wollastonite being present and contemporaneously to wollastonite. Multiple polymorphic phase transi-tions of dicalcium silicate were observed during firing. The γ to α'_L -transition took place during firing from 838 to 882 ± 5°C, while the a'_L to β-transition occurred during cooling between 569 and 478 ±5°C.

The first calcium alumina silicate that was formed in every experiment in the system SiO_2-CaO-$Al_2O_3 \pm K_2O$ was gehlenite ($Ca_2Al_2SiO_7$). The sorosilicate from the melilite solid solution series was already formed at temperatures of about 660°C which is about 140°C lower than previously reported[70]. This may result from the high sensitivity of the analytical technique, the use of different precursor materials, different milling procedures[204], and/or multiple solid-solid interfaces created by the pressing during sample preparation.

With increasing temperature, the amount of gehlenite increased in all experiments up to a temperature of around 970°C. At temperatures above 950°C gehlenite is expected to react with silica and Al_2O_3 from metakaolinite and fine quartz to anorthite. This is supported by the observation of small anorthite grains that crystallized in the *in situ*/quench experiment (Exp. 2-3-7-2) above 840°C and thereby spatially associated to gehlenite and wollastonite. In the isothermal experiments (Chapter 4) anorthite was also formed in contact to gehlenite at temperatures above about 930°C. In contrast, anorthite was not detected in the *in situ* or quench experiments with the mixture of kaolinite, kalifeldspar, quartz, and calcite [59]. In these experiments, most of the gehlenite seemed to disappear at the expense of wollastonite. This solid-solid replacement was first identified at 802 ± 5°C (S-Exp, Exp. 0-7) and 838 ± 5°C (F-Exp.; Exp. 0-5) (Figures 2.3 and 2.4[59]). At temperatures above about 1020°C (S-Exp.) the gehlenite grains within the imaged area seemed to be fully replaced by wollastonite, although gehlenite could still be detected by Raman spectroscopy and XRD in the finally quenched ceramic[59]. It is important to note that the XRD analysis gives information about the bulk composition. A temperature gradient of around 50°C (Supplementary material V.V) occurs between sample surface and sample body. Therefore, the bulk composition is always a mixture of different temperature areas within the sample.

In this project wollastonite was formed at different temperatures and from different precursors depending on the experimental conditions. Ptáček and colleagues (2013) also analyzed calcite-kaolinite mixtures using *in situ* XRD and ascribed the formation of wollastonite to a reaction of dicalcium silicate and free lime at temperatures of about 1050°C[155]:

$$\underset{Chalcio-olivine\ or\ larnite}{Ca_2SiO_4} + \underset{Silica}{SiO_2} \rightarrow \underset{Wollastonite}{2CaSiO_4}$$

Such a reaction would be in agreement with the observation made in the Raman images of the quenched ceramic fired at 1016°C (Q- Exp., Exp. 0-8), in which wollastonite occurred as rim around Ca_2SiO_4 (Figure 2.6[59]). As already stated, wollastonite was formed in the expense of gehlenite already at temperatures of 802 ± 5°C (S-Exp., Exp. 0-7) and 838 ± 5°C (F-Exp., Exp. 0-5)[59]. In the experiments of the CaO-SiO_2 system, wollastonite was formed above about 750°C from quartz and lime (Exp. 2-4-3, 2-4-4, 2-4-6, 2-4-7) and above about 800°C from quartz and calcite[196].

During firing of a kaolinite-calcite mixture an unknown phase was formed between at 660 ± 5°C and 971± 5°C (Chapter 4, and [170]). Between 750 and 880°C the amount of the unknown phase seemed to be the highest. In contrast to all other minerals the amount of this phase increased during the first couple of hours of firing and then was dissolved again with increasing dwell time (Chapter 4, Figure S4.12). This can be interpreted as an indication for the metastability of the phase. The unknown phase had one characteristic band at about 562 cm^{-1} (at RT). During cooling to RT the unknown phase mostly disappeared and was only preserved in one experiment fired below 930°C. This observation supports the assumption that the phase formed metastable.

The only mineral whose Raman spectrum closely corresponds to the spectrum of the unknown phase is cowlesite $Ca(Si_3Al_2)O_{10} \cdot 5\text{-}6H_2O$, which is a natural Ca-rich zeolite. Cowlesite has only two week Raman bands near 325 and 393 cm^{-1} and one characteristic band near 534 cm^{-1} at RT[163]. This is surprising at the first glance as zeolites are usually water-rich aluminosilicates and crystallize under hydrothermal conditions. It is thus conceivable that the water released from the kaolinite was not fully removed from the sample, which locally may have led to water-rich pores that are comparable to fluid-rich, miarolitic cavities in cooling magmatic systems. After a couple of hours, the fraction of the unknown phase decreased again with increasing dwell time. Following the argument, the water concentration at the sample surface was likely decreased at this stage, because the water continuously escaped the sample and the furnace. This caused the hydrous calcium alumina silicate phase to become unstable. It is noteworthy that the disappearance of the unknown phase correlates with the increase of gehlenite, which may indicate that gehlenite was later also crystallized from the unknown phase. This assumption was also supported by a marked change in the activation energy and grain size distribution of gehlenite around 880°C, which is clear evidence for a change in the formation mechanism.

At temperatures in excess of about 1000°C local congruent and incongruent melting reactions at grain boundaries may occur[53,54,169]. In triaxial silicate ceramics (composed of kaolinite, quartz, and alkali feldspar) it is commonly assumed that the melting process is initiated at the ternary eutectic mullite-tridymite-K-feldspar at about 985°C[169]. Melting is regarded as a grain boundary-controlled dissolution process that is controlled by the diffusion of elements through the steadily increasing melt phase. Initiated at the interface between two or three phases the melting front advances into the interior of the grains along a moving melt-grain interface, but due to the sluggish kinetics does not reach chemical equilibrium beyond the local micro-scale[53,169]. In particular, feldspars seem to play a key role as fluxing agents in triaxial ceramics[54]. This assumption is corroborated by the observation that partial melts only occurred in experiments in which kalifeldspar was part of the precursor material. In the experiments in which kaolin

(kaolinite, kalifeldspar, and quartz) was mixed with calcite a broad band with a maximum near 1050 cm^{-1} appeared in the Raman spectra recorded above 950°C (S-Exp., Exp. 0-7). Considering the high carbonate content in the starting material, this band may be assigned to a partial melt. Kalampounias assigned a band near 1050 cm^{-1} to the Q^3 species in a quenched melt (glass) of 0.4 CaO · 0.6 SiO_2[212]. In all other experiments, no evidence for a partial melt was found. Gehlenite, anorthite, (pseudo-) wollastonite, and dicalcium silicate crystallized via a solid-state reaction. Since the K content is the major difference between the experiments presented in Chapter 2 and in all other experiments, this is most likely the reason for the occurrence of a partial melt at this temperature. This interpretation is in line with those of Tschegg and colleagues, who suggested that alkalis such as K act as a flux agent and reduce the melting point drastically[70].

9 Conclusion and outlook

The results of this projects show that *in situ* hyperspectral Raman imaging is a powerful tool to investigate the firing process of silicate ceramics. High-temperature hyperspectral Raman imaging makes it possible

a) to identify crystalline and amorphous phases which form during firing,

b) to differentiate between polymorphs,

c) to detect metastable phases which form,

d) to investigate the reaction processes during ceramic firing *in situ* and *in operandi*, without the need to stop the process and quench the sample before analyzing,

e) to obtain spatially resolved information about the phase assemblage and textures on a micrometer scale at high temperature,

f) to gain kinetic information about different solid state or solid-melt reactions, leading to the formation of new mineral phases, and

g) to quantitatively study grain growth and decay in situ and at high temperatures.

Currently, there is no other technique with which all this information can be gained from one experiment.

During this project an experimental procedure and data treatment was established that can be used to investigate the firing process of several materials. The most striking results of this study were that

(a) the decomposition temperature of calcite is strongly decreased by the addition of kaolinite and calcite recrystallized during cooling,

(b) wollastonite and pseudowollastonite can be formed in direct contact to each other and more than 350°C under the proposed transformation temperature,

(c) a turn-over in the migration direction of dicalcium silicate can be followed *in situ*, and

(d) the kinetics of the crystallization of gehlenite seem to be influenced by a previously unidentified hydrous calcium silicate phase which has never been described before.

Regarding the challenges and findings of this PhD project some further steps are conceivable or planned, to improve the experimental processing and data reduction of *in situ* hyperspectral Raman imaging which were shortly described in the following. All high-temperature Raman spectra of the heating studies should be published in a data journal, to make them available to all scientists. Therefore, the Raman spectra must firstly be corrected for any device parameters and the recording temperature by using the Einstein-Bohse- correction.

The calibration of local mineral thermometers to account for the temperature gradient that almost unavoidably exists between the position of the thermocouple and the location where the reactions take place was not possible so far. The ν_i -T relationships of the reference spectra are determined accurate and precise. However, at this point, the position of

the Raman bands in the images were not precise enough due to the fast recording times of 1.6 µm/s, which results in a low signal to noise ratio. Larger recording times or a better intensity output would improve the HT-spectra and would enable an accurate and precise determination of the temperature, where the reactions take place.

Future experiments are conceivable in which the precursors are labeled with ^{18}O as *in situ* tracers to gain insights into mechanistic and dynamic processes like transport of matter and crystal growth. The principle behind analyzing the ^{18}O content in condensed matter by vibrational spectroscopy is that the energies or frequencies associated with vibrational motions are dependent on the masses of the vibrating atoms.

In situ high-temperature hyperspectral Raman imaging opens new perspectives to study reaction mechanism and textural changes during firing processes. Besides the ceramic industry this method is suitable to investigate almost every industrial firing process. There are many open questions regarding the production of bioactive materials or the interaction of refractories and the engineering materials in the cement or steel industry, which could potentially be solved by in situ, high-temperature Raman spectroscopy.

10 Reference list (main thesis)

1. Heimann, R. B. & Maggetti, R. B. H. M. *Ancient and Historical Ceramics*. (2014).
2. Vandiver, P., Klima, B., Svoboda, J. & Soffer, O. Linked references are available on JSTOR for this article : The Origins of Ceramic Technology at Dolni Vestonice , Czechoslovakia. *Science (80-.).* **246**, 1002–1008 (2016).
3. Wu, X. *et al.* Early pottery at 20,000 years ago in Xianrendong Cave, China. *Science (80-.).* **336**, 1696–1700 (2012).
4. Carter, C. B. & Norton, G. *Ceramic Materials: Science and Engineering*. *SpringerLink : Bücher* (2013). doi:10.1007/978-1-4614-3523-5.
5. Riedel, H. & Blug, B. A Comprehensive Model for Solid State Sintering and Its Application to Silicon Carbide. *Multiscale Deform. Fract. Mater. Struct.* 49–70 (2005) doi:10.1007/0-306-46952-9_4.
6. Tite, M. S. Ceramic production, provenance and use - A review. *Archaeometry* **50**, 216–231 (2008).
7. Elert, K., Cultrone, G., Rodriguez Navarro, C. & Sebastián Pardo, E. Durability of bricks used in the conservation of historic buildings - Influence of composition and microstructure. *J. Cult. Herit.* **4**, 91–99 (2003).
8. Traoré, K., Kabré, T. S. & Blanchart, P. Gehlenite and anorthite crystallisation from kaolinite and calcite mix. *Ceram. Int.* **29**, 377–383 (2003).
9. Chen, Y. F., Wang, M. C. & Hon, M. H. Phase transformation and growth of mullite in kaolin ceramics. *J. Eur. Ceram. Soc.* **24**, 2389–2397 (2004).
10. Cultrone, G., Sebastián, E. & De La Torre, M. J. Mineralogical and physical behaviour of solid bricks with additives. *Constr. Build. Mater.* **19**, 39–48 (2005).
11. Saboya, F., Xavier, G. C. & Alexandre, J. The use of the powder marble by-product to enhance the properties of brick ceramic. *Constr. Build. Mater.* **21**, 1950–1960 (2007).
12. Trindade, M. J., Dias, M. I., Coroado, J. & Rocha, F. Mineralogical transformations of calcareous rich clays with firing: A comparative study between calcite and dolomite rich clays from Algarve, Portugal. *Appl. Clay Sci.* **42**, 345–355 (2009).
13. Shoval, S., Boudeulle, M. & Panczer, G. Identification of the thermal phases in firing of kaolinite to mullite by using micro-Raman spectroscopy and curve-fitting. *Opt. Mater. (Amst).* **34**, 404–409 (2011).
14. Sokolář, R., Vodová, L., Grygarová, S., Štubňa, I. & Šín, P. Mechanical properties of ceramic bodies based on calcite waste. *Ceram. Int.* **38**, 6607–6612 (2012).
15. Aras, A. The change of phase composition in kaolinite- and illite-rich clay-based ceramic bodies. *Appl. Clay Sci.* **24**, 257–269 (2004).
16. Stange, K. Investigations into the methodology of in situ and real-time hyperspectral Raman imaging of phase transformation reactions during thermal annealing of ceramic materials. (Rheinische Friedrich-Wilhelms-Universität Bonn, 2015).
17. McMillan, P. A Raman spectroscopic study of glasses in the system CaO-MgO-SiO_2. *Am. Mineral.* **69**, 645–659 (1984).
18. Swamy, V. & Dubrovinsky, L. S. Thermodynamic data for the phases in the CaSiO<inf>3</inf> system. *Geochim. Cosmochim. Acta* **61**, (1997).
19. Richet, P., Mysen, B. O. & Ingrin, J. High-temperature X-ray diffraction and Raman spectroscopy of diopside and pseudowollastonite. *Phys. Chem. Miner.* **25**, 401–414 (1998).
20. Bouhifd, M. A., Gruener, G., Mysen, B.

O. & Richet, P. Premelting and calcium mobility in gehlenite (Ca2Al2SiO7) and pseudowollastonite (CaSiO3). *Phys. Chem. Miner.* **29**, 655–662 (2002).

21. Khoo, T. C. *et al.* Quantitative label-free imaging of iron-bound transferrin in breast cancer cells and tumors. *Redox Biol.* **36**, 101617 (2020).

22. Brun, N. *et al.* In situ monitoring of styrene polymerization using Raman spectroscopy. Multi-scale approach of homogeneous and heterogeneous polymerization processes. *J. Raman Spectrosc.* **44**, 909–915 (2013).

23. Wulfman, C., Djaker, N., Sadoun, M. & Lamy De La Chapelle, M. 3Y-TZP in-depth phase transformation by raman spectroscopy: A comparison of three methods. *J. Am. Ceram. Soc.* **97**, 2233–2240 (2014).

24. Hemberger, Y., Wichtner, N., Berthold, C. & Nickel, K. G. Quantification of yttria in stabilized zirconia by Raman spectroscopy. *Int. J. Appl. Ceram. Technol.* **13**, 116–124 (2016).

25. Wulfman, C. *et al.* Raman spectroscopy evaluation of subsurface hydrothermal degradation of zirconia. *J. Am. Ceram. Soc.* **95**, 2347–2351 (2012).

26. M. Becker; H. P. Strunk, S. C. Raman imaging of grain orientation, strain, crystallinity and doping levels in solar silicon. in *Raman Imaging:Techniques and Applications* (ed. Zoubir, A.) 256–299 (Springer Series in Optical Sciences, 2012).

27. Pasteris, J. D. & Beyssac, O. Welcome to Raman spectroscopy: Successes, challenges, and pitfalls. *Elements* **16**, 87–92 (2020).

28. Yaseen, T., Sun, D. & Cheng, J. Raman imaging for food quality and safety evaluation : Fundamentals and applications. *Trends Food Sci. Technol.* **62**, 177–189 (2017).

29. Qin, J., Chao, K. & Kim, M. S. *Introduction to Raman Chemical Imaging Technology*. *Computer Vision Technology for Food Quality Evaluation: Second Edition* (Elsevier Inc., 2016). doi:10.1016/B978-0-12-802232-0.00006-2.

30. Everall, N. Depth profiling with confocal Raman microscopy, part I. *Spectroscopy* **19**, 22–28 (2004).

31. Geisler, T., Dohmen, L., Lenting, C. & Fritzsche, M. B. K. Real time in situ observations of reaction and transport phenomena during silicate glass corrosion by fluid-cell Raman spectroscopy. *Nat. Mater.* in press (2019) doi:10.1038/s41563-019-0293-8.

32. Hövelmann, J., Putnis, A., Geisler, T., Schmidt, B. C. & Golla-Schindler, U. The replacement of plagioclase feldspars by albite: Observations from hydrothermal experiments. *Contrib. to Mineral. Petrol.* **159**, 43–59 (2010).

33. King, H. & Geisler, T. Tracing mineral reactions using confocal Raman spectroscopy. *Minerals* **8**, 158 (2018).

34. Daniel, I., Gillet, P., Poe, B. T. & McMillan, P. F. In-situ high-temperature Raman spectroscopic studies of aluminosilicate liquids. *Phys. Chem. Miner.* **22**, 74–86 (1995).

35. Borer, W. J., Mitra, S. S. & Namjoshi, K. V. Line shape and temperature dependence of the first order Raman spectrum of diamond. *Solid State Commun.* **9**, 1377–1381 (1971).

36. Liu, M. S., Bursill, L. A., Prawer, S. & Beserman, R. Temperature dependence of the first-order Raman phonon line of diamond. *Phys. Rev. B - Condens. Matter Mater. Phys.* **61**, 3391–3395 (2000).

37. Hirata, T. & Ohuchi, F. . Temperature dependence of the Raman spectra of ZrO2. *J. Am. Ceram. Soc.* **117**, 361–364 (2001).

38. Cuscó, R. *et al.* Temperature dependence of Raman scattering in

<math display="inline"> <mrow> <mi>ZnO</mi> </mrow> </math>. *Phys. Rev. B* **75**, 165202 (2007).

39. Menéndez, J. & Cardona, M. Temperature dependence of the first-order Raman scattering by phonons in Si, Ge, and -Sn: Anharmonic effects. *Phys. Rev. B* **29**, 2051–2059 (1984).

40. Hart, T., Aggarwal, R. & Lax, B. Temperature Dependence of Raman Scattering in Silicon. *Phys. Rev. B* **1**, 638–642 (1970).

41. Ohsaka, T. Temperature Dependence of the Raman Spectrum in Anatase TiO2. *J. Phys. Soc. Japan* **48**, 1661–1668 (1979).

42. Herchen, H. & Cappelli, M. A. First-order Raman spectrum of diamond at high temperatures. *Phys. Rev. B* **43**, 11740–11744 (1991).

43. Gillet, P., Biellmann, C., Reynard, B. & Mcmillan, P. Raman-Spectroscopic Studies of Carbonates .1. High-Pressure and High-Temperature Behavior of Calcite, Magnesite, Dolomite and Aragonite. *Phys. Chem. Miner.* **20**, 1–18 (1993).

44. Daniel, I., Gillet, P., McMillan, P. F. & Richet, P. An In-situ High-Temperature Structural Study of Stable and Metastable CaAl2Si2O8 Polymorphs. *Mineral. Mag.* **59**, 25–33 (1995).

45. Shoval, S., Boudeulle, M., Yariv, S., Lapides, I. & Panczer, G. Micro-Raman and FT-IR spectroscopy study of the thermal transformations of St. Claire dickite. *Opt. Mater. (Amst).* **16**, 319–327 (2001).

46. McKeown, D. A. Raman spectroscopy and vibrational analyses of albite: From 25 °C through the melting temperature. *Am. Mineral.* **90**, 1506–1517 (2005).

47. Boussois, K., Tessier-Doyen, N. & Blanchart, P. Anisotropic kinetic of the kaolinite to mullite reaction sequence in multilayer ceramics. *J. Eur. Ceram. Soc.* **33**, 243–249 (2013).

48. L'vov, B. V. Mechanism and kinetics of thermal decomposition of carbonates. *Thermochim. Acta* **386**, 1–16 (2002).

49. Maximenko, A. L. & Olevsky, E. A. Effective diffusion coefficients in solid-state sintering. *Acta Mater.* **52**, 2953–2963 (2004).

50. Djohari, H. & Derby, J. J. Transport mechanisms and densification during sintering: II. Grain boundaries. *Chem. Eng. Sci.* **64**, 3810–3816 (2009).

51. Milke, R., Wiedenbeck, M. & Heinrich, W. Grain boundary diffusion of Si, Mg, and O in enstatite reaction rims: A SIMS study using isotopically doped reactants. *Contrib. to Mineral. Petrol.* **142**, 15–26 (2001).

52. Milke, R. & Heinrich, W. Diffusion-controlled growth of wollastonite rims between quartz and calcite: Comparison between nature and experiment. *J. Metamorph. Geol.* **20**, 467–480 (2002).

53. Cultrone, G., Rodriguez-Navarro, C., Sebastian, E., Cazalla, O. & De La Torre, M. J. Carbonate and silicate phase reactions during ceramic firing. *Eur. J. Mineral.* **13**, 621–634 (2001).

54. Raith, M. M., Hoffbauer, R., Spiering, B., Shinoto, M. & Nakamura, N. Melting behaviour of feldspar clasts in high-fired Sue ware. *Eur. J. Mineral.* **28**, 385–407 (2016).

55. Salmag & Scholze. *Keramik*. (Springer, 2007).

56. Nkou Bouala, G. I. *et al.* From in Situ HT-ESEM Observations to Simulation: How Does Polycrystallinity Affects the Sintering of CeO2Microspheres? *J. Phys. Chem. C* **120**, 386–395 (2016).

57. Podor, R. *et al.* Dynamic aspects of cerium dioxide sintering: HT-ESEM study of grain growth and pore elimination. *J. Eur. Ceram. Soc.* **32**, 353–362 (2012).

58. Zhang, J., Huang, F. & Lin, Z. Progress of nanocrystalline growth kinetics based on oriented attachment. *Nanoscale* **2**, 18–34 (2010).

59. Stange, K., Lenting, C. & Geisler, T. Insights into the evolution of carbonate-bearing kaolin during sintering revealed by in situ hyperspectral Raman imaging. *J. Am. Ceram. Soc.* **101**, 897–910 (2018).

60. Hauke, K., Kehren, J., Böhme, N., Zimmer, S. & Geisler, T. In situ Hyperspectral Raman Imaging: A new Method to investigate Sintering Processes of Ceramic Material at High Temperature. *Appl. Sci.* submitted (2019) doi:10.3390/app9071310.

61. Stewart, S., Priore, R. J., Nelson, M. P. & Treado, P. J. Raman imaging. *Annu. Rev. Anal. Chem.* **5**, 337–360 (2012).

62. Hibbert, R., Price, M. C., Kinnear, T. M., Cole, M. J. & Burchell, M. J. The effects of temperature on the Raman spectrum of high purity quartz crystals. in *46th Lunar and Planetary Science Conference* 2–3 (The Woodlands, TX, USA, 16–20 March 2015, 2015).

63. Swamy, V., Dubrovinsky, L. S. & Tutti, F. High-Temperature Raman Spectra and Thermal Expansion of Wollastonite. *J. Am. Ceram. Soc.* **80**, 2237–2247 (1997).

64. Sharma, S. K., Simons, B. & Yoder, H. S. Raman study of anorthite, calcium Tschermak's pyroxene, and gehlenite in crystalline and glassy states. *Am. Mineral.* **68**, 1113–1125 (1983).

65. Daniel, I., Gillet, P., McMillan, P. F. & Richet, P. An in-situ high-temperature structural study of stable and metastable CaAl 2 Si 2 O 8 polymorphs . *Mineral. Mag.* **59**, 25–33 (1995).

66. Kieffer, S. W. Thermodynamics and lattice vibrations of minerals: 5. Applications to phase equilibria, isotopic fractionation, and high-pressure thermodynamic properties. *Rev. Geophys.* **20**, 827–849 (1982).

67. Gale, J. D. & Rohl, A. L. The General Utility Lattice Program (GULP). *Mol. Simul.* **29**, 291–341 (2003).

68. Richet, P., Robie, R. A. & Hemingway, B. S. Thermodynamic properties of wollastonite, pseudowollastonite and CaSiO3 glass and liquid. *Eur. J. Mineral.* **3**, 475–484 (1991).

69. Seryotkin, Y. V., Sokol, E. V. & Kokh, S. N. Natural pseudowollastonite: Crystal structure, associated minerals, and geological context. *Lithos* **134**–**135**, 75–90 (2012).

70. Tschegg, C., Ntaflos, T. & Hein, I. Thermally triggered two-stage reaction of carbonates and clay during ceramic firing - A case study on Bronze Age Cypriot ceramics. *Appl. Clay Sci.* **43**, 69–78 (2009).

71. Shoval, S. Using FT-IR spectroscopy for study of calcareous ancient ceramics. *Opt. Mater. (Amst).* **24**, 117–122 (2003).

72. Shoval, S., Yofe, O. & Nathan, Y. Distinguishing between natural and recarbonated calcite in oil shale ashes. *J. Therm. Anal. Calorim.* **71**, 883–892 (2003).

73. Schmid, T. & Dariz, P. Shedding light onto the spectra of lime: Raman and luminescence bands of CaO, Ca(OH)2 and CaCO3. *J. Raman Spectrosc.* **46**, 141–146 (2014).

74. Putnis, A. *Introduction to mineral sciences*. vol. 5 (Cambridge University Press, 2003).

75. Holm, E. A. & Foiles, S. M. How grain growth stops: A mechanism for grain-growth stagnation in pure materials. *Science (80-.).* **328**, 1138–1141 (2010).

76. Geisler-wierwille, T., Schaltegger, U. & Tomaschek, F. Re-equilibration of Zircon in Aqueous Fluids and Melts. (2007) doi:10.2113/gselements.3.1.43.

77. Putnis, A. Mineral replacement reactions: from macroscopic

observations to microscopic mechanisms. *Mineral. Mag.* **66**, 689–708 (2002).

78. Johannes, W., Koepke, J., Behrens, H. & Hannover, D. Partial melting reactions of plagioclases and plagioclase-bearing systems. in *Feldspars and their Reactions* (ed. Parson, I.) 161–194 (Springer, Dordrecht, 1994).

79. Geisler, T., Burakov, B. E., Zirlin, V., Nikolaeva, L. & Pöml, P. A Raman spectroscopic study of high-uranium zircon from the Chernobyl 'lava'. *Eur. J. Mineral.* **17**, 883–894 (2005).

80. Van Nguyen, C. *et al.* A comparative study of different sintering models for Al2O3. *J. Ceram. Soc. Japan* **124**, 301–312 (2016).

81. German, R. M. Critical Overview of Sintering Computer Simulations. *V. Arnhold, C.L. Chu, W.F. Jandeska, H.I. Sanderow (Eds.), Adv. Powder Metall. 6 Part. Mater.* **9**, 1–15 (2002).

82. Böhme, N., Hauke, K., Neuroth, M. & Geisler, T. In situ Raman imaging of high-temperature solid-state reactions in the CaSO 4 – SiO 2 system. *Int. J. Coal Sci. &Technology* **6**, (2019).

83. Böhme, N., Hauke, K., Neuroth, M. & Geisler, T. In Situ Hyperspectral Raman Imaging of Ternesite Formation and Decomposition at High Temperatures. *Minerals* **10**, 287 (2020).

84. Gaidies, F., Milke, R., Heinrich, W. & Abart, R. Metamorphic mineral reactions: Porphyroblast, corona and symplectite growth. *EMU Notes Mineral.* **16**, 469–540 (2017).

85. Abart, R., Kunze, K., Milke, R., Sperb, R. & Heinrich, W. Silicon and oxygen self diffusion in enstatite polycrystals: The Milke et al. (2001) rim growth experiments revisited. *Contrib. to Mineral. Petrol.* **147**, 633–646 (2004).

86. Tzvetanova, Y., Kadyiski, M. & Petrov, O. Parawollastonite (wollastonite-2M polytype) from the skarns in Zvezdel pluton, Eastern Rhodopes - A single crystal study. *Bulg. Chem. Commun.* **44**, 131–136 (2012).

87. Remy, C., Reynard, B. & Madon, M. Raman Spectroscopic Investigations of Dicalcium Silicate: Polymorphs and High-Temperature Phase Transformations. *J. Am. Ceram. Soc.* **80**, 413–423 (1997).

88. Hoy, C. & Luidold, S. Das Dreistoffsystem Al2O3-CaO-SiO2 – ein Vergleich von berechneten und gemessenen Daten. *BHM Berg- und Hüttenmännische Monatshefte* **157**, 7–13 (2012).

89. Gou, Z. & Chang, J. Synthesis and in vitro bioactivity of dicalcium silicate powders. *J. Eur. Ceram. Soc.* **24**, 93–99 (2004).

90. Gou, Z., Chang, J. & Zhai, W. Preparation and characterization of novel bioactive dicalcium silicate ceramics. *J. Eur. Ceram. Soc.* **25**, 1507–1514 (2005).

91. Hazar, A. B. Y. Preparation and in vitro bioactivity of CaSiO3 powders. *Ceram. Int.* **33**, 687–692 (2007).

92. Groves, G. W. Phase transformations in dicalcium silicate. *J. Mater. Sci.* **18**, 1615–1624 (1983).

93. Liu, X., Morra, M., Carpi, A. & Li, B. Bioactive calcium silicate ceramics and coatings. *Biomed. Pharmacother.* **62**, 526–529 (2008).

94. Hench, L. L. & Thompson, I. Twenty-first century challenges for biomaterials. *J. R. Soc. Interface* **7 Suppl 4**, S379-91 (2010).

95. Wu, C. & Chang, J. A review of bioactive silicate ceramics. *Biomed. Mater.* **8**, (2013).

96. Lee, K. Y. *et al.* Ceramic bioactivity: Progresses, challenges and perspectives. *Biomed. Mater.* **1**, (2006).

97. Ou, J. *et al.* Preparation and in vitro bioactivity of novel merwinite ceramic.

Biomed. Mater. **3**, (2008).

98. Zhong, H. *et al.* Mechanical properties and bioactivity of β-Ca2SiO4ceramics synthesized by spark plasma sintering. *Ceram. Int.* **37**, 2459–2465 (2011).

99. Zhao, W., Chang, J., Wang, J., Zhai, W. & Wang, Z. In vitro bioactivity of novel tricalcium silicate ceramics. *J. Mater. Sci. Mater. Med.* **18**, 917–923 (2007).

100. Abramczyk, H. & Brozek-pluska, B. Raman imaging in biochemical and biomedical applications . Diagnosis and treatment of breast cancer. *Chem. Rev.* **113**, 5766–5781 (2012).

101. Toporski, J. *Confocal Raman microscopy*. vol. 66 (Springer Series in Surface Sciences, 2018).

102. Geisler, T., Burakov, B. E., Zirlin, V., Nikolaeva, L. & Pöml, P. A Raman spectroscopic study of high-uranium zircon from the Chernobyl 'lava'. *Eur. J. Mineral.* **17**, 883–894 (2005).

103. Geisler, T., Popa, K. & Konings, R. J. M. Evidence for lattice strain and non-ideal behavior in the (La1−xEux)PO4 solid solution from X-ray diffraction and vibrational spectroscopy. *Front. Earth Sci.* **4**, (2016).

104. Klemens, P. G. Anharmonic decay of optical phonon in diamond. *Phys. Rev. B* **11**, 3206–3207 (1975).

105. Huang, F. *et al.* Temperature dependence of the Raman spectra of carbon nanotubes. *J. Appl. Phys.* **84**, 4022–4024 (1998).

106. Richet, P., Ingrin, J., Mysen, B. O., Courtial, P. & Gillet, P. Premelting effects in minerals: an experimental study. *Earth Planet. Sci. Lett.* **121**, 589–600 (1994).

107. Malfait, W. J. & Halter, W. E. Structural relaxation in silicate glasses and melts: High-temperature Raman spectroscopy. *Phys. Rev. B - Condens. Matter Mater. Phys.* **77**, 1–6 (2008).

108. Neuville, D. R. & Mysen, B. O. Role of aluminium in the silicate network: In situ, high-temperature study of glasses and melts on the join SiO2-NaAlO2. *Geochim. Cosmochim. Acta* **60**, 1727–1737 (1996).

109. Voron'ko, Y. K., Sobol', A. A., Ushakov, S. N., Jiang Guochang & You Jinglin. Phase transformations and melt structure of calcium metasilicate. *Inorg. Mater.* **38**, 825–830 (2002).

110. Gillet, P. Raman spectroscopy at high pressure and high temperature. Phase transitions and thermodynamic properties of minerals. *Phys. Chem. Miner.* **23**, 263–275 (1996).

111. Osipov, A. A. & Osipova, L. M. Raman scattering study of barium borate glasses and melts. *J. Phys. Chem. Solids* **74**, 971–978 (2013).

112. Saloman, E. B. Wavelengths, energy level classifications, and energy levels for the spectrum of neutral mercury. *J. Phys. Chem. Ref. Data* **35**, 1519–1548 (2006).

113. von Salje, E. Experimentelle Untersuchung der Ramanstreuung an Kristallpulvern (experimental investigation of Raman scattering of crystall powder). *J. Appl. Cryst.* **6**, 442–446 (1973).

114. Linkam Scientific Instruments TS1500. Linkam Scientific Instruments TS1500. (2018).

115. Neuville, D. R., de Ligny, D. & Henderson, G. S. Advances in Raman spectroscopy applied to earth and material sciences. *Rev. Mineral. Geochemistry* **78**, 509–541 (2014).

116. Vajna, B. *et al.* Comparison of chemometric methods in the analysis of pharmaceuticals with hyperspectral Raman imaging. *J. Raman Spectrosc.* **42**, 1977–1986 (2011).

117. Nasdala, L., Beyssac, O., Schopf, J. W. & Bernd Bleisteiner. Application of Raman-based images in the Earth Sciences. in *Raman*

Imaging:Techniques and Applications 145–189 (Springer Series in Optical Sciences, 2012).

118. Kramida, A., Ralchenko, Yu., Reader, J. and N. A. T. (20l6). NIST: Atomic Spectra Database - Version History. *National Institute of Standards and Technology* (2016).

119. Tian, H., Wachs, I. E. & Briand, L. E. Comparison of UV and visible Raman spectroscopy of bulk metal molybdate and metal vanadate catalysts. *J. Phys. Chem. B* **109**, 23491–23499 (2005).

120. Zouboulis, E., Renusch, D. & Grimsditch, M. Advantages of ultraviolet Raman scattering for high temperature investigations. *Appl. Phys. Lett.* **72**, 1–3 (1998).

121. Hope, G. A., Woods, R. & Munce, C. G. Raman microprobe mineral identification. *Miner. Eng.* **14**, 1565–1577 (2001).

122. Hopkins, J. B. & Farrow, L. A. Raman microprobe determination of local crystal orientation. *J. Appl. Phys.* **59**, 1103–1110 (1986).

123. Chaigneau, M., Picardi, G., Girard, H. A., Arnault, J. C. & Ossikovski, R. Laser heating versus phonon confinement effect in the Raman spectra of diamond nanoparticles. *J. Nanoparticle Res.* **14**, (2012).

124. Bersani, D., Lottici, P. P. & Ding, X. Phonon confinement effects in the Raman scattering by TiO 2 nanocrystals. *Appl. Phys. Lett.* **72**, 72–75 (1998).

125. Swamy, V. *et al.* Finite-size and pressure effects on the Raman spectrum of nanocrystalline anatase Ti O2. *Phys. Rev. B - Condens. Matter Mater. Phys.* **71**, 15–17 (2005).

126. Swamy, V. Size-dependent modifications of the first-order Raman spectra of nanostructured rutile TiO2. *Phys. Rev. B - Condens. Matter Mater. Phys.* **77**, 15–18 (2008).

127. Namba, Y., Heidarpour, E. & Nakayama, M. Size effects appearing in the Raman spectra of polycrystalline diamonds Size effects appearing in the Raman spectra of polycrystalline. *J. Appl. Phys.* **1748**, 1–5 (2012).

128. Yoshikawa, M. *et al.* Raman scattering from nanometer-sized diamond Raman scattering from nanometer-sized diamond. *Appl. Phys. Lett.* **694**, 5–8 (2008).

129. Zhao, X. Z., Cherian, K. A., Roy, R. & White, W. B. Downshift of Raman peak in diamond powders. *J. Mater. Res.* **13**, 1974–1976 (1998).

130. Polsky, C. H., Smith, K. H. & Wolf, G. H. Effect of pressure on the absolute Raman scattering cross section of SiO2 and GeO2 glasses. *J. Non. Cryst. Solids* **248**, 159–168 (1999).

131. Quittet, A. M. & Lambert, M. Temperature dependence of the Raman cross section and light absorption in cubic BaTiO3. *Solid State Commun.* **12**, 1053–1055 (1973).

132. Demos, S. G. *et al.* Measurement of the Raman scattering cross section of the breathing mode in KDP and DKDP crystals. *Opt. Express* **19**, 21050 (2011).

133. Rappoport, D. Berechnung von Raman-Intensitäten mit zeitabhängiger Dichte-Funktionaltheorie. (Universitätsverlag Karlsruhe, 2007).

134. Neuville, D. R., Cormier, L. & Massiot, D. Al coordination and speciation in calcium aluminosilicate glasses: Effects of composition determined by27Al MQ-MAS NMR and Raman spectroscopy. *Chem. Geol.* **229**, 173–185 (2006).

135. Neuville, D. R. Viscosity, structure and mixing in (Ca, Na) silicate melts. *Chem. Geol.* **229**, 28–41 (2006).

136. Guerette, M. & Huang, L. A simple and convenient set-up for high-temperature Brillouin light scattering. *J. Phys. D. Appl. Phys.* **45**, 1–7 (2012).

137. Behrens, H., Roux, J., Neuville, D. R. & Siemann, M. Quantification of dissolved H2O in silicate glasses using confocal microRaman spectroscopy. *Chem. Geol.* **229**, 96–112 (2006).

138. Everall, N. J. Confocal Raman microscopy: Why the depth resolution and spatial accuracy can be much worse than you think. *Appl. Spectrosc.* **54**, 1515–1520 (2000).

139. Everall, N. J. Depth Profiling with confocal Raman microscopy, part II. *Spectroscopy* **19**, 16–27 (2004).

140. Everall, N. J. Confocal Raman microscopy: common errors and artefacts. *Analyst* **135**, 2512 (2010).

141. Presser, V., Keuper, M., Berthold, C. & Nickel, K. G. Experimental determination of the Raman sampling depth in zirconia ceramics. *Appl. Spectrosc.* **63**, 1288–92 (2009).

142. Everall, N. Optimising image quality in 2D and 3D confocal Raman mapping. *J. Raman Spectrosc.* **45**, 133–138 (2014).

143. Zoubir, A. *Raman Imaging: Techniques and Applications*. *Springer Series in Optical Sciences* vol. 168 (Springer Series in Optical Sciences, 2012).

144. Everall, N. J. Modeling and measuring the effect of refraction on the depth resolution of confocal Raman microscopy. *Appl. Spectrosc.* **54**, 773–782 (2000).

145. Juang, C. B., Finzi, L. & Bustamante, C. J. Design and application of a computer-controlled confocal scanning differential polarization microscope. *Rev. Sci. Instrum.* **59**, 2399–2408 (1988).

146. Nankervis, J. C. & Furlong, R. B. Phase changes in mineral matter of North Dakota lignites caused by heating to 1200 °C. *Fuel* **59**, 425–430 (1980).

147. Lin, K. *et al.* Study of the mechanical property and in vitro biocompatibility of CaSiO3ceramics. *Ceram. Int.* **31**, 323–326 (2005).

148. Avrami, M. Kinetics of phase change. I: General theory. *J. Chem. Phys.* **7**, 1103–1112 (1939).

149. Knudsen, F. P. Dependence of mechanical strength of brittle polycrystalline specimens on porosity and grain size. *J. Am. Ceram. Soc.* **42**, 376–387 (1959).

150. Schneider, C. A., Rasband, W. S. & Eliceiri, K. W. NIH Image to ImageJ: 25 years of image analysis. *Nat. Methods* **9**, 671–675 (2012).

151. Herzberg, G. *Atomic Spectra and Atomic Structure*. (Dover puplications, 1944).

152. Geisler, T., Pöml, P., Stephan, T., Janssen, A. & Putnis, A. Experimental observation of an interface-controlled pseudomorphic replacement reaction in a natural crystalline pyrochlore. *Am. Mineral.* **90**, 1683–1687 (2005).

153. King, H. E., Plümper, O., Geisler, T. & Putnis, A. Experimental investigations into the silicification of olivine: Implications for the reaction mechanism and acid neutralization. *Am. Mineral.* **96**, 1503–1511 (2011).

154. Pan, X., Zhang, D., Wu, Y. & Yu, H. Synthesis and characterization of calcium aluminate compounds from gehlenite by high-temperature solid-state reaction. *Ceram. Int.* **44**, 13544–13550 (2018).

155. Ptáček, P., Opravil, T., Šoukal, F., Havlica, J. & Holešinský, R. Kinetics and mechanism of formation of gehlenite, Al-Si spinel and anorthite from the mixture of kaolinite and calcite. *Solid State Sci.* **26**, 53–58 (2013).

156. Majerová, M. *et al.* Crystallization kinetics of gehlenite glass microspheres. *J. Therm. Anal. Calorim.* (2020) doi:10.1007/s10973-020-09305-7.

157. Jia, D., Kim, D. & Kriven, W. M.

Sintering behavior of gehlenite. Part I: Self-forming, macro-/mesoporous gehlenite - Pore-forming mechanism, microstructure, mechanical, and physical properties. *J. Am. Ceram. Soc.* **90**, 1760–1773 (2007).

158. Abràmoff, M. D., Magalhães, P. J. & Ram, S. J. Image processing with imageJ. *Biophotonics Int.* **11**, 36–41 (2004).

159. Dvořáková, P., Kloužková, A., Kohoutková, M. & Kolářová, M. Moisture expansion of Ca-rich ceramic body. *IOP Conf. Ser. Mater. Sci. Eng.* **1050**, 012004 (2021).

160. Klosek-Wawrzyn, E., Malolepszy, J. & Murzyn, P. Sintering behavior of kaolin with calcite. *Procedia Eng.* **57**, 572–582 (2013).

161. Freundlich, H. *Kapillarchemie: Eine Darstellung der Chemie der Kolloide und verwandter Gebiete [Capillary Chemistry: A presentation of colloid chemistry and related fields]*. (Akademische Verlagsgesellschaft, 1909).

162. Mugnaioli, E. *et al.* Electron Diffraction on Flash-Frozen Cowlesite Reveals the Structure of the First Two-Dimensional Natural Zeolite. *ACS Cent. Sci.* **6**, 1578–1586 (2020).

163. Tsai, Y. L. *et al.* Raman spectroscopic characteristics of zeolite group minerals. *Minerals* **11**, 1–14 (2021).

164. Allegretta, I., Pinto, D. & Eramo, G. Effects of grain size on the reactivity of limestone temper in a kaolinitic clay. *Appl. Clay Sci.* **126**, 223–234 (2016).

165. Redaoui, D., Sahnoune, F., Heraiz, M., Belhouchet, H. & Fatmi, M. Thermal decomposition kinetics of Algerian Tamazarte kaolinite by thermogravimetric analysis. *Trans. Nonferrous Met. Soc. China (English Ed.* **27**, 1849–1855 (2017).

166. Fabbri, B., Gualtieri, S. & Leonardi, C. Modifications induced by the thermal treatment of kaolin and determination of reactivity of metakaolin. *Appl. Clay Sci.* **73**, 2–10 (2013).

167. Cheng, H., Liu, Q., Yang, J., Ma, S. & Frost, R. L. The thermal behavior of kaolinite intercalation complexes-A review. *Thermochim. Acta* **545**, 1–13 (2012).

168. Saraya, M. E. I. & Sayed, M. Characterization and Evaluation of Natural Zeolite As a Pozzolanic Material. *Al-Azhar Bull. Sci.* **29**, 17–34 (2018).

169. Heimann, R. B. *Classic and Advanced Ceramics: From Fundamentals to Applications*. (WILEY-VCH Verlag GmbH & Co. KGaA, 2010).

170. Zimmer, S. In Situ Hyperspectral Raman Imaging of High Temperature Solid-solid Reactions in the System Al 2 O 3 - SiO 2 -CaO. (2019).

171. Lafuente, B., Downs, R. T., Yang, H. & Stone, N. RRUFF™ Project. *power databases RRUFF Proj. Highlights Mineral. Crystallogr. T Armbruster R M Danisi, eds.* 1–30 (2015).

172. Gualtieri, A., Bellotto, M., Artioli, G. & Clark, S. M. Kinetic study of the kaolinite-mullite reaction sequence. Part II: Mullite formation. *Phys. Chem. Miner.* **22**, 215–222 (1995).

173. Bellotto, M., Gualtieri, A., Artioli, G. & Clark, S. M. Kinetic study of the kaolite-mullite reaction sequence-Part_1_kaolinite dehydroxylation. *Phys. Chem. Miner.* **22**, 207–214 (1995).

174. Frost, R. A. Y. L. & Vassallo, A. M. The dehydroxylation of kaolinite clay minerals using infrared emission spectroscopy. **44**, 635–651 (1996).

175. Frost, R. L. & Van Der Gaast, S. J. Kaolinite Hydroxyls-A Raman Microscopy Study. *Clay Miner.* **32**, 471–484 (1997).

176. Sperinck, S., Raiteri, P., Marks, N. &

Wright, K. Dehydroxylation of kaolinite to metakaolin - A molecular dynamics study. *J. Mater. Chem.* **21**, 2118–2125 (2011).

177. Gasparini, E. *et al.* Thermal dehydroxylation of kaolinite under isothermal conditions. *Appl. Clay Sci.* **80**–**81**, 417–425 (2013).

178. Traoré, K., Kabré, T. & Blanchart, P. Low temperature sintering of clay for pottery from Burkina Faso. *Appl Clay Sci.* **17**, 279–292 (2000).

179. Ptáček, P. *et al.* The kinetics and mechanism of kaolin powder sintering I. The dilatometric CRH study of sinter-crystallization of mullite and cristobalite. *Powder Technol.* **232**, 24–30 (2012).

180. Ptáček, P. *et al.* The influence of structure order on the kinetics of dehydroxylation of kaolinite. *J. Eur. Ceram. Soc.* **33**, 2793–2799 (2013).

181. Dion, P. Kinetic Study by Controlled-Transformation Rate Thermal Analysis of the Dehydroxylation of Kaolinite. *Clay Miner.* **33**, 269–276 (1998).

182. Dubois, J., Murat, M., Amroune, A., Carbonneau, X. & Gardon, R. High-temperature transformation in kaolinite: the role of the crystallinity and of the firing atmosphere. *Appl. Clay Sci.* **10**, 187–198 (1995).

183. Ptáček, P. *et al.* Isothermal kinetic analysis of the thermal decomposition of kaolinite: The thermogravimetric study. *Thermochim. Acta* **501**, 24–29 (2010).

184. Piga, L. thermochimica acta Thermogravimetry of a kaolinite-alunite ore. *Thermochim. Acta* **265**, 177–187 (1995).

185. Gualtieri, A. & Bellotto, M. Modelling the structure of the metastable phases in the reaction sequence kaolinite-mullite by X-ray scattering experiments. *Phys. Chem. Miner.* **25**, 442–452 (1998).

186. De Noni, A., Hotza, D., Soler, V. C. & Vilches, E. S. Influence of composition on mechanical behaviour of porcelain tile. Part I: Microstructural characterization and developed phases after firing. *Mater. Sci. Eng. A* **527**, 1730–1735 (2010).

187. Heimann, R. B. Mineralogy and Chemistry of the Ceramic Firing Process. *Class. Adv. Ceram.* 99–118 (2010) doi:10.1002/9783527630172.ch4.

188. Bost, N., Duraipandian, S., Guimbretière, G. & Poirier, J. Raman spectra of synthetic and natural mullite. *Vib. Spectrosc.* **82**, 50–52 (2016).

189. Santana, L. N. L. *et al.* Mullite formation from bentonites containing kaolinite: Effect of composition and synthesis parameters. *Appl. Clay Sci.* **87**, 28–33 (2014).

190. Sun, J., Wu, Z., Cheng, H., Zhang, Z. & Frost, R. L. A Raman spectroscopic comparison of calcite and dolomite. *Spectrochim. Acta - Part A Mol. Biomol. Spectrosc.* **117**, 158–162 (2014).

191. Osborn, E. F. & Schairer, J. F. The ternary system pseudowollastonite-akermanite-gehlenite. *Am. J. Sci.* **239**, 715–763 (1941).

192. Rodriguez-Navarro, C., Ruiz-Agudo, E., Luque, A., Rodriguez-Navarro, A. B. & Ortega-Huertas, M. Thermal decomposition of calcite: Mechanisms of formation and textural evolution of CaO nanocrystals. *Am. Mineral.* **94**, 578–593 (2009).

193. Ewing, J., Beruto, D. & Searcy, A. W. The Nature of CaO Produced by Calcite Powder Decomposition in Vacuum and in CO2. *J. Am. Ceram. Soc.* **62**, 580–584 (1979).

194. Beruto, D. & Searcy, A. W. Calcium oxides of high reactivity. *Nature* **263**, 221–222 (1976).

195. Wieczorek-Ciurowa, K., Paulik, J. &

Paulik, F. Influence of foreign materials upon the thermal decomposition of dolomite, calcite and magnesite Part 1. *Thermichimica Acta* **38**, 157–164 (1980).

196. Kehren, J. The Formation of Calcium Silicates in the CaO-SiO2-System studied by In situ Hyperspectral Raman Imaging. (Rheinische Friedrich-Wilhelms-Universität Bonn, 2018).

197. Beruto, D. T., Searcy, A. W. & Kim, M. G. Microstructure, kinetic, structure, thermodynamic analysis for calcite decomposition: Free-surface and powder bed experiments. *Thermochim. Acta* **424**, 99–109 (2004).

198. Beruto, D., Barco, L. & Searcy, A. W. Rearrangement of Porous CaO Aggregates During Calcite Decomposition in Vacuum. *J. Am. Ceram. Soc.* **66**, 893–896 (1983).

199. Zhong, Q. & Bjerle, I. Calcination kinetics of limestone and the microstructure of nascent CaO. *Thermochim. Acta* **223**, 109–120 (1993).

200. Shoval, S., Gaft, M., Beck, P. & Kirsh, Y. Thermal behaviour of limestone and monocrystalline calcite tempers during firing and their use in ancient vessels. *J. Therm. Anal.* **40**, 263–273 (1993).

201. Shoval, S. Mineralogical changes upon heating calcitic and dolomitic marl rocks. *Thermochim. Acta* **135**, 243–252 (1988).

202. Kehren, J., Zimmer, S., Hauke, K. & Geisler, T. The Formation of Calcium Silicates in the CaO-SiO2-System studied by In situ Hyperspectral Raman Imaging (HSRI). in *62nd International Colloquium on Refractories 2019 – Supplier Industries enabling REFRACTORIES* 111–114 (2019).

203. Kehren, J., Hauke, K., Zimmer, S. & Geisler, T. Hyperspectral Raman Imaging : A Powerful Tool for Time- , Space- , and Temperature-Resolved In Situ Studies Using the Example of the. in *United International Technical Conference of Refractories* 10–13 (2019).

204. Abd Rashid, R., Shamsudin, R., Abdul Hamid, M. A. & Jalar, A. Low temperature production of wollastonite from limestone and silica sand through solid-state reaction. *J. Asian Ceram. Soc.* **2**, 77–81 (2014).

205. Adylov, G. T. *et al.* Use of wollastonite from the Koitashskoe deposit in the production of ceramics and refractory materials. *Refract. Ind. Ceram.* **43**, 359–361 (2002).

206. Deer, W. A., Howie, R. A. & Zussman, J. Rock-forming minerals Single-Chain Silicates. 668 (1997).

207. Diella, V., Adamo, I., Pagliari, L., Pavese, A. & Francescon, F. Effects of particle size distribution and starting phase composition in Na-feldspar/kaolinite system at high temperature. *J. Eur. Ceram. Soc.* **35**, 1327–1335 (2015).

208. Vichaphund, S., Kitiwan, M., Atong, D. & Thavorniti, P. Microwave synthesis of wollastonite powder from eggshells. *J. Eur. Ceram. Soc.* **31**, 2435–2440 (2011).

209. Mazzucato, E. & Gualtieri, a. F. Wollastonite polytypes in the CaO-SiO 2 system. *Phys. Chem. Miner.* **27**, 565–574 (2000).

210. Zhao, C. & Wang, G. The melting reaction mechanism of NaOH in decomposing Ca2SiO4. *Miner. Process. Extr. Metall. Rev.* **36**, 385–390 (2015).

211. Adamo, I., Diella, V., Pavese, A., Vignola, P. & Francescon, F. Na-feldspar (F) and kaolinite (K) system at high temperature: Resulting phase composition, micro-structural features and mullite-glass Gibbs energy of formation, as a function of F/K ratio and kaolinite crystallinity. *J. Eur. Ceram. Soc.* **33**, 3387–3395 (2013).

212. Kalampounias, A. G. IR and Raman spectroscopic studies of sol – gel

derived alkaline-earth. **34**, 299–303 (2011).

213. Fintor, K., Park, C., Nagy, S., Pál-Molnár, E. & Krot, A. N. Hydrothermal origin of hexagonal CaAl2Si2O8 (dmisteinbergite) in a compact type A CAI from the Northwest Africa 2086 CV3 chondrite. *Meteorit. Planet. Sci.* **49**, 812–823 (2014).

214. Zolotarev, A. A., Krivovichev, S. V., Gurzhiy, T. L. P. V. V., Bocharov, V. N. & Rassomakhin, M. A. Dmisteinbergite, CaAl2Si2O8, a Metastable Polymorph of Anorthite: Crystal-Structure and Raman Spectroscopic Study of the Holotype Specimen. *Minerals* **9**, 1–12 (2019).

215. Fritz, J. *et al.* Donwilhelmsite, [CaAl4Si2O11], a new lunar high-pressure Ca-Al-silicate with relevance for subducted terrestrial sediments. *Am. Mineral.* **105**, 1704–1711 (2020).

216. Kimura, M. *et al.* Kushiroite, CaAlAlSiO6: A new mineral of the pyroxene group from the ALH 85085 CH chondrite, and its genetic significance in refractory inclusions. *Am. Mineral.* **94**, 1479–1482 (2009).

217. Roskosz, M., Toplis, M. J., Besson, P. & Richet, P. Nucleation mechanisms: A crystal-chemical investigation of phases forming in highly supercooled aluminosilicate liquids. *J. Non. Cryst. Solids* **351**, 1266–1282 (2005).

218. Hofmeister, A. M., Wopenka, B. & Locock, A. J. Spectroscopy and structure of hibonite, grossite, and CaAl2 O4: Implications for astronomical environments. *Geochim. Cosmochim. Acta* **68**, 4485–4503 (2004).

219. Brohsonn, N. High temperature Raman spectroscopy of wollastonite. (Rheinische Friedrich-Wilhelms-Universität Bonn, 2017).

List of Tables:

List of Figures:

V Supplementary and additional material

V.I Co-authored article abstracts

Article in '*Minerals*'

In situ Raman imaging of high-temperature solid-state reactions in the $CaSO_4$–SiO_2 system

Nadine Böhme[1], Kerstin Hauke[1], Manuela Neuroth[2], Thorsten Geisler[1]

[1] Institut für Geowissenschaften, Universität Bonn, 53115 Bonn, Germany; kerstinhauke@uni-bonn.de (K.H.); tgeisler@uni-bonn.de (T.G.)

[2] RWE Power AG, F und E, Kraftwerk Niederaußem, 50129 Bergheim, Germany; m.neuroth@rwe.com

** Correspondence: nadine.boehme@uni-bonn.de*

Received: 12 June 2018 / Revised: 9 April 2019 / Accepted: 10 May 2019 / Published online: 27 May 2019

The deposition of mineral phases on the heat transfer surfaces of brown coal power plants may have a negative effect on power plant boilers. The paragenesis of these deposits contains information about the actual temperature prevailed during the combustion of lignite, if the temperature-dependences of distinct mineral transformations or reactions are known. Here, we report results of a sintering study (to ~ 1100°C) with samples containing anhydrite, quartz, and gehlenite, which are typical components of Rhenish lignite ashes. Thermal decompositions and solid-state reactions were analyzed (1) in situ and (2) both in situ and after quenching using confocal hyperspectral Raman imaging. This novel application of confocal Raman spectroscopy provides temperature- and time-resolved, 2-dimensional information about sintering processes with a micrometer-scale resolution. In the course of the sintering experiments with anhydrite and quartz with a weight ratio of 2:1 both polymorphs wollastonite and pseudowollastonite were identified *in situ* at about 920 and 1000°C, respectively. The formation of pseudowollastonite was thus observed about 120°C below the phase transition temperature, demonstrating that it can form metastably. In addition, a'_L-Ca_2SiO_4 was identified at about 1100°C. In samples containing equal weight fractions of anhydrite and quartz that were quenched after firing for 9 h at about 1100°C, β-Ca_2SiO_4 (larnite) crystallized as rims around anhydrite grains and in direct contact to wollastonite. We furthermore observed that, depending on the ratio between quartz and anhydrite, wollastonite replaced quartz grains between 920 and 1100°C., i.e., the higher the quartz content, the lower the formation temperature of wollastonite.

Keywords: Ash deposition, Calcium silicate, Calcium sulfate, High-temperature, Raman imaging

Article in *'International Journal of Coal Science & Technology'*

In Situ Hyperspectral Raman Imaging of Ternesite Formation and Decomposition at High Temperatures

Nadine Böhme[1], Kerstin Hauke[1], Manuela Neuroth[2], Thorsten Geisler[1]

[1] Institut für Geowissenschaften, Universität Bonn, 53115 Bonn, Germany; kerstinhauke@uni-bonn.de (K.H.); tgeisler@uni-bonn.de (T.G.)

[2] RWE Power AG, F und E, Kraftwerk Niederaußem, 50129 Bergheim, Germany; m.neuroth@rwe.com

** Correspondence: nadine.boehme@uni-bonn.de*

Received: 8 February 2020/ Accepted: 19 March 2020/ Published: 21 March 2020

Abstract: Knowledge of the high-temperature properties of ternesite ($Ca_5(SiO_4)_2SO_4$) is becoming increasingly interesting for industry in different ways. On the one hand, the high-temperature product has recently been observed to have cementitious properties. Therefore, its formation and hydration characteristics have become an important field of research in the cement industry. On the other hand, it forms as sinter deposits in industrial kilns, where it can create serious problems during kiln operation. Here, we present two highlights of *in situ* Raman spectroscopic experiments that were designed to study the high-temperature stability of ternesite. First, the spectra of a natural ternesite crystal were recorded from 25 to 1230 °C, which revealed a phase transformation of ternesite to the high-temperature polymorph of dicalcium silicate ($\alpha'L$-Ca_2SiO_4), while the sulfur is degassed. With a heating rate of 10 °C/h, the transformation started at about 730 °C and was completed at 1120 °C. Using *in situ* hyperspectral Raman imaging with a micrometer-scale spatial resolution, we were able to monitor the solid-state reactions and, in particular, the formation properties of ternesite in the model system CaO-SiO_2-$CaSO_4$. In these multi-phase experiments, ternesite was found to be stable between 930 to 1020–1100 °C. Both ternesite and $\alpha'L$-Ca_2SiO_4 were found to co-exist at high temperatures. Furthermore, the results of the experiments indicate that whether or not ternesite or dicalcium silicate crystallizes during quenching to room temperature depends on the reaction progress and possibly on the gas fugacity and composition in the furnace.

Keywords: ternesite; dicalcium silicate; calcium sulfate; high-temperature; *in situ*; Raman imaging

V.II Abstracts of the supervised Bachelor- and Master theses that are related to the PhD project

Synthese und Charakterisierung eines Aluminium-Silizium-Spinells
Florian Wintersberg (2017)
Bachelor thesis

Beim Brennen von Keramiken spielen eine Vielzahl von Mineralphasen eine Rolle. Eine dieser Phasen wird als Aluminium-Silizium-Spinell betitelt. Ziel dieser Arbeit soll die Synthese und Charakterisierung, mittels Ramanspektroskopie, dieser Mineralphase werden. Dies ist von besonderer Bedeutung, da es sich bei Aluminium-Silizium-Spinell um eine Mineralphase aus der Kaolinit/Mullit Reaktionsserie handelt.
Die Reaktionsfolge beschreibt die Mineralphasenumwandlungen welche ein Kaolinit beim Sintern des Grünkörpers, also des ungebrannten Keramik Rohlings, durchläuft. Im ersten Schritt dehydriert der Kaolinit und wird zu einem Metakaolinit. Dieser wird durch weiteres Aufheizen zu einem Aluminium-Silizium-Spinell, welcher wiederum nach weiterem heizen zu Mullit umgewandelt wird. Der Mullit ist ein wichtiges Bindemittel für Keramiken. Die Reaktionsfolge ist jedoch leider nicht ausreichend gut erforscht. Während es über Kaolinit, Metakaolinit und Mullit zahlreiche Abhandlungen mit guten Datengrundlagen gibt, ist der Aluminium-Silizium-Spinell bisher nicht so detailliert mit einem Raman-Spektrometer, untersucht worden. Trotz zahlreicher Abhandlungen über das Mineral gibt es leider kein gutes Referenzspektrum für die Ramanspektroskopie an einem solchen Spinell. Zum Zweck der Synthese wurden mit verschiedenen Kaoliniten Aufheiz-Experimente durchgeführt. Die Ergebnisse wurden mit dem Raman-Spektroskop untersucht. Die Kontrolle erfolgte durch Untersuchungen an der Elektronenstrahl-Mikrosonde und mittels Röntgenpulverdiffraktometrie. Ziel sollte es sein eine Probe zu finden, in der möglichst viele, große und gut kristallisierte Aluminium-Silizium-Spinelle enthalten sind. Ein einzelnes, möglichst großes Mineralkorn sollte dann für eine Messung des Referenzspektrums ausgewählt werden, um möglichst wenig störende Einflüsse auf die Messung zu erhalten.

High temperature Raman spectroscopy of wollastonite
Nils Brohsonn (2017)
Bachelor thesis

Due to its high melting point (1540°CC) (Okrusch and Matthes, 2013) and other characteristics such as low dielectric loss, thermal stability, low thermal expansion, low shrinkage, lack of volatile constituents, fluxing characteristics, whiteness, body permeability, acicular shape renders, and low thermal conductivity, wollastonite is an important material in ceramic industry (Jean et al., 2004; Swamy et al., 1997). The mineral (CaSiO3) consists of calcium and quartz and forms a solid-state solution. Furthermore, it may contain iron, magnesium and manganese substituting calcium. Wollastonite is deployed in dental roots and in artificial bones because of its outstanding bioactivity and biocompatibility (Liu et al., 2004). Due to those properties the production of wollastonite increased during the last years (Rieger, 1995). The purpose of this study was to obtain a reliable calibration of the Raman shift at high temperature in-situ measurements of wollastonite. For further experiments this data provides a basis to determine spatial coherences between mineral phases. Therefore, the high temperature Raman data of synthetic wollastonite and natural wollastonite should be compared. For this purpose wollastonite was synthesized according
to the described method of Kaifi et al. (2004) in Manufacturing of synthetic wollastonite. First, quartz and calcite were analyzed by XRD to determine if the raw material contained impurities of other minerals. Subsequently, the raw material was pressed into pellets of diverse sizes. The pellets were fired by 5°C/min until the
temperature reached 650°C and 750°C, respectively. This temperature was kept

for an hour. Afterwards two other samples were heated up to 1100°C and were kept at this temperature for 5 and 24 hours, respectively. Furthermore, the fired samples were analyzed by Raman spectroscopy, whilst the sample that was fired up to 1100°C and kept there for 24 hours, was analyzed by XRD additionally. However, the fired samples did not form enough wollastonite to perform a heating study.
Following this, only one heating study of a natural wollastonite from Baja California, Mexico, was performed. In this study the sample was fired up to 1200°C, whereby every 10°C a spectrum was recorded. Finally, the results of the study were compared to the Raman data of Swamy et al. (1997).

The formation of calcium silicates in the CaO-SiO_2-system studied by *in situ* hyperspectral Raman imaging (HSRI)
Johannes Kehren (2018)
Master thesis

In the present study the formation of calcium silicates in the CaO-SiO_2-system during sintering was investigated. Green bodies containing lime/calite and quartz/vitreous silica were fired in air to temperatures up to 1100 °C. In the process mineral reactions and the textural evolution were studied at different temperature steps *in situ* by confocal hyperspectral Raman imaging. During the experiments the formation of different polymorphs of $CaSiO_3$ and Ca_2SiO_4 was observed. Dicalcium silicate was firstly detected at ~524 °C and wollastonite formed at 749 °C. Both phases grew rims around the present SiO_2-phase, and partly dissolved it during further firing. Pseudowollastonite crystallized already at 749 °C without wollastonite being present. This is ~375 °C below the accepted critical temperature (1125 ± 10 °C) for the wollastonite-to-pseudowollastonite transformation. In addition, multiple polymorphic phase transformations between Ca_2SiO_4-polymorphs were observed. Between 838 and 882 °C γ-Ca_2SiO_4 transformed to α'_L -Ca_2SiO_4 during firing and during cooling the $\alpha'_L \rightarrow \beta$ transition took place below 524 °C. β-Ca_2SiO_4 was preserved at RT without the use of stabilizers. At last the decarbonation and carbonation reactions of calcite were observed at temperatures from 793 to 838 °C and 749 to 704 °C, respectively.

***In situ* hyperspectral Raman imaging of high temperature solid-solid reactions in the system Al_2O_3-SiO_2-CaO**
Sinje Zimmer (2019)
Master thesis

In situ hyperspectral Raman images were used to study mineral reactions during firing of calcite-kaolinite mixtures. Two types of experimental series were carried out. For the quenching experiment the samples were fired from 660°C to 1110°C in 100°C steps. At each temperature a Raman image was recorded. The samples were subsequently cooled, and a Raman image was recorded at RT before it was fired to the next temperature step. The second type were isothermal experiments at temperatures between 750°C and 931°C with a total dwelling time of 48 h. The quenching experiment mimic normal ex situ experiments and was performed to prof if there are difference between the results of common ex situ and *in situ* experiments. In both experiments the decarbonation, at temperature from 660 to 840°C, and recrystallization of calcite, from 660 to 930°C, could be observed. In addition to that, gehlenite and dicalcium silicate could be detected from 660°C until the end of the experiments. Wollastonite and anorthite were for the first time present at 840°C and were also stable until the end of each experiment. Furthermore, two unknown phases occurred, which could not be identified yet. A phase with a main band near 562 cm^{-1} mostly occurred at HT and only at RT during the quenching experiment.

Investigation of high temperature processes in the CaO-FeO-Al_2O_3-SiO_2-System studied by *in situ* hyperspectral Raman imaging

Annika Zöller (2019)

Bachelor thesis

The CaO-Al_2O_3-FeO-SiO_2 system represents a simplified system of slag. The understanding of this system contributes to the general understanding of metallurgical and material processes. As this complex system has not been studied before, we examined the even more simplified systems CaO-SiO_2 and CaO-SiO_2-Al_2O_3, which represent the basis for the present study. Through high temperature Raman spectroscopy, as a special method for *in situ* experiments, it is possible to gain information about the textural evolution as a function of time, temperature and space (Stange et al., 2018). With this data, it is possible to monitor phase transitions *in situ* (Gaufres et al., 2018; Stange et al., 2018). In combination with hyperspectral Raman imaging, which is an analytical method to display a detailed chemical image based on Raman spectra, it is a powerful method to acquire quantitative as well as qualitative information. A better understanding of the structures and processes within slag minerals is expected to be of benefit to both the steel industry and the environmental protection. *In situ* high-temperature Raman imaging provides entirely new insights into transport and solid-solid or solid-melt reaction processes in multi-component systems at high temperatures. For example, the question whether a mineral is a product from reactions during heating or cooling can be answered.

V.III Conference abstracts (Oral presentation)

Conference abstract *PacRim12, Hawaii, 2017*

Space-, time-, and temperature-resolved hyperspectral Raman imaging of high-temperature sintering reactions in kaolinite-based ceramics

K. Hauke[1], C. Lenting, T. Geisler[1]

[1] *Institute of Geosciences, Rheinische Friedrich-Wilhelms Universität, Bonn, Germany*

Sintering reactions of clay bodies have previously been studied by numerous experiments that involve quenching to RT and analyzing the reaction product by different techniques. In this study, green bodies containing kaolin and calcite, were progressively fired in air at various temperatures from RT to about 1060°C. For the first time, mineral reactions and textural relationships were studied *in situ* as a function of temperature, time, and space with a few micrometer resolution by hyperspectral Raman imaging. Gehlenite, wollastonite, and pseudowollastonite could be identified as new phases during sintering, and their textural evolution could be followed with temperature and time. Gehlenite was first observed at a temperature of 660°C. From 800°C wollastonite formed at the direct contact to gehlenite, whereby at temperatures higher 990°C wollastonite seems to be gradually replacing gehlenite. The crystallization of pseudowollastonite was observed already ~290°C below the accepted critical temperature (~1125°C) for the wollastonite-to-pseudowollastonite transformation, suggesting that pseudowollastonite can form metastably. The results of this study demonstrate that hyperspectral Raman imaging is a powerful method to study *in situ* phase transitions and recrystallization processes at grain boundaries during high-temperature sintering of ceramic.

Conference abstract *Deutsche Mineralogische Gesellschaft Workshop, Bad Windsheim 2018*

Untersuchungen von keramischen Sinterprozessen im System CaO-Al_2O_3-SiO_2 mit Hilfe der bildgebenden *in situ* Raman-Spektroskopie

K. Hauke[1], N. Böhme[1], T. Geisler[1]

[1] *Institute of Geosciences, Rheinische Friedrich-Wilhelms Universität, Bonn, Germany*

Zahlreiche Untersuchungsmethoden keramischer Sinterprozesse haben den Nachteil, dass die Keramik vor der Analyse auf Raumtemperatur abgeschreckt werden muss und/oder nur das gesamte Produkt analysiert werden kann. Mit Hilfe der bildgebenden *in situ* Ramanspektroskopie ist es möglich die Bildung neuer Mineralphasen entlang von Korngrenzen im Mikrometerbereich und *in situ* zu untersuchen. Dies kann dazu beitragen die Prozesse und Mechanismen zu verstehen, die bei der Bildung neuer Phasen während des Sinterprozesses beteiligt sind. In ersten Experimenten konnten wir bereits zeigen, das sich Pseudowollastonit bereits bei Temperaturen unter 900°C bildet, was weit außerhalb des Stabilitätsfeldes (>1125°C) liegt.

Conference abstract *GeoBonn Abstracts, Bonn 2018*

In situ hyperspectral Raman imaging: A new method to investigate solid-solid reactions in Ceramic materials during firing

K. Hauke[1], S. Zimmer[2], J. Kehren[2], N. Böhme[1], T. Geisler[1]

[1] *Institute of Geosciences, Rheinische Friedrich-Wilhelms Universität, Bonn, Germany*

[2] *University of Applied Science Koblenz, Höhr-Grenzhausen, Germany*

In the last decades Raman spectroscopy became an important tool to investigate minerals, gases, glasses, and organic material at room temperature. In combination with high temperature and high pressure devices the *in situ* investigation of mineral reactions and transformations became also possible. Here, we present a novel method to study the sintering process in silicate ceramics by *in situ* hyperspectral Raman imaging. We demonstrate that solid-solid phase transitions can be studied *in situ* at high temperature and thereby spatially resolved, providing completely new possibilities to study high-temperature solid-solid reactions in multi-component systems. Thermodynamic and kinetic phenomena can be studied without the need to quench the sample before analyzing the phase relations. In the present study, hyperspectral Raman spectroscopic imaging has been applied to *in situ* study the sintering process in the system CaO-Al_2O_3-SiO_2. Confocal micro-Raman spectra were recorded with a Horiba Scientific HR800 Raman spectrometer equipped with a 2W Nd:YAG laser (532.09 nm) and an electron-multiplier CCD detector. The samples were subsequently fired with a heating rate of 10°C/min (50°C steps) from about 700°C to 1200°C. At each temperature step one to several hyperspectral Raman images (100 x 100 µm, 1 µm step size) were recorded within a dwell time of 4 to 24 hours. The counting time varied between 0.6 to 1.3 s per pixel, which resulted in total imaging exposure times between about 2 to 4 hours. A Classical least squares (CLS) fitting procedure with house-intern reference spectra was used to obtain the relative phase proportions. The hyperspectral Raman images were created by false-colouring each pixel of the image relative to the fraction of each component in the spectrum. Three application examples will be presented to show (i) the effect of quenching, (ii) the investigation of the migration of a solid-solid reaction front at a micrometer scale, and (iii) the semi quantitative estimation of relative mineral fractions from which kinetic information can be gained.

Conference abstract *Deutsche Mineralogische Gesellschaft Workshop, Bad Windsheim,* 2019

***In situ* Untersuchungen von Mineralreaktionen während des keramischen Sinterprozesses mit Zeit-, Raum-, und Temperaturaufgelöster Ramanspektroskopie**

K. Hauke[1], S. Zimmer[2], J. Kehren[2], N. Böhme[1], T. Geisler[1]

[1] *Institute of Geosciences, Rheinische Friedrich-Wilhelms Universität, Bonn, Germany*

[2] *University of Applied Science Koblenz, Höhr-Grenzhausen, Germany*

Mit Hilfe der bildgebenden Ramanspektroskopie ist es möglich, die Bildung neuer Mineralphasen entlang von Korngrenzen räumlich auf der Mikrometerskala und zeitlich aufgelöst und bei Temperaturen bis zu 1400°C zu untersuchen. Räumlich, zeitlich und temperatur- aufgelöste *in situ* Untersuchungen können zu einem besseren Verständnis der Reaktionsmechanismen beitragen, die an keramischen Sinterprozessen beteiligt sind, sowie kinetische Informationen über die beteiligten Festkörperreaktionen liefern.

Conference abstract *Inside Raman Seminar*, Reutlingen, 2019 *invited talk*

Investigation of phase reactions during firing with *in situ* hyperspectral Raman imaging with temperature and time

K. Hauke[1], S. Zimmer[2], J. Kehren[2], N. Böhme[1], T. Geisler[1]

[1] *Institute of Geosciences, Rheinische Friedrich-Wilhelms Universität, Bonn, Germany*

[2] *University of Applied Science Koblenz, Höhr-Grenzhausen, Germany*

Here, we present a novel method to study the sintering process in silicate ceramics by *in situ* hyperspectral Raman imaging in the system CaO-Al_2O_3-SiO_2. Thermodynamic and kinetic phenomena can be investigated without the need to quench the sample before analyzing the phase relations. At each temperature step one or several subsequent hyperspectral Raman images (100 x 100 µm, 1 µm step size, total exposure time 2 hours) were recorded within a dwell time of 2 to 48 hours. The classical least squares (CLS) fitting procedure with house-intern reference spectra was used to obtain the relative phase proportions. The hyperspectral Raman images were created by false-colouring each pixel of the image relative to the fraction of each component in the spectrum. Three application examples will be presented that show (i) effects of quenching, (ii) the migration of solid-solid reaction fronts at a micrometer scale, and (iii) how kinetic information about grain growth can be gained.

Conference abstract *Deutsche Mineralogische Gesellschaft virtual Workshop, 2020.*

***In situ* Untersuchung der Bildungskinetik von Gehlenit bei verschiedenen Brenntemperaturen mit bildgebender Ramanspektroskopie**

K. Hauke[1], S. Zimmer[2], J. Kehren[2], N. Böhme[1], T. Geisler[1]

[1] *Institute of Geosciences, Rheinische Friedrich-Wilhelms Universität, Bonn, Germany*

[2] *University of Applied Science Koblenz, Höhr-Grenzhausen, Germany*

In dieser Studie wird der keramische Brennprozess von Gehlenit *in situ* mithilfe der bildgebenden Ramanspektroskopie untersucht. Dafür wurden sechs Grünkörper aus Kaolinit und Calcit wurden für 48 Stunden bei Temperaturen zwischen ~800 und 1000°C gebrannt. In allen isothermen Experimenten hat sich Gehlenit gebildet und sein Gehalt nimmt in fast allen Experimenten mit zunehmender Zeit zu. Mit Hilfe der Methode „time to a given fraction“ konnte eine Aktivierungsenergie von 231 ± 10 kJ mol^{-1} der Bildung und des Wachstums von Gehlenit berechnet werden. Anhand der Raman Maps kann auch das Kornwachstum von Gehlenit bei den verschiedenen Temperaturen untersucht werden. Die Ergebnisse zeigen, dass sich die bildgebende Ramanspektroskopie sehr gut eignet, um die mineralogischen Prozesse während des keramischen Brandes *in situ* zu untersuchen.

V.IV Conference abstracts (Poster presentation)

Conference Abstract *16th Confocal Raman Imaging Symposium,* Ulm, *awarded with the poster prize in bronze*

Studying the mineralogical and textural evolution of a kaolinite-calcite mixture with time at temperatures between 800 and 1100°C with hyperspectral Raman imaging

K. Hauke[1], S. Zimmer[2], J. Kehren[2], N. Böhme[1], T. Geisler[1]

[1] *Institute of Geosciences, Rheinische Friedrich-Wilhelms Universität, Bonn, Germany*

[2] *University of Applied Science Koblenz, Höhr-Grenzhausen, Germany*

Here, we present a novel method to study the sintering process in silicate ceramics by *in situ* hyperspectral Raman imaging. Solid-solid reactions and phase transitions can be *studied in situ* at high temperature and thereby spatially resolved. Thermodynamic and kinetic phenomena can be investigated without the need to quench the sample to room temperature before analyzing the run products. In the present study, hyperspectral Raman spectroscopic imaging has been applied to *in situ* study the isothermal sintering process of a calcite-kaolinite mixture at different temperatures. Confocal micro-Raman spectra were recorded with a 2W Nd:YAG laser (532.09 nm) and an electron-multiplier CCD detector. Six samples were fired with a heating rate of 10°C/min to temperatures between about 800°C and 1100°C. For each experiment 24 hyperspectral Raman images (100 x 100 µm, 1 µm step size) were recorded within a dwell time of about 48 hours. With a counting time of 0.6 s per pixel, the total exposure time was about 2 hours per image. The classical least squares (CLS) fitting procedure with house-intern reference spectra was used to obtain the relative phase proportions from each Raman spectrum (i.e., pixel of the image). The hyperspectral Raman images were then created by false-colouring each pixel of the image relative to the fraction of each component in the spectrum. From the data, the fraction of each phase (e.g., gehlenite, wollastonite, and anorthite) in an imaged area can semi quantitatively be determined as a function of time from which kinetic information can be gained.

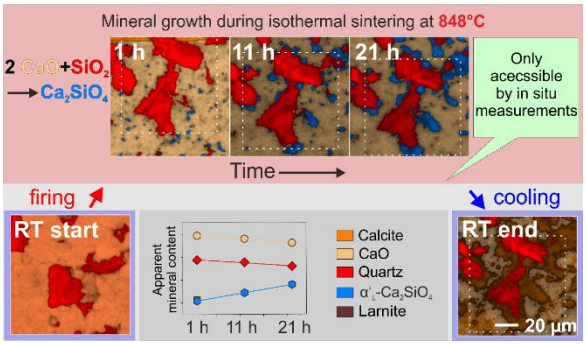

Fig. 1: In situ hyperspectral Raman imaging enables the investigation of the firing process of silicate ceramics temperature-, time-, and spatially resolved (adapted from Hauke et al. 2019).

High Temperature Raman Imaging

Studying the mineralogical and textural evolution of a kaolinite-calcite mixture with time at temperatures between 800 and 1100°C by hyperspectral Raman imaging

K. Hauke[1], S. Zimmer[2], J. Kehren[2], N. Böhme[1], T. Geisler[1]
[1] Institute of Geosciences, Rheinische Friedrich-Wilhelms-Universität, Bonn, Germany
[2] University of Applied Science Koblenz, Höhr-Grenzhausen, Germany

UNIVERSITÄT BONN
Rheinische Friedrich-Wilhelms-Universität Bonn

HT-Raman imaging:

- Novel method to study sintering processes in situ by hyperspectral Raman imaging
- Temperature-, time-, and spatially resolved
- No quenching necessary
- Possibility to identify polymorphes

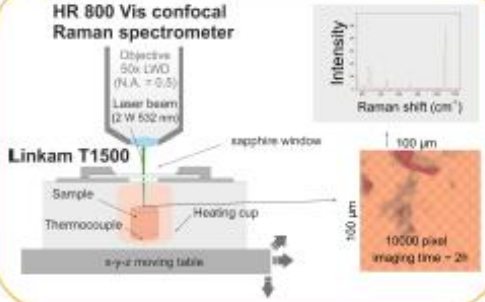

Classical least squares (CLS) fitting with house-intern reference spectra

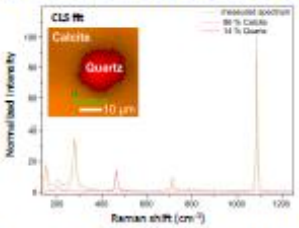

For more details see [1] and [2]

Isothermal experiments- Phase evolution within time

- Six samples of a kaolinite-calcite mixture
- Isothermal sintering at temperatures between ~ 800 and 1010°C
- 24 Raman images (~ 2 h per image)
- Dwell time of 48 h
- Heating and cooling rate 10°C/min

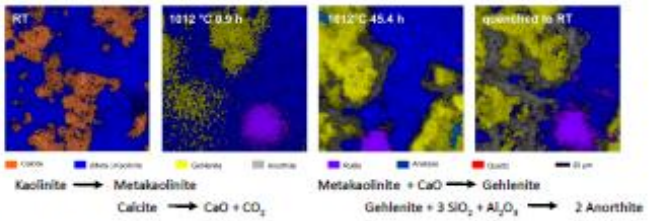

Phase evolution of a kaolinite-calcite mixture at 931°C within ~48 h

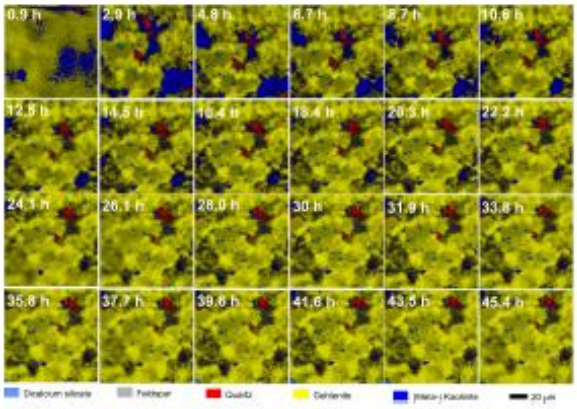

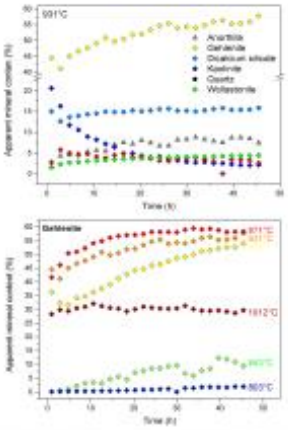

In situ investigations of grain growth

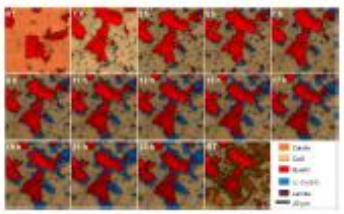

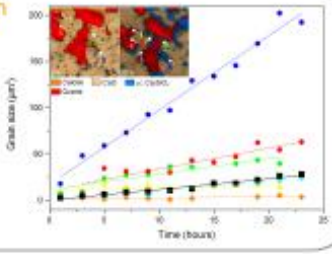

Conclusion:

- Semi quantitative estimation of relative mineral fractions
- In situ investigations of grain growth
- Kinetic informations like activation energies can be obtained
- The method can be applied to study the firing process of various materials like brown coal ash [3] or refractories [4].

Literatur:
[1] Stange et al. J. Am. Ceram. Soc. (2018)
[2] Hauke et al. Appl. Sci. (2019)
[3] Böhme et al. (2019)
[4] Zimmer et al. (2019)

Acknowledgements: We acknowledge the German Research Foundation (grant number GE1094/22-1) for financial support. Many thanks go to T. Schulz and D. Lüsdorf for the technical support with the heating stage.

Contact: Kerstin Hauke
Kerstinhauke@uni-bonn.de

September 2019 16th Confocal Raman Imaging Symposium Ulm, Germany

Conference Abstract *Deutsche Mineralogische Gesellschaft* virtual poster session, 2020.

Crystallization Kinetics and Phase Relations of Calcium-Aluminate-Silicates Investigated by In Situ Hyperspectral Raman Imaging

Hauke, K.[1], Böhme, N.[1], Zimmer, S.[2], Geisler, T.[1]*

[1]Institute for Geosciences, University of Bonn, Germany

[2] University of Applied Science Koblenz, Höhr-Grenzhausen, Germany

** Corresponding email: kerstinhauke@uni-bonn.de*

Keywords: ***hyperspectral Raman imaging, sintering, silicate ceramics, crystallization kinetics***

Here, we present a novel method to study the sintering process in silicate ceramics by in situ hyperspectral Raman imaging. Solid-solid reactions and phase transitions can be studied in situ at high temperature and thereby spatially resolved. Thermodynamic and kinetic phenomena can be investigated without the need to quench the sample to room temperature before analyzing the run products. In the present study, hyperspectral Raman spectroscopic imaging has been applied to in situ study the isothermal sintering process of a calcite-kaolinite mixture at six temperatures between about 800°C and 1100°C. Confocal micro-Raman spectra were recorded with a 2W Nd:YAG laser (532.09 nm) and an electron-multiplier CCD detector. For each experiment 24 hyperspectral Raman images (100 x 100 µm, 1 µm step size) were recorded within a dwell time of about 48 hours. A Classical least squares (CLS) fitting procedure with house-intern reference spectra was used to obtain the relative phase proportions from each Raman spectrum (i.e., pixel of the image). The hyperspectral Raman images were then created by false-coloring each pixel of the image relative to the fraction of each component in the spectrum. From the data, the fraction of each phase (e.g., gehlenite, wollastonite, and anorthite) in an imaged area can be determined as a function of time from which kinetic information can be gained. Mainly gehlenite, dicalcium silicate, wollastonite and an unknown phase 560 (which has one broad band near 560 cm^{-1}) are formed. In general, the amount of this phases increases with time, whereas the amount of kaolinite and CaO decreases. Gehlenite is formed in all six experiments and in almost all the gehlenite content increases with time. Up to 971°C a higher sintering temperature leads to a higher gehlenite content. At a firing temperature of 971°C gehlenite makes up 60 % of the map after a dwell time of 48 h. At the highest firing temperature far less gehlenite is present and anorthite has formed instead. The results demonstrate that in situ hyperspectral Raman imaging is a suitable technique to investigate the crystallization kinetics and phase relations of calcium-aluminate-silicates during firing.

Crystallization Kinetics and Phase Relations of Calcium-Aluminate-Silicates Investigated by In Situ Hyperspectral Raman Imaging

K. Hauke[1], S. Zimmer[2], N. Böhme[1], T. Geisler[1]
[1] Institute of Geosciences, Rheinische Friedrich-Wilhelms-Universität, Bonn, Germany
[2] University of Applied Science Koblenz, Höhr-Grenzhausen, Germany

Introduction

High temperature Raman imaging is a novel method to in situ study the sintering processes of ceramics. Here, we demonstrate that a semi-quantitative phase content can be estimated and the crystallization kinetics of calcium-aluminate-silicates can be determined.

Six isothermal firing experiments were performed with green bodies of a kaolinite-calcite mixture for a dwell time of 48 h. The samples were fired with a heating rate of 10°C/min to temperatures between ~ 800 and 1010°C. At the respective firing temperature 24 Raman images (~ 2 h per image) were subsequently recorded.

Experimental setup

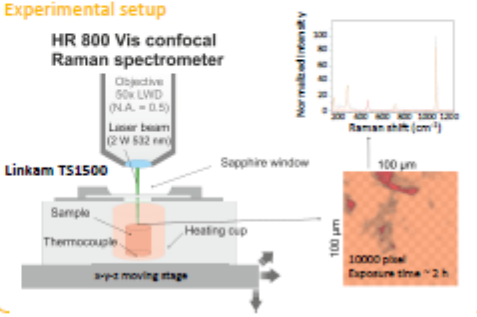

CLS fitting with house-intern reference spectra

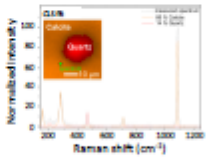

Within the multidimensional spectral array, the CLS fitting procedure finds a linear combination of reference spectra from the pure phases, which best fits the raw spectrum at each position. House-intern high-temperature reference spectra where used for the fitting procedure. For more details see [1] and [2].

Results - Formation of Calcium-Aluminate-Silicates

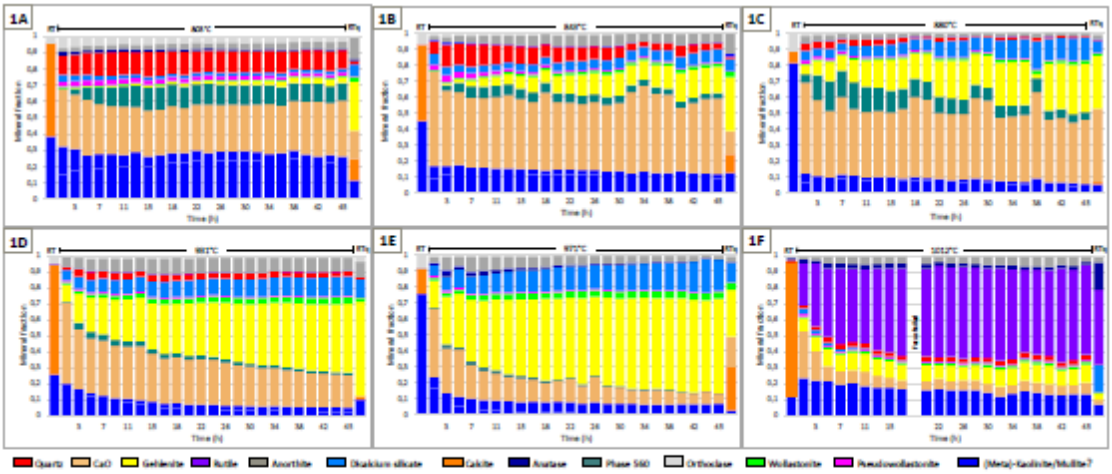

In the RT maps of all experiments calcite and kaolinite are the major phases (1A-F). Accessory phases of the kaolinite precursor material are orthoclase, anatase, and quartz. During firing to the sintering temperature calcite was decomposed to CaO and CO_2 (1A-F). Kaolinite was dehydroxylated to metakaolinite (1A-F). In all experiments new calcium (aluminum) silicates could be observed in the HT Raman images (1A-F, 2A-D). Mainly gehlenite (yellow arrow in 2A), dicalcium silicate (blue arrow in 2B), anorthite (grey arrow in 2B),nd wollastonite (1A-F) are formed. In general, the amount of these phases increased with time, whereas the amount of kaolinite and CaO decreases (1A-F). During the first two hours of all experiments, gehlenite crystallized at the expense of metakaolinite and CaO (2A, 3A-B). In the experiments above 880°C anorthite formed in contact to gehlenite (2B-D).

At low firing temperatures an unknown phase with a main Raman band near 560 cm⁻¹ (mainly in 1A-C) crystallized. No further Raman band could be assigned to this unknown phase, suggesting that it has a high symmetry.Above 880°C only minor amounts of this phase were formed and this amount decreased with time. Because phase 560 could not be detected in the quenched samples the phase seems to be metastable.

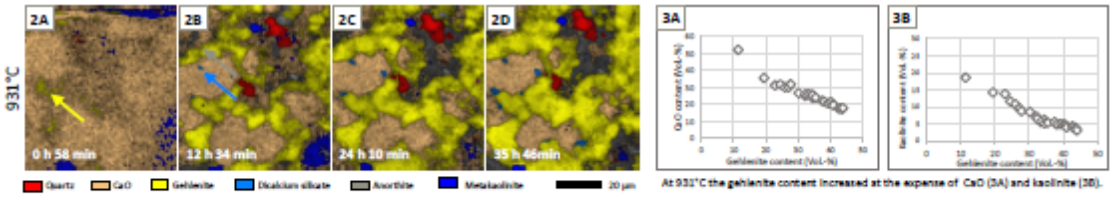

At 931°C the gehlenite content increased at the expense of CaO (3A) and kaolinite (3B).

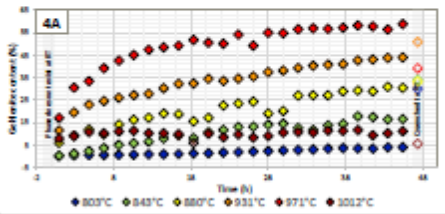

Gehlenite is formed in all six experiments (4A). Within one experiment the gehlenite content increases with time. Up to 971°C the gehlenite content increases with increasing sintering temperature. At 971°C gehlenite makes up 60 % of the map after a dwell time of 48 h. Using the time-to-a-given-fraction method, we could determine a reasonable empirical activation energy for the nucleation and growth of gehlenite of 231 ± 10 kJ mol⁻¹.

Conclusion:

High-temperature Raman imaging is a novel method to study the sintering processes of ceramics temperature-, time-, and, in particular, spatially resolved. It is not necessary to quench the sample before recording the Raman images, which allows the detection of metastable phases. Due to the spatial resolution at the micrometer scale, it is possible to follow the phase relations and thus determine from which phases a new mineral is formed.
Moreover, the fraction of each phase (e.g., gehlenite, wollastonite, and anorthite) in an imaged area could be semi-quantitatively determined as a function of time from which kinetic information can be gained.
The combination of spatial resolution and semi-quantitative phase determination makes the method a suitable tool to investigate the firing process of various materials such as lignite ash [3,4] or refractory materials [5].

Literatur:
[1] Stange et al. J. Am. Ceram. Soc., 101, 897 (2018)
[2] Hauke et al. Appl. Sci., 9, 1310 (2019)
[3] Böhme et al. Int. J. Coal Technol., 6, 247 (2009)
[4] Böhme et al. Minerals, 10, 287 (2020)
[5] Zimmer et al. Conference paper (2019)

Acknowledgements: We acknowledge the German Research Foundation (grant number GE1094/23-1) for financial support. N. Böhme also thanks the RWE power AG for financial support. Many thanks go to T. Schulz and D. Lilladorf for the technical support with the heating stage.

DMG Virtual Poster Session 2020
Contact: Kerstin Hauke
kerstinhauke@uni-bonn.de

V.V Supplement Chapter 2
Hyperspectral Raman imaging-Phase identification and data reduction

(1) Phase identification

The mineral phases were identified by using the CrystalSleuth software [1] linked to the RRUFF database [2]. The Raman bands used for mineral identification are given in Table S1. In agreement with the XRD data alkali feldspar (AFsp), quartz (Qtz), and calcite (Cal) could be identified in the precursor material by Raman spectroscopy. Kaolinite has relatively weak Raman bands located at 271 cm^{-1}, 355 cm^{-1}, 429 cm^{-1}, and 463 cm^{-1} [3]. These bands could not be detected anymore at high temperatures, because they were broadened and covered by bands of other minerals with higher intensities. The same is valid for metakaolinite that exhibits only weak bands near 812 cm^{-1} and 995 cm^{-1} [3]. Furthermore, lime crystallizes in the halite structure and does not give a first-order Raman spectrum [4], and could thus not be detected.

Quartz was identified by its A_1 modes near 205, 355, 465, and 1080 cm^{-1} (Table S1). At the phase transition at 573°C from low-temperature α-phase to the high-temperature β-phase, the 355 and 1080 cm^{-1} bands decrease continuously in intensity with increasing temperature and are not present in the β-phase while the 205 cm^{-1} band broadens and shifts towards lower frequencies [5]. For that reason only the strong A_1 mode near 465 cm^{-1} is used to identify quartz at high temperatures.

Three types of feldspar were identified by Raman measurements at RT (Q-Exp) by determining the band position of the rotation-translation modes of the four-membered rings and cage-shear modes (<400 cm^{-1}) and the ring-breathing modes of the four-membered rings of the SiO_4 tetrahedra from 450 and 520 cm^{-1} (Table S1; [6]). Based on the wavenumber of the main band near 510 cm^{-1} that varies between 509 and 512 cm^{-1} in alkali feldspars (at RT), it is clearly shown that during all experiments exclusively solid solutions of alkali feldspar occurred. The main band of plagioclase varies between 509 cm^{-1} for pure albite to 504 cm-1 for the Ca end member anorthite that was not detected [6]. However, at high temperature a differentiation between the alkali feldspars was impossible, due to the reduced quality of Raman images recorded at HT, but the formation of Ca-rich plagioclase could potentially be detected by the significant wavenumber difference of the main band.

Calcite was identified by its intense $v_1(CO_3)$ symmetric stretching mode near 1085 cm^{-1}. At RT, the weak bands near 155 cm^{-1} and 280 cm^{-1}, assigned to translational (E_g) and rotational (E_g) modes, and the internal E_g mode of calcite near 715 cm^{-1} corresponding to in-plane bending (v_4) mode were detected [7].

Table S1: Frequencies of observed Raman bands at room temperature for the different identified phases (in cm^{-1}). The frequencies of the Raman bands used for the main band method are given in bold.

Olg	Mi	Alb	Qtz	Wo	Gh	PWo	Cal	Anh	Ca_2SiO_4	Ti
						142 w				
	152 w						154 w			
159 sh		160 m								
180 m	175 w	184 m								
						189 w				
207 m	205 w	209 m	205 w							
254 w	256 w	253 w						258 sh		254 s
			266 w							
274 sh		275 w					280 m			
290 s	289 s	291 s						287 m		
					304 m					
330 w	330 w	330 w								336 w
	356 w		356 w							
						372 m				
	380 w									
407 w	408 w	408 w		410 m						406 m
418 w	417 sh	418 sh						418 m		
										454 m
	460 sh	464 sh	**464 s**							
477 s	477 s	479 s								
								498 w		
511 s	**512 s**	**509 s**				507 w				
										537 s
						556 m				
		562 w								501 sh
578 w						**579 s**				
								609 w		605 m
					614 s					
								628 w		
	632 sh			**637 s**						
644 w	647 w	641 w								
					658 s					
								675 w		670 m
							713 w			
	756 w	762 w								
764 w	769 w	774 sh								
815 w	815 w	814 w	809 w						808 m	810 w
									847 s	
904 w	902 w				**906 s**				859 s	
										865 m
										909 w
					933 sh					
				973 s						
977 w										
	983 w					982 s				
								1016 s		
1031 w	1032 w	1027 w								
							1054 w			
			1082 w							
							1087 s			
1105 w		1097 w								
1116 w	1113 w	1113 sh						1111 sh		
								1127 m		
								1158 w		

Abbreviations: s= strong band, m= medium band, w=weak band, sh = shoulder, Ca_2SiO_4 = Larnite or calcio-olivine. For mineral abbreviations see text and Ref. [8].

Anhydrite (Anh) was only identified as a reaction product in the quenched ceramic by its intense $\nu_1(SO_4)$ symmetric stretching mode near 1017 cm^{-1} and its $\nu_3(SO_4)$ antisymmetric stretching modes at 1110, 1128, and 1159 cm^{-1} (Table S1; [9]).

Gehlenite (Gh), the Ca end member of the melilite solid solution series, was identified by its convoluted Raman bands near 620 and 850 cm^{-1} (Table S1; [10]) and wollastonite (Wo) by its Raman bands near 640 and 970 cm^{-1} at RT that shift to 620 and 950 cm^{-1} at a temperature of 1069°C (Table S1; [11]). The Raman spectra of wollastonite and its high-temperature polymorph pseudowollastonite (PWo) are broadly similar. Pseudowollastonite, however, can be distinguished from wollastonite by its intense Raman bands near 580 and 985 cm^{-1} that shift to 565 and 965 cm^{-1}, respectively, at a temperature of 1069°C (Table S1; [12]).

A phase with intense Raman bands near 560, 810, and 847 cm^{-1} could not yet been identified beyond doubt by a comparison with reference spectra from the RRUFF database [2] or from the literature [13]. However, as discussed in the main text, its stoichiometry can be defined as Ca_2SiO_4. Dicalcium silicate can occur as two polymorphs, namely the high-T (> 425°C) polymorph β-Ca_2SiO_4 (larnite) and the corresponding low-T polymorph γ-Ca_2SiO_4 (calcio-olivine).

(2) Temperature calibration

A type S Pt-10% Rh/Pt thermocouple, accurate to 0.01°C, measured the temperature at the bottom of the cell. However, to obtain the accurate temperature at the surface of the green body, *i.e.*, 2.7 mm above the thermocouple, the temperature gradient inside the cell had to be determined. For this, a natural diamond was used, because diamond has one first-order Raman mode near 1332 cm^{-1} (at RT) that shows a strong frequency shift with increasing temperature (e.g., [14]). The temperature-related frequency shift of this first order band was measured as a function of temperature up to 800°C at the bottom of the cell as well as at the top of a green body with a height of 3.1 mm. From these data, the temperature gradient could be determined. The corrected temperatures (at the sample surface) are accurate and precise within about ± 5°C.

(3) Hyperspectral Raman data reduction

Raman spectra were analyzed and visualized using the LabSpec 6.3.40.5 software. The spectral range between 350 and 1120 cm^{-1} (S-Exp), and 170 and 1250 cm^{-1}, respectively (Q-Exp and F-Exp), were used for interpretation, the reduction of the spectral range simplified the band fitting procedure. After spike correction, the spectra were corrected for any spectrometer shift during long-time measurements using the Ne line at 1707.461 cm^{-1} [15]. A Gaussian function was fitted to this Ne spectral line and the line position was then used to correct for the frequency shift, mainly caused by temperature fluctuations (< ± 0.5°C) in the Raman laboratory. With such internal standard, the precision and

accuracy of the frequency of a Raman band, obtained by least-squares fitting, was usually between ± 0.05 and ± 0.10 cm^{-1} (2σ) for RT. This estimate is based on error propagating of the fitting results the error of the reference frequency of the Ne line is negligible.

To find the best approach to visualize the phase distribution and their textural relationship during sintering as a function of temperature, space, and time from a multi-dimensional hyperspectral Raman data set three data reduction methods were tested that are described in the following.

Main band method: As a first approach to analyze the complex multi-dimensional data set, the intensity of one intense and characteristic Raman band of the identified phases was used to visualize their spatial distribution (Fig. S1a). The integrated intensity of the characteristic bands (bold numbers in Table S1) was obtained by fitting a polynomial baseline function of 2^{nd} order to each spectrum, representing the background that at high temperature is mainly composed of black body radiation, along with an appropriate number of Gauss-Lorentz functions (Fig. S2). A maximal frequency shift of ± 3 cm^{-1} around the initially approximated band position was allowed during fitting. Additional fitting parameter like the Intensity or the full width of half maximum of the bands were degrees of freedom.

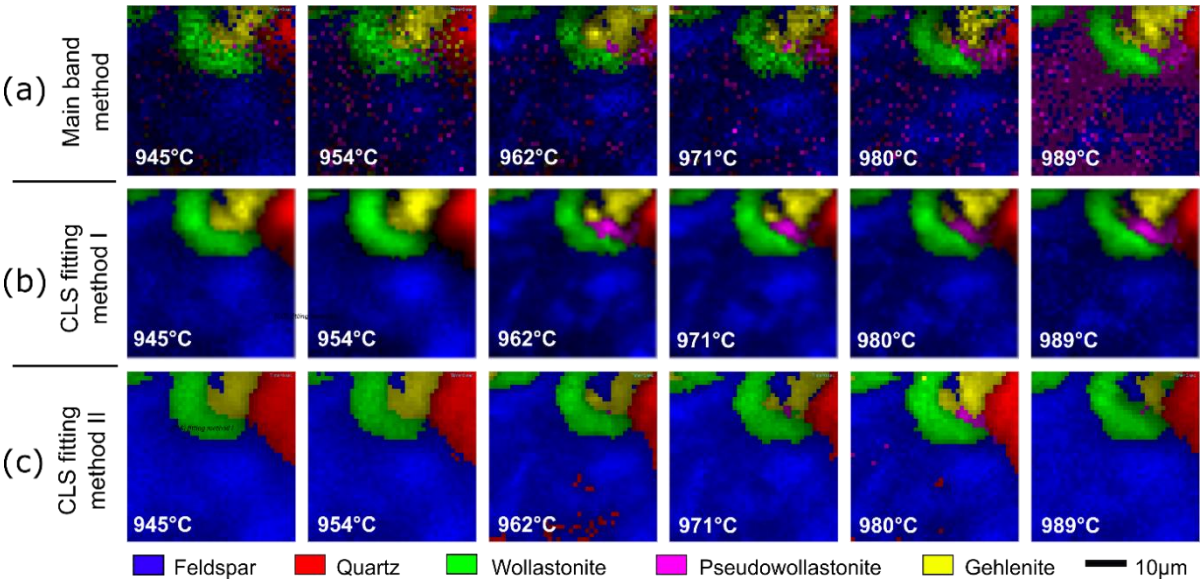

Figure S1: Comparison of the three different data reduction methods as described in the text exemplarily shown for a temperature range of Exp. #3 between 945 to 989°C. (a) Main band method. (b) Classical least-squares (CLS) method I. (c) CLS fitting method II using synthetic spectra (see text for further details).

The baseline was subtracted not until the least-squares fit has been successful, as controlled by the overall X^2 value of the least-squares fits of an image. The images were then created by false-coloring each pixel of the image relative to the intensity fractions of the different characteristic bands in the spectrum. Hence, the overall quality of the image is limited by the fact that each phase is only represented by one single Raman band.

Classical least-squares (CLS) fitting method I: The CLS method is based on the assumption that a spectrum from a polyphase material is a simple mixture of the spectra from the pure phases. Within the multidimensional spectral array the CLS fitting procedure finds a linear combination of reference spectra from the pure phases, which best fits the raw spectrum at each position (pixel). The resulting image is created by false-coloring each pixel of the image relative to the fraction of each component in the spectrum. In the unmixed color-coding algorithm that is used in this work, the phase with the highest intensity contribution in a Raman spectrum will be displayed in a color assigned to that particular phase. Such a procedure is straightforward if pure reference spectra are available.

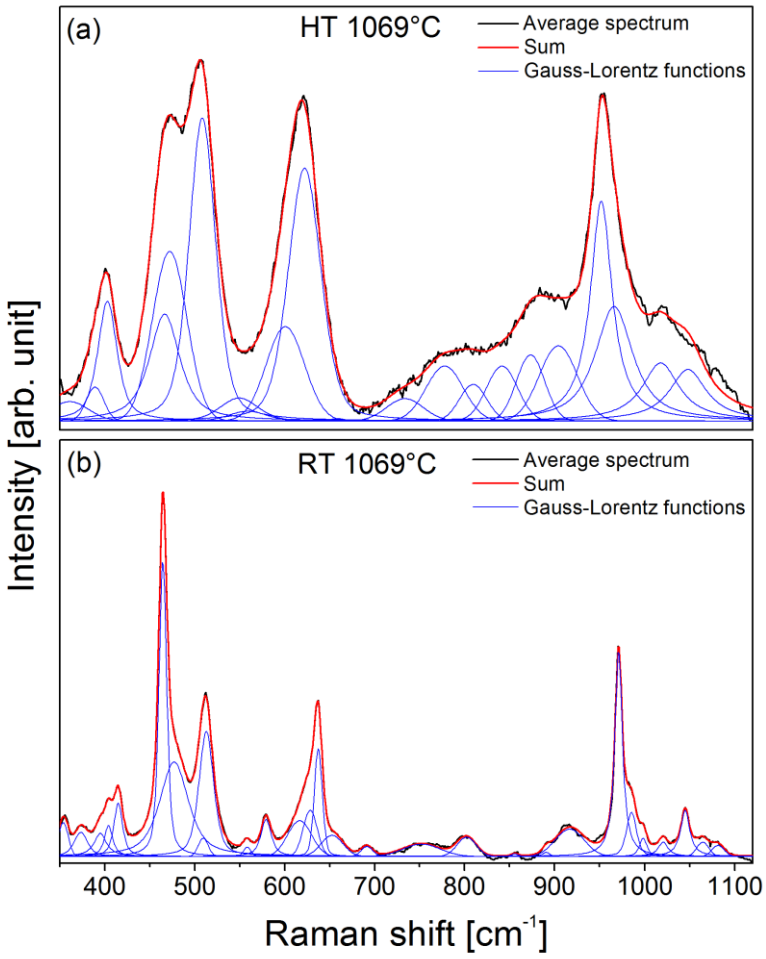

Figure *S2*: A representative background corrected average (8 pixels) Raman spectra of the S-Exp, taken (a) at 1069°C and (b) cooled down to RT. The spectra were fitted using an appropriate number of Gauss-Lorentz functions that were then assigned to the individually observed phases. See text for further details.

However, for the time being high-temperature spectra were not available for the observed phases and, as a first approach, reference spectra for each phase and temperature step used for the fitting procedure were obtained by averaging eight spectra from an area, where the respective phase was most prominent. All reference spectra other than for quartz and feldspar obtained in this way contained bands of other phases. This leads to an overestimation of minor phases, because of the concurrent presence of bands from other major phases. One example is the apparent overestimation of pseudowollastonite (purple) in Fig. S1b. If pure reference spectra can be extracted from a hyperspectral Raman data set, this method is the method of choice. However, due to limitations of the spatial resolution, pure reference spectra could not been identified for all phases.

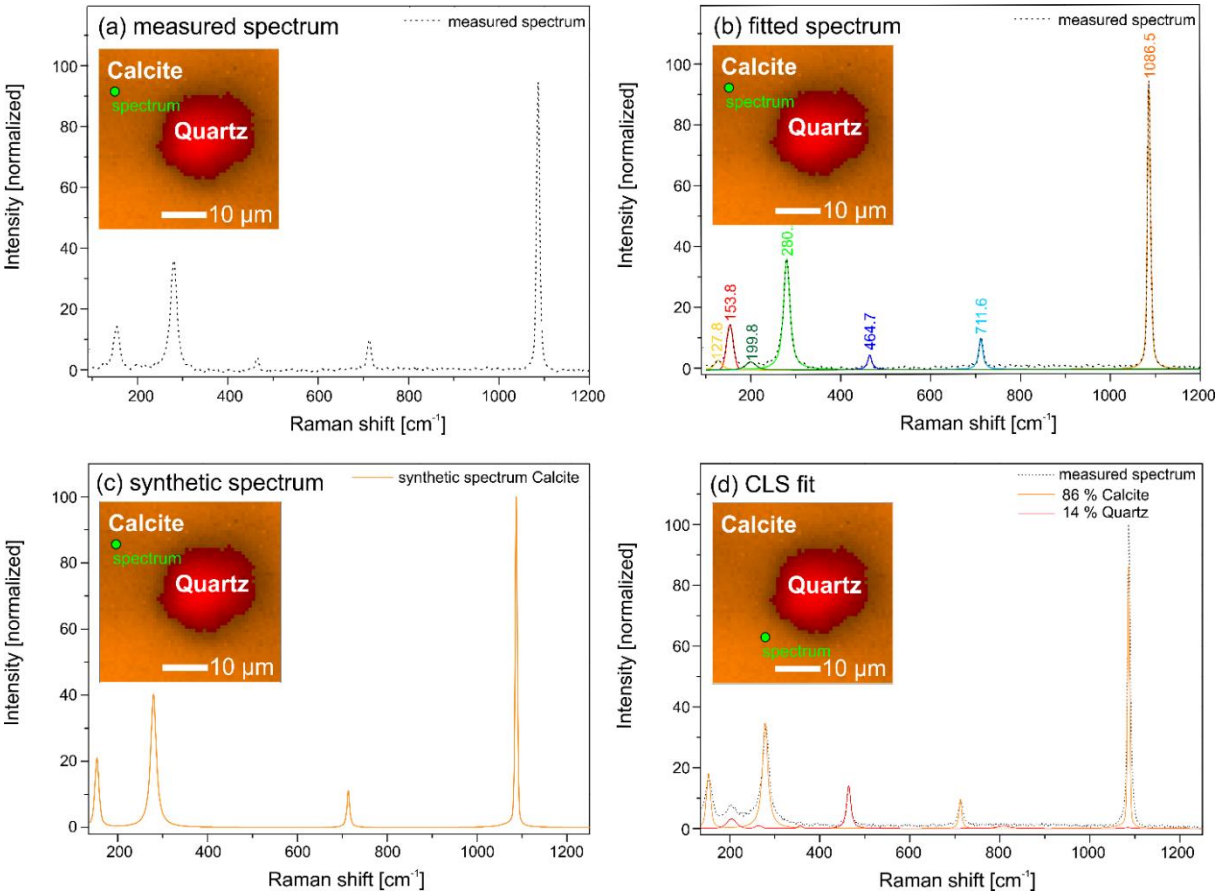

Figure S3: Example for the creation of a synthetic calcite spectrum. Basis for the preparation of a synthetic is a pure spectrum (or an average spectrum) or a spectrum with a high proportion of the current phase. (a) Mixed spectrum of calcite and quartz where the background is subtracted. (b) The spectrum is fitted with an appropriate number of Gauss-Lorentz functions. Than the functions are assigned to calcite regarding a calcite reference spectrum. (c) Synthetic spectrum of calcite, where all bands related to quartz are deleted. (d) CLS fit of one spectrum composed of 86% Calcite and 14 % Quartz.

Classical least-squares (CLS) fitting method II: An advanced approach is the creation of synthetic reference spectra for each phase at each temperature from the fits of Gauss-Lorentz functions to the observed mixed spectra (see Sec. "*Main band method*"; Fig. S1a and S3). Most of the observed Gauss-Lorentz functions could be assigned to the respective phases. All fitted Gauss-Lorentz functions that

do not belong to the phase of interest were deleted and the remaining functions were added together and saved as a synthetic spectrum of that phase. In Fig. S4 representative synthetic spectra of the observed phases at different temperatures, showing broadening and frequency shifts of their fundamental modes at HT, are compared with RT reference spectra from the RRuff Raman data base [2].

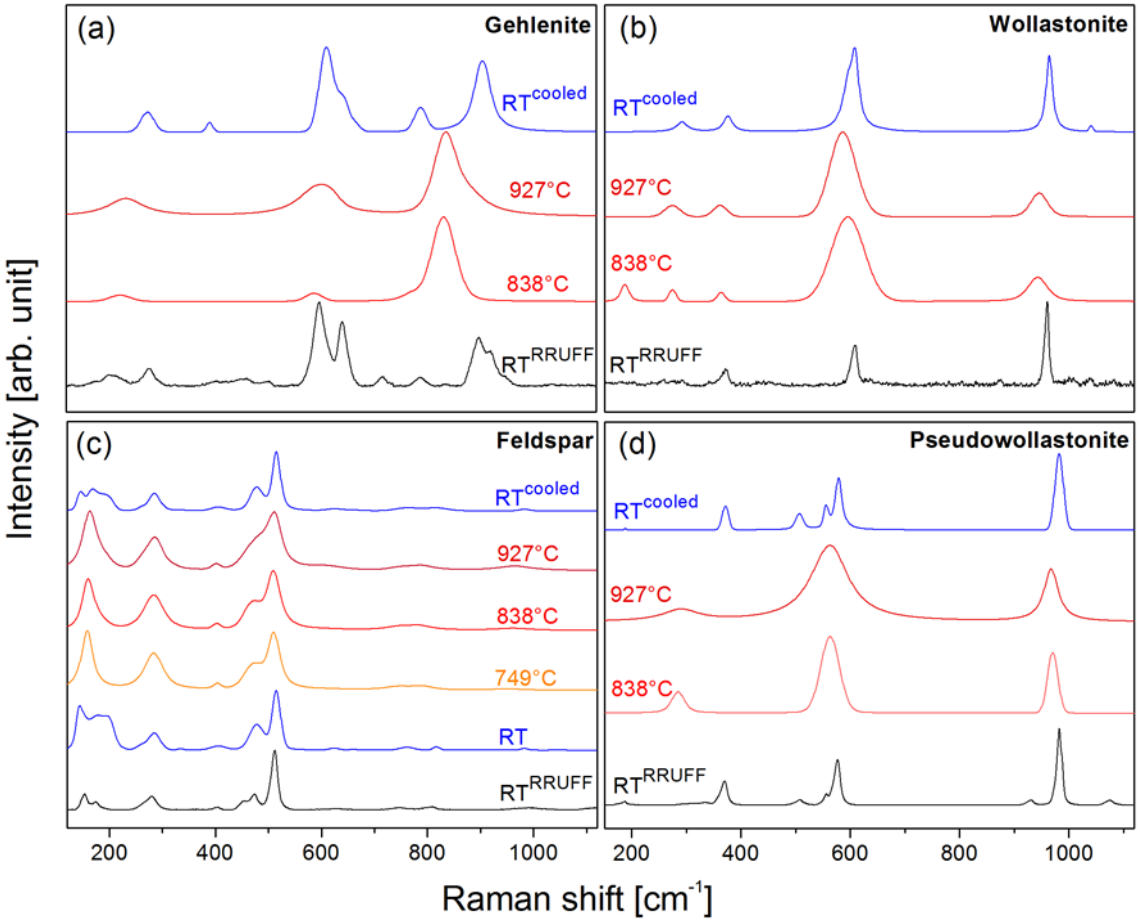

Figure S4: Representative synthetic spectra of (a) gehlenite, (b) wollastonite, (c) feldspar, and (d) pseudowollastonite created from average spectra (8 pixels) at room temperature and different sintering temperatures compared to a reference spectra [2]. Note that the Raman bands shift with temperature towards lower frequencies and become broader.

The overall quality of the CLS fits, in particular for HT spectra, was limited by the fact that some weak bands could not be assigned confidently to any phase, leaving still high residuals that partly contribute to the fraction of black in the images (Fig. S1c). For the *ex situ* experiments measured at RT, however, all observed Raman bands could be assigned. These spectra were taken with longer acquisition times, resulting in a better signal to noise ratio (Fig. S2 and S5). Also, the narrower band widths at RT simplified the assignment significantly.

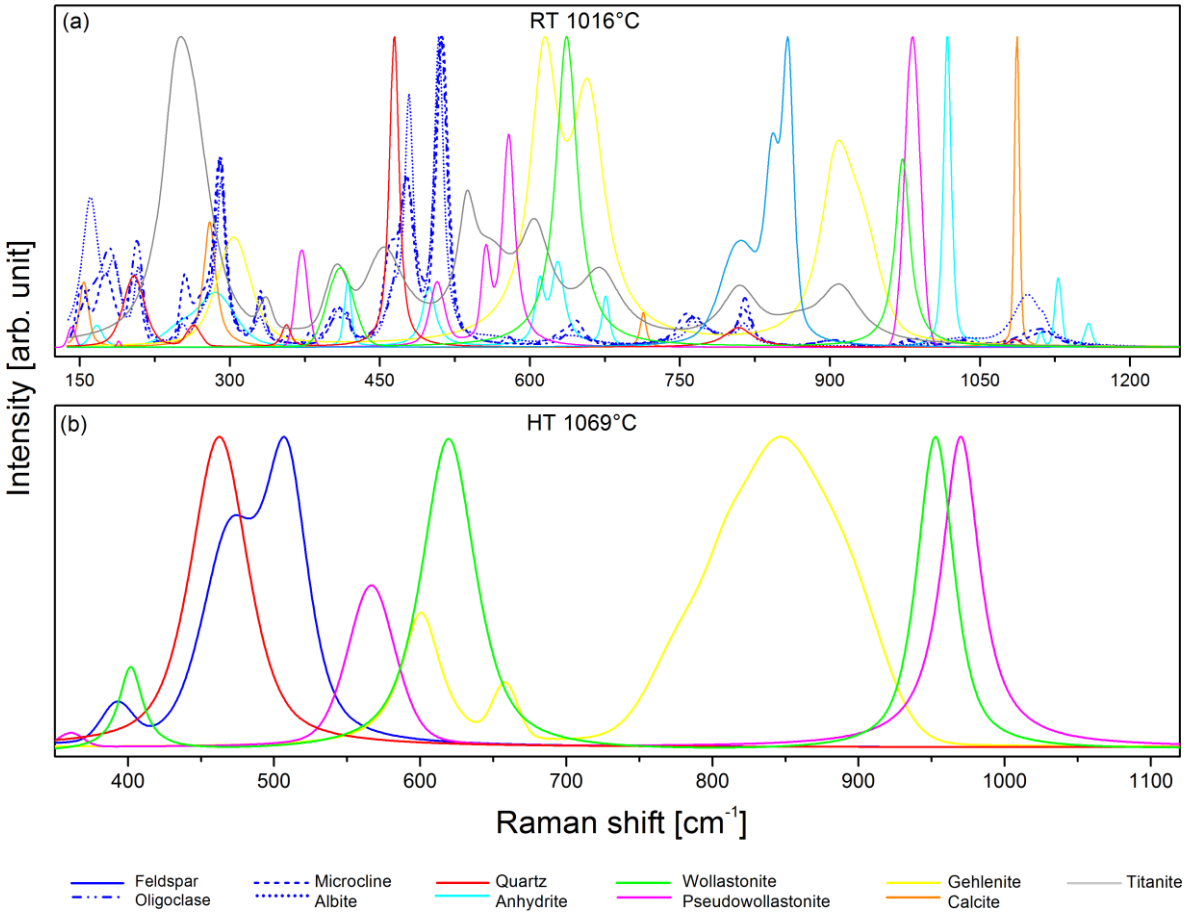

Figure S5: Representative synthetic spectra of the identified phases, which were used for the CLS-fitting procedure. The spectra were fitted using an appropriate number of Gauss-Lorentz functions that were then assigned to the individually observed phases to generate synthetic reference spectra for each phase and temperature. Room temperature synthetic spectra used (a) for the quench experiment (Q-Exp). (b) Synthetic spectra of the S-Exp at 1069°C.

References

[1] Laetsch T, Downs R. Software for Identification and Refinement of Cell Parameters from Powder Diffraction Data of Minerals Using the RRUFF Project and American Mineralogist Crystal Structure Databases." Abstracts from the 19th General Meeting of the International Mineralogical Association, Kobe, Japan, 23-28 July (2006).

[2] Lafuente B, Downs RT, Yang H, et al. The power of databases: the RRUFF project. In: Armbruster T, Danisi RM, *eds. Highlights in Mineralogical Crystallography.* Berlin, DE: De Gruyter; 2015:1-30.

[3] Shoval S, Boudeulle M, Panczer G. Identification of the thermal phases in firing of kaolinite to mullite by using micro-Raman spectroscopy and curve-fitting. *Opt. Mater*.2011;**34**:404-409.

[4] Schmid T, Dariz P. Shedding light onto the spectra of lime: Raman and luminescence bands of CaO, $Ca(OH)_2$ and $CaCO_3$. *J. Raman Spectrosc*.2014;**46**:141-146.

[5] Shapiro SM, O'Shea DC, Cummins HZ. Raman scattering study of alpha-beta phase transition in quartz. *Phys. Rev. Lett.* 1967;**19**:361-364.

[6] Freeman JJ, Wang A, Kuebler KE, et al. Characterization of natural feldspars by Raman spectroscopy for future planetary exploration. *Can. Mineral.* 2008;**46**:1477-1500.

[7] Urmos J, Sharma SK, Mackenzie FT. Characterization of some biogenic carbonates with Raman spectroscopy. *Am. Mineral.*1991;**76**: 641-646.

[8] Whitney DL, Evans BW. Abbreviations for names of rock-forming minerals. *Am. Mineral.*2010;**95**:185-187.

[9] Liu Y, Wang A, Freeman JJ. Raman, MIR and NIR spectroscopic study of calcium sulfates: Gypsum, Bassanite, and Anhydrite; presented at the 40th Lunar and Planetary Science Conference, Houston, 2009 (abstract No. 2128).

[10] Bouhifd MA, Gruener G, Mysen BO et al. Premelting and calcium mobility in gehlenite ($Ca_2Al_2SiO_7$) and pseudowollastonite ($CaSiO_3$). *Phys. Chem. Min.*2002;**29:**655-662.

[11] Swamy V, Dubrovinsky LS, Tutti F. High-Temperature Raman Spectra and Thermal Expansion of Wollastonite. *J. Amer. Ceram. Soc.*1997;**80**:2237-2247.

[12] Richet P, Mysen BO, Ingrin J. High-temperature X-ray diffraction and Raman spectroscopy of diopside and pseudowollastonite. *Phys. Chem. Miner*.1998;**25**:401-414.

[13] Sokol EV, Seryotkin YV, Kokh SN. Flamite, $(Ca,Na,K)_2(Si,P)O_4$, a new mineral from ultrahigh-temperature combustion metamorphic rocks, Hatrurim Basin, Negev Desert, Israel. *Mineral. Mag.* 2015;**79**:583-596.

[14] Cui JB, Amtmann K, Ristein J et al. Noncontact temperature measurements of diamond by Raman scattering spectroscopy. *J. Appl. Phys.* 1998;**83**:7929-7933.

[15] Kramida A, Ralchenko Yu Reader J and NIST ASD Team (2015). NIST Atomic Spectra Database (version 5.3), [Online]. Available: http://physics.nist.gov/asd [Mon Aug 22 2016]. National Institute of Standards and Technology, Gaithersburg, MD.

V.VI Supplement Chapter 4

1 The mineralogical and textural evolution with time

All six green bodies contained mainly calcite and kaolinite (Figure S4.1-S4.6). In addition, small amounts of orthoclase, quartz, anatase, or millerite occurred within the kaolinite precursor material. It was not always possible to find the same area in the RT Raman images and the HT series, because there were no distinctive markings in the RT images that were useful for orientation. In experiment T803 the mixture of kaolinite and calcite was fired at 803°C for about 48 hours. Figure S4.1 shows the 91 x 91 µm area that was present in all high temperature images. At room temperature (RT) kaolinite and calcite were present.

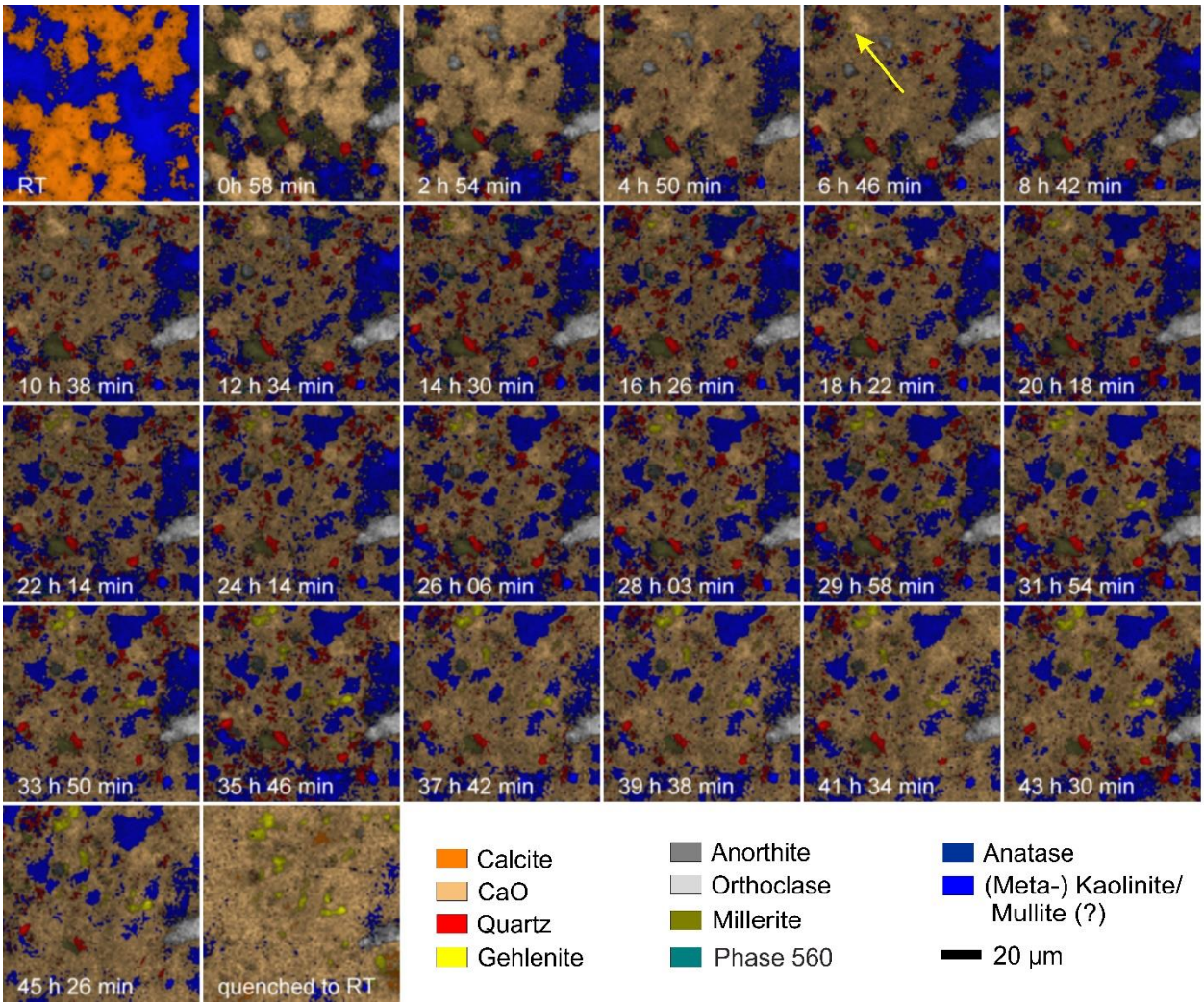

Figure S4.1: Normalized false-color hyperspectral Raman images of experiment T803. A mixture of kaolinite and calcite was fired at 803°C for about 48 hours. The area that was present in all high-temperature Raman images despite shifting of the sample, was chosen from the original image of 100 x 100 µm. In this experiment an area of 91 x 91 µm was used for further interpretation. At room temperature (RT) kaolinite and calcite were present. In the first image of the isothermal sintering that was recorded during the first two hours of firing (the average dwell time is shown on the pictures) quartz and orthoclase were visible. These phases were impurities within the kaolinite precursor material. Kaolinite was dehydroxylated to metakaolinite (not visible, because kaolinite and metakaolinite are depicted in the same color) and calcite was decomposed to lime. Gehlenite firstly occurred in the fourth map (marked by a yellow arrow in image 6 h 46 min). With time the gehlenite content increased.

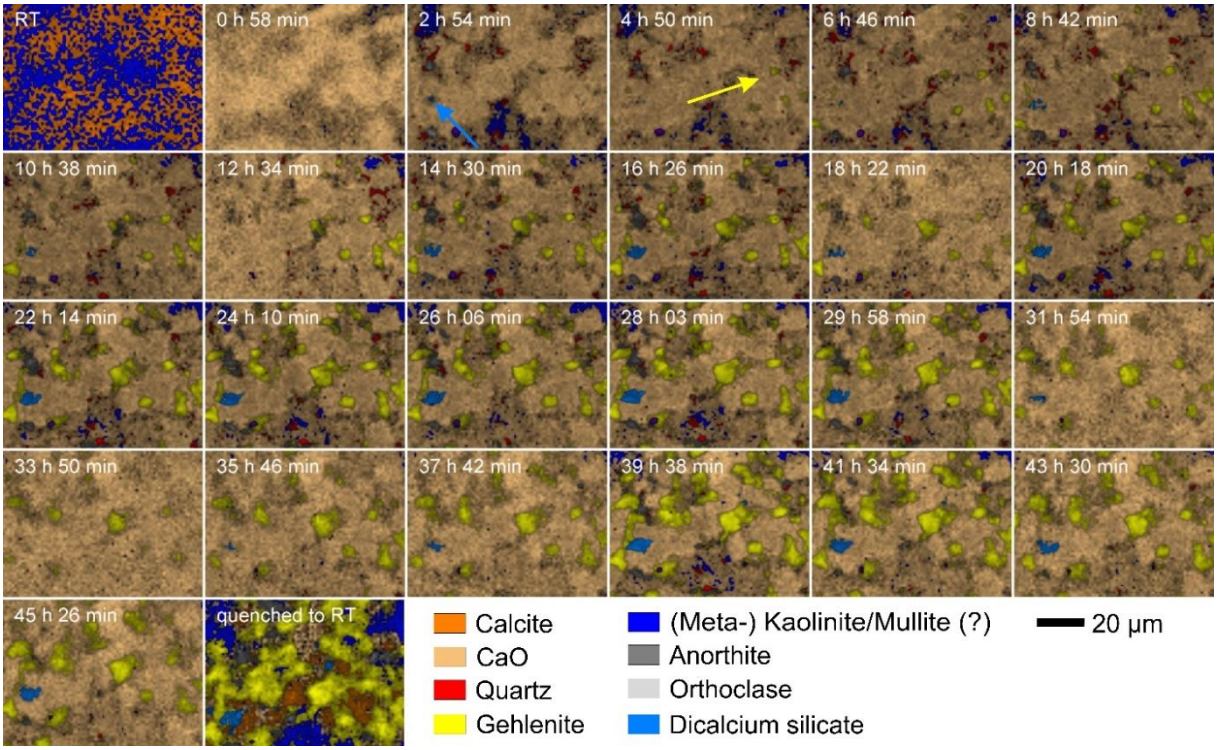

Figure S4.2: Normalized false-color hyperspectral Raman images of experiment T843. A mixture of kaolinite and calcite was fired at 843°C for about 48 hours. The area that was present in all high-temperature Raman images despite shifting of the sample, was chosen from the original image of 100 x 100 µm. In this experiment an area of 81 x 60 µm was used for further interpretation. At room temperature (RT) kaolinite and calcite were present. In the first image of the isothermal sintering that was recorded during the first two hours of firing (the average dwell time is given on the pictures) mostly CaO was visible that is next to CO_2 a product of the calcite decomposition. Kaolinite was dehydroxylated to metakaolinite (not visible, because kaolinite and metakaolinite are depicted in the same color). In the second map at sintering temperature (image 2 h 54 min) dicalcium silicate was present (marked by a blue arrow). Gehlenite firstly occurred in the third map at sintering temperature (marked by a yellow arrow in image 4 h 50 min). With time the contents of dicalcium and gehlenite were increased.

In the first image of the isothermal sintering that was recorded during the first two hours of firing (the average dwell time is given on the pictures) quartz and orthoclase were visible impurities within the kaolinite precursor material. Kaolinite was dehydroxylated to metakaolinite (not visible, because kaolinite and metakaolinite are displayed in the same color) and calcite was decomposed to lime. Gehlenite firstly occurred in the fourth map (marked by a white arrow in image 6 h 46 min). With time the gehlenite content increased. The greenish-yellow phase millerite was an impurity of the kaolinite precursor material. For further interpretation millerite was assigned to kaolinite and not distinguished as a single phase. During quenching some of the CaO was recrystallized to calcite. Dicalcium silicate and gehlenite were still present.

In T843 the kaolinite-calcite mixture was fired for 48 hours at 843°C. In the first image of the isothermal sintering that was recorded during the first two hours of firing (the average dwell time is given on the pictures) mostly CaO was visible that is next to CO_2 a product of the calcite decomposition (Figure S4.2). Kaolinite was dehydroxylated to metakaolinite (not visible, because kaolinite and metakaolinite are depicted in the same color). The first newly formed silicate was dicalcium silicate, which firstly occurred in the second HT map (image 2 h 54 min). Gehlenite firstly occurred in the third map at sintering temperature (marked by a yellow arrow in image 4 h 50 min). With time the contents of dicalcium and gehlenite increased. During cooling to RT some of the CaO was recrystallized to calcite with CO_2, which was present in the stage atmosphere.

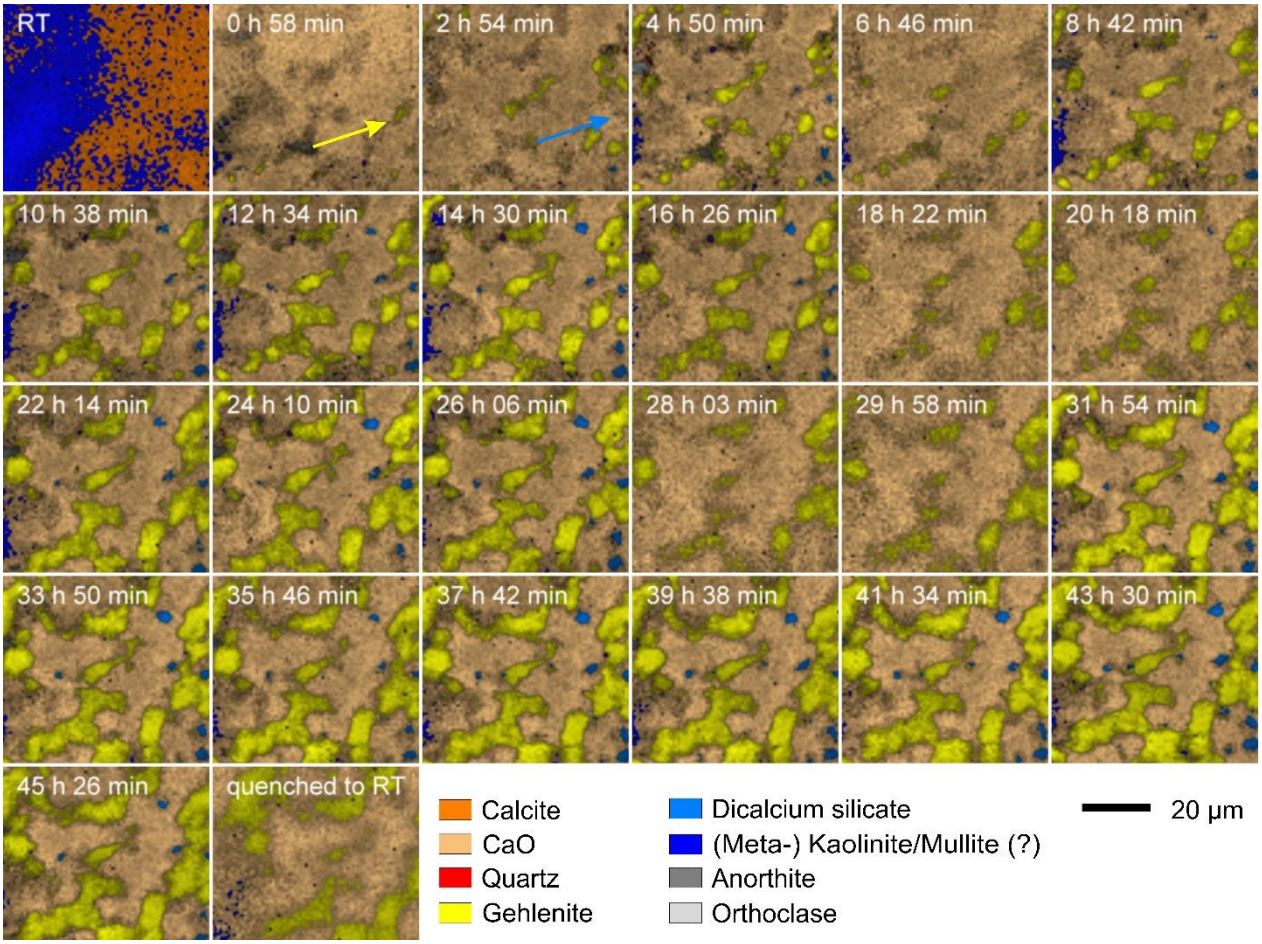

Figure S4.3: Normalized false-color hyperspectral Raman images of experiment T880. A mixture of kaolinite and calcite was fired at 880°C for about 48 hours. The area that was present in all high-temperature Raman images despite shifting of the sample, was chosen from the original image of 100 x 100 µm. In this experiment an area of 75 x 68 µm was used for further interpretation. At room temperature (RT) kaolinite and calcite were present. In the first image of the isothermal sintering that was recorded during the first two hours of firing (the average dwell time is given on the pictures) mostly CaO, the reaction product of the calcite decomposition, was visible. Kaolinite was dehydroxylated to metakaolinite (not visible, because kaolinite and metakaolinite are depicted in the same color). Gehlenite was also present (marked by a yellow arrow). In the second HT map (2 h 54 min) dicalcium silicate was also present (marked by a light blue arrow). With time the dicalcium and especially the gehlenite content were increased.

Before the sample was fired to 880°C only kaolinite and calcite were visible (Figure S4.3). During firing to the sintering temperature calcite was decomposed to CaO and CO_2 and kaolinite was dehydroxylated to metakaolinite. Traces of newly formed gehlenite were visible in the first HT map. In the next time step (2 h 54 min) dicalcium silicate was formed and with time the amount increased. During the first hours many gehlenite grains were formed all over the map and grew with time. After about 48 hours gehlenite constituted 40 vol.-% of the map. During cooling to RT no calcite was recrystallized. In this experiment the auto-focus did not work reliably. Therefore, minor phases like dicalcium silicate were not visible in the images (for example map 6 h 46 min and map 18 h 22 min).

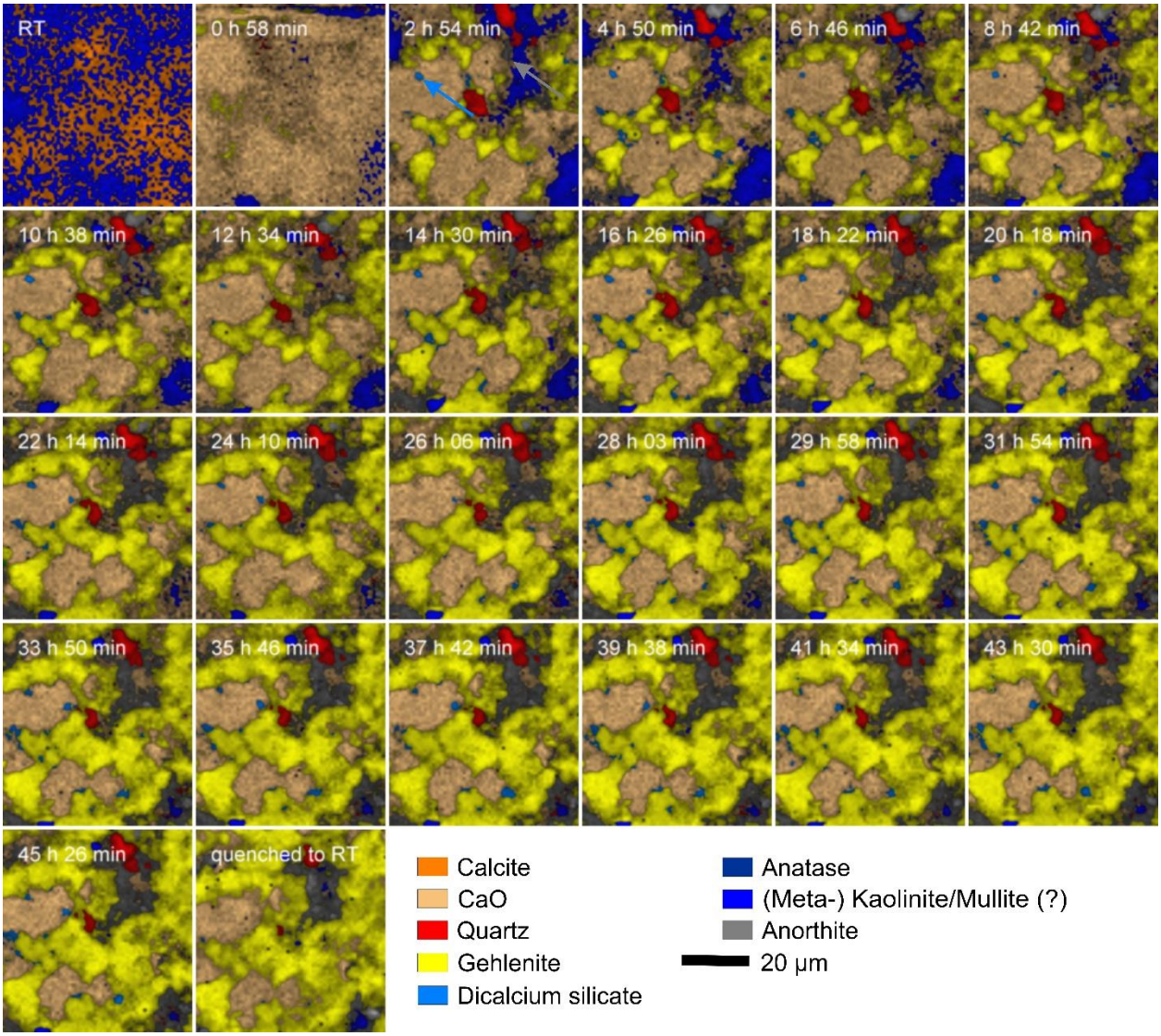

Figure S4.4: Normalized false-color hyperspectral Raman images of experiment T931. A mixture of kaolinite and calcite was fired at 931°C for about 48 hours. The area that was present in all high-temperature Raman images despite shifting of the sample, was chosen from the original image of 100 x 100 µm. In this experiment an area of 68 x 73 µm was used for further interpretation. At room temperature (RT) kaolinite and calcite were present. The first map at sintering temperature that was recorded during the first two hours of firing (the average dwell time is shown on the pictures) seems to be out of focus. In the second image (2 h 54 min) the reaction product of the calcite decomposition CaO, and metakaolinite were present. The hydroxylation of kaolinite is not visible, because both phases have the same color. Quartz was also present, which is an impurity of kaolinite. Additionally, dicalcium silicate, anorthite (marked by a grey arrow), and gehlenite were visible. With time the content of these three phases increased. Gehlenite constituted the main part of the analyzed area.

At RT kaolinite and calcite were present in T931 (Figure S4.4). The first map at sintering temperature that was recorded during the first two hours of firing (the average dwell time is shown on the pictures) seems to be out of focus. In the second image (2 h 54 min) the reaction product of the calcite decomposition CaO, and metakaolinite were present. The hydroxylation of kaolinite is not visible, because both phases were depicted in the same color. Quartz was also present, which is an impurity of kaolinite. Additionally, dicalcium silicate, anorthite (marked by a grey arrow), and gehlenite were visible as newly formed phases. With time the content of these three phases increased. After 48 hours of firing gehlenite constituted the main part of the analyzed area.

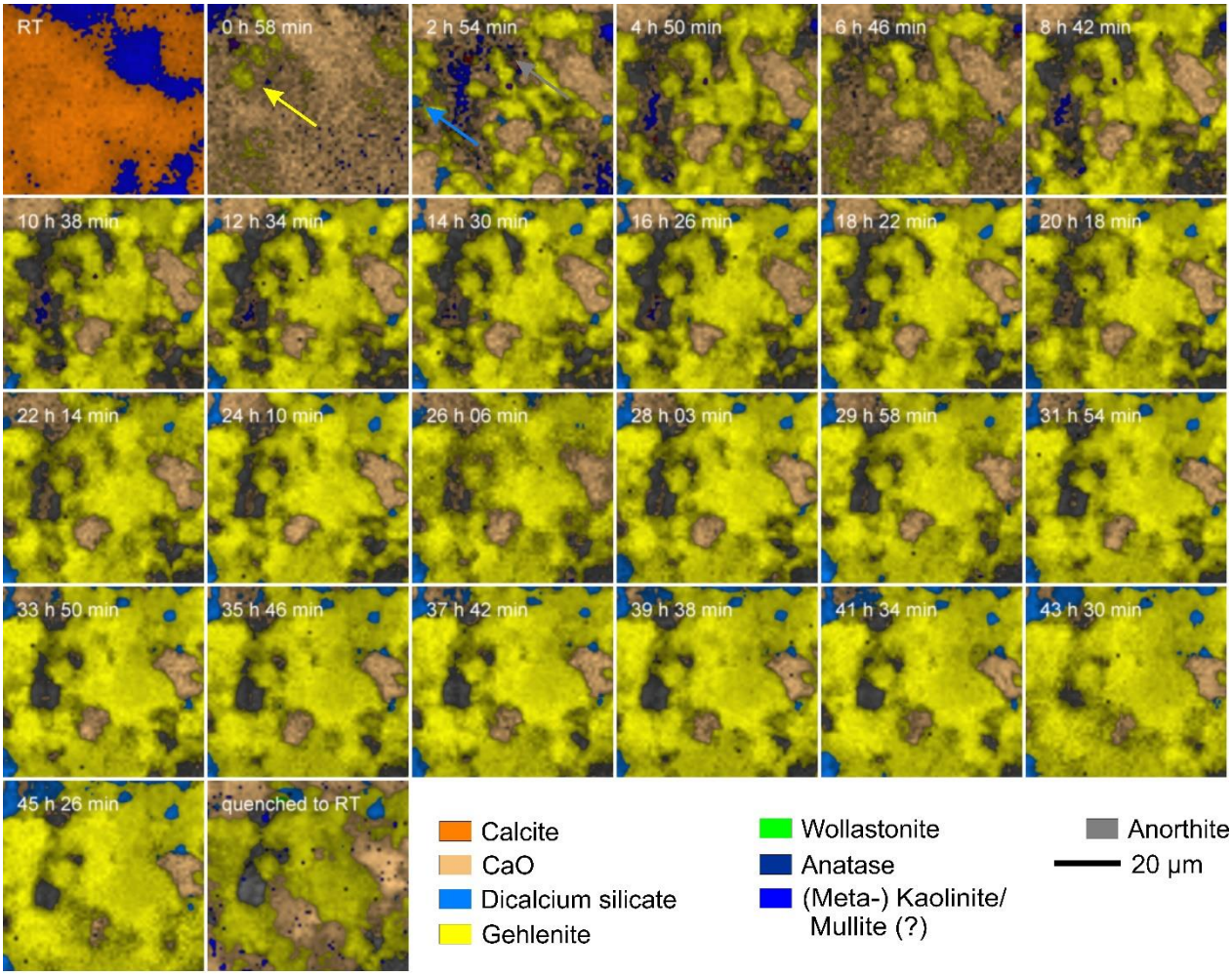

Figure S5: Normalized false-color hyperspectral Raman images of experiment T971. A mixture of kaolinite and calcite was fired at 971°C for about 48 hours. The area that was present in all high-temperature Raman images despite shifting of the sample, was chosen from the original image of 100 x 100 µm. In this experiment an area of 61 x 58 µm was used for further interpretation. At room temperature (RT) kaolinite and calcite were present. Gehlenite (marked by a yellow arrow) was already formed when recording the first map (0 h 58 h). Calcite was decomposed to CaO and CO_2. Kaolinite was dehydroxylated to metakaolinite. The hydroxylation of kaolinite was not visible, because both phases were depicted in the same color. Dicalcium silicate and anorthite (marked by a light blue and grey arrow, respectively) were firstly visible in the second HT map (2 h 54 min). With time the contents of the phases dicalcium silicate, anorthite, and gehlenite phases were increased. Gehlenite constituted up the main part of the analyzed area.

At room temperature (RT) kaolinite and calcite were present. Gehlenite (marked by a yellow arrow) was already formed when recording the first map (0 h 58 h). Calcite was decomposed to CaO and CO_2. Kaolinite was dehydroxylated to metakaolinite. The hydroxylation of kaolinite was not visible, because both phases were depicted in the same color. Dicalcium silicate and anorthite (marked by a light blue and grey arrow, respectively) were firstly visible in the second HT map (2 h 54 min). With time the contents of the phases dicalcium silicate, anorthite, and gehlenite phases were increased. Gehlenite constituted the main part of the analyzed area.

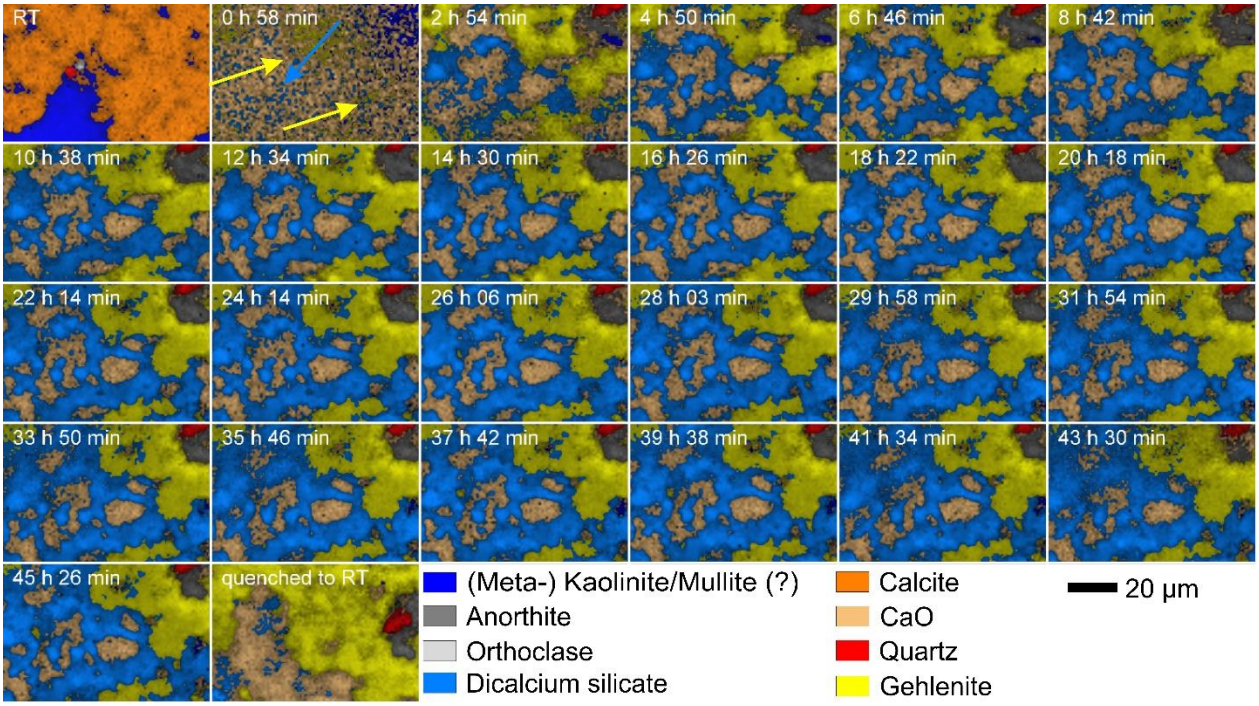

Figure S6: Normalized false-color hyperspectral Raman images of experiment T1020. A mixture of kaolinite and calcite was fired at 1020°C for about 48 hours. The area that was present in all high-temperature Raman images despite shifting of the sample, was chosen from the original image of 100 x 100 µm. In this experiment an area of 66 x 44 µm was used for further interpretation. The area of the RT map was not the same as in the HT images. Therefore, only a part of this map is shown. At room temperature (RT) kaolinite, quartz, orthoclase, and calcite were present. Quartz and orthoclase were impurities within the kaolinite. In the first map at sintering temperature that was recorded during the first two hours of firing (the average dwell time is shown on the pictures) CaO, metakaolinite, dicalcium silicate (marked by a light blue arrow), and gehlenite (marked by a yellow arrow) were present. In the second map at sintering temperature (image 2 h 54 min) anorthite was formed. With time the contents of gehlenite, dicalcium silicate, and anorthite increased.

Sample T1020 was fired for about 48 hours at 1020°C. Unfortunately, the area mapped at RT was not the same as in the HT images. Therefore, only a part of this map is shown (Figure S6). In the RT map calcite, kaolinite, and anatase were present. At room temperature (RT) kaolinite, quartz, orthoclase, and calcite were present. Quartz and orthoclase were impurities within the kaolinite. The first map at sintering temperature that was recorded during the first two hours of firing (the average dwell time is shown on the pictures) CaO, metakaolinite, dicalcium silicate (marked by a light blue arrow), and gehlenite (marked by a yellow arrow) were present. In the second map at sintering temperature (image 2 h 54 min) anorthite was formed. With time the contents of gehlenite, dicalcium silicate, and anorthite increased.

2 The semi-quantitative mineral content with time and temperature

A semi-quantitative mineral content was obtained from the matrices behind the unnormalized images of all 13 pure phases (end members) of the CLS fit and plotted against the dwell time (Figure S7-S18). Because the total intensities of the Raman images of the experiments differ, the phase contents were normalized to the sum of intensity within each Raman image. Some variations in the phase content were due to technical reasons resulting from auto-focus problems. This applies especially to T880 and can best be seen in the false-color hyperspectral Raman images (Figures S4.1-S4.6). All samples were a 1:1 mixture of calcite and kaolinite. Due to heterogeneity the proportions of these phases differed in the analyzed areas of the six experiments. Small amounts of accessory phases like anatase, quartz, orthoclase, and millerite occured within the kaolinite precursor material. The apparent millerite content was added to the apparent kaolinite content (see chapter S4.1 for details). It was not always possible to find the same area in the RT Raman images and the HT series, because there were no distinctive markings in the RT images that were useful for orientation. Therefore, the phase proportions of the RT and HT images within one experiment can only be compared to a limited extent.

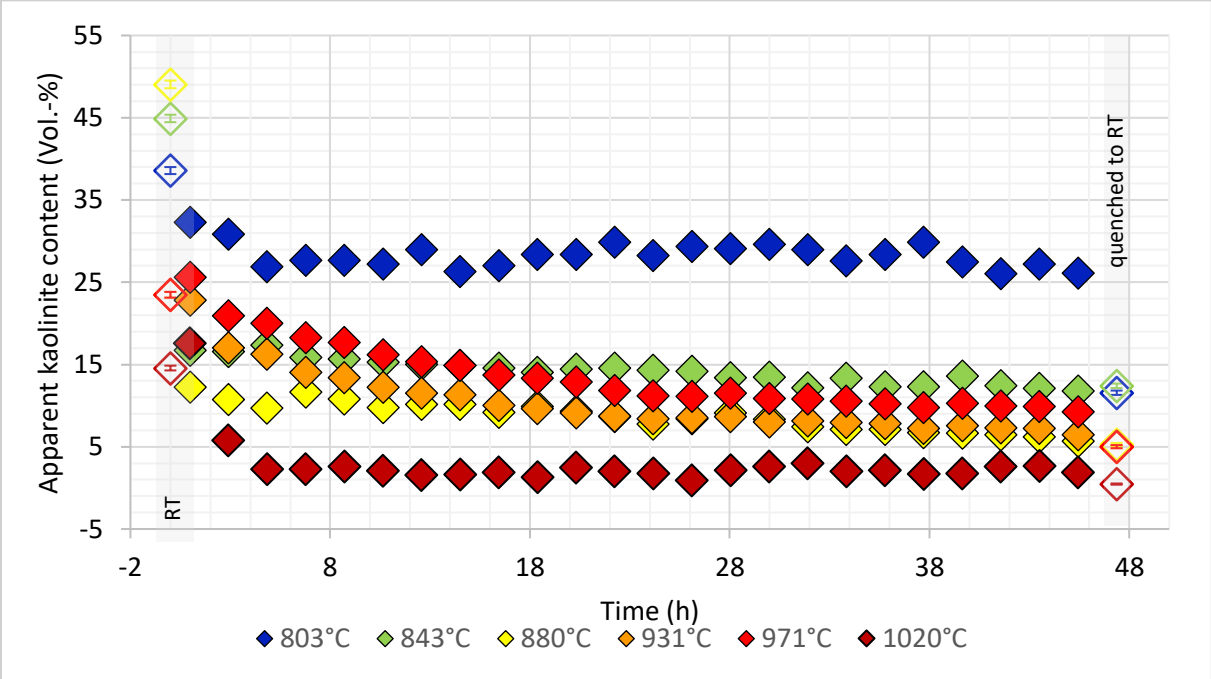

Figure S4.7: The apparent kaolinite content obtained from the matrices of the CLS fit as a function of time. Experiment T803 had the highest content of metakaolinite that remained stable during the experiment. In all other experiments the kaolinite content exponentially decreased with time. The millerite content was added to the kaolinite content (see chapter S4.1 for details).

The kaolinite content was between about 15 vol.-% (T1020) and 50 vol.-% (T880) in the RT images of the six experiments. During firing to the sintering temperature all kaolinite was dehydroxylated to metakaolinite. This can distinctly be observed in the Raman spectra by the disappearing of the weak kaolinite bands. All other reactions of the kaolinite-mullite reaction sequence cannot be directly observed by Raman spectroscopy [13] until now and therefore these phases are not distinguishable in the Raman images. So far, it has only been possible to estimate which phase is present on the basis of the firing temperature. The Raman image in experiment T803 had with about 30 vol.-% the highest content of metakaolinite that remained stable during the experiment (Figure S4.1 and S4.7). In all other experiments the metakaolinite content exponentially decreased with time. In the RT image the calcite content was between 45 vol.-% (T880) and 80 vol.-% (1020) (Figure S4.8). Calcite decomposed during firing to sintering temperature to CaO and CO_2 and was not detectable in any HT image. During cooling after the dwell time of about 48 hours small amounts of calcite were formed in some experiments. The

lower the sintering temperature, the higher the calcite content after cooling. In the experiments with a sintering temperature higher than 843°C the calcite content after cooling was under 2 vol.-%. In T803 the CaO content slightly decreased and seemed to increase in the last third (Figure S4.9).

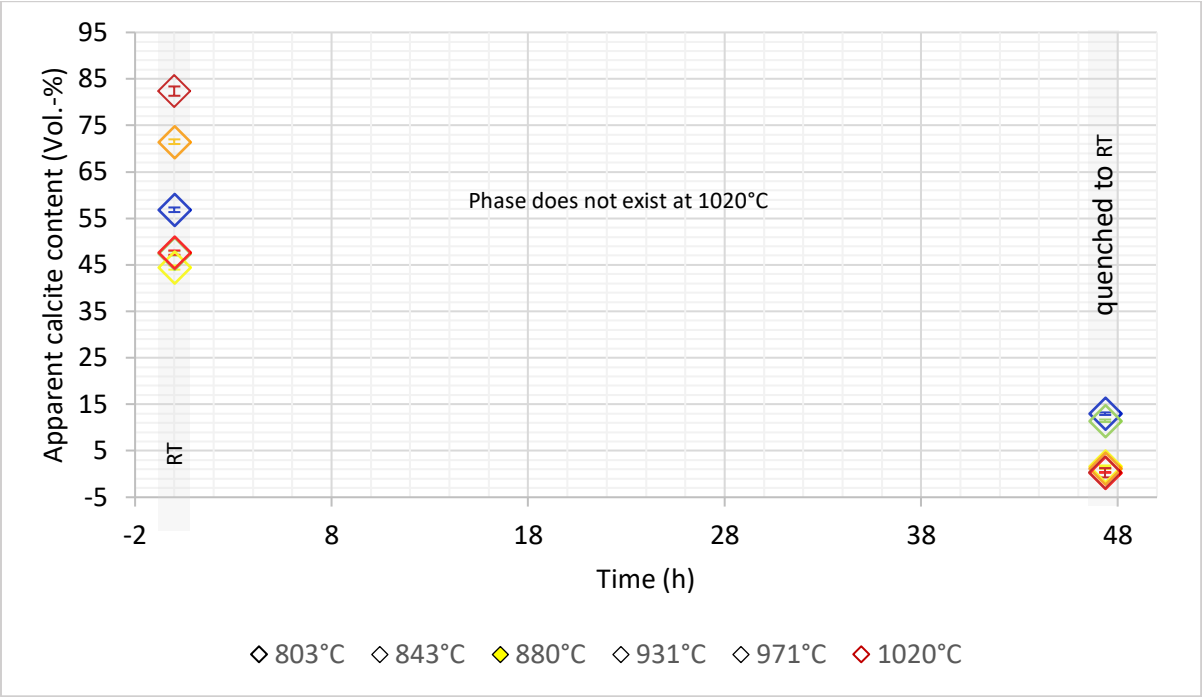

Figure S4.8: The apparent calcite content obtained from the matrices of the CLS fit as a function of time. In the RT image the calcite content was between 45 vol.-% (T880) and 80 vol.-% (1020). During firing calcite was not detectable. During cooling small amounts of calcite were formed. The lower the sintering temperature, the higher the calcite content was after cooling. It was not always possible to find the same area in the RT Raman images and the HT series, because there were no distinctive markings in the RT images that were useful for orientation.

In the beginning of all other experiments the CaO content decreased strongly within the first hours. The higher the firing temperature, the more pronounced was the decrease. In T843 and T880 the CaO decrease was only slight after the first eight hours. In T931 and T971 the CaO content decreased linearly after the exponential decrease during the first hours. At T1020°C the CaO content behaved similarly to that in T971°C during the first 15 hours and then remained stable at around 15 vol.-%. During firing new minerals occurred within the hyperspectral Raman images. Calcium silicates like wollastonite, pseudowollastonite, and dicalcium silicate as well as calcium aluminum phases like gehlenite and anorthite were formed. Additionally, an unknown phase with a broad Raman band near 560 cm^{-1} (value for RT, the phase was metastable preserved in another experiment that is not presented here). During firing to sintering temperature little amounts of gehlenite were formed in all experiments which increased during the dwell time of 48 hours. Up to 971°C the gehlenite content increased more strongly the higher the firing temperature was set. In the experiments T803, T843, and T880, the increase was more or less linear. In T931 the gehlenite content was increased fast during the first 8 hours and the increase was linear, as well. For the first 28 hours of T971 the gehlenite increase was exponential. Then the increase slowed down and after a dwell time of about 48 hours gehlenite constituted 60 vol.-% of the map. The gehlenite content in T1020 exponentially increased during the first six hours and then slightly decreases to 30 vol.-% after 48 hours. Dicalcium silicate increased linearly with time in experiments T843, T880, and T931. In the last third the dicalcium silicate content in T880 exceeded the content in T931.

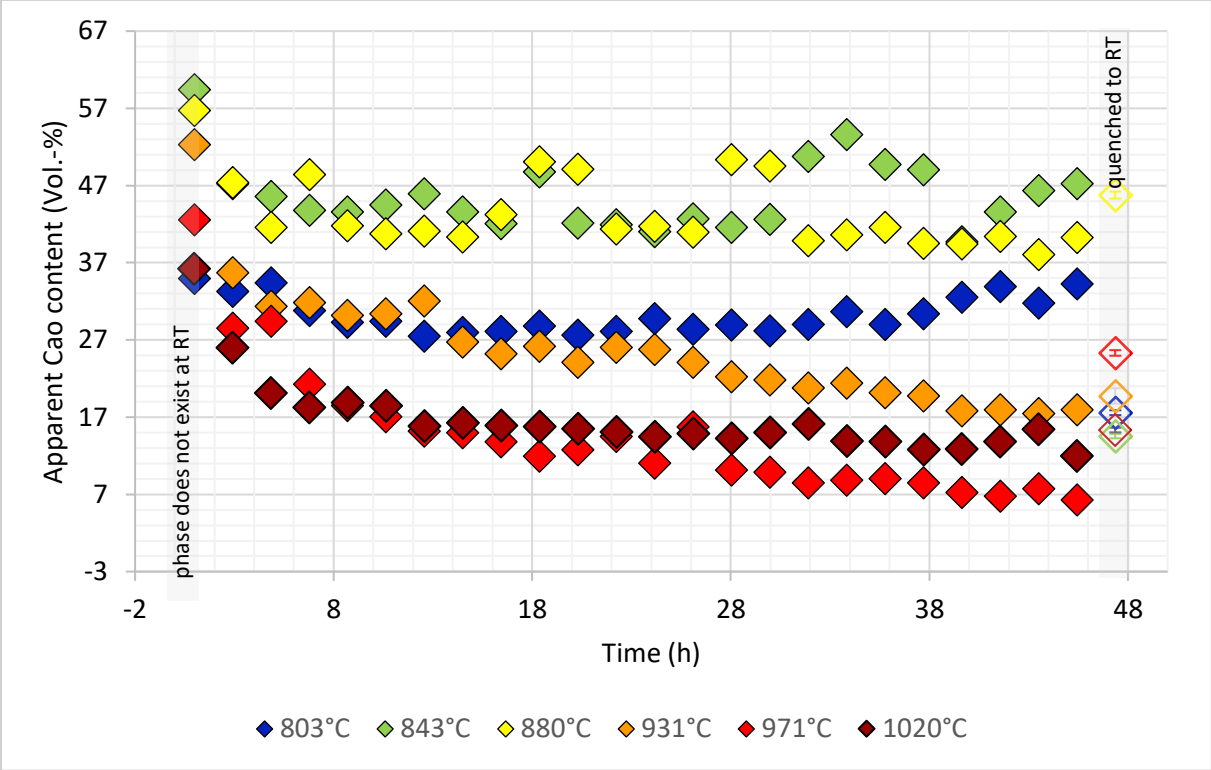

Figure S4.9: The apparent CaO content obtained from the matrices of the CLS fit as a function of time. In T803 the CaO content slightly decreased and seemed to increase in the last third. In the beginning of all other experiments the CaO content decreased strongly within the first hours. The higher the firing temperature, the more pronounced was the decrease. In T843 and T880 the CaO decrease was only slight after the first eight hours. In T931 and T971 the CaO content decreased linearly after the exponential decrease during the first hours. In T1020 the CaO content behaved similarly to that in T971°C during the first 15 hours and then remains stable at around 15 vol.-%.

In T971 the increase of dicalcium silicate was the highest in the first eight hours, followed by a linear increase up to 40 hours. Then the dicalcium silicate formation seemed to increase more strongly. At the highest sintering temperature, the dicalcium silicate content exponentially increased during the first eight hours and then the increase slowed down. After a dwell time of about 48 hours dicalcium silicate constituted 50 vol.-% of the map. In general, the content of the unknown phase 560 increased fast during the first hours and then slowly decreased again. The lower the sintering temperature, the higher was the content of phase 560. One exception was T880 with the highest content of about 20 vol.-% after a dwell time of six hours. However, after firing for 48 hours the content of phase 560 was lower than in T803. At a sintering temperature of 1020°C phase 560 was not formed. Phase 560 disappeared during cooling and could not be detected in any room temperature map. The anorthite content behaved very differently in the experiments. In T803 anorthite seemed to increase linearly with time. In T843 and T931 the anorthite content increased with a maximum at a dwell time of 24 hours and then decreases slightly. In T931 the highest amount of anorthite was formed after a dwell time of 48.

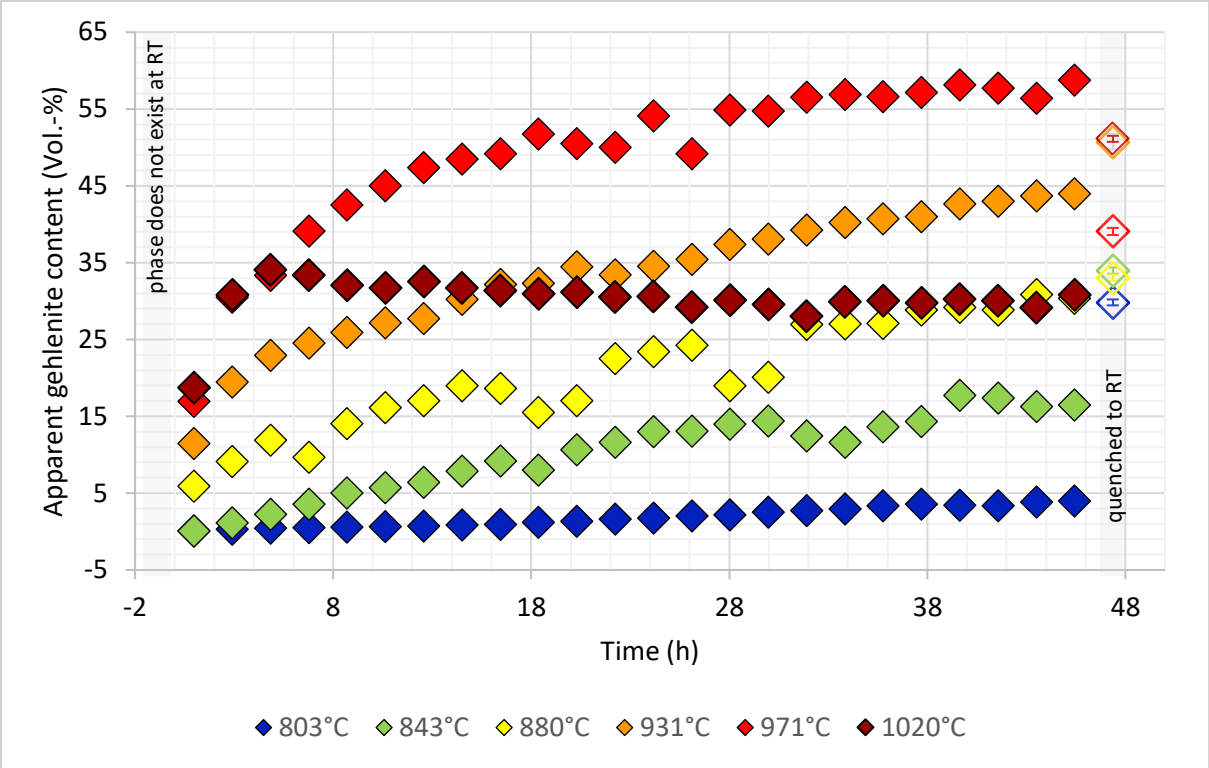

Figure S4.10: The apparent gehlenite content obtained from the matrices of the CLS fit as a function of time. Up to 971°C the gehlenite content increased more strongly the higher the firing temperature of the experiment was set. In the experiments T803, T843, and T880, the increase was more or less linear. In T931 the gehlenite content was increasing fast during the first eight hours. Afterwards, the increase was linear as well. For the first 28 hours of T971 the gehlenite increase was exponential. Then the increase slows down and after a dwell time of about 48 hours gehlenite constituted 60 vol.-% of the map. The gehlenite content in T1020 exponentially increases during the first six hours and then slightly decreases with time to 30 vol.-% after 48 hours.

In T880 and T1020 anorthite did not increased with time and in T971 increased during the first eight hours and then decreased. Wollastonite and pseudowollastonite were formed only in small quantities under 5 vol.-%. Up to a sintering temperature of 931°C the wollastonite content increased linearly with time. In T931 the content increased fast during the first eight hours and then linearly. In T931°C there was the highest amount of wollastonite. Here the increase was exponential during the first 20 hours and then increased only slightly. In T1012°C only 2 vol.-% wollastonite formed during 48 hours of firing. Pseudowollastonite seemed to decrease with time.

Quartz, orthoclase, and anatase were accessory minerals within the kaolinite precursor material. Quartz occurred in different proportions of up to 15 vol.-% in the experiments. In T843 the quartz content seemed to decrease with time. In all other experiments the quartz content remained more or less the same. In experiment T803 eight percent orthoclase were present in the first HT map. With time the amount of orthoclase was decreased. In the other experiments the orthoclase content remained more or less the same during the dwell time of 48 hours. Anatase occurred in little proportions under 2.5 vol.-% in all experiments. With time it seemed to decrease or remained stable during the dwell time.

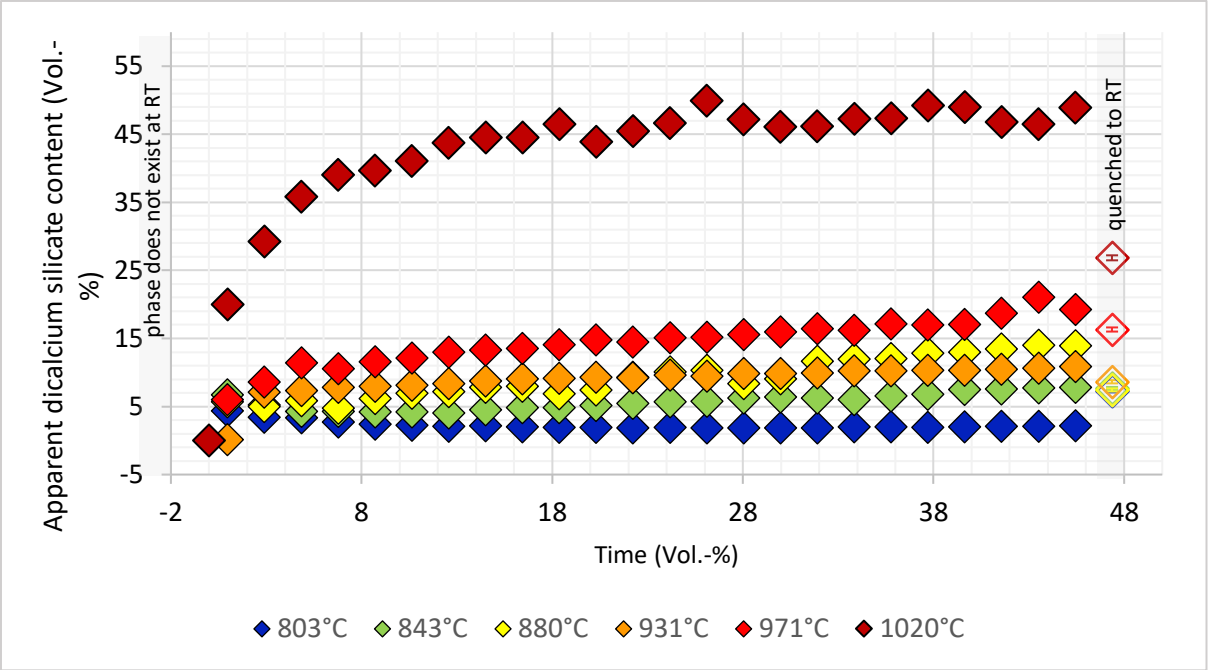

Figure S4.11: The apparent dicalcium silicate content obtained from the matrices of the CLS fit as a function of time. In experiments T843, T880, and T931, dicalcium silicate increased linearly with time. In the last third the dicalcium silicate content in T880 exceeded the content in T931. In T971 the increase of dicalcium silicate was the highest in the first eight hours, followed by a linear increase up to 40 hours. Then the dicalcium silicate formation seemed to increase more strongly again. At the highest sintering temperature, the dicalcium silicate content exponentially increased during the first eight hours and then the increase slowed down and after a dwell time of about 48 hours dicalcium silicate constitutes 50 vol.-% of the map.

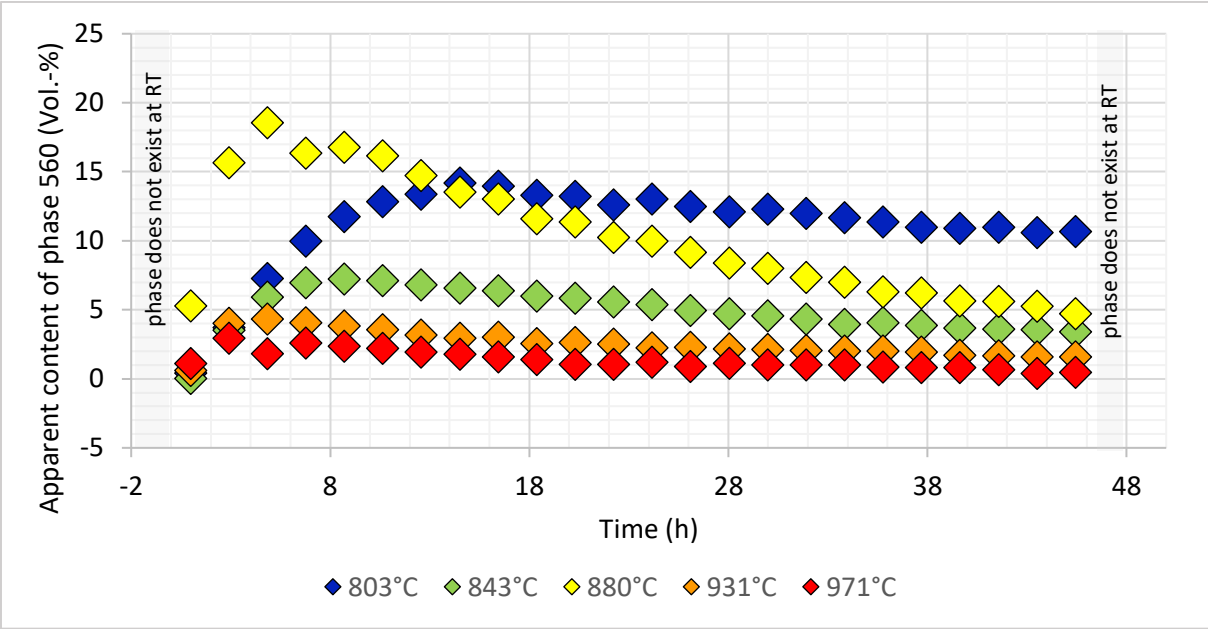

Figure S4.12: The apparent content of the unknown phase obtained from the matrices of the CLS fit as a function of time. In general, the content of phase 560 increased fast during the first hours and then slowly decreased again. The lower the sintering temperature, the higher is the content of phase 560. One exception is T880 with the highest content of about 20 vol.-% after a dwell time of six hours. However, after firing for 48 h the content of phase 560 was lower than in the experiment at 803°C. At a sintering temperature of 1020°C phase 560 was not formed. Phase 560 disappeared during cooling and cannot be detected in any room temperature map.

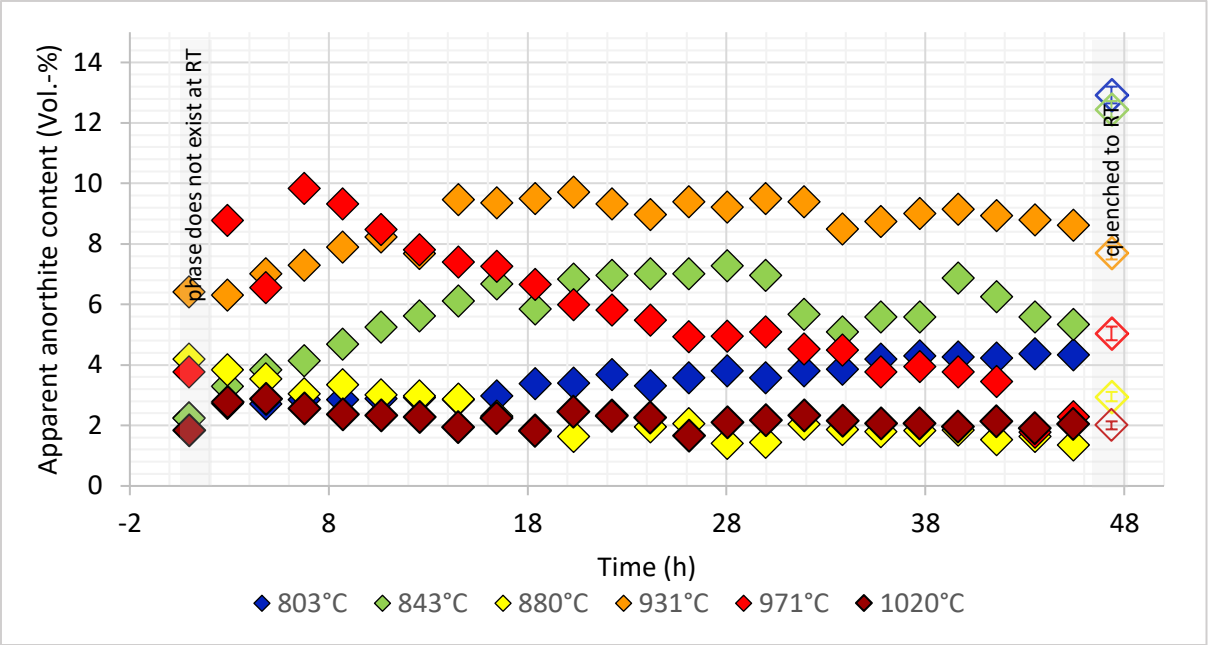

Figure S4.11: The apparent anorthite content obtained from the matrices of the CLS fit as a function of time. The anorthite content behaved very differently in the experiments. In T803 anorthite seemed to increase linearly with time. In T843 and T931 the anorthite content increased to a maximum at a dwell time of 24 hours and then decreased slightly. In T931 there was the highest amount of anorthite after a dwell time of 48 hours. In T880 and T1020 anorthite decreased with time. In T971 it increased during the first eight hours and then decreased.

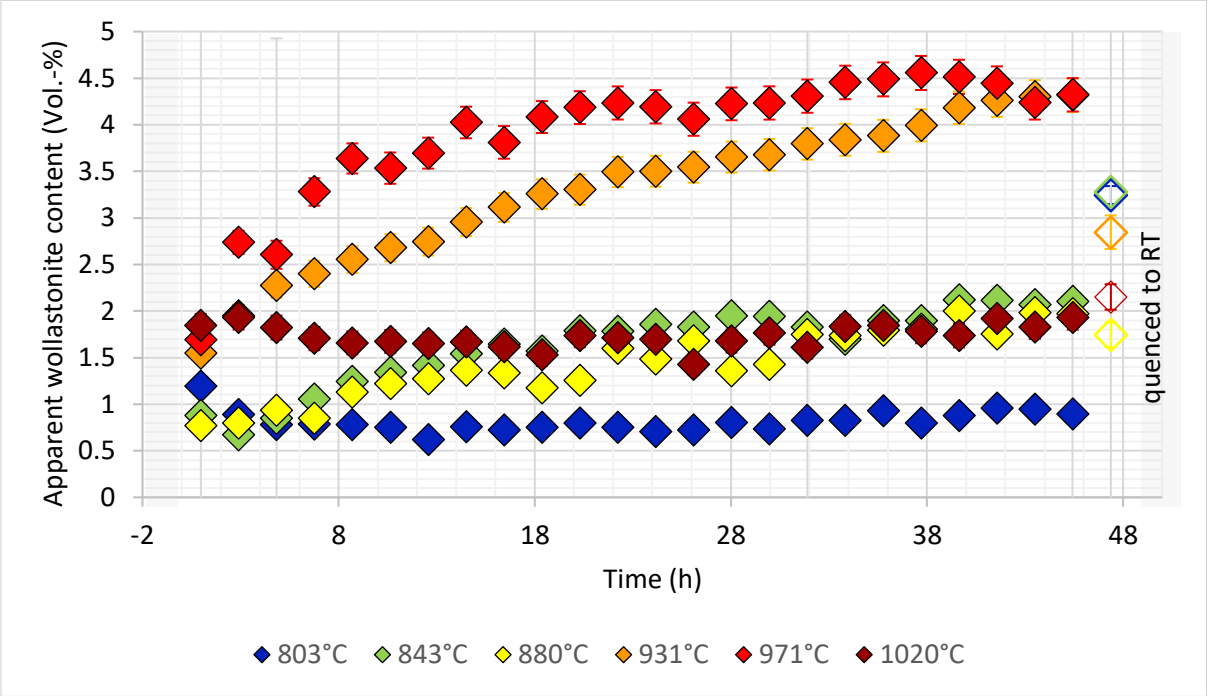

Figure S4.12: The apparent wollastonite content obtained from the matrices of the CLS fit as a function of time. Wollastonite was formed in small quantities only. Up to a sintering temperature of 931°C the wollastonite content increased linearly with time. In T931 the content increased fast during the first eight hours which was followed by a linear increase. In T931°C the wollastonite content was the highest. Here the increase was exponential during the first 20 hours. After that, it increased only slightly. In T1020°C only 2 vol.-% wollastonite formed during the 48 hours of firing.

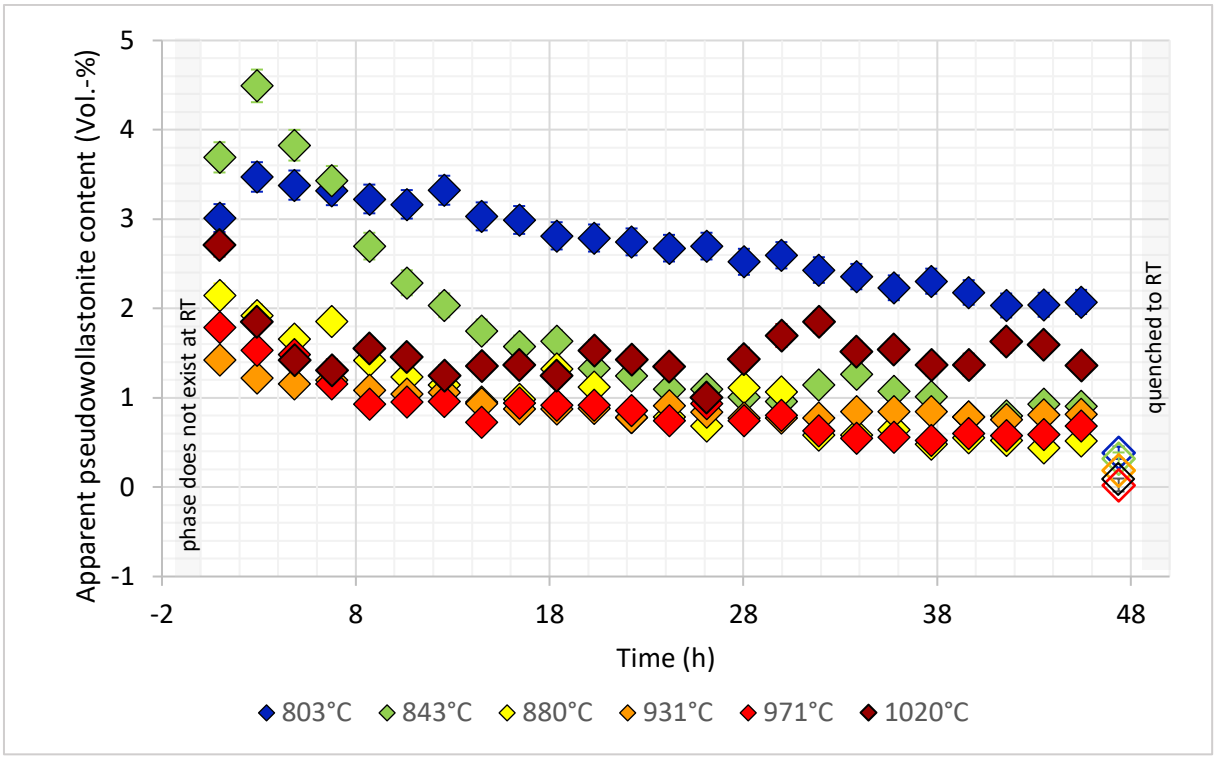

Figure S4.13: The apparent pseudowollastonite content obtained from the matrices of the CLS fit as a function of time. Pseudowollastonite seemed to decrease with time.

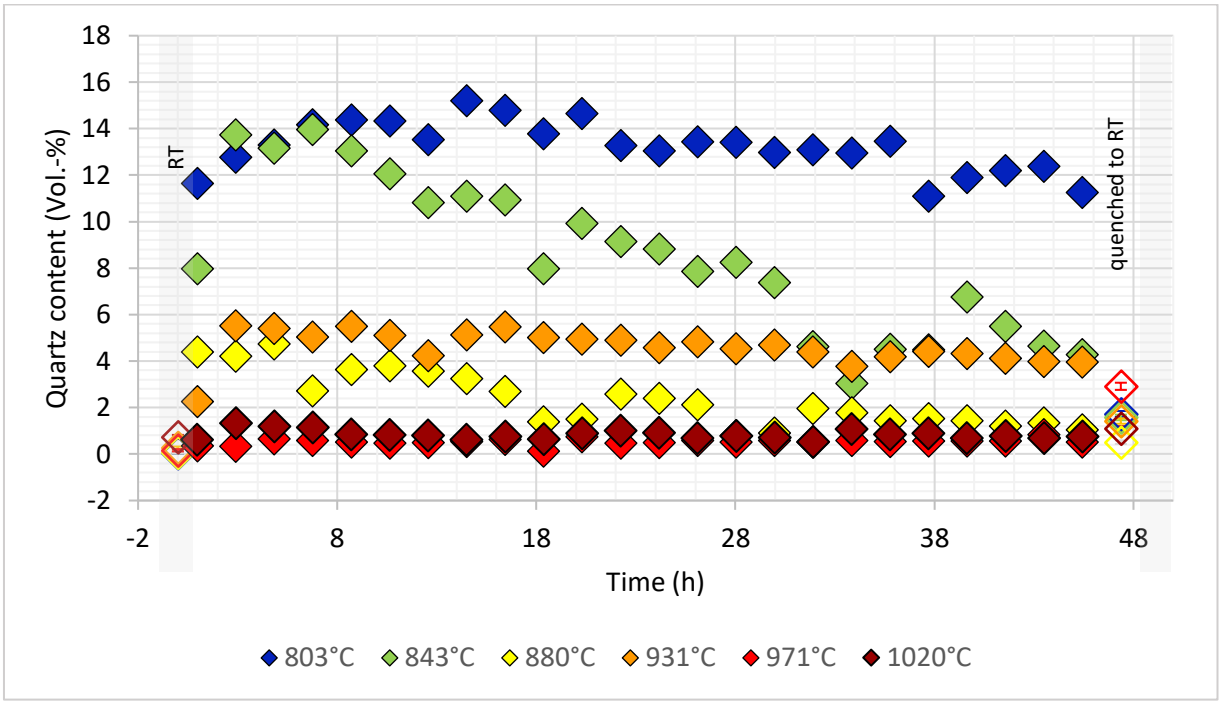

Figure S4.14: The apparent quartz content obtained from the matrices of the CLS fit as a function of time. Quartz was an accessory mineral within the kaolinite precursor material. It occurred in different amounts in the experiments. In T843 the quartz content seemed to decrease with time. In all other experiments the quartz content remained more or less the same.

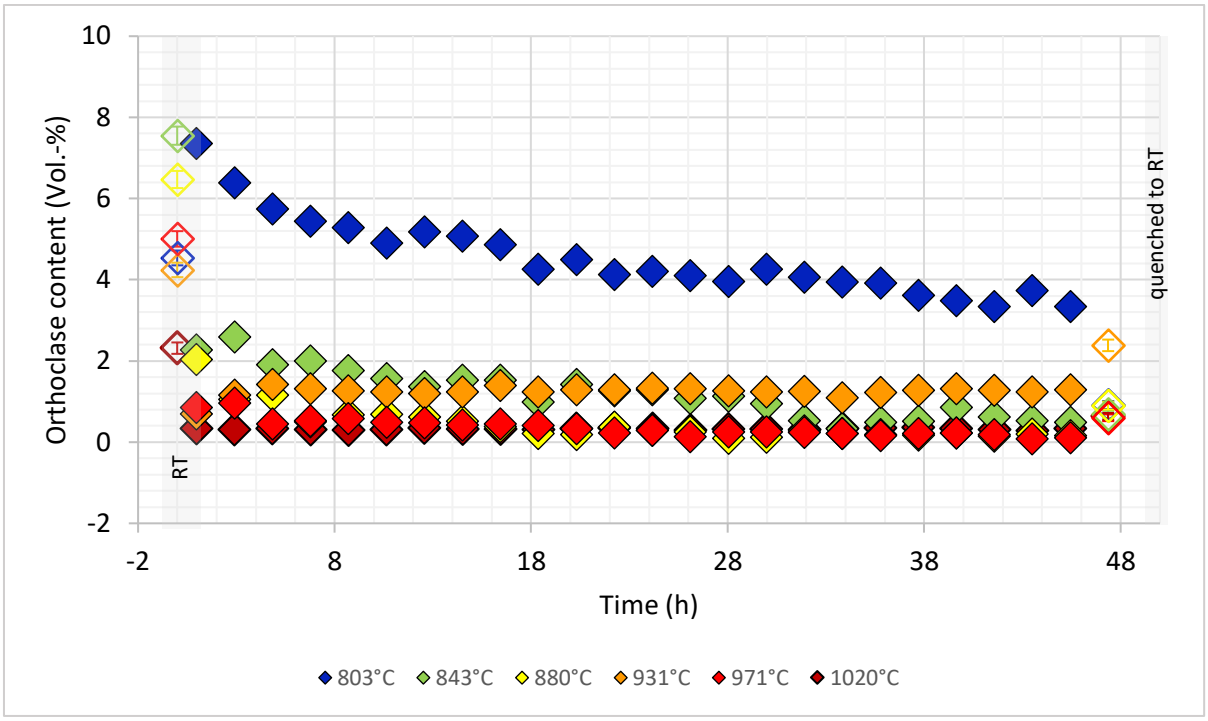

Figure S4.15: The apparent orthoclase content obtained from the matrices of the CLS fit as a function of time. Orthoclase was an accessory mineral within the kaolinite precursor material. In experiment T803 8 vol.-% of orthoclase were present in the first HT map. With time the amount of orthoclase decreased. In the other experiments the orthoclase content remained more or less the same during the dwell time of 48 hours.

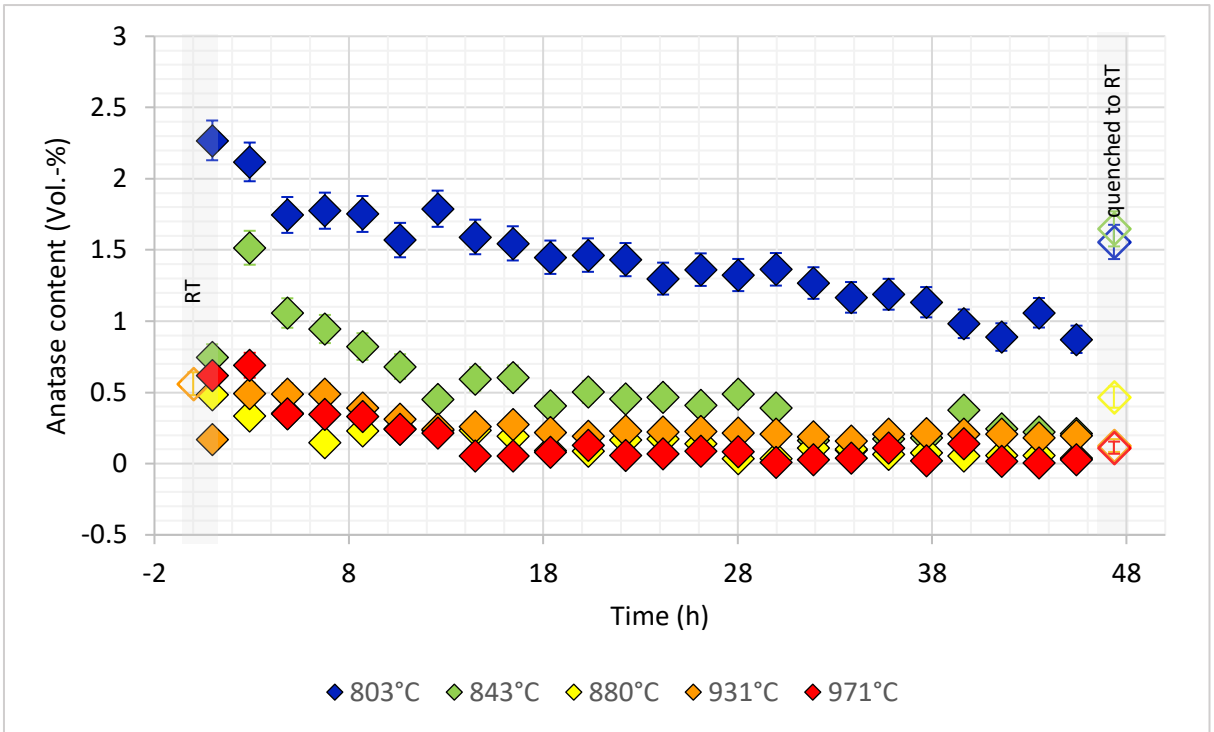

Figure S4.18: The apparent anatase content obtained from the matrices of the CLS fit as a function of time. Anatase was an accessory mineral within the kaolinite precursor material. It occurred in small amounts in the experiments. With time it seemed to decrease.

Table S1: Calcium alumosilicates along with the chemical formula, crystal system, space group and the main Raman bands.

Name	Chemical formula	Crystal system	Space group	Main Raman bands
Anorthite	$CaAl_2Si_2O_8$	triklinic	*P-1*	487, 504, 557 [213]
Dmisteinbergite	$CaAl_2Si_2O_8$	hexagonal	*P6/mmm*	115, 439, 912 [214]
				327, 442, 912[213]
Donwilhelmsite	$CaAl_4Si_2O_{11}$	hexagonal	$P6_3/mmc$	420, 618, 912[215]
Gehlenite	$Ca_2Al(AlSi)O_7$	tetragonal	$P\text{-}42_1m$	626, 655, 914[64]
Grossular	$\{Ca_3\}[Al_2](Si_3)O_{12}$	cubic	Ia-3d	211, 342, 589[171]
Kushiroite	$CaAl_2SiO_6$	monoclinic	C2/c	675, 959 [216]
Stöfflerite	$CaAl_2Si_2O_8$	tetragonal	I4/m	
Svyatoslavite	$CaAl_2Si_2O_8$	orthorhombic	$P2_12_12$	171, 223, 508[34]
Yoshiokaite	$Ca(Al,Si)_2O_4$	trigonal	P-3	430, 473[217]
Zagamiite	$CaAl_2Si_{3.5}O_{11}$	hexagonal	$P6_3/mmc$	No spectrum available
Hibonite	$CaAl_{12}O_{19}$	hexagonal	$P6_3/mmc$	330, 946 [218]
Grossite	$CaAl_4O_7$	monoclinic	C2/c	269, 412, 909 [218]
Cowlesite	$Ca(Si_3Al_2)O_{10}$*5-6H_2O	orthorhombic	*Ccme*	325, 393, 534 [163]

V.VII Experimental conditions

Table V.II.1: Experimental conditions of all single-phase (heating study) experiments, two-phase (heating ramp) experiments, isothermal experiments, methodical experiments and test experiments that were performed within this project.

No.	Phase(s)	Exp.	Furnance	Temperature						Time	Instrument				Acquisition			Map		Published
				Range			Step	Heating rate	Cooling rate	Dwell time	Laser	Power	Slit	Hole	Spectral range	Aq. time	Accumulations.	Area	Step	
				°C				°C/min		min	nm	W			cm^{-1}	s		µm	µm	
Single phase experiments																				
1-1-1	Calcite	*in situ*	T1500	30	→	380	10	10	10	10	532	0,25	100	1000	100-1730	2	300			
1-1-2	Calcite	*in situ*	T1500	800	→	30	10	10	10	10	532	?	50	1000	50-4000	3	50			
1-1-3	Calcite	*in situ*	T1500	30	→	800	10	10	10	10	532	0,25	50	1000	100-1730	3	5			
1-1-4	Calcite	*in situ*	T1500	30	→	1200	10	5	200	5	532	2	100	500	100-1730	5	3			
1-1-5	Calcite	*in situ*	T1500	30	→	1100	10	5	10	5	532	2	100	300	100-1730	1	100			Chap. 5,[60]
1-1-6	Calcite	*in situ*	T1500	30	→	900	10	5	50	5	532	2	100	300	100-1730	1	100			
1-1-7	Calcite	*in situ*	T1500	30	→	1250	10	5	50	5	532	2	100	300	100-1730	1	100			
1-1-8	Calcite	*in situ*	T1500	30	→	1300	10	5	10	5	532	2	100	300	100-1730	1	100			
1-1-9	Calcite	*in situ*	T1500	30	→	1300	10	5	10	5	532	2	100	300	100-1730	1	100			
1-2-1	Gehlenite	*in situ*	T1500	30	→	1200	10	10	10	10	532	0,25	100	1000	100-1725	3	30			
1-2-2	Gehlenite	*in situ*	T1500	30	→	1200	10	10	10	5	532	0,8	100	1000	100-1730	3	30			
1-2-3	Gehlenite	*in situ*	T1500	30	→	1400	10	10	10	5	532	2	100	300	100-1725	1	100			
1-2-4	Gehlenite	*in situ*	T1500	30	→	1400	10	10	10	5	532	2	100	300	100-1725	1	100			
1-2-5	Gehlenite	*in situ*	T1500	30	→	1400	10	10	10	5	532	1	100	300	100-1730	1	100			
1-2-5-2	Gehlenite	*in situ*	T1500	700	→	1200	10	10	10	5	532	2	100	300	100-1730	1	100			
1-2-5-3	Gehlenite	*in situ*	T1500	600	→	1200	10	10	10	5	532	1	100	300	100-1730	1	200			
1-2-6	Gehlenite	*in situ*	T1500	600	→	1200	10	10	10	5	532	2	100	300	100-1730	1	200			
1-3-1	Wollastonite	*in situ*	T1500	30	→	1200	10	5	200	5	532	0,5	100	1000	80-1720	2	100			Chap. 5
1-3-2	Wollastonite	*in situ*	T1500	30	→	1270	10	5	200	5	532	0,5	100	1000	80-1720	2	100			[219]
1-3-3	Wollastonite	*in situ*	T1500	1200	→	30	10	5	200	5	532	0,5	100	1000	100-1730	3	100			[219]
1-3-4	Wollastonite	*in situ*	T1500	1075	→	1127	1	5	200	5	532	2	100	300	90-1730	10	10			
1-3-5	Wollastonite	*in situ*	T1500	1075	→	1201	2	1	200	5	532	2	100	300	90-1730	10	10			
1-3-6	Wollastonite	*in situ*	T1500	1100	→	1206		1	?	5	532	2	100	300	100-1730	10	10			
1-3-7	Wollastonite	*in situ*	T1500	30	→	1250	10	10	10	2,5	532	2	100	300	95-1725	10	50			
1-3-8	Wollastonite	*in situ*	T1500	30	→	1200	10	10	10	5	532	2	100	300	100-1725	1	100			
1-3-9	Wollastonite	*in situ*	T1500	30	→	1400	10	10	10	5	532	2	100	300	100-1730	1	100			Chap. 5
1-3-A	Wollastonite	*in situ*	HT-RDX	30	→	1200	10	10	10		-	-	-	-	-	-	-			
1-4-3	Anhydrite	*in situ*	T1500	30	→	1350	10	10	200	5	532	2	100	300	90-1725	1	150			
1-4-1	Anhydrite	*in situ*	T1500	30	→	320	10	10	200	5	532	2	100	300	90-1725	5	20			
1-4-2	Anhydrite	*in situ*	T1500	30	→	700	10	10	200	5	532	2	100	300	90-1725	1	150			
1-4-3	Anhydrite	*in situ*	T1500	30	→	1350	10	10	200	5	532	2	100	300	90-1725	1	150			
1-4-4	Anhydrite	*in situ*	T1500	30	→	1020	10	10	200	5	532	2	100	300	90-1725	1	150			
1-4-5	Anhydrite	*in situ*	T1500	30	→	1400	10	10	10	5	532	2	100	300	90-1725	1	100			
1-5-1	Pseudowollastonite	*in situ*	T1500	30	→	1400	10	10	200	5	532	2	100	300	90-1725	2	100			
1-5-2	Pseudowollastonite	*in situ*	T1500	30	→	1200	10	10	10	5	532	2	100	300	100-1725	1	100			
1-6-5	Quartz	*in situ*	T1500	30	→	1400	10	10	200	5	532	2	100	300	100-1725	0,1	1000			
1-6-1	Quartz	*in situ*	T1500	30	→	1000	10	5	200	5	532	1,5	100	1100	80-1723	1	180			
1-6-2	Quartz	*in situ*	T1500	30	→	1000	10	5	200	2	532	1,5	100	1100	80-1723	1	300			
1-6-3	Quartz	*in situ*	T1500	560	→	590	1	5	200	2	532	1,5	100	1100	50-650 (2 windows)	1	300			
1-6-4	Quartz	*in situ*	T1500	590	→	560	1	5	5	2	532	1,5	100	1100	50-650 (2	1	300			

															windows)				
1-6-5	Quartz	*in situ*	T1500	30	→	1400	10	10	200	5	532	2	100	300	100-1725	0,1	1000		
1-6-6	Quartz	*in situ*	T1500	565	→	585	1	1	10	1	532	2	100	300	100-1725	1	50		
1-6-7	Quartz	*in situ*	T1500	30	→	1250	10	10	10	5	532	2	100	300	100-1725	1	100		
1-7-1	Albite	*in situ*	T1500	30	→	1390	10	10	200	5	532	2	100	300	100-1725	1	100		
1-8-1	Kaolinite	*in situ*	T1500	30	→	700	10	5	10	5	532	2	100	500	180 to 1750; 3200 to 4200	20	10		
1-8-2	Kaolinite	*in situ*	T1500	700	→	1240	10	5	10	5	532	2	100	500	180 to 1750	40	20		
1-8-3	Kaolinite	*in situ*	T1500	30	→	1300	50	10	10	5	532	2	100	300	100-1725	1	100		
1-8-4a	Kaolinite	*in situ*	T1500	RT	→	600	100	10	10	5	532	1	100	300	100-1730; 3200-4300	1	200		Chap. 5
1-8-4b	Kaolinite	*in situ*	T1500	600	→	1400	10	10	200	5	532	2	100	300	100-1730	1	200		Chap. 5
1-8-5	Kaolinite	*ex situ*	T1500	RT,700,1000,1300°C							532	1	100	300		1	300		
1-9-1	CaO	*in situ*	T1500	30	→	1030	10	10	10	5	532	2	200	300	100-4000	1	100		
1-9-2	CaO	*in situ*	T1500	30	→	250	10	10	10	5	532	2	100	300	100-1730	1	100		
1-9-3	CaO	*in situ*	T1500	30	→	250	10	10	10	5	532	2	100	300	100-1730	1	100		
1-9-4	CaO	*in situ*	T1500	30	→	1200	10	10	10	5	532	2	100	300	100-1730	1	100		
1-10-1	fused silica	*in situ*	T1500	30	→	1400	10	10	10	5	532	2	100	300	100-4000	1	100		
1-11-1	Dolomite	*in situ*	T1500	30	→	1400	10	10	10	5	532	2	100	300	100-4000	1	100		
1-11-2	Dolomite	*in situ*	T1500	30	→	1400	10	10	10	5	532	2	100	300	100-1730	1	100		
1-12-1	Orthoclase	*in situ*	T1500	30	→	1400	10	10	10	5	532	2	100	300	50 to 1750	1	100		
1-13-1	Anorthite	*in situ*	T1500	30	→	1400	10	10	10	5	532	2	100	300	100-1730	1	100		
1-14-1	Mullite	*in situ*	T1500	30	→	1400	10	10	10	5	532	2	100	300	100-1730	1	100		
1-15-1	Larnite	*in situ*	T1500	30	→	1400	10	10	10	5	532	2	100	300	100-1730	1	100		
1-15-2	Larnite	*in situ*	T1500	30	→	1400	10	10	10	5	532	2	100	300	100-1730	1	100		
1-15-3	Larnite	*in situ*	T1500	30	→	1200	10	10	10	5	532	0,5	100	300	100-1730	1	100		
1-16-1	Calcio-olivine	*in situ*	T1500	30	→	1400	10	10	10	5	532	2	100	300	100-1730	1	100		
1-16-2	Calcio-olivine	*in situ*	T1500	30	→	1400	10	10	10	0	532	2	100	300	100-1730	1	100		
1-17-1	Diamond	*in situ*	T1500	30	→	800	10	50	?	?	532	0,15	100	1000	1290 to 1713	1	180		[59]
1-17-2	Diamond	*in situ*	T1500	700	→	800	10	50	?	?	532	0,15	100	1000	1290 to 1713	1	180		
1-18-1	Al_2O_3 fused	*in situ*	T1500	30	→	1400	10	10	10	5	532	2	100	300	100-1730	1	100		
1-19-1	Anatase	*in situ*	T1500	30	→	1130	10	10	10	5	532	0,1	100	300	100-1730	1	100		
1-20-1	Corundum	*in situ*	T1500	30	→	1300	10	10	10	5	532	2	100	300	100-1730	1	100		
2-3 CaO-Al_2O_3-SiO_2																			
2-3-1	Kln-CaO stoich	ex situ	Nabertherm	800				10?	120		532	2	100	300	100-1725	0,5	1	221x221	1
2-3-2	Kln-CaO	ex situ	Nabertherm					10?	120		532	2	100	1283	100-1725	0,1	1	341x341	1
2-3-3	Kln-CaO 1:1	*in situ*	Nabertherm																
2-3-4	Kln-Cal stoich	*in situ*	T1500	700	→	1200	50	10	10	120x2	532	2	200	300	100-1725	Swift 0.6		100x100	1
2-3-5	Kln-CaO stoich	*in situ*	T1500	700	→	1200	50	10	10	120x2	532	2	200	300	100-1725	Swift 0.6		100x100	1
2-3-6	Kln-Cal stoich	*in situ*	T1500	750	→	950	100	10	10	100	532	2	100	300	100-1730	Swift 0.5		41x41	1
2-3-7-1	Kln-Cal 1:1	*in situ/quench*	T1500	700	→	1200*	100	10	10	375	532	2	200	300	100-1730	Swift 1 s		150x150	1
2-3-7-2	Kln-Cal 1:1	*in situ/quench*	T1500	700	→	1200*	100	10	10	375	532	2	200	300	100-1730	Swift 1 s		150x150	1	[170]
2-3-8	Kln-Cal	*in situ*	T1500	1000	isotherm			10	10		532	2	200	300	100-1730	Swift 1 s		100x100	1
2-3-9	Kln-Cal	*in situ*																	
2-3-10	Cal-Al2O3+SiO2 fused	*in situ*	T1500	700	→	1200	50	10	10	120x2	532	2	200	300	100-1725	Swift 0.6		100x100	1
2-3-11	Kln-Cal 1:1	*in situ*	T1500	700	→	1200	50	10	10	120x2	532	2	200	300	100-1725	Swift 0.6		100x100	1
2-3-12	Cal-Al2O3+SiO2 fused	*in situ*	T1500	700	→	1200	50	10	10	120x2	532	2	200	300	100-1725	Swift 0.6		100x100	1
2-3-13	Kln-Cal 1:1	*in situ*	T1500	700	→	1200	50	10	10	120x2	532	2	200	300	100-1725	Swift 0.6		100x100	1
2-3-14	Kln-Cal 1:1	*in situ*	T1500																

2-3-15	Kln-Cal 1:1	*in situ*	T1500	800 (750)		isotherm		10	10	120x24	532	2	200	300	100-1725	Swift	0.6	100x100	1	[170]
2-3-16	Kln-Cal 1:1	*in situ*	T1500	950 (886)		isotherm		10	10	120x24	532	2	200	300	100-1725	Swift	0.6	100x100	1	
2-3-16-2	Kln-Cal 1:1	*in situ*	T1500	950 (885)		isotherm		10	10	131x24	532	2	200	300	100-1725	Swift	0.65	100x100	1	[170]
2-3-17	Kln-Cal 1:1	*ex situ*	T1500	885°C		isotherm			10	2880x1	532	0,5	200	300						
2-3-20	Kln-Cal 1:1	*in situ*	T1500	850 (803)		isotherm		10	10		532	2	200	300	100-1725	Swift	0.6	100x100	1	Chap. 4, [170]
2-3-21	Kln-Cal 1:1	*in situ*	T1500	900 (843)		isotherm		10	10		532	2	200	300	100-1725	Swift	0.6	100x100	1	Chap. 4, [170]
2-3-22	Kln-Cal 1:1	*in situ*	T1500	1000 (931)		isotherm		10	10		532	2	200	300	100-1725	Swift	0.6	100x100	1	Chap. 4, [170]
2-3-23-2	Kln-Cal 1:1	*in situ*	T1500	950 (880)		isotherm		10	10	120x24	532	2	200	300	100-1725	Swift	0.6	100x100	1	Chap. 4
2-3-24	Kln-Cal 1:1	*in situ*	T1500	1050 (971)		isotherm		10	10	120x24	532	2	200	300	100-1725	Swift	0.6	100x100	1	Chap. 4
2-3-25	Kln-Cal 1:1	*in situ*	T1500	1100 (1017)		isotherm		10	10	120x24	532	2	200	300	100-1725	Swift	0.6	100x100	1	
2-3-25-2	Kln-Cal 1:2	*in situ*	T1501	1100 (1020)		isotherm		10	10	120x24	532	2	200	300	100-1725	Swift	0.6	100x100	1	Chap. 4
2-4 CaO-SiO_2																				
2-4-1	Qtz-Cal	*ex situ*	Nabertherm	800*	-	-	-	10	-	120	532	2	100	300	100-1725	0.5	1	261x261	1	
2-4-2	Qtz-CaO	*ex situ*	Nabertherm	1200*	-	-	-	10	-	120	532	2	100	1200	100-1750	0.1	1	341x341	1	
2-4-3	Qtz-CaO 1:1	*in situ*	T1500	700	→	1200	50	10	10	-	-	-	-	-	-	-	-	-	-	Chap. 7
2-4-4	Qtz-CaO 1:1.01	*in situ*	T1500	700	→	1200	50	10	10	120x2	532	2	200	300	100-1725	Swift	0.6	100x100	1	Chap. 7, [196,203]
2-4-5	Qtz-Cal 1:1.03	*in situ*	T1500	700	→	1200	50	10	10	120x2	532	2	200	300	100-1725	Swift	0.6	100x100	1	[196,202,203]
2-4-6	Qtz-CaO 1:1.09	*in situ*	T1500	700	→	1200	50	10	10	120x2	532	2	200	300	100-1725	Swift	0.6	100x100	1	Chap. 7, [196,202]
2-4-7	Qtz-CaO 1:1.05	*in situ*	T1500	400	→	1200	50	10	10	120x3	532	2	200	300	100-1725	Swift	0.6	100x100	1	[196]
2-4-8	Qtz-Cal 1:0.61	*in situ*	T1500	700	→	1200	50	10	10	120x2	532	2	200	300	100-1725	Swift	0.6	100x100	1	
2-4-9	fused silica + Cal 1:0.95	*in situ*	T1500	700	→	1200	50	10	10	120x2	532	2	200	300	100-1725	Swift	0.6	100x100	1	Chap 7, [196,202,203]
2-4-10	Qtz-Cal 1:0.61	*in situ*	T1500	1000	→	400	50	10	10	120x2	532	2	200	300	100-1725	Swift	0.6	100x100	1	[196,202]
2-4-14	fused silica + CaO 1:1.07	*in situ*	T1500	700	→	1200	50	10	10	120x2	532	2	200	300	100-1725	Swift	0.6	100x100	1	Chap. 7, [196]
2-4-15	Qtz-Cal 0.8:1	*in situ*	T1500	700	→	1200	50	10	10	120x2	532	2	200	300	100-1725	Swift	0.6	100x100	1	[196]
2-4-17	Qtz-Cal single grains	*ex situ*	T1500	850		isotherm		10	10	120x10	532	0,3	200	300	100-1725	Swift	0.6			
2-4-18	Qtz-CaO 1:1	*in situ*	T1500	900		isotherm		10	10	120x10	531	2	200	300	100-1725	Swift	0.6	100x100	1	
2-4-18-2	Qtz-CaO 1:2	*in situ*	T1500	900 (848)		isotherm		10	10	120x13	532	2	200	300	100-1725	Swift	0.6	100x100	1	[60]
2-4-19	fused silica + Cal 1:1	*in situ*	T1500	900		isotherm		10	10	120x13	532	2	200	300	100-1725	Swift	0.6	100x100	1	
3 Multi-phase experiments																				
3-1-1	$Kln_{60}+Qtz_{15}+Cal_{25}$	*in situ*	T1500	700	→	1200	50	10	10	120x2	532	2	200	300	100-1725	Swift	0.6	100x100	1	Chap. 6
3-2-1	$Kln_{40}+Qtz_{15}+Al_2{}_0+Cal_{25}$	*in situ*	T1500	700	→	1200	50	10	10	240	532	2	200	300	100-1725	Swift	1	100x100	1	
4 Methodical experiments																				
4-1-1	3D effect	*ex situ*	T1500	700	→	1200-q	50	10	10	120x10	532	2	200	300	100-1725	Swift	0.6	100x100	1	[60]
4-1-2	3D effect	*ex situ*	T1500	700	→	1200-q	50	10	10	120x10	532	2	200	300	100-1725	Swift	0.6	100x100	1	[60]
4-2-1	depth resolution h-x-y	*ex situ*	T1500	700	→	1200-q	50	10	10	120x10	532	2	200	100 to 1300	100-1725	Swift	0.6	100x100	1	[60]
4-2-2	depth resolution z-y	*ex situ*	T1500	700	→	1200-q	50	10	10	120x10	532	2	200	300	100-1730	Swift	0.6		1	
4-2-3	depth resolution h-z-y	*ex situ*	T1500	700	→	1200-q	50	10	10	120x10	532	2	200		100-1730	Swift	0.6	100x100	1	
4-4-1	depth resolution h-z-y	*in situ*	T1500	1200	isotherm						-	-	200	300	100-1730	Swift	0.6	100	1	
4-3-3a	line scan y-z	*ex situ*	T1500	700	→	1200-q	50	10	10	120x10	532	2	200	300	100-1730	1	10	100	1	
4-3-3b	line scan y-z	*ex situ*	T1500	700	→	1200-q	50	10	10	120x10	532	2	200	300	100-1730	1	10	100	1	
4-4-1	black body radiation h-x-y	*in situ*	T1500	1200	isotherm						532	2	200		100-1730	Swift	0.6		1	
0 Test experiments																				
0-1	T8	*in situ*	T1500								532	2	100	1000	102-1741	0,25	4			
0-2	T8	*in situ*	T1500	RT,300,550,600,650,RT				5			532	2	100	1000	102-1741	0,1	20	81x81	1	
0-3	T8	*in situ*	T1500												102-1741					
0-4	T8	*in situ*	T1500	800	→	900	5;10	200	200	10	532	2	100	1000	102-1741	Swift	0.5	55x55;26x51	1	
0-5	F-Exp	*in situ*	T1500	800	→	1000 (1100)	100	5	50	10	532	2	200	1000	102-1741	Swift	0.5	45x45	1	[59]
0-6	TPC	*in situ*	T1500	600	→	1050	50	5	50	10	532	2	200	1000	102-1741	Swift	0.5			
0-7	S-Exp	*in situ*	T1500	800	→	1160	10	5	50	1200x6	532	2	200	1000	102-1741	Swift	0.5	40x40;90x90	1	[59]

0-8	Q-Exp	*ex situ*	T1500	700	→***	1100	100	10;5	50	120	532	2	200	1000	135-1769	Swift	0.5		90x90	1	[59]
0-9	Black body radiation	*in situ*	T1500	500	→	1200	100	5			532	2	100	1000	102-1741	0,1	20				